11 EXPERIMENTAL FACILITIES

11.1 Introduction

In this chapter, we discuss the conceptual design for the experimental facilities at NSLS-II. These facilities, and the planning for them, have driven and informed the design of both the conventional facilities and the accelerator complex.

We first address beamline development at NSLS-II (Section 11.2). Next we address issues that will confront all beamlines (Section 11.3), including issues of heat load and standard components. We note here that it is expected that at NSLS-II the facility will play an active role in the design and management of most of the beamlines. A benefit of this approach will be the standardization of various components across all similar beamlines.

It is anticipated that each beamline will be optimized for a particular technique—an approach that has proven to be efficient for producing high scientific output. These beamlines will be chosen through a rigorous peer-reviewed process and with the active participation of the user community. The beamlines are likely to be funded through a variety of mechanisms, including the construction project itself, other DOE funding, funding from other federal agencies, and from other sources. In all cases, the facility will play a major role in determining beamline capabilities and design, and ensuring that the development of the beamline portfolio is consistent with the overall strategic plan for the usage of the facility.

Prior to this full peer-reviewed process, we have chosen in the CDR to discuss the design constraints and capabilities for a number of likely beamlines. In particular, we discuss the conceptual design for five beamlines at a reasonably detailed level. These beamlines have been chosen as examples of high-performance beamlines that will take maximum advantage of the state-of-the-art characteristics of the NSLS-II beam. These beamlines would: 1) probe physical and electronic structures with a spatial resolution of 1 nm (Section 11.4, A Hard X-Ray Nanoprobe Beamline); 2) measure excitations in condensed matter, with resolutions down to 0.1 meV (Section 11.5, An Inelastic X-Ray Scattering Beamline); 3) measure the dynamics of soft-matter systems on timescales of microseconds, and image nanostructures to sub-nm precision (Section 11.6, An X-Ray Coherent Scattering Beamline); 4) probe electronic orderings and excitations in transition metal compounds (Section 11.7, A Soft X-Ray Resonant Scattering and RIXS Beamline); and 5) use soft x-rays to image a wide range of samples from biological to chemical to electronic systems, with ~10 nm spatial resolution (Section 11.8, A Soft X-Ray Coherent Scattering Beamline).

Note that the precise missions of these beamlines will likely evolve as their scientific goals and required technical capabilities are further refined by continued interactions with the user community.

Ultimately, of course, NSLS-II will feature a full complement of beamlines serving a wide variety of techniques and user communities. To design the NSLS-II facility appropriately for future development, it is necessary to consider the requirements for these additional beamlines that might have an impact in the conceptual design of the accelerator and conventional facilities. Examples of these requirements include specialized insertion devices for high-energy x-rays, ultra-long beamlines for imaging purposes, beamlines with a particular need for a suite of labs for biological purposes, and so on.

To ensure that the impact of these requirements is properly taken into account, we have carried out conceptual designs of several such beamlines or techniques. Again, the intent here is not that these will be the first beamlines built outside the project scope or that these have the strongest scientific case, but, rather, to explore their implications for the design of the NSLS-II accelerator and conventional facilities.

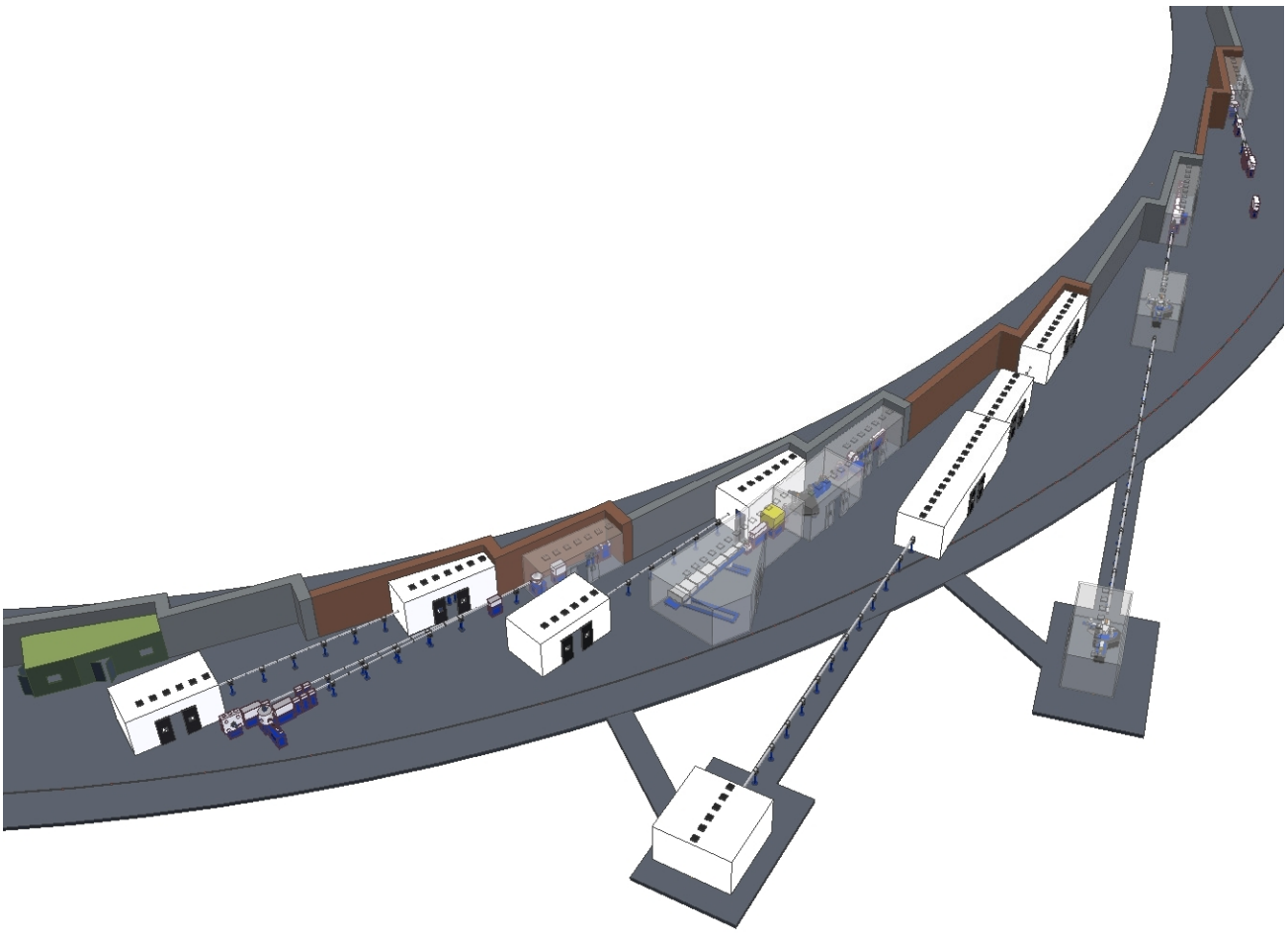

Figure 11.1.1 The experimental floor at NSLS-II showing a number of beamlines. Included here, purely for illustration purposes, are two soft x-ray insertion device beamlines, two bending magnet beamlines, an IR beamline (green enclosure), and three hard x-ray insertion device beamlines.

11.2 Beamline Development at NSLS-II

In this section, we outline the mechanisms and strategies for developing, constructing, and operating the full portfolio of beamlines at NSLS-II. In particular, the guiding philosophy that will be used to develop the strategic plan for NSLS-II will be discussed. In addition, the fully built-out capabilities of the facility are presented, together with a possible distribution of uses of the facility. This latter is purely for the purpose of illustrating the capabilities of the facility. The actual use of the various ports will be determined in the context of a strategic plan that will be developed in the coming years through a process of consultations with the various stakeholders, including the user community, advisory committees, funding agencies, and facility staff.

11.2.1 Strategy for Beamline Development

As a newly constructed third-generation synchrotron, NSLS-II will face a number of challenges and opportunities in developing its beamline portfolio. Specifically, it will be important to optimize the use and maximize the scientific output of the facility to ensure that important needs are addressed and that capabilities are not omitted or needlessly duplicated. To achieve this end, a strategic plan for the use of the facility will be created to guide the development of the portfolio of scientific programs and the experimental facilities

required to support them. As a general philosophy, we anticipate that each beamline will be optimized for a particular technique in order to maximize productivity.

Decisions on approval to construct and operate a particular type of beamline will be made in the context of this overall strategic plan. In addition, the needs and interests of the existing large user community of the current NSLS must be considered in planning for NSLS-II. Their presence means that it is very desirable for the user capacity of NSLS-II to ramp up significantly faster than at other "green field" new facilities without existing user communities. In order to accelerate the growth of user capacity, the strategic plan for NSLS-II will therefore consider opportunities to transition programs and, in some cases, hardware, from NSLS to NSLS-II.

An important component of the strategic plan will be the funding avenues for beamline construction, a number of which are anticipated. The first of these is through the construction project itself. A suite of beamlines will be built as part of the NSLS-II construction project and will deliver state-of-the art user facilities when NSLS-II is commissioned. These beamlines will be constructed and operated by the facility. Beamline Teams will guide the development of these beamlines, as discussed in Section 11.2.1.1. The precise scientific mission, and required capabilities, of beamlines will be determined by continued interaction with the user community.

It is anticipated that a second source of funding for beamline construction will be provided by DOE in the form of Major Items of Equipment (MIE) proposals, and that the facility will bundle a number of beamline proposals together and propose multiple, sequential MIEs to DOE. These will be submitted as early as possible. The MIEs are expected to fund the construction of beamlines that meet needs relevant to the BES mission of DOE. These beamlines would also by guided by BTs and be built and operated by the facility.

A third source of funding that is anticipated is funding from sources other than DOE-BES. Examples include funding from other federal agencies, such as NIH, DOE–BER, DoC, DoD, NSF, and funding from industrial companies. Such sources may fund either specialized equipment, such as end stations, or entire beamlines. In the latter case, the beamline would also by guided by a BT.

11.2.1.1 Beamline Teams

BTs are teams formed to advise the facility on the construction and operation of beamlines. The teams are expected to be comprised of a relatively small number of people who are committed to establishing a beamline to serve a well defined scientific mission. BT members will be closely involved in the specification and design of the beamline and end stations. They will interact strongly with the expected user community—for example through annual workshops—and will be responsive to that community's needs.

BTs will be selected by the facility on the basis of scientific impact, quality of the team, alignment with the NSLS-II strategic plan, utilization of NSLS-II, technical feasibility, and community need. A call for Letters of Intent, LOIs, from potential BTs is expected to be issued shortly after a positive CD-1 decision. Following submission, the various LOIs will be reviewed by the facility and by the Experimental Facilities Advisory Committee (EFAC), who may also chose to utilize external peer review. Upon selection, the BT will work with facility staff to pursue funding and to oversee the beamline design, construction, and commissioning, to ensure that it optimally meets the scientific requirements.

11.2.2 Facility Usage

NSLS-II will have 27 straight sections available for user insertion devices (of the remaining three, one is used for injection and two for RF systems). Of these 27 straight sections, 15 will be 5 m straights and 12 will be 8 m straights. The 5 m straights are expected to be populated with undulators of various types, while most of the 8m straights will be likely populated with damping wigglers and undulators. Of the damping wigglers, the initial build-out is expected to include three 7 m devices. The fully built-out facility would likely include

eight 7 m devices for a total length of 56 m. These devices are likely to be extremely attractive for a large number of users, offering high flux and broad spectra.

Clearly, optimizing the use—and location—of the varied devices that will populate the ring is a many-variable problem. Further enriching the picture is the potential to "cant" devices, allowing multiple devices to be located in a single straight section. With these constraints in mind, we have constructed a picture for the fully built-out facility to illustrate its capacity and provide a guide to its capabilities, and to ensure that the various user communities' needs are met. In doing so, we have used the existing NSLS suite of instruments, user demand, and productivity—as well as the capabilities of existing sources around the world - as a guide to the requirements of the mature facility.

In this strawman arrangement, we have assigned beamlines to particular disciplines and techniques, taking into account such factors as user demand, NSLS-II capability, physical constraints (imposed by the layout of the accelerator), site constraints (for example, possible long beamlines that extend beyond the experimental floor), and scientific constraints (beamlines that address related science questions or use similar techniques are grouped together). This is not meant to reflect any decisions that have been made as to the future development of beamlines, but rather it is an exercise to show the range and capacity of science programs that NSLS-II could host.

Table 11.2.1 summarizes this distribution, where the beamlines have been categorized according to the classification scheme currently in use at NSLS. While these categories are somewhat ambiguous in certain cases, this table nevertheless serves the useful purpose of allowing a comparison with the beamline distribution of the existing NSLS, a mature facility. It shows that NSLS-II can provide a comparable number of beamlines as the NSLS x-ray and VUV rings together provide, when the possibility of canting is included, while providing a similar range of capabilities. The difference, of course, is that at NSLS-II many of the beamlines will be served by insertion device sources (either undulators or wigglers) and therefore will be orders of magnitude brighter than the bending magnet sources currently serving most beamlines at NSLS. Even beamlines served by bending magnets at NSLS-II will be vastly superior to those at NSLS.

Table 11.2.1 Possible Distribution of Beamlines at NSLS-II by Beamline Type. A comparison is made with the existing NSLS facility using the same classification scheme.

		NSLS-II			NSLS		
Category	**Type**	**IDs**	**BMs**	**Total**	**IDs**	**BMs**	**Total**
A	IR/UV/Soft x-ray spectroscopy	1	11	12	3	7	10
B	x-ray spectroscopy	6	3	9	0	9	9
C	soft matter/biophysics scattering	4	0	4	0	8	8
D	hard matter/strongly correlated scattering	9	1	10	3	5	8
E	powder/single crystal/high P/optics	7	3	10	3	8	11
F	Imaging/micro-probe	4	5	9	2	7	9
G	macromolecular crystallography	7	0	7	2	8	10
		38	23	61	13	52	65

The distribution of the beamlines around the ring is shown graphically in Figures 11.2.1 and 11.2.2, which represent the insertion devices and bending magnet usage, respectively.

Although NSLS-II is expected to have a similar number of beamlines as NSLS, the high brightness is expected to increase the throughput of users dramatically for certain types of experiments. Based on this and extrapolating from the current user population of ~2400 users/year at the current NSLS, we estimate that NSLS-II will be able to host ~3500 or more users/year. There is ample evidence from current beamtime oversubscription rates to expect that demand for beamtime at NSLS-II will exceed even this level of service.

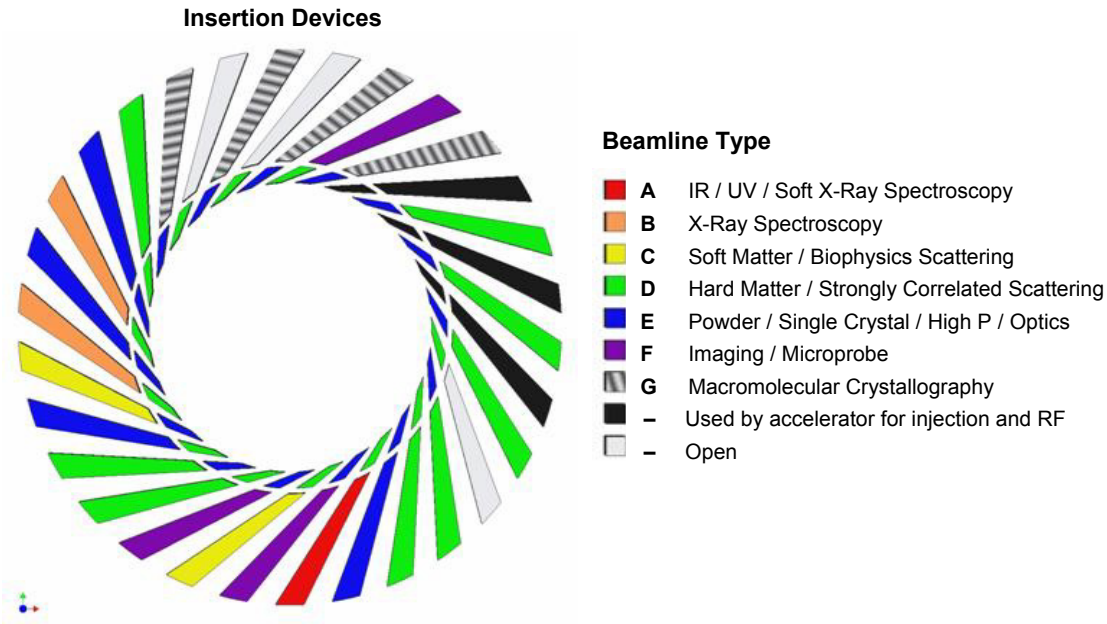

Figure 11.2.1 Possible use of insertion devices, by beamline type at NSLS-II. The inner ring is color coded by the straight section type, with blue indicating 5 m straights, green indicating 8 m straights, and black representing the RF and injector straights that are not available to the user program. Open beamlines are not assigned in this scheme.

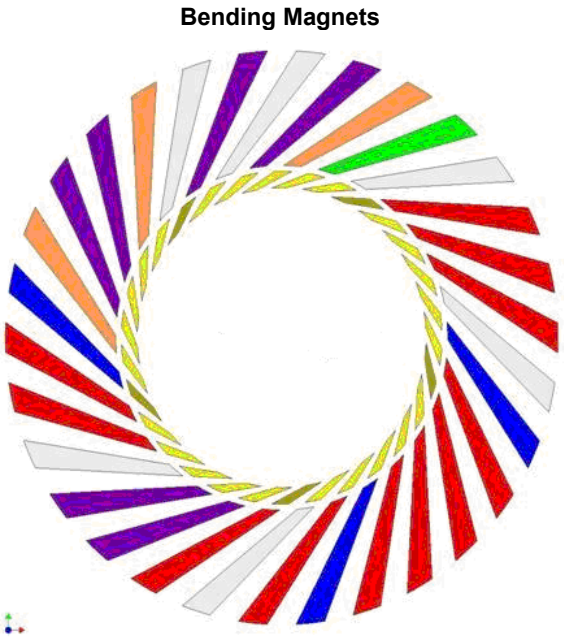

Figure 11.2.2 Possible use of bending magnet beamlines, using the same color key as Figure 11.2.1. The inner ring represents the bending magnet sources, with darker segments signifying large gap dipoles for far-IR sources.

11.3 Standard X-Ray Beamline Components

Standard x-ray beamline components that are addressed in this section consist of filters, slits, photon shutters, double-crystal monochromators, and focusing mirrors. Of these components, the double-crystal monochromators and focusing mirrors have the greatest importance, complexity, and cost.

11.3.1 Double-Crystal Monochromator

Nearly all x-ray beamlines at NSLS-II, regardless of radiation source, will include a double-crystal monochromator in their design. Designs for these are very mature and several commercial versions are available that could satisfy the needs of NSLS-II beamlines. Most monochromators will employ silicon crystals using the (111), (220), or (311) Bragg reflections; some monochromators might employ diamond crystals using the (111) Bragg reflection. For accessing low photon energies, crystals that have larger lattice parameters than silicon or diamond will need to be used, such as germanium, indium antimonide, or, for the lowest photon energies (down to about 1 keV), beryl and YB_{66}. In most cases, both crystals used in the monochromator will be flat, but in some applications the second crystal will be sagittally bent to focus the x-ray beam horizontally. Proven crystal benders are also available commercially.

The mechanics of double-crystal monochromators allow the crystal pair to rotate to provide a range of incidence angles, from a few degrees to as much as 70 degrees, yet still preserve the exit height of the doubly diffracted beam.

Thermal considerations dominate the design aspects of modern double-crystal monochromators, and in view of the extremely high power and power densities of NSLS-II insertion device beams, we will focus most of our attention on these considerations. Thermal issues are associated not only with the first crystal that is impacted by the direct white beam, but also with the second crystal, which may be subjected to parasitic Compton scattered beam from the first crystal and from elsewhere. Appropriate scatter shields and, if necessary, cooling of the second crystal can address the latter effects, but to properly handle the incident heat load on the first crystal requires special measures, usually cryogenic cooling of silicon or the use of water-cooled diamond. In most cases, cryogenic cooling of silicon is employed, usually with liquid nitrogen but sometimes with closed-cycle circulating gaseous helium. This last option is employed on four existing NSLS insertion device beamlines. We anticipate that NSLS-II monochromators that employ cryogenically cooled silicon crystals will use liquid nitrogen. Several recent studies [11.3.1] have established the acceptability of liquid-nitrogen cooled silicon crystal monochromators at higher energy third-generation synchrotron sources, with incident power levels of up to several hundred Watts. Commercial cryogenic cooling systems that are specifically optimized for use with x-ray monochromators are available.

11.3.1.1 Cryogenically Cooled Silicon Monochromator

To gain an understanding of how a cryogenically cooled silicon crystal will be able to withstand NSLS-II ID beams having power levels that are unprecedented for a lower energy, third-generation synchrotron sources. We have examined the performance of a variation of a cryogenically cooled silicon crystal design used on several undulator beamlines at APS, the so-called “hockey puck” crystal design [11.3.2]. The top surface of this crystal is polished and serves as the diffracting surface, and the crystal is cooled from below with flowing liquid nitrogen that makes direct contact with the underside of the crystal, which must therefore be clamped onto a support and sealed. Beneath the crystal are large fins that are in contact with the flowing liquid nitrogen, to enlarge the cooling surface area, Figure 11.3.1. The version of this design that is used at APS includes a milled-out channel beneath the top diffracting surface, to allow the high photon energy components of the APS undulator spectrum to transmit through the diffracting surface and continue past the monochromator, reducing the power absorbed by the crystal. The NSLS-II undulator spectrum will be of much lower energy and the power will be absorbed completely in the top layer of the crystal; therefore, the milled-out channel is unnecessary and has been “filled in” in the design that we are modeling.

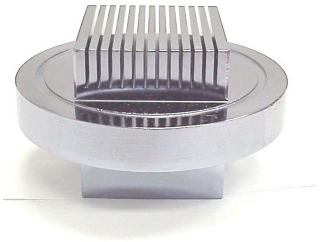

Figure 11.3.1 Photo of a "hockey puck" silicon crystal, upside down. Because it is resting on its diffracting surface, the cooling fins appear on top. The round portion of the crystal clamps onto a cooling manifold, and the circular groove contains a gasket that serves as the seal.

We have carried out initial worst-case calculations based on the 14 mm period superconducting undulator. At 30 m from the source position (a typical monochromator position), the power density for this device can exceed 100 W/mm^2. In this position it has a power of >400 W in a useful beam cross-section 2.4 mm wide and 1.5 mm high. (This is the 4σ beam size for the undulator's fifth harmonic at 8.9 keV, for which the undulator would operate at its highest K, 2.2.) The crystal was subjected to this power load condition (407 W total power) and oriented at an angle of 12.7 degrees to the incident beam, which gives a diffracted photon energy of 8.9 keV for a Si(111) Bragg reflection. Finite element analysis, FEA, shows a maximum thermal slope error, in the scattering plane, of ±10.8 μrad, with the distribution of thermal slope errors in the scattering plane having an RMS value of ~6 μrad. For comparison, the Darwin width for Si(111) at this photon energy is 31.5 μrad. Thus, in this circumstance the thermal distortion is a fraction of the Darwin width, and might be acceptable; its implications are discussed in the following paragraphs. These calculations were repeated after the model was modified with a vacuum isolation window (for hard x-ray beamlines, to separate the storage ring and beamline spaces) of CVD diamond that is 100 μm thick. This window absorbs 16% of the total radiated power in the above-quoted beam dimension, resulting in 343 W of power striking the crystal. The maximum thermal slope error, in the scattering plane, is then ±7.35 μrad, and the slope error distribution has an RMS value of ~4 μrad. Figure 11.3.2 shows the thermal and slope error (in the scattering plane) profiles for these two cases. The maximum crystal temperature is 145K for the unfiltered beam and 127K for the filtered beam; for comparison, the thermal expansion coefficient of silicon crosses zero at 125K.

The implications of these thermal distortions on the brightness of the diffracted beam can be treated individually for each component factor of the brightness, as follows:

Flux. The transmission of flux (compared with the case of no thermal distortion) is given approximately by the ratio of the intrinsic Darwin width to the width of the intrinsic Darwin curve convoluted with the thermal slope error variation; the latter is approximately the quadrature combination of the Darwin width and the RMS thermal slope error. The resulting transmission is about 98% for the unfiltered beam and 99% for the filtered beam. We conclude that the impact of the thermal slope error on the diffracted flux is negligible in either case. Note that the diamond window (100 μm thick) itself absorbs about 10% of the flux at 8.9 keV.

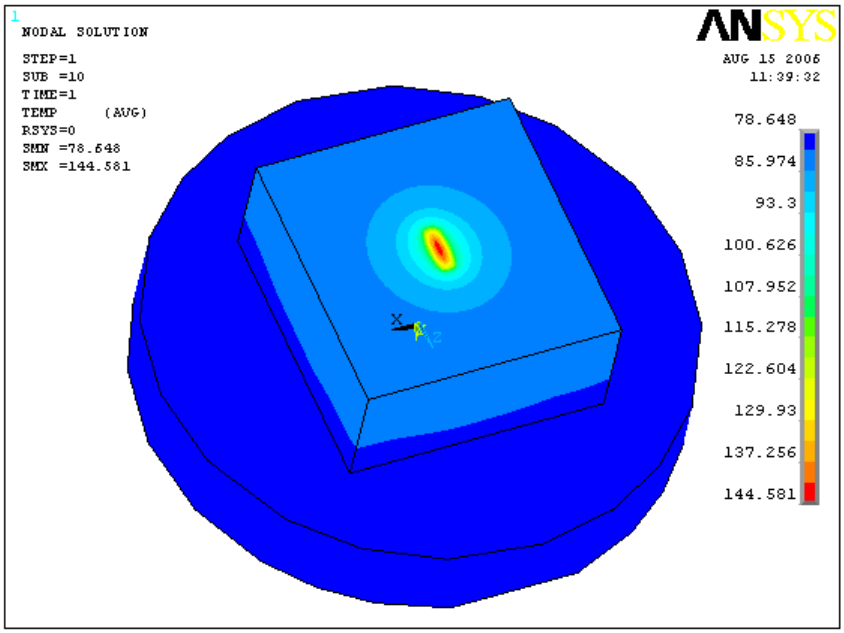

Figure 11.3.2 Profiles of crystal subjected to the NSLS-II undulator power load described in the text.

a)
Thermal profile for unfiltered beam.

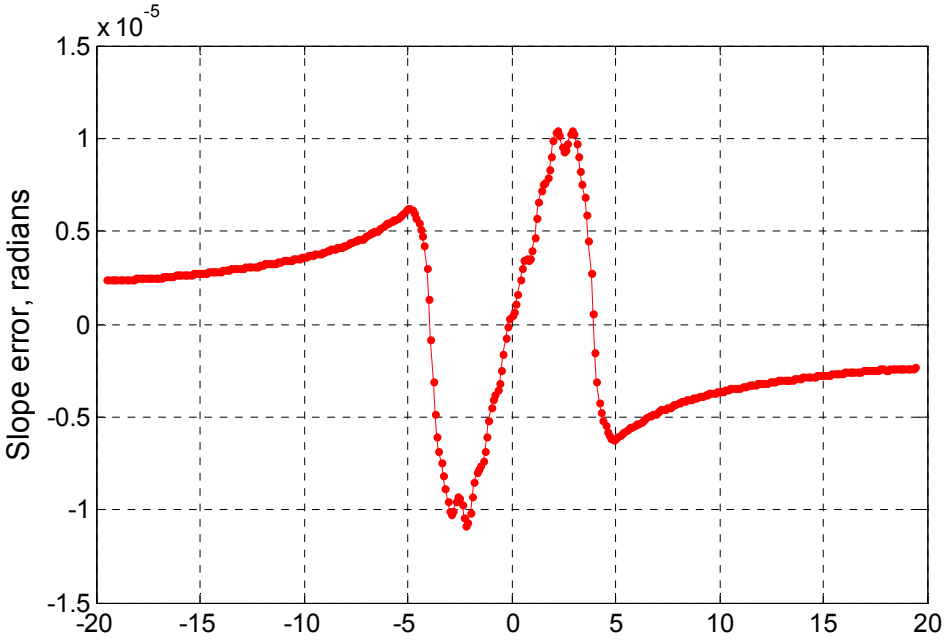

b)
Slope error variation in scattering plane for unfiltered beam. (x-axis is distance from the center in the y-direction, in mm.)

(continues next page)

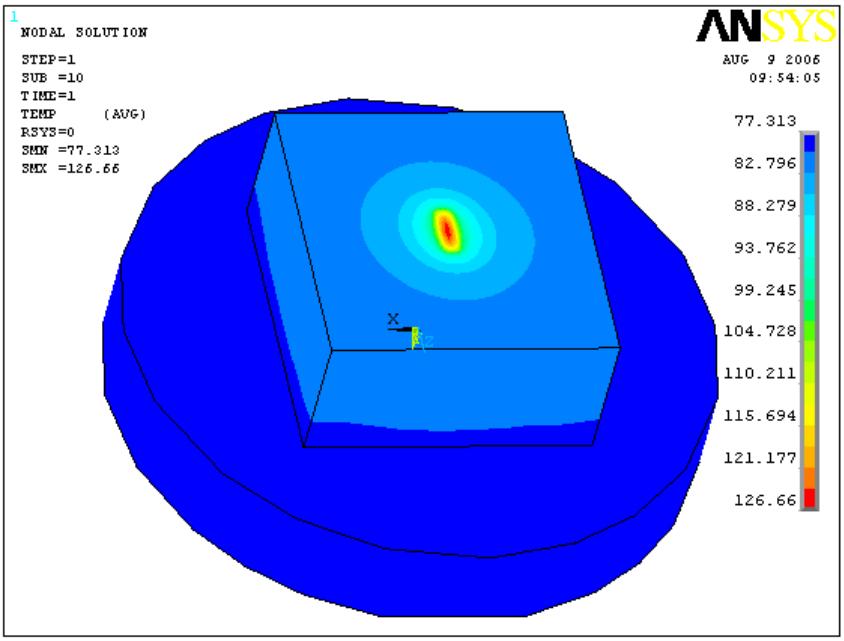

c

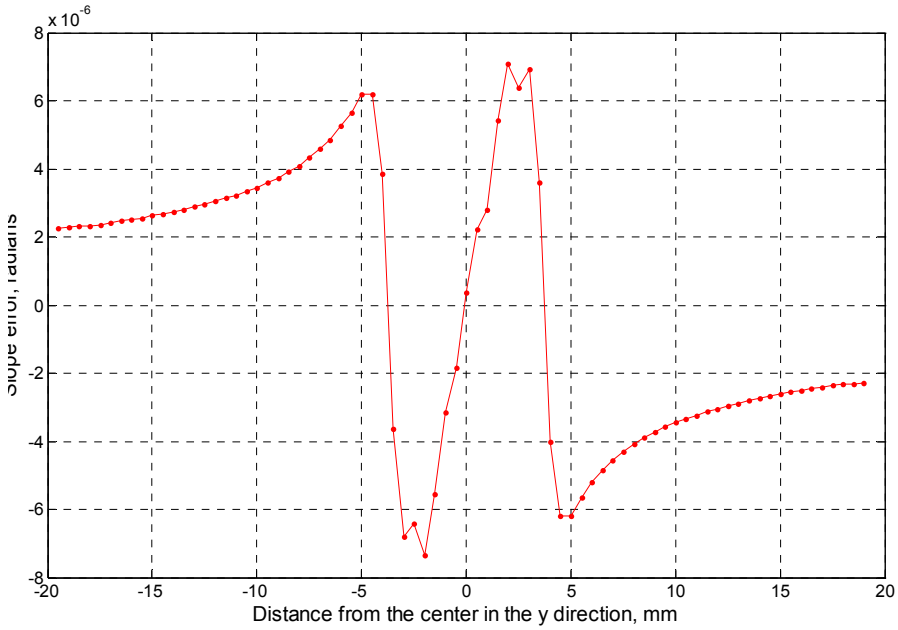

d

Figure 11.3.2 (cont.) Profiles of crystal subjected to the NSLS-II undulator power load described in the text.

c)
Thermal profile for filtered beam.

d)
Slope error variation in scattering plane for filtered beam. The entire extent of the illuminated footprint consists only of the central 6.8 mm in (b) and (d).

Relative wavelength spread. The relative wavelength spread is determined by the range of incidence angles striking the Bragg planes, weighted by the cotangent of the Bragg angle. For flat Bragg planes, the range of incidence angles is given approximately by the quadrature combination of the photon beam opening angle (48 μrad for the case considered here) and the intrinsic Darwin width of 31.5 μrad. When thermal distortion exists, the wavelength spread is broadened further through convolution with the thermal slope error variation. For the cases treated here, the impact is less than 1% and is negligible.

Angular spread. The considerations are the same as for the wavelength spread. The resultant impact of the thermal slope errors calculated for the cases treated here is less than 1% and is negligible.

Position spread. Careful attention must be paid to this aspect of the diffracted beam brightness. Thermal slope errors of monochromator crystal Bragg planes have the same blurring impact on the beam dimension in the vertical plane as mirror figure errors would. It is determined by twice the RMS slope error multiplied by the distance from the monochromator. The effect of a 6 μrad RMS thermal slope error is a blurring of the beam dimension by 240 μm at a distance of 20 m downstream of the monochromator. For an NSLS-II superconducting undulator beamline, these effects might be significant, given that existing state of the art focusing mirrors (with figure errors of 2 μrad or less) will attain vertical focus sizes less than 50 μm. (Mirror issues are discussed in the next section.)

Thus, cryogenic cooling of a silicon monochromator crystal in an NSLS-II superconducting undulator beam appears to be a viable solution to preserving most, but not all, of the aspects of the beam brightness. To compensate the impact of the monotonic thermal distortion variation (see Figures 11.3.2b and d) on the position spread of the diffracted beam in the vertical direction, it should be feasible to mechanically adjust, only slightly, the curvature of the vertical focusing mirror that would typically be used downstream of the monochromator. Such adaptive compensation has been employed successfully in operation of the NSLS beamline X25 for the past 14 years, through mechanical adjustment of the curvature of the silicon crystal [11.3.3]. We will analyze this possibility through ray tracing. Implementing this curvature adjustment method will require the installation of a high-resolution beam profile monitor.

11.3.1.2 Water Cooled Diamond Monochromator

Although less commonly used than silicon, diamond holds particular promise for use as a monochromator crystal in an NSLS-II undulator beam. The superior thermal and mechanical properties of diamond, compared with silicon, are well known, and permit the possibility of using water-cooled, room temperature diamond crystals in high-heat-load applications (although, interestingly, the thermal properties of diamond do also improve at cryogenic temperatures). However, the property that makes diamond more attractive than silicon is its x-ray absorption coefficient. At 8 keV, where NSLS-II undulators would emit substantial power, the 1/e penetration length in diamond is 710 μm, whereas for silicon it is only 70 μm. This is why it is a good approximation to assume that for silicon, the full brunt of the undulator beam power will be absorbed in the top layer of the material. In the case of diamond, however, the absorption of the undulator beam power will be distributed through the material, and if the crystal is thin enough (e.g., ~1 mm), a substantial fraction of the power will be transmitted through the crystal, while the crystal remains thick enough to fully diffract the photon energy of interest. (The required thickness to fully "extinguish" the diffracted x-rays into the reflected beam is several μm.) The resulting thermal distortion of the Bragg planes in the diamond material is reduced significantly, even were diamond's thermal properties to be the same as those of silicon. For these reasons, diamond merits special consideration as a candidate monochromator crystal material in an NSLS-II undulator beamline.

Historically, the major challenge in using diamond crystals in an x-ray monochromator has been the quality of the diamond crystals. Only a few vendors offer diamond crystals of sufficiently high quality. Typically, users must purchase a supply of crystals with no guarantees as to their quality, and determine the quality themselves. Recently, however, ESRF has explored, with a European vendor of synthetic diamond crystals, testing diamond crystals and weeding out crystals of insufficient quality [11.3.4]. The best quality diamonds currently are produced synthetically using a high-pressure, high-temperature process, resulting in crystals of 5–10 mm, from which wafers of perhaps 0.5–1 mm thickness and 5–7 mm cross-section can be sectioned. Wafers with orientation of (001) are the simplest to section and polish, although (111) oriented wafers, which are more useful for monochromators, are also produced. Diamond wafers of this size are relatively costly, typically $20,000 each, and it is usually necessary to purchase extras. The net cost, however, is less than the cost of a cryogenic cooling system.

We carried out initial FEA modeling of diamond crystal monochromators in an NSLS-II undulator beam. The monochromator model is shown in Figure 11.3.3. It consists of a diamond single-crystal wafer of

dimensions 8 mm long (along the beam direction) by 5 mm wide (transverse to the beam direction) by 0.5 mm thick, and is gently clamped atop a water-cooled copper support, using a thin liquid gallium-indium eutectic layer. Because a large fraction of the incident beam power is transmitted by the diamond wafer, the copper support has a hole beneath the crystal wafer that permits the transmitted beam to propagate to a remote beam dump. The hole has dimensions of 6 mm long (along the beam direction) by 3 mm wide (transverse to the beam direction), and therefore there is 1 mm of overlap, all around the hole, between the diamond wafer and copper support, that serves as the thermal contact interface. This design is in use on the Sector 30 (IXS-CDT) undulator beamline at APS. We assumed the same beam parameters as above. For the (111) Bragg reflection of diamond, the Bragg angle at this photon energy is 19.7 degrees. For a diamond wafer 0.5 mm thick oriented at this incidence angle to the undulator beam, 166 W (40% of the total) is absorbed by the crystal and 240 W (60% of the total) is transmitted. In undertaking the calculations, special attention was paid to the volumetric absorbance of the incident beam power; i.e., we did not assume, as we did for the silicon monochromator discussed earlier, that the absorbed power was fully absorbed at the surface layer; we calculated and employed the actual depth profile of the absorbed power.

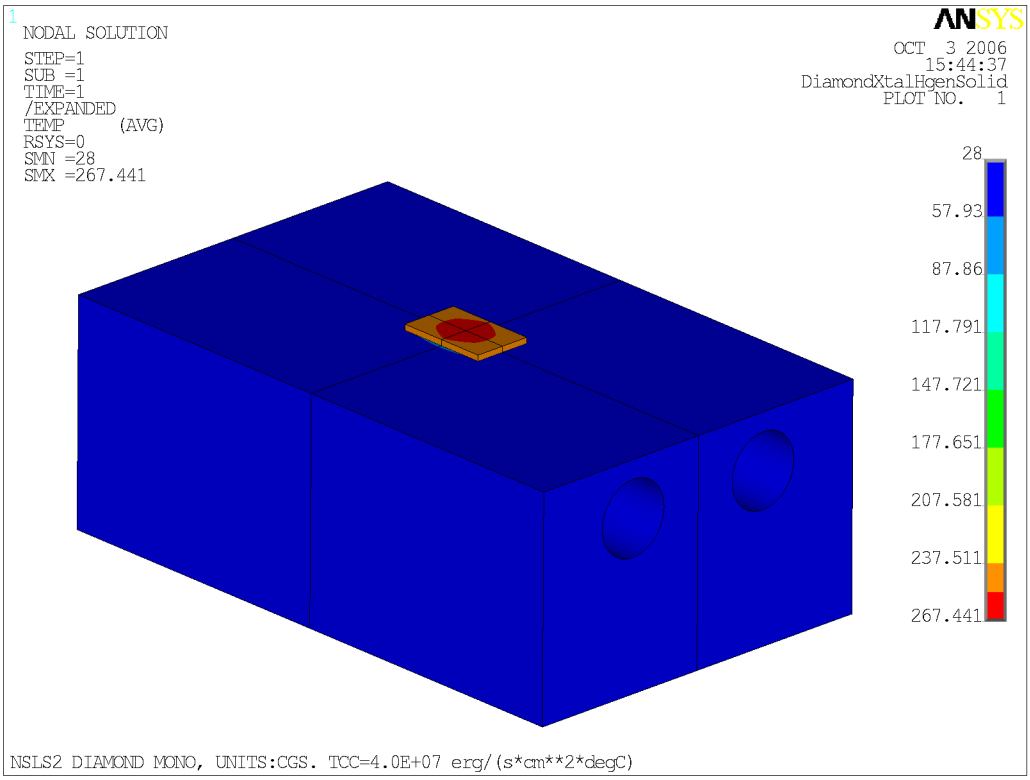

Figure 11.3.3 Model of a diamond wafer atop a water-cooled copper support. The cooling channels through the copper support are shown. The **temperature distribution** is based on the understood heat transfer coefficient of gallium-indium eutectic in contact with solid material.

Figure 11.3.3 shows the calculated temperature distribution in both the diamond wafer and the copper support under these power loading conditions. Of particular note is the enormous difference in temperature between the copper support (which reaches a maximum of 88ºC) and the diamond (which reaches a maximum of 267ºC). This is due to substantial thermal resistance at the interfaces between the gallium-indium eutectic and the diamond, and between the gallium-indium eutectic and the copper; we used a heat transfer coefficient value for these interfaces of 0.04 W/mm^2-ºC [11.3.5]. The resulting diamond wafer thermal distortion map is shown in Figure 11.3.4. Within the beam footprint, the maximum slope error projected into the x-ray scattering plane is ±30 μrad. Compared with the Darwin width of 22 μrad for the (111) Bragg reflection of diamond at 8.9 keV, this is rather severe.

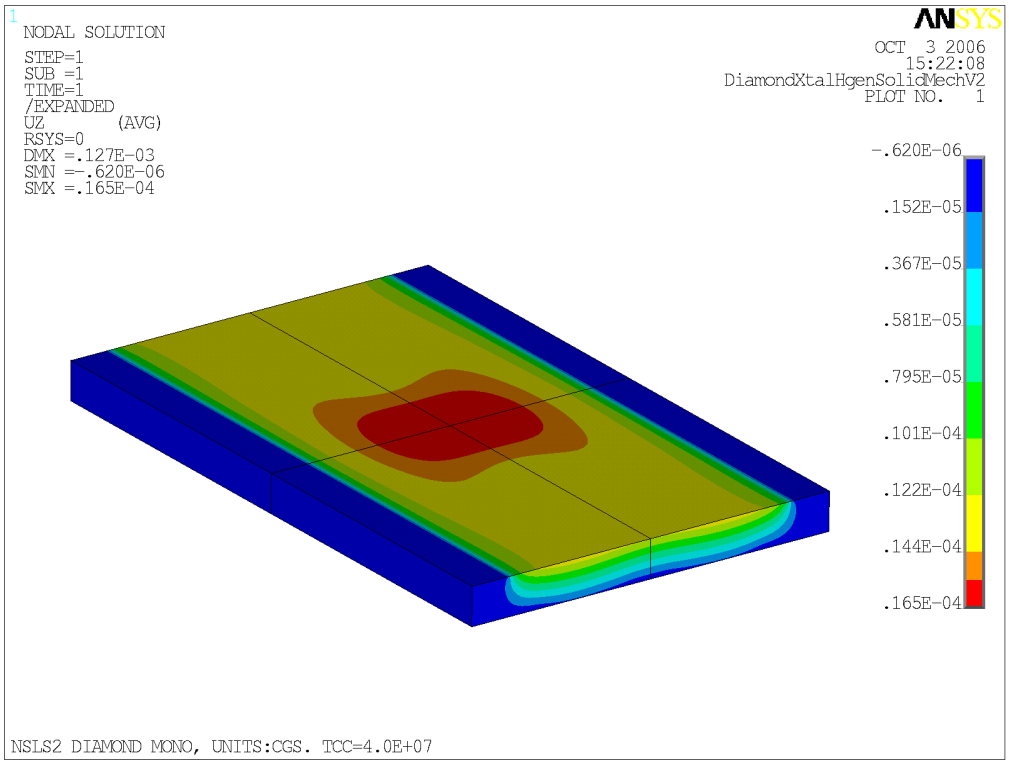

Figure 11.3.4 Calculated **thermal distortion profile** in diamond wafer corresponding to the temperature distribution shown in Figure 11.3.3.

We repeated the FEA calculation after arbitrarily lowering the thermal resistance of the gallium-indium/solid material interfaces, by increasing the heat transfer coefficient by a factor of 10, to 0.4 W/mm^2-ºC, to see what the potential impact of achieving a better thermal contact of the diamond to the copper support via, e.g., brazing might be. The resulting temperature distribution in the diamond wafer is shown in Figure 11.3.5, and its accompanying thermal distortion profile is shown in Figure 11.3.6. The maximum temperature in the wafer is 103ºC (versus 267ºC) and the maximum slope error within the beam footprint projected into the x-ray scattering plane is ±9 µrad (versus ±30 µrad), which is smaller than the (111) Bragg reflection Darwin width. Thus the slope error is greatly improved as a result of the better thermal contact.

This simple exercise reveals the improvement pathways that could be pursued in order to utilize diamond crystal monochromators on NSLS-II undulator beamlines, primarily through measures to reduce the temperature difference between the diamond and its cooled support. The ideal case would be to eliminate the thermal resistance at the interface between the diamond and its support entirely, but this could only be achieved via a monolithic diamond, which is a highly unlikely possibility, although it has been suggested [11.3.6]. More likely measures involve seeking a strain-free braze contact between the diamond and its support, enlarging the contact area (here, the total contact area was 22 mm^2) by obtaining a larger cross-section diamond wafer, or reducing the thickness of the wafer to reduce the absorbed power.

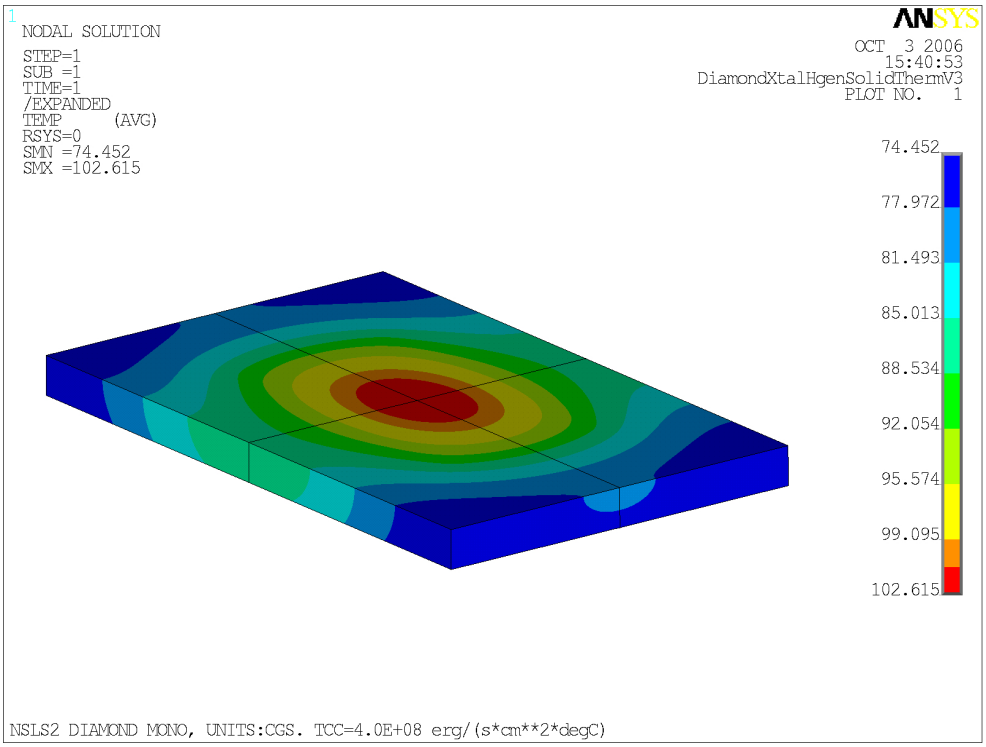

Figure 11.3.5 Calculated **temperature distribution** in diamond wafer assuming a 10 times larger heat transfer coefficient, compared to the distribution shown in Figure 11.3.3.

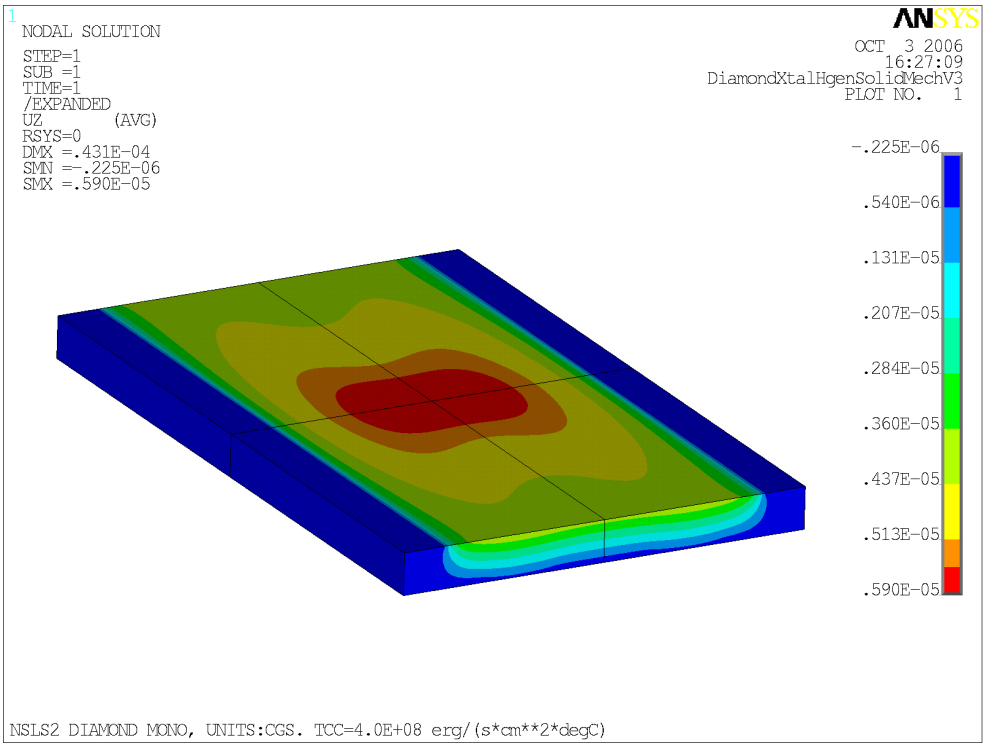

Figure 11.3.6 Calculated **thermal distortion profile** in diamond wafer assuming a 10 times larger heat transfer coefficient, compared to the distribution shown in Figure 11.3.4.

A concern with using diamond crystals is that their small size forces special attention to be paid to the mechanics of positioning the second crystal to center it in the diffracted beam as the monochromator angle is

scanned through its full range. Also, because of diamond's stiffness, its use as a crystal mounted in a sagittal bender that can be curved is rather doubtful.

11.3.2 Focusing Mirror

Many NSLS-II beamlines will use grazing incidence total reflection mirrors to focus the beam in a meridional geometry, with the mirrors used in a monochromatic beam (i.e., downstream of a monochromator). By combining two such mirrors in succession, one to focus the beam horizontally and the other vertically, a low-aberration KB focusing mirror pair configuration is achieved. The low emittance of NSLS-II results in undulator beams of small enough cross-section that KB mirrors with a length shorter than 1 m for horizontal focusing and 0.5 m for vertical focusing could be used. Many commercial versions of such mirrors are available.

To achieve the proper curvature radius (usually several hundred m to a few kilometers) to focus the beam, these mirrors (which are ground and polished flat) are mounted in a bender, that can shape the mirror into a cylindrical or an elliptical cross-section. An example of such a mirror bender system is shown in Figure 11.3.7; this is the focusing mirror system that will be installed on NSLS beamline X25 in the near future. It contains several actuators to orient the mirror and bend it into a cylindrical or an elliptical shape. This particular mirror has a glass substrate and is coated with two different materials, silicon and palladium (each providing a different upper-energy cutoff); other substrates commonly used are silicon and Glidcop, the latter usually for use in a white beam (in which case the mirror is cooled). Either one or the other coating is positioned in the beam at a given time. To realize a KB mirror configuration, two of these in succession are needed, one turned sideways.

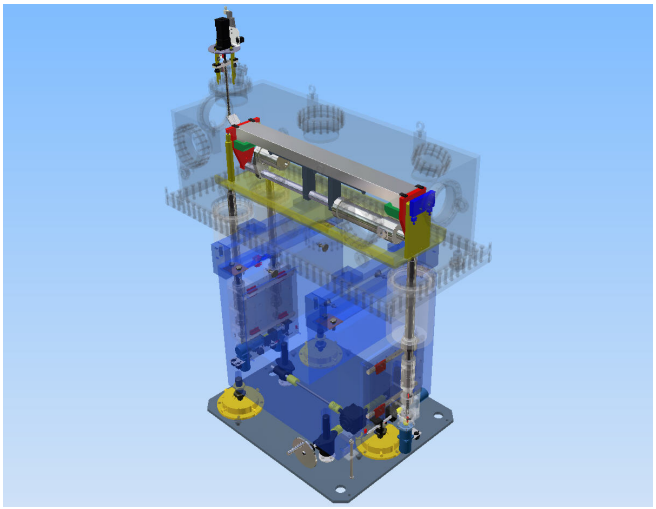

Figure 11.3.7 Focusing mirror system to be installed in the current NSLS beamline X25.

An alternative means of shaping mirrors employs electromechanical methods with segmented bimorph mirrors, where each segment is composed of oppositely biased piezoelectric ceramic plates that are surrounded by polished glass. These mirrors can bend concavely or convexly and be programmed into practically any arbitrary shape. They thereby nullify intrinsic figure errors, to a certain extent, while achieving the desired curvature, through application of an appropriate combination of voltages to the piezoelectric plate electrodes [11.3.7]. These mirror systems also are available commercially, though they tend to be more expensive than conventional, mechanically bent mirrors.

The mirror parameter that will ultimately determine its performance in an NSLS-II beam is figure error. The sensitivity of the performance of an NSLS-II undulator beamline to the figure error is demonstrated in Table 11.3.1. The current mirror figure error, for state-of-the-art mirrors of the size needed for NSLS-II, is ~2 μrad, and there have been recent reports of even smaller figure errors for mirrors of this size; for example, a

figure error of 0.8 μrad was reported for a mirror 78 cm long installed on beamline ID23-1 at ESRF [11.3.8]. In Table 11.3.1, values for the perfect mirror (zero figure error) are shown for comparison, along with intermediate values. The impact of mirror figure error on the performance of the beamline is very clear, particularly in the vertical direction. As discussed in Chapter 12, we have identified challenges and steps that might be taken to achieve sub-100 nrad figure errors in mirror substrates.

Table 11.3.1 NSLS-II Undulator-Based X-Ray Beamline Performance vs. Mirror Figure Error. The red (upper text line in each pair) signifies the "high" demagnification mode for this beamline, and the blue (lower text line) signifies the "low" demagnification mode.

RMS figure error [μrad]	0	0.1	0.5	1.0	2.0
Vertical focus size FWHM [μm]	1.0	2.6	11.8	23.5	47.0
	2.4	6.1	28.3	56.5	112.8
Horizontal focus size FWHM [μm]	15.5	15.8	21.0	32.2	58.5
	33.6	34.2	45.4	69.7	126.7
Monochromatic intensity at 12 keV [ph/s/μm^2]	1.0×10^{13}	4.5×10^{12}	7.9×10^{11}	2.7×10^{11}	7.7×10^{10}
	2.0×10^{12}	8.6×10^{11}	1.5×10^{11}	5.2×10^{10}	1.5×10^{10}

Note: FWHM = Full Width at Half Maximum

11.3.3 Beam Position Monitors

This section addresses beam position monitors that will be used in beamlines for monitoring and stabilizing the position of the monochromatic beam downstream of beamline optics.

A number of beam position monitor designs exist and are in current use, and all of them merit careful attention for use in the NSLS-II beamlines. Commercial versions of these are available. Blade-type monitors have insulated metal blades that graze opposite edges of the beam, and the induced photocurrents in the blades are measured and compared; this indicates the beam position between the blades. This design is intended for use in front ends and could also be used in beamlines. An advantage of this design is that the position monitor material does not intercept the central portion of the beam, which is eventually used in the experimental station. For this reason, blade-type monitors are a good choice for use with VUV or soft x-ray beams. One potential disadvantage of this type is that, because the fringes of the beam are measured, the induced signals in the blades can be very weak, and because the fringes themselves can be diffuse, the position resolution for this design may be modest (up to several μm). When blade-type monitors are used in front ends, as proposed for NSLS-II, the signal is very strong because of the presence of white beam; therefore, this drawback does not apply. Another disadvantage of this design, when used in the downstream sections of beamlines, is that beam-defining slits may be placed upstream of the position monitor, and the slits may decrease the beam dimension to the point where its fringes are not intercepted by the monitor blades. This results in no signal (and therefore no information) from the monitor.

Other beam position monitor designs derive their signals from the entire beam rather than from the fringes. One design, due to R. Alkire [11.3.9]. determines the beam position horizontally and vertically by comparing the doses of radiation scattered from a thin foil placed in the beam path, measured by four PIN diodes placed at 90˚ intervals around the beam. Since the entire beam contributes to the signals, they can be rather strong, and from their relative strengths a determination of the true center-of-mass of the beam can be made. The position resolution of this design is 1–2 μm. This design can be used in the vacuum of the beamline or in the atmosphere of the hutch.

Another design that derives its signal from the entire beam is a split ionization chamber, in which the collector electrode consists of two halves positioned symmetrically relative to the beam centerline. The difference in collector currents measured by these electrodes is due to the position of the beam relative to the electrodes (i.e., the electrode that overlaps more of the beam path will show a higher signal). As in the case of

the quadrant PIN diode monitor described above, the generated signals in this design can be rather strong, and the true center-of-mass of the beam can be determined (two orthogonal pairs of electrodes must be used to determine the beam position in both directions); a similar position resolution for this design of 1–2 μm is obtainable. Because this is a gas-based design, it cannot be used in the vacuum of the beamline, unless it is surrounded by windows.

We envision that NSLS-II beamlines will incorporate two beam position monitors, one placed just downstream of the optical system and the second placed in the hutch. Aside from their use in diagnosing the beam position, they can also be used for stabilizing the beam position, when included in feedback loops in which actuators that adjust the pitch or roll of optical components (such as mirrors, monochromator crystals or gratings) are employed. We anticipate that a position resolution of 1 μm or better will be necessary for many applications. NSLS-II will work with vendors to achieve such resolution. There is no inherent limitation in reaching such resolutions, and it is not expected that R+D on the part of NSLS-II will be required to achieve this.

11.3.4 Other Standard X-Ray Beamline Components

Other standard x-ray beamline components include filters, slits, and shutters. Some commercial versions of these are available, but normally these components are custom manufactured to suit local needs.

Filters can be used to attenuate the low-energy portion of the NSLS-II undulator (or wiggler) spectra, thereby reducing the power load on beamline components. Most existing filters are based on very thin layers of pyrolytic graphite, arranged in a stack in such a way that each filter absorbs a particular amount of power. The power is predominantly thermally radiated away by each graphite layer, from both of its surfaces, as the graphite gets very hot. NSLS beamlines X17, X21, and X25 use such filters to reduce the incident power by as much as 60–70%. We will investigate the efficacy of using graphite filters in NSLS-II insertion device beams.

An alternative choice of filter material is CVD diamond, which can also be used as a vacuum window material [11.3.10] (note that this does not have to be of diffraction quality, as was the case for monochromator crystals discussed above). We considered earlier the use of a diamond window, 100 μm thick, just upstream of a monochromator, in conjunction with the 14 mm period superconducting undulator operating at its highest K value, 2.2. In this circumstance, the window absorbs 16% of the power (64 W) within the 4σ beam dimension of the fifth harmonic of the undulator (2.4 mm wide × 1.5 mm high). The temperature and stress distributions in the window material and the copper mount were modeled using finite element analysis. The maximum temperature in the diamond is 133ºC and the maximum von Mises stress is 553 MPa, well within the tensile strength for diamond of >1200 MPa. Thus, this is an excellent choice of window and filter material for an NSLS-II superconducting undulator beamline.

Motorized slits that are used to define the beam dimension are now very standard components of beamlines and are available either as independently adjusted jaws or as apertures of fixed widths (horizontally or vertically) that can be positioned anywhere in the beam. Often the preference for which kind to use is beamline specific. Normally, slits are located in multiple positions along the beamline. It is prudent to place slits between successive optical components, as well as near the downstream end of the beamline. Commercial versions are available.

Every NSLS-II beamline that has a monochromator will have at least one pneumatically actuated photon shutter placed downstream, designed for the monochromatic beam properties for that particular beamline. Shutter designs will vary in width to meet the needs of individual beamlines, and in shutter material and shielding to handle the radiation spectrum that the shutter will confront. Whereas copper might be acceptable as a shutter material if only synchrotron radiation must be stopped, heavier materials such as Heavimet tungsten alloy would have to be considered if bremsstrahlung radiation must also be stopped. The prospect of redundant photon shutters to stop a monochromatic beam, rather than one shutter, will also be explored.

References

[11.3.1] For example, A. Chumakov, R. Rüffer, O. Leupold, J.-P. Celse, K. Martel, M. Rossat, and W.-K. Lee, *J. Sync. Rad.* **11**, 132 (2004).

[11.3.2] I. Ivanov, G. Rosenbaum, J. Chrzas, R. Fischetti, C.U. Segre, and L.D. Chapman, *Synchrotron Radiation Instrumentation Eleventh US National Conference,* AIP Conference Proceedings 521, edited by P. Pianetta, J. Arthur and S. Brennan, pp. 271–275. New York: American Institute of Physics (2000).

[11.3.3] See Figure 2 of L.E. Berman, *Rev. Sci. Instr.* **66**, 2041 (1995).

[11.3.4] J. Härtwig, private communication, 2006.

[11.3.5] R.C. Blasdell, L.A. Assoufid, and D.M. Mills, ANL/APS Technical Bulletin 24 [1995].

[11.3.6] A. M. Khounsary, R. K. Smither, and S. Davey, ANL/APS LS Note 215, 1993.

[11.3.7] R. Signorato and T. Ishikawa, R&D on third-generation and multi-segmented piezoelectric bimorph mirror substrates at SPring-8, *Nucl. Instr. & Meth. in Phys. Res. A* (467-468), 271-274, 2001.

[11.3.8] D. Nurizzo et al., *J. Sync. Rad.* **13**, 227 (2006).

[11.3.9] R.W. Alkire, G. Rosenbaum, and G. Evans, *J. Sync. Rad.* **7**, 61 (2000).

[11.3.10] H. Blumer, et al. in *Proceedings of the MEDSI06 Workshop*, to be published.

11.4 A Hard X-Ray Nanoprobe Beamline

A hard x-ray nanoprobe beamline would be designed and optimized to enable the production and use of a beam of hard x–ray photons with a minimum beam size in the nanometer range. As such, it would be a world-leading instrument, enabling spatially resolved versions of many powerful structural and spectroscopic x-ray techniques with unprecedented resolution. In particular, it would allow the study of nanomaterials which today play important roles in many diverse scientific fields. This beamline would take maximum advantage of the low emittance beam provided by the NSLS-II lattice. Figure 11.4.1 shows the conceptual layout.

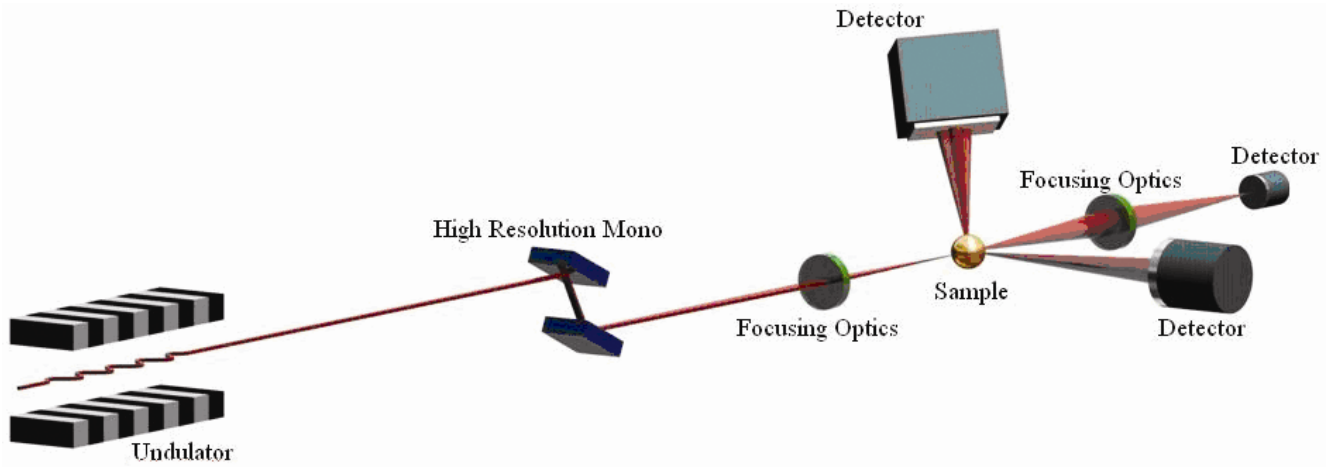

Figure 11.4.1 Conceptual layout of a nanoprobe beamline showing both scanning mode and full-field capability.

The primary experimental techniques for this beamline would likely be scanning nanobeam techniques, but it would also have a limited full-field capability. The limited full-field capability would assist in rapidly locating areas of interest, and would thus allow more efficient use of beam time. For the scanning probe techniques, there are a variety of contrast mechanisms that allow one to extract useful information from the

real-space mapping of a sample. For example, one can spatially resolve the density, elemental composition, crystallographic phase, strain, texture, chemical state, local atomic environment, and magnetization. To access all these aspects of a sample one would need to operate in a number of modes, each of which would place different requirements on the detectors.

First, with a fluorescence detector, one can use fluorescence from the sample to reveal the spatial distribution of individual elements. Second, using a large-area, low-spatial resolution high-sensitivity detector, such as a CCD, one can use diffraction to obtain a spatial map of selected Fourier components of a crystallographic phase, and also a spatial map of the local strain. Third, by scanning the incident photon energy, it is possible to access a number of spectroscopic quantities, such as the local environment from EXAFS and the local chemical state from XANES. Finally, from the back-scattered Compton scattering, one can measure the electron density. This will be especially useful for light elements such as carbon.

11.4.1 Example Experiment on a CNT Device

In Chapter 3, the practicality of carrying out a diffraction experiment on a single carbon nanotube was explored. Here, we outline a procedure that a researcher might follow for such an experiment as a way of illustrating some of the requirements for the nanoprobe beamline. As a first step, when a user brings a sample to the beamline, the local laboratory facilities would be used to align the sample, using a simple optical microscope, onto a sample mount that is pre-aligned with respect to the nanoprobe instrument. Optically aligning the sample on this special mount within a 100-micron sized cube ensures that the sample will be within 100 microns of the x-ray beam when placed in the nanoprobe instrument.

Next, the mounted sample stage is taken through the sample interlock, which keeps the experimental temperature constant within a tight range. Active vibration isolation is turned off. The sample is placed in the instrument mount, device leads are tested, and active vibration isolation is turned back on.

The x-ray beam is turned on and the instrument is brought into full-field mode, with only the low-resolution monochromator inserted. A comparison is made between the optical image and the x-ray full-field image. Next, the high-resolution monochromator is inserted and the instrument is switched to high resolution scanning nanobeam mode. A low-resolution fluorescent scan identifies the metal source and drain contacts, from which the location of the nanotube can be estimated. A high-resolution scan is now performed in this general area to monitor Compton backscattering, and the extra density due to the CNT is observed. With the beam focused on the nanotube, diffraction features characteristic of the nanotube are looked for in the diffraction detector. If none are found, even after an energy scan, the sample is rotated slightly and the alignment procedure repeated. Note that even small rotations can significantly displace the sample at these resolutions.

Once an orientation is found with the beam on the nanotube and a diffraction feature on the diffraction detector, then, since the nanotube is fairly rigid and the diffraction feature is quite broad, it should be possible to scan the sample from source to drain region while continuously monitoring the nanotube diffraction. The nanotube device would then be turned on and the sample scanned again while current is being passed. For this device, infrared photons would be emitted in the central region and a strain difference in the CNT lattice would be observed in the diffraction pattern, consistent with a 100K rise in temperature of that part of the nanotube.

The experiment described above utilizes many of the features the beamline and end stations that are expected to be made available to the user. One important aspect that is not covered by this example is the requirement for EXAFS/XANES capabilities, but other types of samples would require such techniques and they will therefore be implemented.

11.4.2 General Optical Concepts

For scanning mode applications, three optical concepts, referred to as **direct**, **mirror**, and **waveguide** mode, are considered here for achieving a nanometer-size focal spot at the sample position. In addition, a full-field transmission mode with absorption and phase contrast imaging will be implemented to gain an overview of a larger area ($10 \times 10\ \mu m^2$) of the sample before zooming in on smaller features of interest.

Direct and mirror concepts rely on selecting the coherent portion of radiation from the x-ray source and using it to illuminate a high-resolution diffractive/refractive focusing optics, based on Fresnel zone plates, multi-layer Laue lenses, or kinoform lenses. The difference is in the power management of the incident white beam coming from the undulator source, which in the first case will be accomplished by an absorptive filter and in the second case by a mirror.

For both concepts the length of the optical path, and with it the overall length of the beamline, are directly related to the demagnification of the primary source to the final nanometer size focal spot, and the "working distance" between the focusing optics and the sample. An important class of experiments to be conducted on the nanoprobe beamline will involve the detection of radiation back-scattered from the sample, either fluorescence or Compton scattering. This requires an appropriately large solid angle with a substantial component along the optical axes and pointing back towards the focusing optics. Given the spatial extensions of both detectors and focusing optics, a working distance of 10 mm is targeted for this beamline to ensure that necessary instrumentation can be accommodated and practical experiments with back-scattering detection are feasible. Consequentially, an overall beamline length of approximately 100 m is desirable for a beamline operating in one of these modes, as described below.

The waveguide concept, if successful, would significantly reduce the required optical path length by employing a two-stage focusing scheme in combination with the generation of an intermediate diffraction-limited coherent source.

11.4.2.1 Direct Mode

The direct-mode is shown schematically in Figure 11.4.2. The guiding philosophy here is to have as few optical components along the beam path as possible, to preserve the transverse coherence of the beam as much as possible. In this concept a small aperture is placed as close to the primary source (undulator) as practically possible, restricting the beam horizontally to the size of the effective vertical coherent source size $S_{v,coh}$. Some technical design aspects for this "near-accelerator aperture" are presented in Section 11.4.3.6.

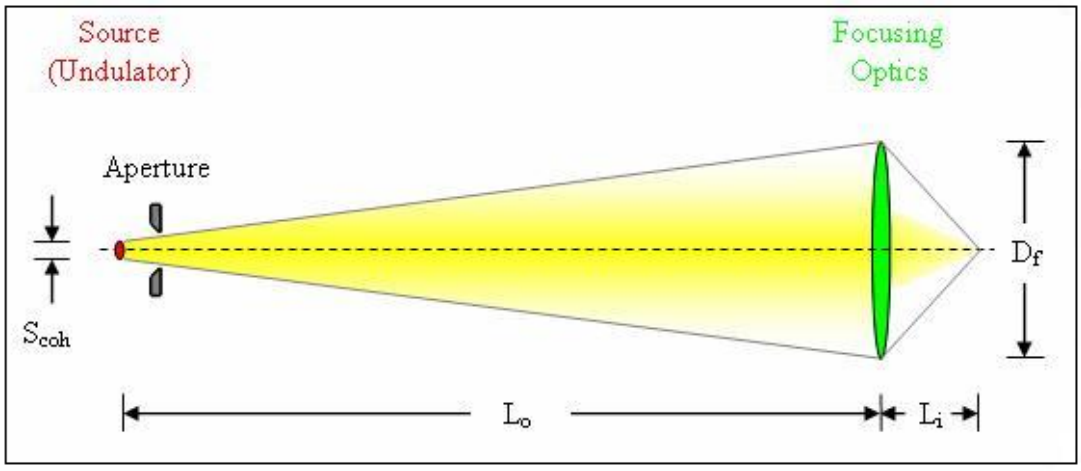

Figure 11.4.2 Direct mode. The coherent portion of the incident beam is selected by an aperture close to the x-ray source and illuminates the focusing optics of diameter D_f at a distance of L_o. The focal spot is located at a distance L_i from the optics.

In terms of the ordinary synchrotron radiation source parameters σ_{xy}, σ_r, and Σ_{xy}—which stand for the particle beam size , the photon beam size, and the size of the combined (effective) source extension—the vertical coherent source size $S_{v,coh}$ is given by

$$S_{v,coh} = \mathrm{FWHM}(\Sigma_y) = 2\sqrt{2\ln 2}\sqrt{\sigma_y^2 + \sigma_r^2} \ . \tag{11.4-1}$$

Thus a near-square, coherent source of dimensions $S_{v,coh} \times S_{v,coh}$ would be generated, which would illuminate the focusing optics placed at a distance L_o from the source. This distance L_o, in combination with the working distance L_i between the focusing optics and the sample, determines the required demagnification of

$$m = \frac{S_{v,coh}}{p} = \frac{L_o}{L_i} \ , \tag{11.4-2}$$

where p is the diameter of the focal spot, ultimately desired to be p = 1 nm.

The diameter D_f of the high-resolution focusing optics should match the transverse coherence length L_T of the incident beam at the position Lo, which is given by

$$D_f = L_T = \frac{\lambda}{2}\frac{L_o}{S_{v,coh}} \ . \tag{11.4-3}$$

Using source parameters for the NSLS-II storage ring in conjunction with one 3 m U19 cryo-cooled permanent-magnet undulator, together with the targeted working distance of 10 mm, the following practical parameters emerge for the direct mode at an x-ray wave length of 1 Å:

Table 11.4.1 Practical Parameters for Direct Scanning Mode, Wavelength 1 Å.

Parameter	Symbol	Value
Horizontal particle beam size	σ_x	38.61 μm
Vertical particle beam size	σ_y	1.62 μm
Photon beam size (λ=1 Å)	σ_r	1.38 μm
Effective coherent vertical source size	$S_{v,coh}$	5.00 μm
Required demagnification	m	5009
Required working distance	L_i	10 mm
Source ↔ optics distance	L_o	50.1 m
Diameter of optics (λ=1 Å)	D	500 μm

The direct mode introduced so far does not include any power management of the incident beam. With the exceptional brightness of the new NSLS-II storage ring, local power densities along the beam path are expected to be large enough to significantly distort optical components and thereby diminish the coherence of the beam. To mitigate these adverse effects, a (high-pass) filter can be inserted into the incident beam to remove unwanted power associated with the lower part of the energy spectrum. This modification is shown in Figure 11.4.3. In the design of the filter, care must be taken to preserve the coherence. A suitable filter material might be highly polished, synthetic or CVD diamond, sufficiently cooled to prevent lattice distortions.

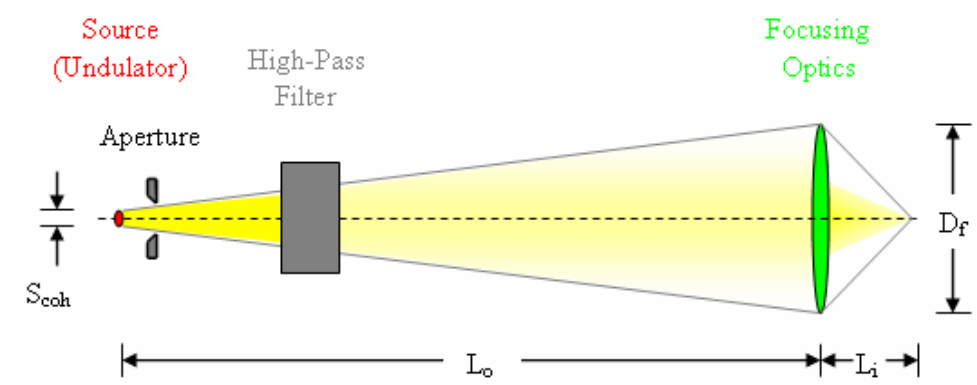

Figure 11.4.3 Modification of the direct mode concept. A high-pass filter in the incident beam reduces the power loading of successive components by removing power associated with the low-energy part of the spectrum.

11.4.2.2 Mirror Mode

An alternative concept to the direct mode, referred to as mirror mode, involves the use of a horizontal mirror system as the power moderating component. In combination with an exit aperture it can act as a spatial filter for the horizontal component of the beam, thereby generating a secondary coherent source downstream of the mirror system which is independent of coherence-diminishing components upstream of it. This concept is shown schematically in Figure 11.4.4. An additional advantage of using a mirror system is to increase the (incoherent) flux due to the larger horizontal acceptance, which is useful for the full-field imaging mode that will be used on the beamline. The disadvantages are, that the total length of the beamline is increased substantially by the distance L_p between the primary and the secondary source and that the coherence associated with the vertical portion of the beam might be adversely affected by figure errors of the mirrors. While the mirror mode constitutes a viable alternative, higher priority will be given to implementing the direct mode for its simplicity and fewer components that could diminish the coherence of the beam.

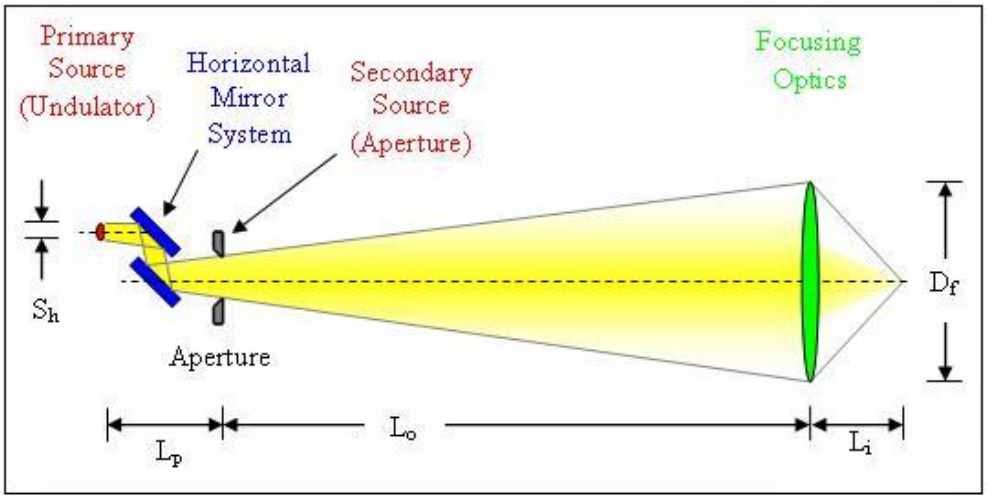

Figure 11.4.4 Mirror mode. A horizontal mirror system in combination with an aperture acts as a spatial filter, generating a secondary coherent source.

11.4.2.3 Waveguide Mode

A novel composite concept, referred to as the waveguide mode, is also being considered. If successful, it promises the advantage of a significant reduction in the required distance between source and experiment, thus allowing for a much shorter beamline to achieve nanometer-size focusing than in the conventional case. Briefly, it involves a two-stage demagnification of the primary source to the final spot size, combined with the generation of a diffraction-limited, coherent secondary source by virtue of an x-ray waveguide. The schematic layout is shown in Figure 11.4.5.

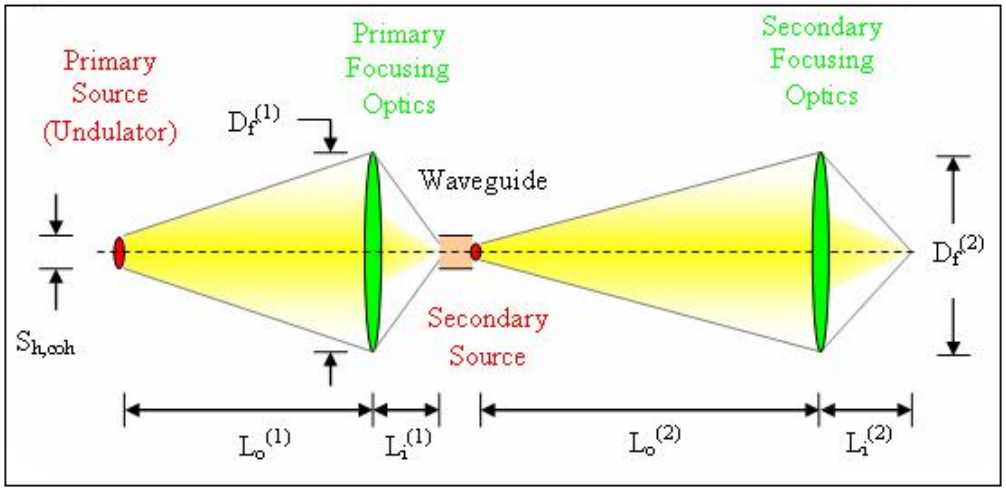

Figure 11.4.5 Waveguide mode. A final nm size focus is achieved by a two-stage demagnification of the primary source; an x-ray waveguide generates an intermediate diffraction-limited, coherent secondary source.

Besides reducing overall length, this system offers the additional advantage that the secondary source isolates the downstream optics from a loss of coherence or vibrational disturbances in the upstream section. In the waveguide mode, the primary focusing optics accepts the full horizontal coherent source size $S_{h,coh}$, given by

$$S_{h,coh} = \mathrm{FWHM}(\Sigma_h) = 2\sqrt{2\ln 2}\sqrt{\sigma_h^2 + \sigma_r^2} \ , \tag{11.4-4}$$

and generates a focal spot of about 50 nm, appropriate to be accepted by the succeeding x-ray wave guide. The demagnification of this stage is determined by

$$m^{(1)} = \frac{S_{h,coh}}{p^{(1)}} = \frac{L_o^{(1)}}{L_i^{(1)}} \ , \tag{11.4-5}$$

where $p^{(1)}$ ~50 nm is the diameter of the focal spot. The succeeding x-ray waveguide effectively collimates the radiation emanating from this focus, generating a diffraction-limited coherent secondary source which can be further demagnified to the final desired spot size by the second stage.

The diameter of the first stage optics is determined by the transverse coherence length at the position of the focusing element:

$$D_f^{(1)} = L_T = \frac{\lambda}{2}\frac{L_o^{(1)}}{S_{coh}} \ . \tag{11.4-6}$$

Due to the asymmetric source size, the coherence length in the vertical direction is an order of magnitude larger than its counterpart in the horizontal direction, thus $D_f^{(1)}$ is chosen to match the vertical coherent source size $S_{v,coh}$. Furthermore, although the full horizontal source size may be accepted, only a small central portion of it will contribute to the effective coherent photon flux through the focusing optics.

The second stage focusing optics demagnifies the intermediate secondary source generated at the exit of the x-ray waveguide to the desired final nanometer-size focal spot. The required demagnification is

$$m^{(2)} = \frac{p^{(1)}}{p^{(2)}} = \frac{L_o^{(2)}}{L_i^{(2)}} \ , \tag{11.4-7}$$

where $p^{(2)}$ is the diameter of the ultimate focal spot, desired to be p = 1 nm.

Requiring an appropriate working distance of ~10 mm behind the second-stage Fresnel zone plate to perform practical nano probe experiments, the distance $L_o^{(2)}$ between secondary source and optics is $L_o^{(2)} = m^{(2)} L_i^{(2)}$ and the diameter of this optics is

$$D_f^{(2)} = L_T = \frac{\lambda}{2}\frac{L_o^{(2)}}{p^{(1)}} \ . \tag{11.4-8}$$

A practical set of parameters to realize this optical scheme at NSLS-II is given in Table 11.4.2.

Table 11.4.2 Practical Parameters for the Waveguide Scanning Mode.

Parameter	Symbol	Value
Effective coherent vertical source size [μm]	$S_{v,coh}$	5.00
Effective coherent horizontal source size [μm]	$S_{h,coh}$	91.0
Required first-stage demagnification	$m^{(1)}$	1820
Suggested first-stage working distance [mm]	$L_i^{(1)}$	25
First-stage source ↔ optics distance [m]	$L_o^{(1)}$	45.5
Diameter of first-stage optics (λ=1 Å) [μm]	$D_f^{(1)}$	455
Required second-stage demagnification	$m^{(2)}$	50
Required second-stage working distance [mm]	$L_i^{(2)}$	10
Second-stage source ↔ optics distance [m]	$L_o^{(2)}$	0.5
Diameter of second-stage optics (λ=1 Å) [μm]	$D_f^{(2)}$	500

11.4.2.4 Full-Field Transmission Mode

The full-field transmission mode will be utilized to gain an overview of a larger sample area before concentrating on smaller features with the scanning focusing mode. The optical concept for the full-field mode is shown in Figure 11.4.6.

A large condenser zone plate illuminates the sample uniformly over a micrometer-sized area. The diameter of the condenser is chosen to accept a large fraction of the incident undulator radiation. Photons transmitted through the sample are imaged onto an area detector by means of an objective zone plate. Depending on the nature of the sample, both absorption and phase contrast generation can be used to optimize the image.

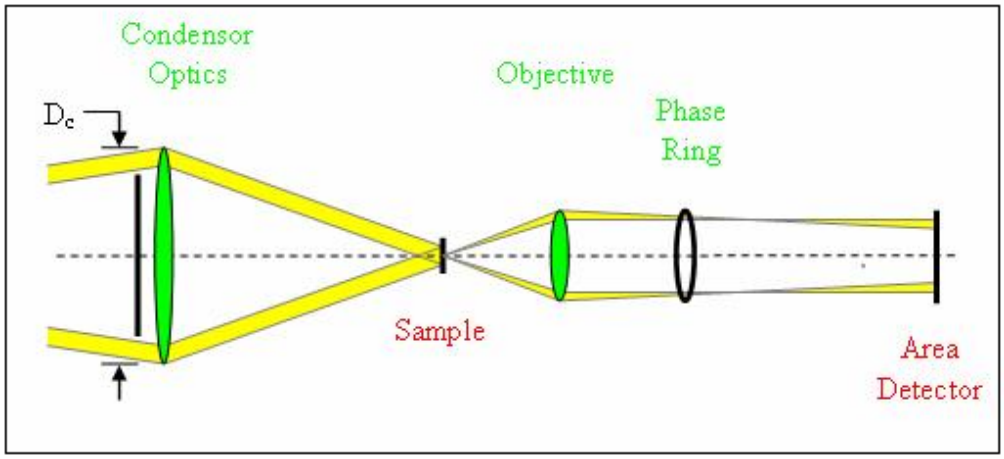

Figure 11.4.6 Full-field transmission mode. A condenser optics illuminates the sample. Transmitted photons are imaged onto an area detector by means of an objective zone plate.

11.4.2.5 Spatial Resolution and Monochromaticity

To achieve nanometer size spatial resolution, a minimum degree of monochromaticity of the x-ray beam incident on the focusing optics is required. In the following argument, Fresnel zone plates are specifically considered, however, similar arguments with similar results hold true for the other optical elements that might be employed in the high-resolution focusing optics.

For a Fresnel zone plate having a total number of zones N, the monochromaticity needs to be better than N^{-1}:

$$\frac{\Delta E}{E} = \frac{\Delta \lambda}{\lambda} \le \frac{1}{N}, \tag{11.4-9}$$

where for a desired focal length (working distance) L_i and an outer zone width, Δr_n, at a particular wave length λ, the required number of zones is given by

$$N = \frac{\lambda L_i}{4\Delta r_N^2}. \tag{11.4-10}$$

By virtue of the Rayleigh criterion, $1.22\ \Delta r_n = 1$ nm. The desired working distance is 10 mm. Therefore the number of zones is of the order of $N \sim 3.8 \times 10^5$ and the associated monochromaticity is

$$\frac{\Delta E}{E} \approx 2.6 \times 10^{-6}, \tag{11.4-11}$$

or approximately 30 meV at 12.4 keV ($\lambda = 1$ Å). In addition to this very high degree of monochromaticity required for extreme focusing, the incident beam divergence has to be preserved by the monochromator, since it was already tailored to fit the high-resolution optics. A monochromator arrangement that can satisfy both conditions is a nondispersive, symmetric, double-crystal combination, using higher-order reflections in near-backscattering geometry. This monochromator concept is further explained below.

11.4.2.6 Choosing Beta for High-Spatial Resolution Optics

The following analysis [11.4.3] shows how beta can be optimized for the maximum coherent flux from an undulator. By definition, for the electron beam the electron source size and angular divergence depend on emittance and beta, as follows:

$$\sigma_y = \sqrt{\varepsilon_y \beta_y} \text{ and } \sigma'_y = \sqrt{\frac{\varepsilon_y}{\beta_y}}. \tag{11.4-12}$$

Substituting these into the expression for effective photon emittance, we find that

$$\overline{\varepsilon_y} = \sqrt{\varepsilon_y \beta_y + \sigma_{ph}^{\ 2}} \sqrt{\frac{\varepsilon_y}{\beta_y} + \sigma'^{\ 2}_{ph}}. \tag{11.4-13}$$

As discussed above, the coherent flux, which is important for zone plate focusing, is proportional to $1/\overline{\varepsilon}$. We thus differentiate with respect to beta to find the extremum:

$$\beta_y = \frac{\sigma_{ph}}{\sigma'_{ph}} = \frac{L}{2\pi}. \tag{11.4-14}$$

For a 3 m undulator, the optimum beta for a zone-plate-based line is independent of wavelength and is 0.5 m.

For asymmetric focusing elements (e.g., KB mirrors or crossed cylindrical refractive lenses), one might assume that the optimum beta function value is not well determined in the nonfocusing direction for a given optic. That is, if one of these optics is focusing in the vertical plane, one might assume that the best beta value in the horizontal would be large, to maximize the acceptance of a given-sized optical element. However, it is likely that off-axis aberrations will couple horizontal source size into vertical image size, leading to the conclusion that source size, not divergence, should be optimized in both directions.

On the basis of these considerations, we chose a small beta, to minimize source size.

11.4.2.7 Consequences of Depth of Focus and Chromatic Optics

The depth of focus, DOF, is given by $\lambda/(\mathrm{NA})^2$. If one defines the optic resolution $\Delta = \lambda/\mathrm{NA}$, then DOF = Δ^2/λ. For a dispersive optic, this puts a constraint on the incident bandwidth of photons in order to not broaden the focus significantly. While solid metal mirrors are non-dispersive, it is not likely that they will reach 1 nm. Many of the likely candidates are dispersive. An example is that of a zone plate, which has $f\lambda$ = constant. For this case, we find $df/f = d\lambda/\lambda = dE/E$. We plot this for a few cases to gain some insight (Figures 11.4.7.a and 11.4.7b.

Figure 11.4.7a shows required bandwidth versus resolution for λ = 0.1 nm (12.4 keV) and for three values of focal length 1 mm,10 mm, and 100 mm. For beamlines of typical length, a reasonable compromise between sufficient experimental working distance and the demagnification required to obtain 1 nm resolution is a focal length of order 10 mm. For this 10 mm focal length, one observes on the plot that a 1×10^{-6} bandwidth is required, significantly narrower than typically available at conventional beamlines. For comparison, a conventional Si(111) monochromator has a bandwidth of 1×10^{-4}. Figure 11.4.7a shows that one can only obtain a 10 nm spot size with this bandwidth. To improve the spatial resolution by one order of magnitude requires a reduction of two orders of magnitude in energy bandwidth.

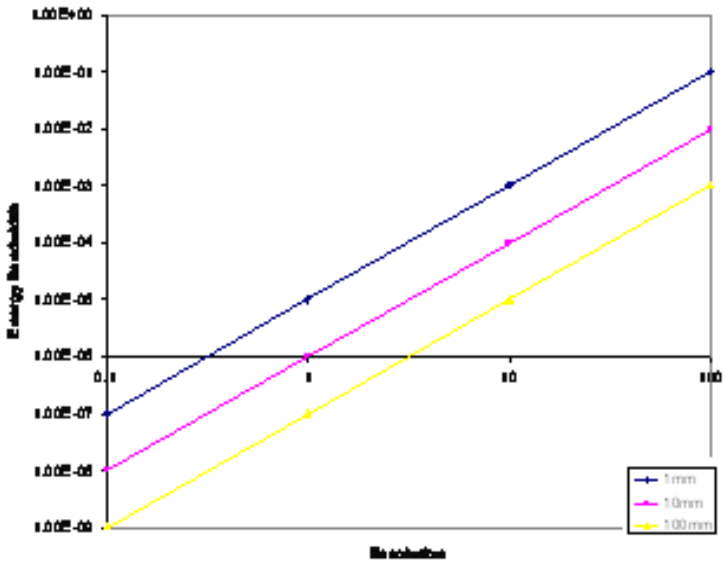

Figure 11.4.7a The energy bandwidth required to obtain a given resolution (in nm) for zone plates of three focal lengths (1 nm, 10 nm, and 100 nm).

Note that at higher energies, the energy bandwidth constraint relaxes. Unfortunately, we gain linearly with photon energy and lose quadratically with spatial resolution, as shown in Figure 11.4.9b, which plots the required energy bandwidth as a function of wavelength from 1.24 keV (λ = 1 nm) to 124 keV (λ = 0.01 nm), for three different resolutions (1 nm, 10 nm, and 100 nm) and for a focal length of 10 mm. One must also consider the energy dependence of the undulator spectrum. Even the relatively modest change from 12.4 keV to 24.8 keV results in a reduction in flux of an order of magnitude, with only a factor of two gained from the relaxed bandpass, thus resulting in a net loss of a factor of five.

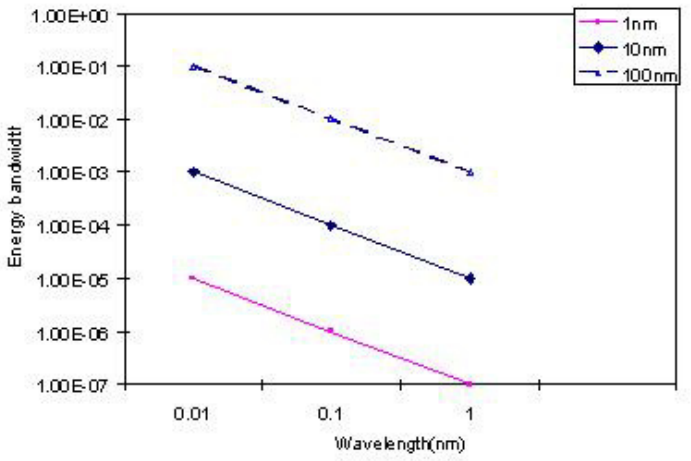

Figure 11.4.7b The energy bandwidth required to obtain various spatial resolutions (1 nm, squares; 10 nm, diamonds; 100 nm, triangles) as a function of photon wavelength.

For the solid refractive optic, the situation is worse by a factor of two in bandwidth. For such optics, $f\lambda^2$ is a constant, so $df/f = 2d\lambda/\lambda$, and all the arguments above can be replicated with an additional factor of two.

In summary, due to the dispersive nature of many of the optics we will consider, we must carefully tailor the bandwidth of incident photons. Due to the quadratic dependence of bandwidth on desired spatial resolution, a relative modest relaxation of resolution results in large reduction in the required bandwidth and hence a large gain in flux on the sample. At a resolution of 10 nm, and a reasonable focal length/working distance of 10 mm, one matches the bandwidth of conventional monochromators. A resolution of 1 nm will be best obtained by reducing the bandwidth, and consequently the flux, by two orders of magnitude relative to this situation.

11.4.2.8 Summary of Optical Concepts

The three optical concepts introduced above for the scanning focusing mode of the beamline (direct mode, mirror mode, and waveguide mode) have certain relative merits and disadvantages. Great advances have been made toward the design and manufacture of coherence-preserving x-ray optical components, such as monochromators, mirrors, and filters. However, in the context of extreme focusing to nanometer-size beams, the limitations for these devices and relative advantages or disadvantages of one component over another still have to be researched further. It is for this reason that, at this stage in the current beamline design, we aim at being able to accommodate all three concepts or combinations thereof, to take advantage of future technical achievements and to have the flexibility of substituting a more favorable component for an outdated or less favorable one.

R&D projects will be initiated or are already ongoing to remove some of the uncertainties regarding coherence preservation of specific components. At APS, for example, a nanoprobe beamline is currently being developed with spatial resolution down to 30 nm or better. Some of the optical components necessary to realize the concepts above will be implemented and tested at the new APS beamline. In particular, a horizontal mirror system and a high-heat load monochromator employed at this beamline are expected to yield a large amount of useful information on which to base further component designs for even better coherence characteristics and higher spatial resolution. Much research at many synchrotron radiation facilities around the world is currently being conducted regarding the use of synthetic or CVD-diamond windows in situations where coherence is an important factor. Calculations are being performed at NSLS-II to explore heat load characteristics of this material and whether new cooling concepts can enhance its coherence capabilities. These proceedings should yield important information helpful in designing a successful power filter appropriate for the brightness of NSLS-II.

The one parameter that has the largest design implications is the length of the optical path, since it determines the experimental locations and thereby the number and distribution of shielding enclosures. Table 11.4.3 lists approximate positions of the effective source and the final focus for the various concepts.

Table 11.4.3 Summary of Characteristics of the Four Modes.

Mode	Effective Source Type	Source Location	Location of Final (1 nm) Focal Spot
Direct	Vertical: Primary	0.0 m	50 m
	Horizontal: Secondary	15 m	
	Tertiary*	35 m	85 m
Modified Direct	Vertical: Primary	0.0 m	50 m
	Horizontal: Secondary	15 m	
	Tertiary*	35 m	85 m
Mirror	Secondary	35 m	85 m
Waveguide	Primary	m	47 m
	Secondary	46 m	

* Even in the direct modes the coherence might not be preserved sufficiently by all optical components. Then a beam-defining aperture downstream of the monochromator will become the effective (tertiary) source.

A shielding enclosure that houses all beam-conditioning components upstream of the 35 m mark (FOE) and two experimental enclosures at around 50 m and 85 m that house focusing optics, sample stages, and detectors, will accommodate all configurations mentioned above. In addition, the concept of having two experimental enclosures with a substantial distance between them allows a dramatic enhancement of phase contrast imaging, when the sample is located in the upstream station while the detector is located in the downstream station.

11.4.3 Nanoprobe Beamline Components

In designing a nanoprobe beamline, the primary effort is to preserve the coherence of the x-ray beam as it passes through the various beam-shaping and beam-controlling components and eventually reaches the sample in a diffraction-limited, nanometer-sized focal spot. At the same time, the photon flux available at the sample position needs to be maximized to ensure that practical experiments can be performed in a timely manner.

The beamline layout features three shielding enclosures, called the A, B, and C stations, as shown in Figure 11.4.8. Station A functions as a First Optics Enclosure, containing the interface to the accelerator, which consists of all beam-conditioning equipment such as slits, mirrors, monochromators, and photon shutters. Its terminal optical component is a beam-defining slit, which can act as a secondary/tertiary source in those optical concepts where coherence preservation of upstream components cannot be relied upon.

The B and C stations, located at around 50 m and 85 m, will house the actual focusing optics, the nanoprobe sample stages, and detectors. Each station can hold a complete set of focusing, sample, and detector optics, or both together can be used in combination to enhance imaging properties of a particular experimental setup. Initially, one set of instruments and detectors will be procured and configured to match a desired optics mode.

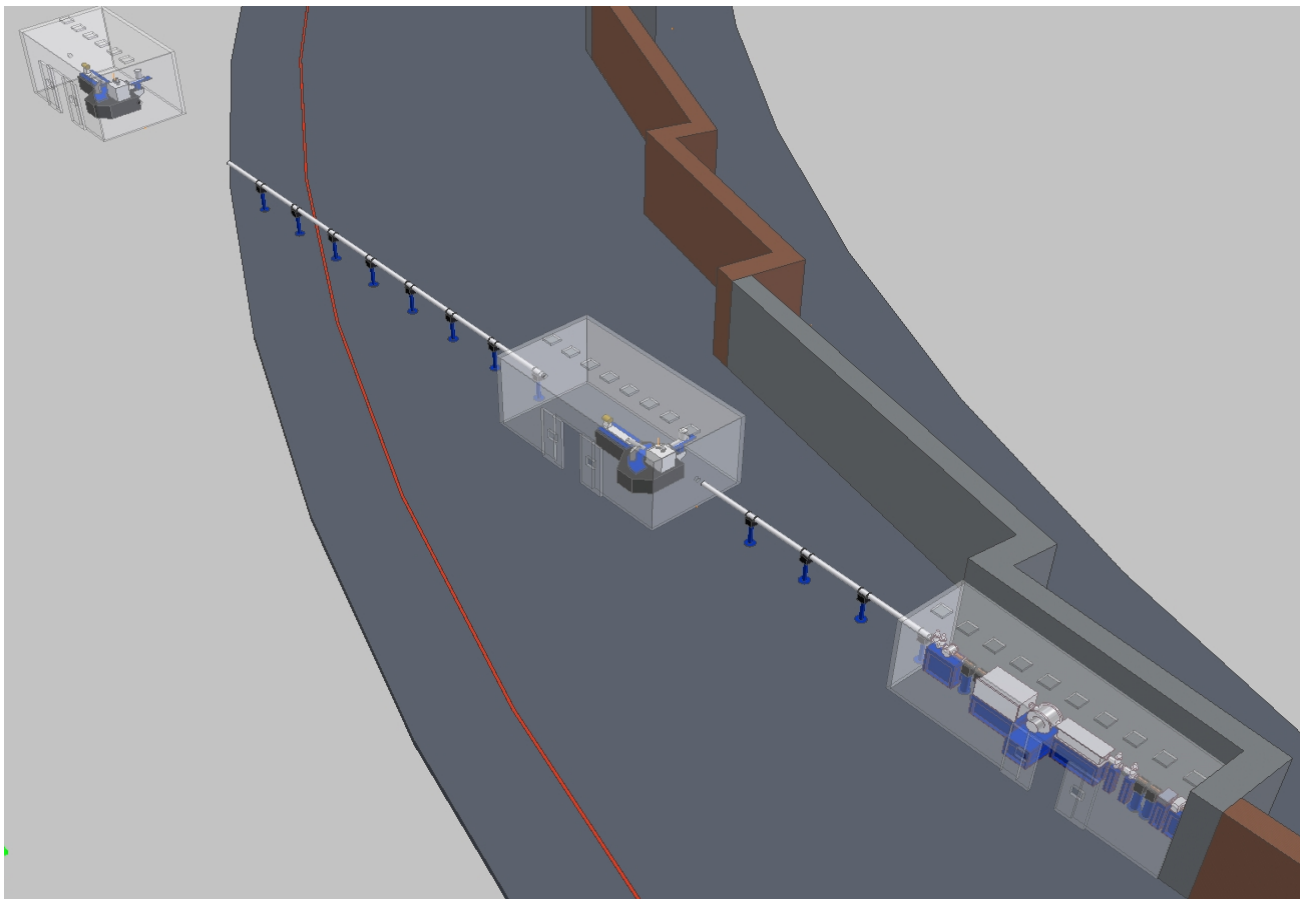

Figure 11.4.8 Overall layout of a hard x-ray nanoprobe beamline.

11.4.3.1 Source

Given the current status of the NSLS-II design, a nanoprobe beamline would be located on a low-β, 5 m straight section of the accelerator, employing one U19 cryogenically cooled permanent-magnet undulator.

The length of this device is presently 3 m. As discussed above, the relevant figure of merit for this beamline is source brightness. If it turns out, during the design phases of NSLS-II, that multiple U19 devices can be accommodated in a single straight, with low β, or SCU U14 devices, these will be the preferred option for this beamline.

11.4.3.2 Layout

The interface between the beamline and the accelerator would be "window-less." A differential pump assembly would largely isolate the beamline vacuum from the accelerator vacuum without the use of a window. A window could potentially diminish the coherence of the x-ray beam; thus, its elimination is one of the coherence-preserving measures. The differential pump assembly is the first component in the A station.

The second component in the FOE is a white beam slit with four slit blades that can be positioned independently around the incident beam. The WBS acts as a variable guard slit, reducing unwanted power and stray scattering into the downstream sections of the beamline, while providing differing aperture sizes to accommodate the various operating modes of the beamline, such as focusing and full-field imaging.

Power management of the very bright white beam generated by the NSLS-II accelerator will be accomplished by a filter assembly and/or a horizontal mirror system. Since the coherence-preserving properties of these two kinds of components are not very well established or characterized at this time, it is expected that they will be used either separately or in conjunction with each other to optimize overall performance for a particular operating mode of the beamline.

A combination of a high heat-load primary monochromator succeeded by a secondary monochromator will enable the selection of photon energy and energy band pass. The assembly is described in more detail below.

The monochromators are followed by a beam-defining slit system with four independent blades. In optical configurations where the coherence-preserving feature of upstream components cannot be relied upon, this slit system will serve as part of a spatial filter, generating a secondary coherent source.

The FOE is terminated by a photon shutter, which allows personnel access to the downstream experimental stations while the x-ray beam is present in the FOE. The FOE is connected to the B station, and the B station is connected to the C station by a beam transport system consisting of shielded beampipe and an in-line ion pump for every 5 m long section.

Instrumentation in the experimental stations consists of a nanoprobe instrument and a suite of transmission and back-scattering detectors.

11.4.3.3 Incident Power Filter

The modified direct mode described earlier relies on an absorptive filter in the incident beam to reduce power loads on the monochromator and focusing optics. To preserve the coherence of the beam, this filter needs to have highly polished, smooth entrance and exit surfaces. These surfaces need to be precisely parallel to each other, and the bulk needs to be perfectly uniform as far as the refraction of x-rays is concerned.

With its high heat conductivity and low thermal expansion, diamond is an attractive material for an incident power filter. Through recent technological advances in the manufacturing of synthetic diamonds, nearly perfect crystals have been grown with a surface roughness of less than 1 nm [11.4.3]. These diamonds are expected to be suitable for x-ray imaging situations where the preservation of coherence is critical. In addition, advances in the production of chemical vapor deposition diamonds might make this material a suitable alternative for coherence applications, although the overall crystalinity is inferior to the synthetic single-crystal diamonds.

Preliminary finite element analysis calculations have been performed to investigate the thermal distortion of diamond for beam conditions in the modified direct mode and using the U19 undulator as a source. Figure 11.4.9 shows a map of local nodal displacements over the copper crystal holder, the crystal, and the actual beam spot of 0.3×0.3 mm^2 (small square in the center) with the temperature held fixed at 20°C at the bottom of the copper block (water cooling). All incident power is assumed to be absorbed. The resulting total range of displacements (red ↔ blue) is about 100 nm.

Close inspection of the map shows that differential displacements within the central beam spot are smaller that 1 nm in this worst-case scenario, leading to only negligible optical phase shifts in the x-ray beam. Thus, coherence of the beam is not expected to be substantially affected.

Further calculation must be performed to study the spectral behavior of a diamond filter of this kind in the context of the particular undulator spectrum. However, the concept appears promising for general use as coherence-preserving power filter and x-ray window.

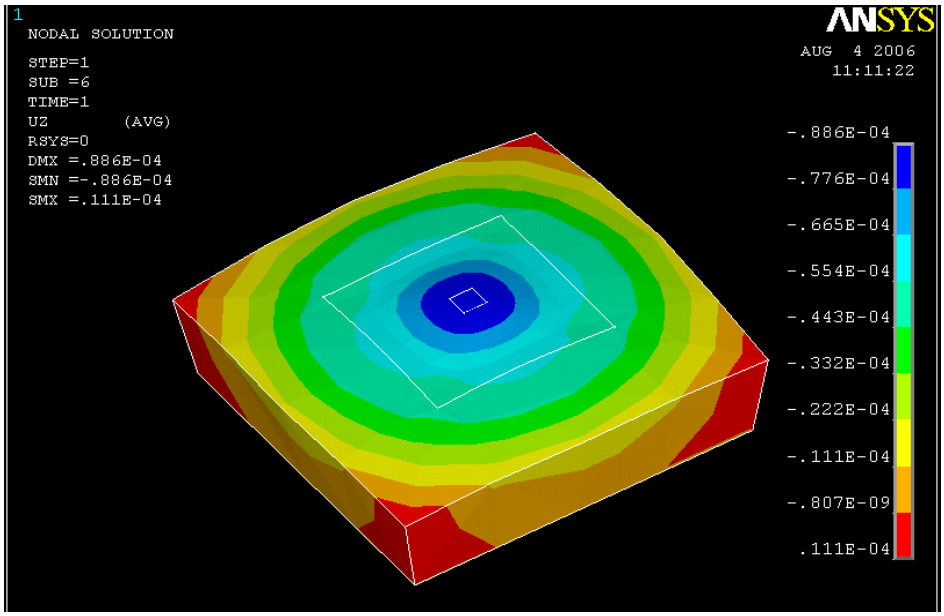

Figure 11.4.9 Contour plot of the nodal displacement along the x-ray beam direction (in mm). The small square in the center marks the extent of the beam; the medium square is the extent of the diamond crystal.

11.4.3.4 Monochromators for a Nanoprobe Beamline

To achieve nanometer-size beams at the desired working distance, the x-ray energy band pass ΔE/E for a nanoprobe beamline needs to be matched to the diffractive focusing optics, as discussed previously. In particular,

$$\cot\Theta_B \Delta\Theta = \frac{\Delta E}{E} = \frac{\Delta\lambda}{\lambda} \le \frac{1}{N} = \frac{4\Delta r_n^2}{L_i}\frac{E}{hc} \qquad (11.4\text{-}15)$$

where Θ_B is the Bragg angle, $\Delta\Theta$ is the incident divergence, N and Δr_n are the number of zones and the outer zone width, and L_i is the working distance between focusing optics and sample. At the same time, the divergence of the incident beam $\Delta\Theta$, already chosen to fit the geometry of the focusing optics, needs to be preserved by the monochromator. A single-stage, double-crystal monochromator arrangement in near back-scattering geometry satisfies both conditions. This arrangement is shown schematically in Figure 11.4.10.

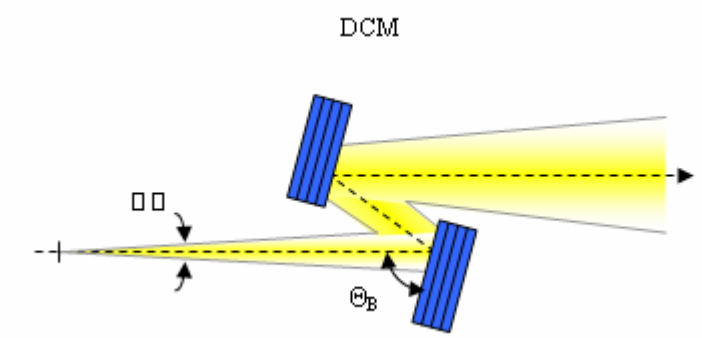

Figure 11.4.10 Basic geometry of the double-crystal monochromator, DCM. The incident divergence is preserved in traversing the monochromator. Near back scattering geometry is necessary to achieve the required energy band pass.

For their favorable thermal and absorptive qualities, water-cooled, symmetric diamond (111) crystals are envisioned for this monochromator, with the sequence of (333), (444), and (555) higher-order reflections providing the reduced band pass and energy scan flexibility. Nevertheless, due to the dependence of the energy band pass on the square of the outer zone width, extreme focusing down to 1 nm can only be achieved for discrete energies, while, with a slight relaxation of the beam size requirement to 2 nm, an extended energy range can be accessed with a single reflection at large working distance. This is indicated in Figures 11.4.11a and 11.4.11b. Here the straight lines indicate maximum band pass boundaries at particular working distances, which cannot be exceeded. The curved lines are actual band pass values generated by the DCM employing a particular reflection and allowing the incident divergence as required by the optical concepts. Where these curved lines dip below a boundary line, focusing to the desired beam size becomes possible.

In the case of a 1 nm beam, three reflections (333, 444, and 555) are necessary to cover an extended but interrupted energy range between 9 keV and 26 keV at a reduced working distance of 4 mm (Figure 11.4.11a). For a slightly larger beam size of 2 nm, the range from 9 keV to 30 keV can becomes accessible with the (333) reflection only, and at 4 nm the (111)-reflection is sufficient to go all the way from 4 keV to 30 keV without change in reflection (Figure 11.4.11b). However, a full range of incident angles, from near 90° to near 0°, is required to achieve this flexibility. This is a requirement that will require careful design of the monochromator.

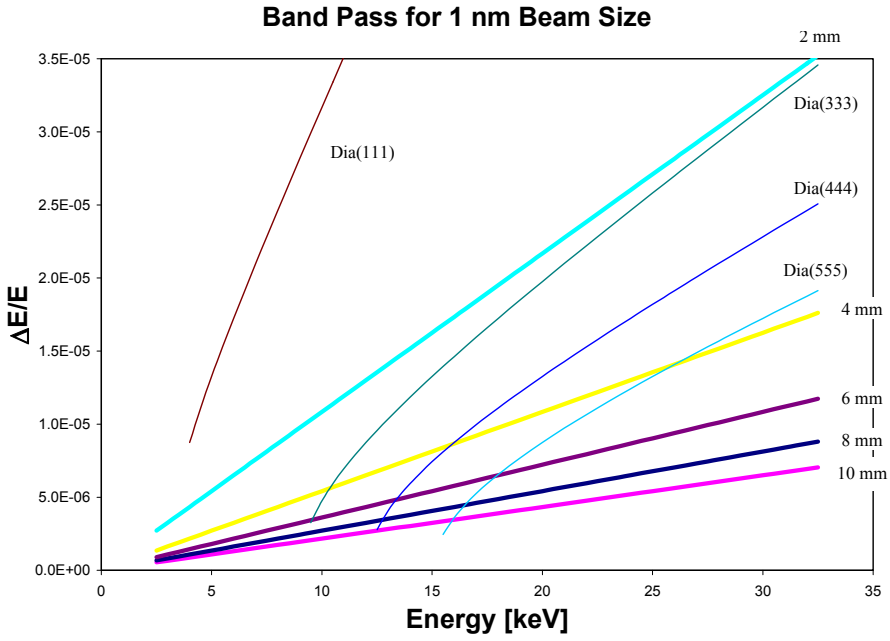

Figure 11.4.11a Band pass boundaries and available band pass values for various reflections of the DCM for a targeted beamsize of 1 nm.

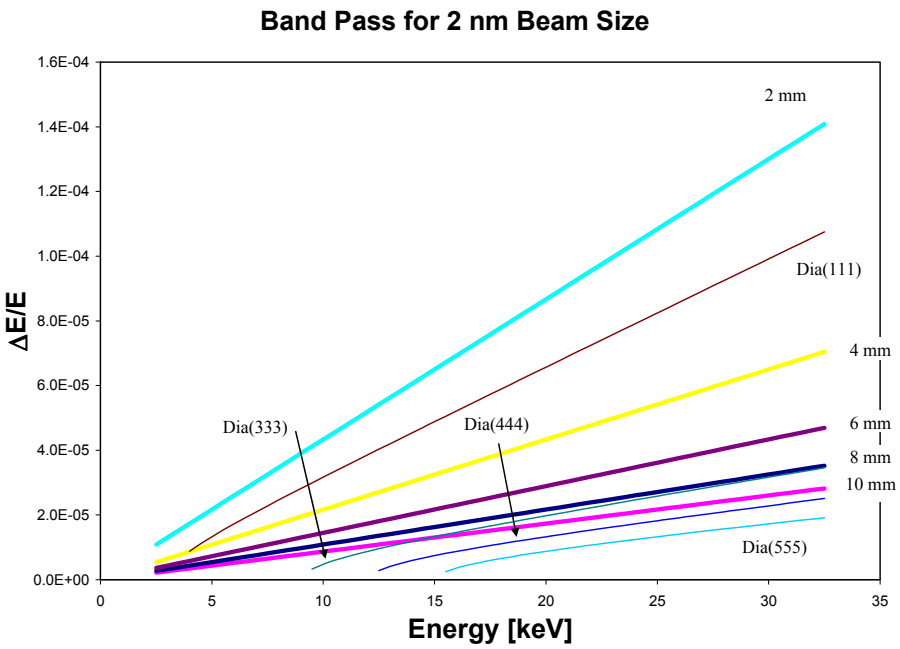

Figure 11.4.11b Band pass boundaries and available band pass values for various reflections of the DCM for a targeted beamsize of 2 nm.

11.4.3.5 The Nanoprobe Instrument

The engineering challenges associated with achieving the sub-nm stability and precision to sample (and optic) positioning stages are severe and will require a dedicated R&D effort. This will be pivotal in the context of NSLS-II, in general, and any nanoprobe beamline, in particular. The specific issues, challenges, and potential approaches are discussed in Chapter 12.

11.4.3.6 Front-End Aperture

The first aperture in a nanoprobe beamline, located in the front end as close to the undulator source as possible, would consist of two separate masks (Figures 11.4.12 and 11.4.13a). The first mask is fixed in space and serves as a guard, reducing the size of the initial undulator x-ray beam to the desired maximum acceptance of the beamline. This maximum acceptance matches the vertical and horizontal FWHM (full width at half maximum) sizes and divergences of the source.

The second mask can be moved vertically to switch between two possible positions. The first position corresponds to a high-spatial-resolution mode of the beamline, while the second corresponds to a high-flux mode. The first position provides a beam-defining horizontal constriction equal to the vertical FWHM extension of the beam, leading to a square-shaped source. When the guard mask is removed, the full beam permitted by the guard mask is passed to the beamline.

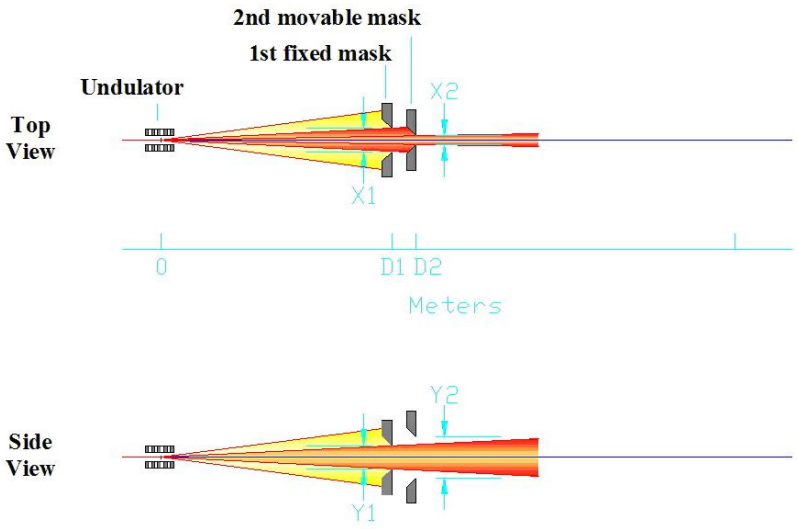

Figure 11.4.12 Geometry of the first aperture.

The locations of the first and second mask will be approximately D_1=14 m and D_2=15 m from the source, respectively. Efforts will be made in the engineering design to reduce these numbers as much as reasonably possible. Given the source parameters described earlier, the sizes of the apertures in the two masks emerge as

horizontal opening, guard mask: $X_1 = 4\Sigma_x + 4\Sigma_x' D_1 \approx 1100\,\mu m$

vertical opening, guard mask: $Y_1 = 4\Sigma_y + 4\Sigma_y' D_1 \approx 400\,\mu m$

horizontal opening, movable mask: $X_2 = \mathrm{FWHM}(\Sigma_y) + \frac{D_f}{L_o} \cdot D_2 \approx 150\,\mu m$

vertical opening, movable mask: $Y2 = 2 \cdot 1mm \approx 2mm(\mathrm{overall})$

Since the required aperture sizes in both the fixed and the movable mask are relatively small and must endure significant heat loads, fabrication of such apertures to the required tolerances will be an engineering challenge. Manufacturing these will be facilitated by having beam-defining constrictions in different locations along the beam direction for the various sides of the masks. This concept is illustrated in Figure 11.4.13b.

The movable mask features two halves, with the lower half containing a horizontal constriction and the upper half allowing unobstructed passage of the beam.

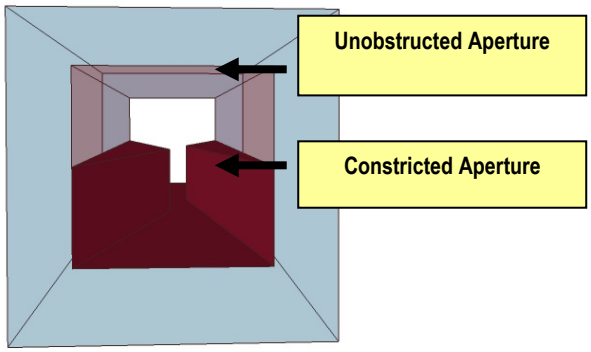

Figure 11.4.13a: Movable mask, beam entrance face.
Lower half with horizontal constriction, upper half straight-through.

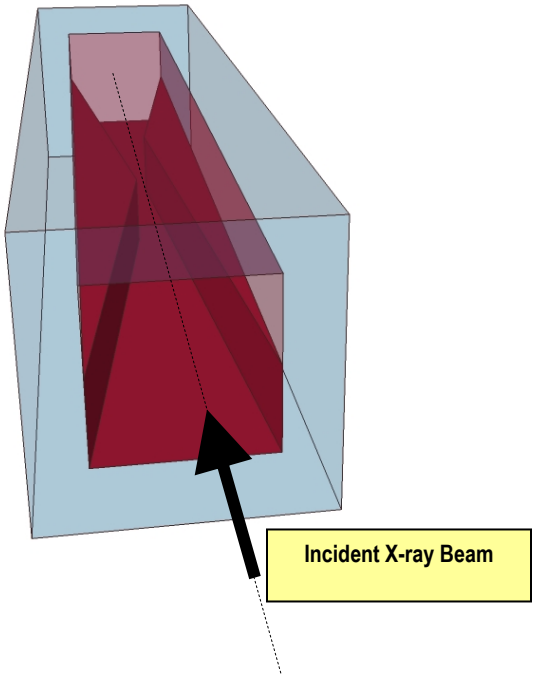

Figure 11.4.13b Movable mask. Points of maximum constriction in the lower half are at different locations along the beam direction for the left and right side.

References

[11.4.1] R. Saito, M. Fujita, G. Dresselhaus, M.S. Dresselhaus, "Electronic structure of graphene tubules based on C_{60}," *Phys. Rev. B,* **46** (1992), pp 1804-1811.
[11.4.2] N. Hamada, S. Sawada, A. Oshiyama, "New one-dimensional conductors: Graphitic microtubules," *Phys. Rev. Lett.,* **68** (1992), pp. 1578-1581.
[11.4.3] Q. Shen, CHESS Technical Memo 01-002, March 8, 2001.

11.5 An Inelastic X-Ray Scattering Beamline

11.5.1 Introduction

Inelastic X-ray Scattering is a momentum-resolved technique for studying dynamics and excitations in condensed matter systems. Of increasing importance, IXS has been used to study excitations ranging from phonons in solids, to sound modes in liquids and polymers, to plasmons in simple metals, to complex electronic excitations in strongly correlated electron systems. Further, there are many new, as yet largely unexplored, areas to which the technique could well make important contributions, including surface dynamics, excitations in extreme environments, time-resolved studies, and non-equilibrium dynamics.

As a technique that probes one of the fundamental response functions of a system, namely $S(q, \omega)$, IXS is an extremely powerful method for addressing some of the most important questions in condensed matter science today. Its principle limitation to date has been the dearth of active instruments in the world, and the very low count rates achievable on such instruments. Despite these limitations, IXS has the intrinsic

advantages of a weak cross-section (so that multiple scattering effects are negligible) and the ability to study very small samples (this latter attribute has been used, for example, to study phonons in high Tc compounds, in MgB_2, and in plutonium micro crystals, etc., for which larger, neutron-sized crystals are simply not available). Finally, there is no need to deuterate samples, as there is for inelastic neutron scattering from many soft-condensed-matter systems. As a result, given sufficient availability of instruments and reasonable count rates, IXS should have an impact at least as large as that of triple-axis neutron spectrometry, its direct analog. IXS beamline(s) at NSLS-II would feature unprecedented resolution and count rates and thus would be expected to offer the potential for high scientific impact.

In this section, we outline the design considerations necessary to construct a state-of-the-art IXS beamline at NSLS-II. We discuss three end stations, each focusing on a different energy-resolution regime: ~50 meV, 1 meV, and 0.1 meV. Of these, 0.1 meV is by far the most challenging, and we discuss a spectrometer based on an entirely new approach utilizing highly asymmetrically cut crystals operating in near-back-scattering. This approach has yet to be demonstrated in a working device and has a number of challenges associated with it. These challenges, and the R&D necessary to address them, are discussed in Chapter 12.

For the purposes of this report, the three end stations are treated as a single beamline, and indeed they could share the same upstream optics and have similar requirements of the undulator. However, although in principle it would be possible to construct all three end stations in series (Figure 11.5.1), in practice this would lead to inefficiencies in operation and in scientific productivity. A more optimized approach would likely move the medium-resolution (50 meV) instrument to it's own, dedicated beamline, with the 0.1 meV and 1 meV end stations sharing a second beamline. This has the advantage of grouping related science and techniques together, as well as providing optimized instruments and sufficient capacity for both regimes. In this scenario, the 50 meV instrument would focus on electronic excitations, while the 0.1 meV and 1 meV instruments would focus on the excitations involving the nuclei (phonons, diffusive modes, etc.), with the 1.0 meV instrument likely to be the work horse instrument, with a relatively high flux, and the 0.1 meV instrument utilized when the very highest resolution is required.

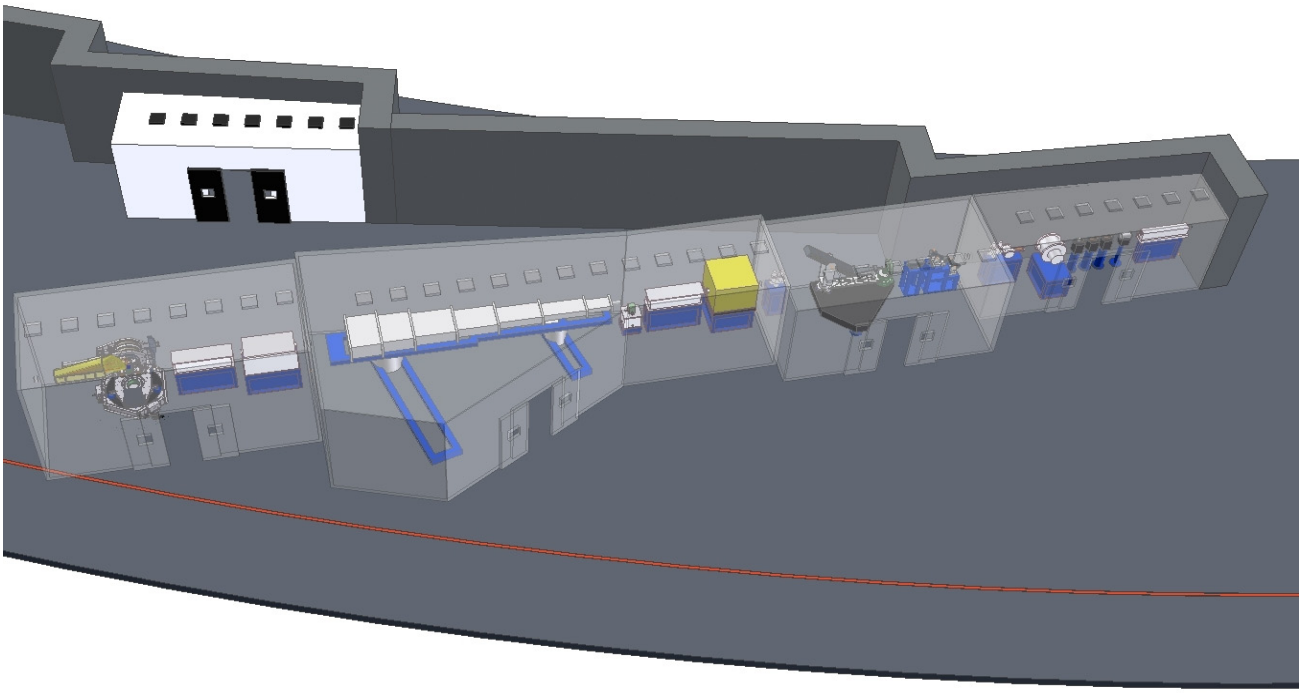

Figure 11.5.1 Three inelastic x-ray scattering end stations shown on a single beamline. These are, respectively, 0.1 meV, 1 meV, and 50 meV instruments, from right to left. Note, however, that these end stations are shown in this way for illustration purposes only. As discussed in the text, a more optimum arrangement would be to have one dedicated straight for the 50 meV and another for the 0.1 meV and 1 meV programs.

11.5.2 Conceptual Design for the Inelastic X-Ray Scattering Beamline

11.5.2.1 Source

The figure-of-merit for a radiation source for an IXS beamline is photons per second per meV. Of the devices considered in this CDR, the 3 m U19 device offers the best performance in this regard in the relevant energy range. However, because of the extreme need for photons for these experiments, it is worth considering further optimization for the IXS beamlines. In particular, longer length devices, if allowed by the machine parameters, improve the incident flux linearly with the length of the device. This is a significant factor for experiments for which a typical scan could easily be 24 hours long. A factor of two then makes a big difference in what can be accomplished in a given beamtime allocation. Such an improvement, or possibly more, may be achievable if accelerator studies during the detailed design phase of the project show that multiple narrow-gap devices can be accommodated in the 8 m straight sections. As shown in Figure 11.5.2, a particularly attractive option would be three 2 m SCU devices in an 8 m straight. This assumes the ability to focus the beam between such devices, which requires careful investigation. The increase in flux, compared to a single 3 m U19 device, would be a factor of five. These beamlines also make a case for yet longer straight sections, if that is possible.

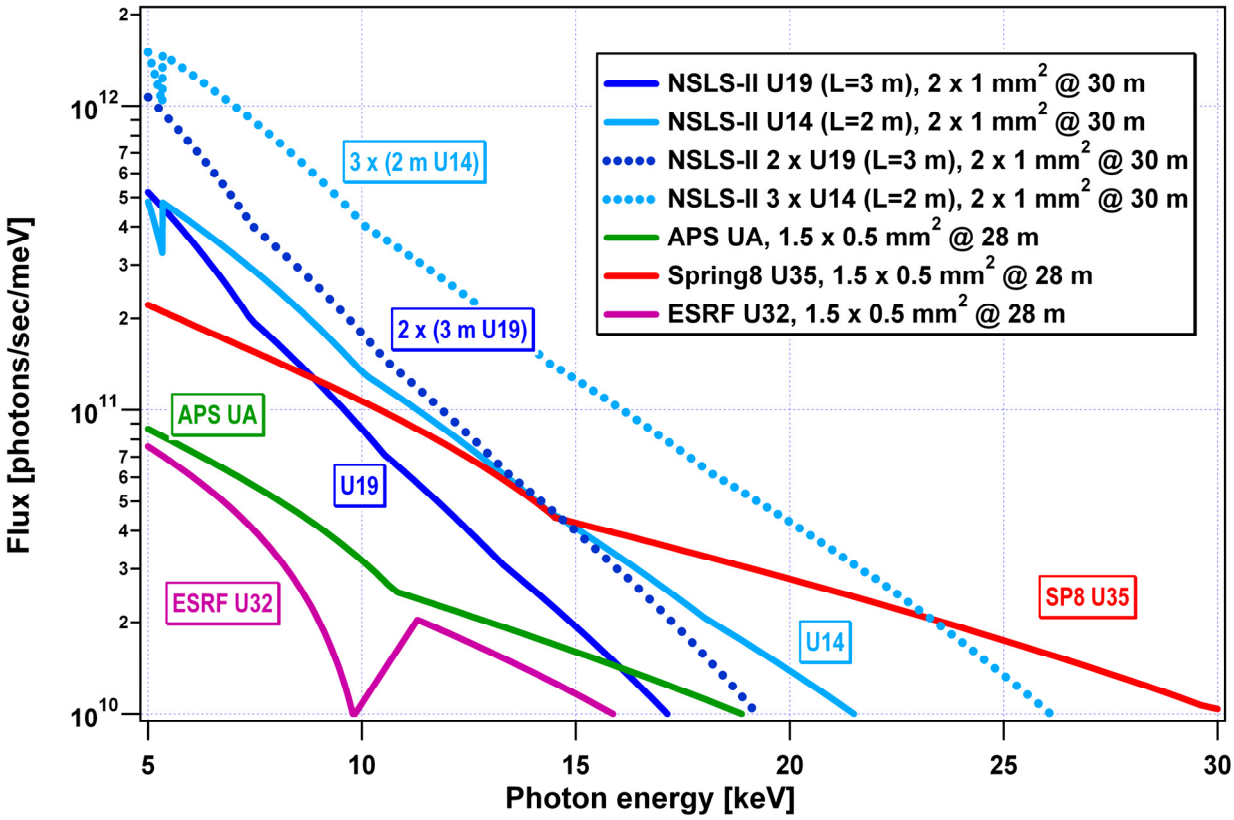

Figure 11.5.2 Comparison of various devices at NSLS-II and elsewhere, as measured in ph/s/meV, the figure of merit for inelastic x-ray scattering beamlines. The advantage of working at lower photon energies is clear. The NSLS-II IXS beamlines would operate around 10 keV and below. The blue dotted curves show the increase associated with placing multiple undulators in a single straight at NSLS-II. The examples shown are two 3 m U19 devices and three 2 m U14 devices and with $\beta_x=\beta_y=3$ m.

11.5.2.2 Beamline Optics

The upstream optics for an IXS beamline are likely to be relatively standard components, including focusing optics and a high heat load monochromator. As discussed elsewhere, this latter will either be a cryogenically cooled Si(111) double-bounce monochromator or a water-cooled diamond monochromator. There would then follow specialized high-resolution monochromators, appropriate to the particular end station served and, if required, appropriate focusing optics to deliver highly monochromatic, focused beam to the sample.

11.5.2.3 End Station I (0.1 meV)

IXS spectroscopy is becoming one of the major techniques for studying vibrational dynamics in solids, liquids, and biological macromacromolecules [11.5.5]. X-ray monochromators and analyzers with meV resolution are the main optical components of IXS spectrometers [11.5.4, 11.5.7, 11.5.18, 11.5.16, 11.5.1].

Single-crystal and multiple-crystal techniques for the meV monochromatization and analysis of x-rays have been developed over the past few decades (for references and reviews see [11.5.8, 11.5.17, 11.5.12]). These techniques all share a basic general property: the higher the required energy resolution, the higher the index of the Bragg reflections used, and thus the higher the energy of photons required. For this reason, photons with E>20 keV are typically used in IXS experiments that achieve meV resolution. To achieve yet higher resolution, that is, approaching ≈ 0.1 meV, with the techniques in use today at high-energy facilities such as ESRF, APS, and SPring-8, then very high-indexed Bragg reflections would be required with incident x-ray photon energies as high as 30 to 35 keV. However, this trend to higher energies conflicts with the basic fact that the brightness of undulators decreases with increasing photon energy, and that the experiments are extremely photon-hungry and can ill afford any reduction in flux. This problem is particularly relevant for NSLS-II, which will be extremely powerful at medium photon energies but not competitive with the higher-energy rings at higher photon energies. Finally, an added disadvantage of the higher energies is that the momentum transfer resolution worsens (for fixed acceptance angle) as the photon energy is increased.

To overcome these problems, and thus to broaden the potential of IXS, an alternative concept of an IXS spectrometer with meV and sub-meV for x-rays in the medium-energy spectral range (5–10 keV) has been proposed [11.5.12]. This approach exploits the effect of angular dispersion in asymmetric Bragg diffraction. One of the advantages of such an approach is that higher energy resolutions are achieved at lower photon energies, typically E<10 keV, a tendency that is consistent with better performance of x-ray undulators at these energies, and with better momentum transfer resolution. It is therefore proposed that the ultra high-resolution instrument at NSLS-II be based on these principles.

Briefly, a monochromator using this scheme requires an arrangement of three crystals, as shown in Figure 11.5.3a, playing the role of a collimator (C), a dispersing element (D), and a wavelength selector (W) in a three-bounce, so-called CDW monochromator. This same monochromator, combined with a parabolic mirror or Kirkpatrick-Baez system with graded multilayer mirrors (M), can also be used as a high-resolution analyzer of scattered radiation from a sample (S in Figure 11.5.3b).

This effect of angular dispersion in backscattering geometry has recently been demonstrated [11.5.15], and the first studies of a prototype CDW angular-dispersive monochromator have been performed [11.5.14], demonstrating an energy resolution of ΔE =2.2 meV for 9.1 keV photons.

In the following discussion, we outline a conceptual design of an IXS spectrometer utililzing 9.1 keV x-rays, providing an energy resolution of 0.1 meV and a momentum transfer resolution of $\approx 0.1 - 0.4$ nm^{-1}. The spectrometer uses the angular-dispersive (CDW-type) monochromator and analyzer. The concept is based on ideas contained in refs. [11.5.12, 11.5.15, 11.5.14, 11.5.13].

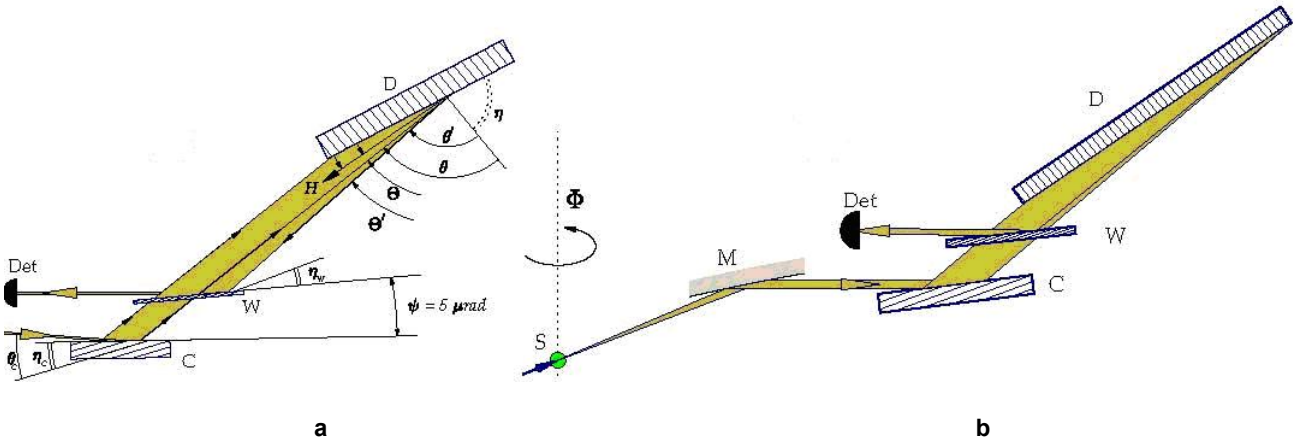

Figure 11.5.3 Schematic of the angular-dispersive backscattering CDW monochromator **a)**, and backscattering CDW analyzer **b)**. [11.5.12, 11.5.14]

11.5.2.3.1 Angular-Dispersive Monochromators

Basic Principle and Features

Any asymmetrically cut crystal diffracting at the Bragg condition behaves like an optical prism, dispersing x-ray photons with different photon energies at different angles. This effect, termed *angular dispersion*, can be used to monochromatize x-rays beyond the limits set by the spectral width of Bragg reflections. For this, in addition to a dispersing element (crystal D in Figure 11.5.3a), two more optical elements are required: a collimator, C, which reduces the angular spread of x-rays incident upon the dispersing element, and a wavelength selector, W. The latter selects x-rays with a desired angular, and hence spectral, spread. Bragg diffraction from single crystals can be used to achieve the required effects of collimation and wavelength selection. The angular dispersion is largest in backscattering. Further, the backscattering geometry is also favorable because the effect of angular dispersion is least affected by the angular spread of the incident radiation here.

The relative energy bandwidth $\Delta E/\mathrm{E}$ of the photons transmitted through the CDW monochromator with the dispersing element in backscattering is given by

$$\frac{\Delta E}{E} = \frac{\Delta\theta'_c + \Delta\theta_w}{2\tan\eta}, \qquad (11.5\text{-}1)$$

where η is the angle of asymmetry, $\Delta\theta'_c$ the angular spread resulting from the collimator, and $\Delta\theta_w$ the angular acceptance of the wavelength selector. Equation 11.5-1 demonstrates an important distinguishing feature of such monochromators: the relative spectral bandwidth $\Delta E/\mathrm{E}$ is independent of the intrinsic spectral width of the Bragg back reflection used. Nor does it depend on the photon energy E. Rather, it simply depends on the strength of the effect of angular dispersion, expressed by tan η, and the geometrical parameters, $\Delta\theta'_c$ and $\Delta\theta_w$. Any Bragg back reflection at any x-ray energy can be used. Importantly, the smaller the photon energy E, the narrower the energy bandwidth, ΔE, that can be obtained. A relative spectral bandwidth of $\Delta E/\mathrm{E} \approx 10^{-6}$ to 10^{-8}, and thus spectral bandwidths of $\Delta\mathrm{E} \approx$ 10 to 0.1 meV at $\mathrm{E} \leq$ 10 keV become possible. A compromise between this requirement for lower photon energy and the higher photon energy favored by smaller photo absorption makes the photon energy range 5 keV $\leq$ E $\leq$ 10 keV most favorable. Here, we have chosen to use 9.1 keV photons for the NSLS-II IXS monochromators and analyzers. We discuss the individual components below.

11.5.2.3.2 CDDW In-Line Monochromator

Despite the merits associated with CDW monochromators, practical difficulties associated with the backscattering geometry make them unwieldy in practice, precisely because of the backscattering geometry; an in-line monochromator would be more practical. Figure 11.5.4a shows such an in-line design, based on the angular dispersion principles. It has two dispersive elements, D1 and D2. The beam is dispersed twice, and therefore the angular dispersion is enhanced by a factor of two. This has the added advantage of then requiring dispersive elements of half the length for the same resolution. The same crystal (labeled C/W) is used as both the collimator and wavelength selection in this scheme.

The spectral function of such a monochromator, with a $\Delta E = 0.1$ meV bandwidth, is shown in Figure 11.5.4b. It has very steep wings, relative to the wings of the spectral function of a single conventional bounce backscattering monochromator. This is an important advantage; frequently, it is the tails of the elastic line (that is, the resolution function) that are the largest source of background in a real experiment, even at very large energy transfers relative to the nominal resolution. Such effects would be significantly reduced by this approach.

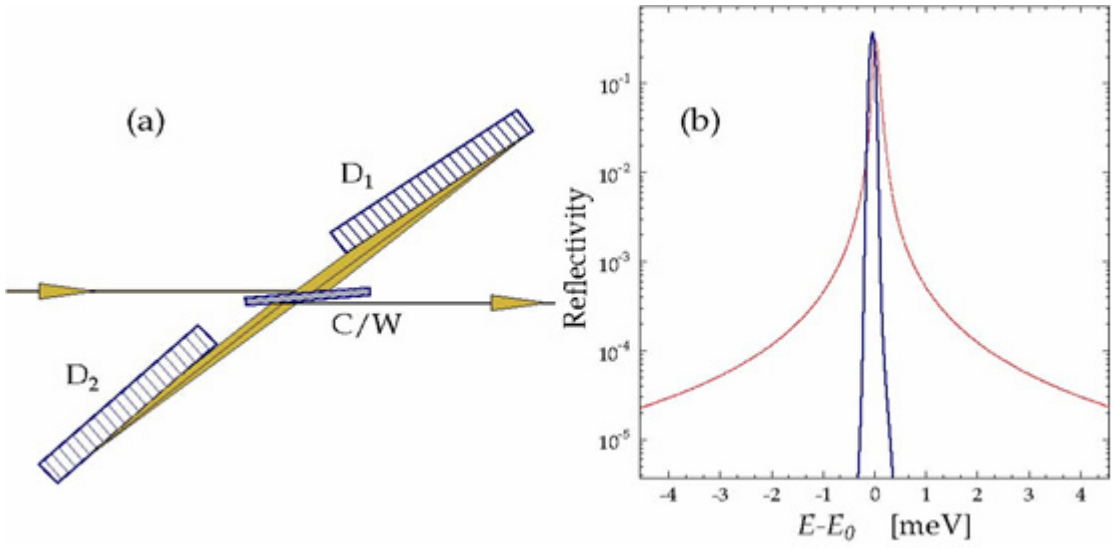

Figure 11.5.4 **a)** Schematic of an in-line angular-dispersive CDDW monochromator [11.5.13].

b) Blue line: dynamical theory calculations for the angular-dispersive CDW monochromator with a $\Delta E = 0.1$ meV bandwidth. Incident photon energy E = 9.1315 keV. Dispersive element: Si(008). Collimator and wavelength selector crystals: Si(220). Red line, shown for comparison: dynamical theory calculations for a single-bounce backscattering monochromator with a $\Delta E = 0.1$ meV bandwidth. Incident photon energy E = 31.02 keV Bragg back reflection Si(1 3 27).

The energy of the photons, selected by the CDDW monochromator, is tuned by varying the temperature of the crystals. The variation of the photon energy with crystal temperature is $\gamma(T) = -23.61(4)$ meV/K at T=300K [11.5.2]. Such an in-line CDDW monochromator is proposed for the IXS beamline at NSLS-II, as shown schematically in Figure 11.5.6.

11.5.2.3.3 Angular-Dispersive Analyzer

As noted earlier, the same optical instrument can be used both as a monochromator and an analyzer. The sole distinguishing functional feature of an analyzer relative to a monochromator is the ability to accept photons in a relatively large solid angle. Typically, an acceptance angle of Υ^2 with $\Upsilon \approx 5$ to 10 mrad is required for IXS experiments. This is a compromise between the required momentum transfer resolution, ΔQ, and the photon flux on the detector. An angular acceptance of $\Upsilon \approx 10$ mrad corresponds to $\Delta Q = 0.46$ nm^{-1} for 9.1 keV photons.

The CDW and CDDW monochromators presented above have an exceptionally large angular acceptance of $\Delta\theta_v = 0.1$ mrad in the vertical scattering plane and $\Delta\theta_h \approx 0.2$. to 0.3 mrad in the horizontal. However, this is still too small an acceptance for the monochromator to be used directly as an analyzer.

Therefore, to utilize either of these optics as an analyzer requires installing collimating optics in front of the analyzer. Collimators are optical elements that collect x-rays scattered from the sample over the required solid angle and deliver them to the analyzer with a reduced angular spread $\leq \Delta\theta_v$ and $\leq \Delta\theta_h$. The basic design concept of the analyzer discussed in this section involves the CDW monochromator and collimating optics integrated into a single instrument, an angular-dispersive x-ray analyzer, as shown in Figures (11.5.3b) and 11.5.6.

11.5.2.3.4 Collimating and Focusing Optics

For the purpose of collecting and collimating medium-energy x-ray photons (5 to 10 keV), it is appropriate to use reflective optics, such as curved grazing incidence mirrors [11.5.6], curved graded multilayer mirrors, KB systems with graded multilayer mirrors [11.5.11, 11.5.9, 11.5.10], or even tapered glass capillaries [11.5.3].

In addition to the requirement of having a rather large angular acceptance Υ, there are certain requirements for the exit parameters of x-rays leaving the collimating optics. First, the angular divergence should match the angular acceptances of the CDW monochromator, $\Delta\theta_v$ and $\Delta\theta_h$. Second, the vertical beam size should not exceed 0.5 to 1 mm (to keep the crystals comprising the angular dispersive analyzer at a manageable length). Optics with such collecting and collimating parameters are commercially available.

The angular divergence of x-rays after the collimating mirror arises from two main contributions, the mirror slope error and the source size contribution. The latter is basically given by the source size (the focal spot size on the sample) S divided by the source-mirror distance. Assuming the distance to be 100 mm (to accommodate the sample environment), the vertical and horizontal focal spot size on the sample should not exceed $S_v \leq 10$ μm and $S_h \leq 20$ to 30 μm, respectively. This requires a focused beam on the sample. Such focusing can be achieved using a commercial focusing system, which is shown schematically on the beamline layout in Figure 11.5.6. While such focusing is certainly a complication, it is also true that, for many experiments, a micro-focused beam is not only a great advantage but a necessity.

11.5.2.3.5 Segmented CDW Analyzer

Achieving a very small energy bandpass of about 0.1 meV requires a very large asymmetry angle, $\eta = 89.5°$, for the dispersing element. This causes an evident technical problem: the dispersive element must be very long, about 2 m, to ensure an angular acceptance of $\Upsilon \leq 2$ to 3 mrad of the analyzer in the vertical plane. The angular acceptance in the horizontal plane can be kept at the level of $\Upsilon_h \leq 10$ to 15 mrad, independent of the beam size.

To overcome the technical problems associated with such an extreme length of the dispersive element, it would be built in independent segments, as shown in Figure 11.5.5 (only three segments are shown). It should be possible to build a 2 m-long dispersive element consisting of about eight to 10 segments, each 20 to 25 cm

long. Note that it is not necessary for the reflecting atomic planes of the segments to be aligned perfectly parallel to each other.

In addition to easing fabrication issues, such a scheme also means that the crystal temperature of a given segment is now only required to be homogeneous to 0.5 mK (corresponding to 0.01 meV energy shift), rather than requiring the same tolerance along an entire 2 m length. Any angular misalignment and temperature shifts of the segments relative to each other will simply result in relative energy shifts of the spectra measured by the different segments. These shifts can be corrected in the data analysis, provided the signal from each segment is recorded independently. For this purpose a position-sensitive detector would be used, as shown in Figures 11.5.5 and 11.5.6. Such corrections are routine in conventional high-energy resolution IXS spectrometers, for which the spectra from multiple analyzers are recorded by independent (point) detectors.

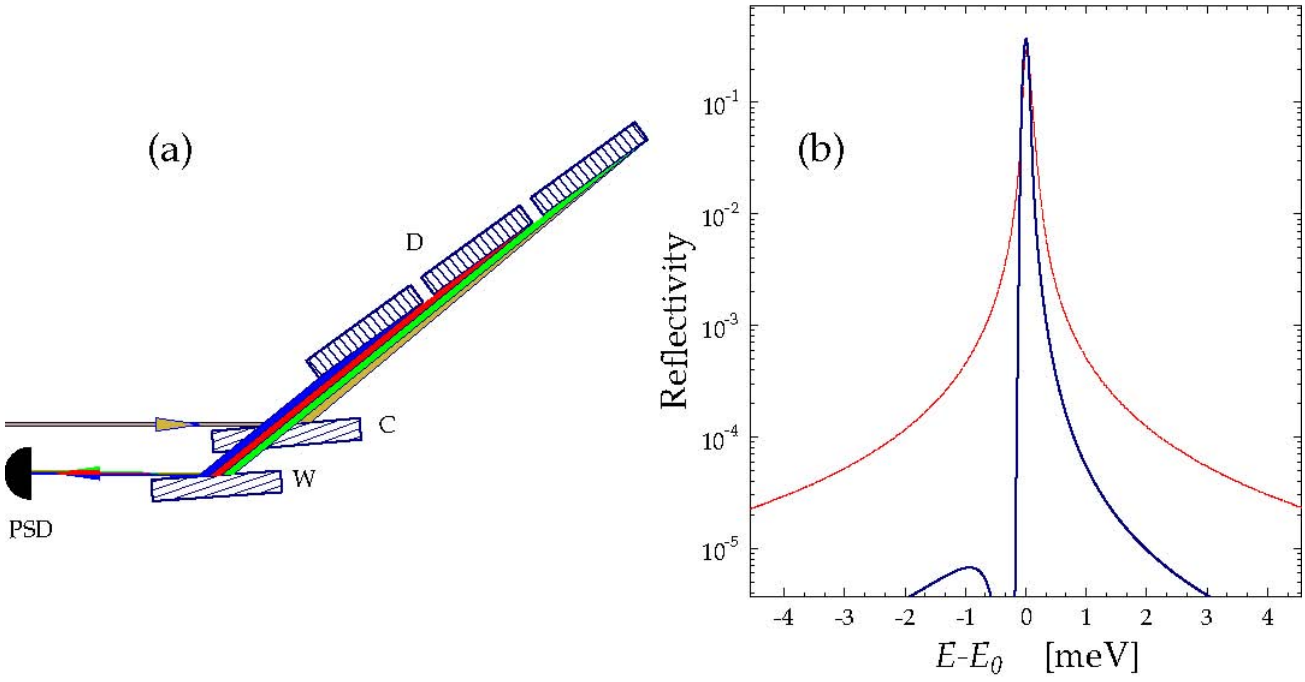

Figure 11.5.5 **a** Schematic of the angular-dispersive CDW backscattering segmented analyzer with the position-sensitive detector, PSD [11.5.13].

b Dynamical theory calculations for the angular-dispersive CDW analyzer with a ΔE = 0.1 meV bandwidth. Incident photon energy E = 9.1315 keV, incident beam angular divergence = 0.1 x 0.2 mrad^2. For comparison, dynamical theory calculations for a single-bounce backscattering monochromator with a ΔE = 0.1 meV bandwidth are shown by the red line.

Figure 11.5.5b shows dynamical theory calculations for the angular-dispersive CDW analyzer with a bandwidth of ΔE = 0.1 meV. The incident photon energy E is 9.1315 keV. Incident beam angular divergence is 0.1 × 0.2 mrad^2, corresponding to the angular divergence of x-rays from the collimating mirror. The spectral function is compared with that of a single-bounce backscattering analyzer of the same resolution, which can be achieved using the high index Bragg reflection Si(1 3 27) and a photon energy E = 31.02 keV. As was the case for the monochromator, the spectral function of the CDW analyzer has much steeper wings relative to conventional approaches, which is a significant advantage.

11.5.2.3.6 Optical Scheme of the IXS Spectrometer

Figure 11.5.6 shows a schematic layout of the entire IXS spectrometer. It comprises the angular-dispersive CDDW in-line monochromator, the focusing mirror, the CDW backscattering segmented analyzer, and the position-sensitive detector. The spectrometer is shown integrated into the IXS beamline, together with other main beamline components: undulator, high heat load monochromator, etc. A possible design of the IXS spectrometer is presented in Figure 11.5.7.

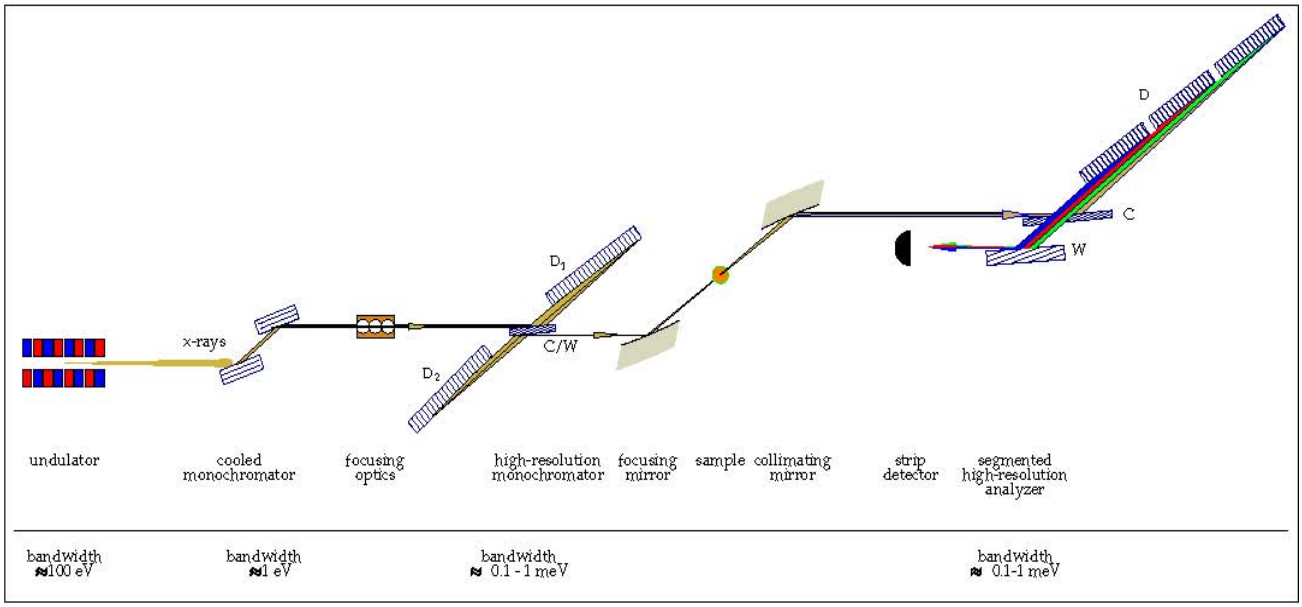

Figure 11.5.6 Optical scheme of the IXS spectrometer with angular-dispersive CDDW in-line monochromator and CDW backscattering segmented analyzer integrated with other main elements of the IXS beamline [11.5.13].

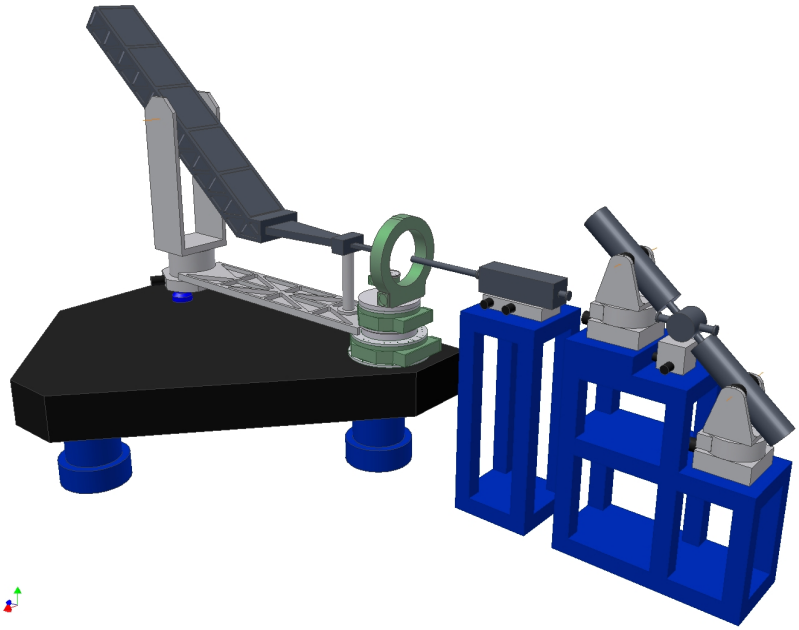

Figure 11.5.7 Possible design of the IXS spectrometer with angular-dispersive CDDW in-line monochromator and CDW backscattering segmented analyzer according to the optical scheme of Figure 11.5.6.

11.5.2.4 End Station II (1 meV)

There currently exist several instruments around the world capable of ~1 to 2 meV energy resolution, notably at ESRF, SPring-8, and APS. Each of these instruments uses backscattering high-order Si reflections (typically, Si[n,n,n] reflections) for analyzers to achieve the appropriate energy resolution. The monochromators used are either also Si(n,n,n) reflections (at ESRF and SPring-8) or high-order reflections utilized in a nested in-line geometry (at APS). To achieve ~1 meV resolution, the photon energy used is in excess of ~20 keV. In principle, one could build a similar instrument at NSLS-II and achieve the same resolution. However, because of the lower storage ring energy at NSLS-II, it would be difficult for such an instrument to be competitive, at these photon energies, with the higher energy third-generation sources.

There are two alternatives to this approach that might be fruitful at NSLS-II.

The first alternative is to again use asymmetric optics discussed above for the 0.1 meV instrument, operating at photon energies of ~9 keV and at smaller asymmetric angles and therefore lower resolutions. The spectrometer itself would look very similar to the one outlined above. The technical challenges associated with such an instrument operating at ~1 meV are significantly more tractable than they are for reaching 0.1 meV. Indeed, as discussed in Chapter 12, the principle has now been demonstrated at 2.2 meV—though there remains a long way to go before a working, high-throughput instrument can be built on these principles. Nevertheless, many of the same advantages described above for the 0.1 meV instrument (sharp resolution functions, good reciprocal space resolution, high flux/meV, etc.) apply equally well here and thus this scheme presents a worthy alternative to the traditional Si(n,n,n)-type approaches of the high-energy rings. Further, the R&D that will be carried out to reach 0.1 meV will necessarily address all of the issues associated with reaching 1 meV. Thus, relatively early in the NSLS-II construction project the answers to the practicality of a 1 meV instrument based on asymmetric optics will be much clearer and one can decide whether to proceed along these lines.

A second alternative would be to move away from Si reflections and utilize other materials with more favorable resolutions at medium energies. As discussed in Chapter 12, such alternatives include sapphire and quartz. There it is stated that inherent limitations in these, and equivalent materials, limited their usefulness at very high resolutions (~0.1 meV). These include very low structure factors and the resulting small reflectivity and large tails in the resolution function. However, the case against such materials is much less clear at resolutions of ~1 meV, and here they may well provide a viable alternative to Si.

In this case, the instrument would look physically similar to the conventional high-resolution instruments with a single-bounce backscattering monochromator and backscattering analyzers. In order to accommodate the large 2θ arm (which would be on the order of 5 to 6 m long), the scattering would be in the horizontal plane. This also greatly reduces the engineering challenges associated with utilizing multiple analyzers. These are commonly arranged in $n \times m$ arrays in which each analyzer is focused onto a dedicated detector (at NSLS-II this might be, say 5×7, with the long side of this array in the scattering plane). This allows data to be collected at multiple points in reciprocal space simultaneously—something that is not simple to do with the asymmetric optics approach. This greatly increases the data throughput—by an order of magnitude, for some experiments. It is difficult to overstate this advantage in a field in which scans routinely take ~24 hrs.

In terms of the analyzer material, one candidate is quartz. As a non-centrosymmetric crystal, quartz offers a number of potential advantages for use as an analyzer material, [11.5.19]. These advantages include providing 184 backscattering reflections between 5–12 keV, many more than the 22 provided by Si, which is of great boon in terms of finding an appropriate reflection if one has to work at a particular energy—for example, a K-absorption edge for a resonance experiment. In addition, quartz has a coefficient of thermal expansion that is three times larger than Si, allowing much greater energy ranges in temperature scans.

Figure 11.5.8 shows some recent results for large-area quartz wafers [11.5.19]. The reflection used was (7, -4, -3, 4) with a Bragg angle of 89.77 at 9.929 keV. When the full 11 cm^2 wafer was illuminated, a resolution of 4 meV was obtained, compared to a theoretical value of 2 meV for a perfect crystal. This

difference was attributed to defects in the quartz associated with strain resulting from the mounting scheme. Figure 11.5.8 show results from two selected areas of the large wafer. It is seen that when an 8×8 mm apparently defect-free area was selected, a resolution of 2.9 meV was obtained, whereas if the beam spot included a defect (dark area in the x-ray topographic image), then the resolution was observed to worsen to 4 meV. However, in addition to the resolution FWHM, another figure of merit for such analyzers is the tails of the resolution function; these were observed to be significantly worse than theoretically expected. Further efforts are required to understand the origin of these tails and to seek to mitigate them.

Such efforts are currently ongoing at SPring-8 (quartz) and APS (quartz and sapphire). If successful, these will offer an alternative route to 1 meV spectroscopy at moderate photon energies. The NSLS-II project will monitor these developments, in addition to carrying out the asymmetric optics R&D for the 0.1 meV effort.

Finally, irrespective of which approach is followed, it is important that the 1 meV instrument cover a wide range in reciprocal space. For example, the scattered intensity from phonons increases with $\sim Q^2$, where Q is the total momentum transfer (though at very large momentum transfers, the Q-dependence of the atomic form factor takes over, driving the intensity to zero). In addition, it is frequently of value to study multiple Brillouin Zones to look for systematic dependencies in the data. For the high photon energy instruments discussed above, this requirement is not too onerous and can be achieved for 2θ scattering angles significantly less than 90°. However, for the photon energies of ~9 keV discussed here, then the requirement that one reach to Q ~8 A^{-1} corresponds to a 2θ angle of ~120°. This presents a problem, because of the horizontal incident polarization and the resulting $cos^2 2\theta$ dependence of the scattering intensity, which reaches zero at 90°.

This problem may be solved by rotating the incident polarization in to the vertical plane by use of two diamond quarter-wave plates. Such arrangements have been shown to be very efficient (~97%) in terms of rotating the polarization, and relatively efficient in terms of transmitted intensity (~40%) at 9.1 keV [3.5.20], and thus should be practical for such purposes.

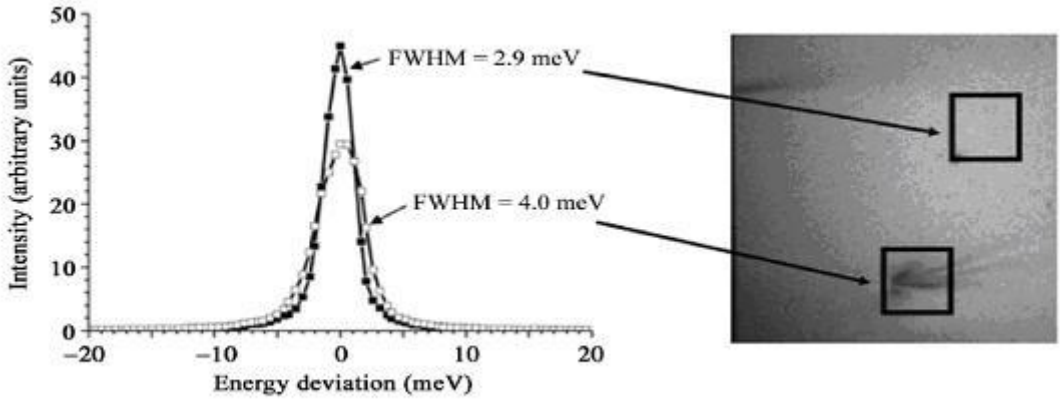

Figure 11.5.8 Quartz offers a potential route to high energy resolutions at medium photon energies. These images show the performance of a quartz wafer at 9.979 keV. The figure shows the energy resolution obtained from two different areas of the same quartz wafer. The right-hand image shows an x-ray topograph of that wafer. The dark spot corresponds to a strain defect believed to be associated with the mounting scheme.

11.5.2.5 End Station III (50 meV)

Achieving ~50 meV bandpass on the incident beam in energy ranges ~5 to 10 keV is a relatively straightforward technical challenge. An example of the state of the art is the MERIX instrument at section 30 at APS, which (at the time of writing) has recently begun final commissioning. This instrument utilizes a four-bounce monochromator of the type shown schematically in Figure 11.5.9. For the reflections show here,

namely Si (800), this device achieves a relatively constant bandpass of ~70 meV and a high spectral efficiency over the energy range 5 keV to 10 keV. By carefully choosing the reflections and mounting multiple crystals simultaneously on the goniometers, it is possible to construct a single monochromator with a number of different resolutions available to the user. Resolutions are chosen by translating the goniometers perpendicular to the beam to select the appropriate crystals. Such an approach gives the user flexibility to choose a higher-flux, lower-resolution mode for part of their experiment, before switching to a high-resolution (and therefore lower flux) mode to examine, for example, a particular feature in more detail. This switch can be made relatively quickly during the course of a single experiment and is therefore highly flexible. Such an approach would likely be followed at an NSLS-II IXS beamline.

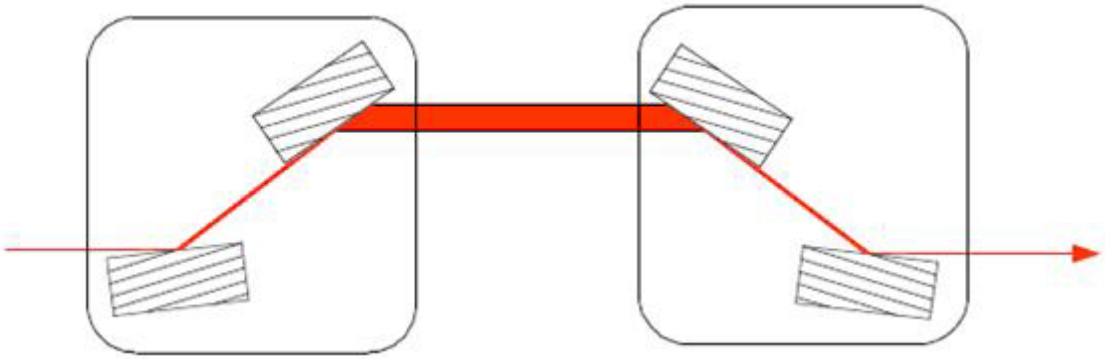

Figure 11.5.9 Medium-energy resolution, constant bandpass monochromator (following Toellner et al., APS [11.5.17]). The use of a four-bounce arrangement of crystals allows a constant bandpass, high-spectral efficiency monochromator (see Figure 11.5.1).

The new Sector 30 beamline at APS also provides a good example of the kind of end station envisaged for the 50 meV instrument at NSLS-II. Figure 11.5.10 shows an illustration of this concept. It features a spectrometer with both horizontal and vertical scattering geometries. This is particularly useful for examining polarization effects in the resonant cross-section, allowing the user to switch between polarization in the scattering plane and perpendicular of the scattering plane, in a single experiment. In addition, the availability of a horizontal scattering geometry allows the accommodation of large sample environments such as pressure cells, cryostats, or superconducting magnets that for various physical reasons only permit horizontal scattering. Finally, having a horizontal scattering geometry available allows the user to position the spectrometer at a 90° scattering angle and thus suppress all the nonresonant elastic scattering. This can greatly increase the visibility of inelastic features at low energy transfers.

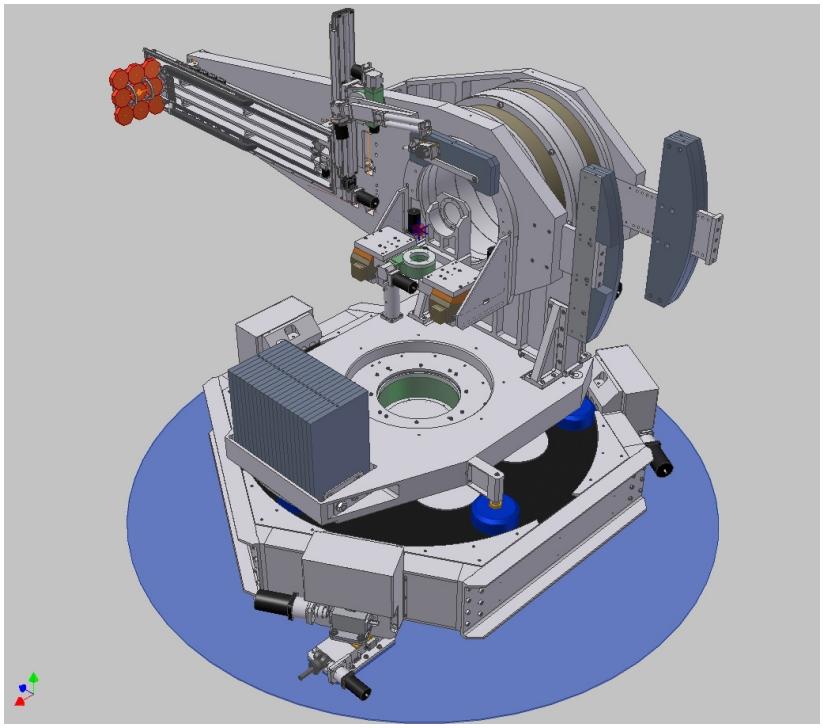

Figure 11.5.10 Possible design for 50 meV IXS end station. Figure shows recently built end station at APS with additional features, including multiple analyzers.

The spectrometer also features 1) a novel counterbalance arrangement to eliminate twisting of the arm as it moves from zero to 90° in the vertical, so the analyzer remains lined up even at the very highest resolutions, and 2) a motorized analyzer stage that allows analyzers of different radii to be used in the same instrument.

There are also several improvements that one would make to such an instrument at NSLS-II. The first would be to take advantage of the increased count rates at NSLS-II relative to existing sources, to carry out polarization analysis of the scattered beam. This has not been attempted before in the hard x-ray regime because of the prohibitively low count rates, but it may be possible at NSLS-II. Such experiments would utilize an analyzer working at 45°; count rates could be expected to be very low, but it may be feasible for certain experiments. If possible, such experiments would provide quantitatively new information, allowing the symmetry of the excitations to be probed directly. This would greatly facilitate the identification of the various observed excitations—something that presently can only be done with theoretical input or by comparison with other techniques, a process that is not always unambiguous.

An additional improvement shown in the figure would be to include multiple analyzers. Such an approach has been utilized in a number of other IXS spectrometers, notably in this energy resolution range at BL12XU at SPring-8. Typically, for such spectrometers the multiple analyzers focus on a single detector and the count rate is increased at the expense of reciprocal space resolution. As discussed below (Section 11.5.3), we are proposing to use position-sensitive detectors to improve both the resolution and data throughput (by simultaneously collecting data for a range of energy transfers). Thus we propose a detector for each analyzer crystal. This would therefore allow data to be taken at multiple q values simultaneously. For single-crystal work, the cut taken by such an area of analyzers through reciprocal space would not be a linear one because the sample is fixed while the data is collected; rather, it would represent a curved path. However, this only allows a slight complication in the data analysis, and by careful choice of scattering angles the impact of this can be minimized. Such an approach would dramatically increase the data rates of the instrument. Also note that similar approaches are routine at spallation neutron sources, where sophisticated software is available to reconstruct the path through (q, E) space in much more complicated geometries than are proposed here. Finally, we note that Figure 11.5.10 illustrated nine analyzers; there is no reason, in principle, that this number could not be extended, though it would be an engineering challenge to handle the associated

additional weight. A conceptual layout for this instrument is show in Figure 11.5.11, in which only a single analyzer is illustrated, for clarity.

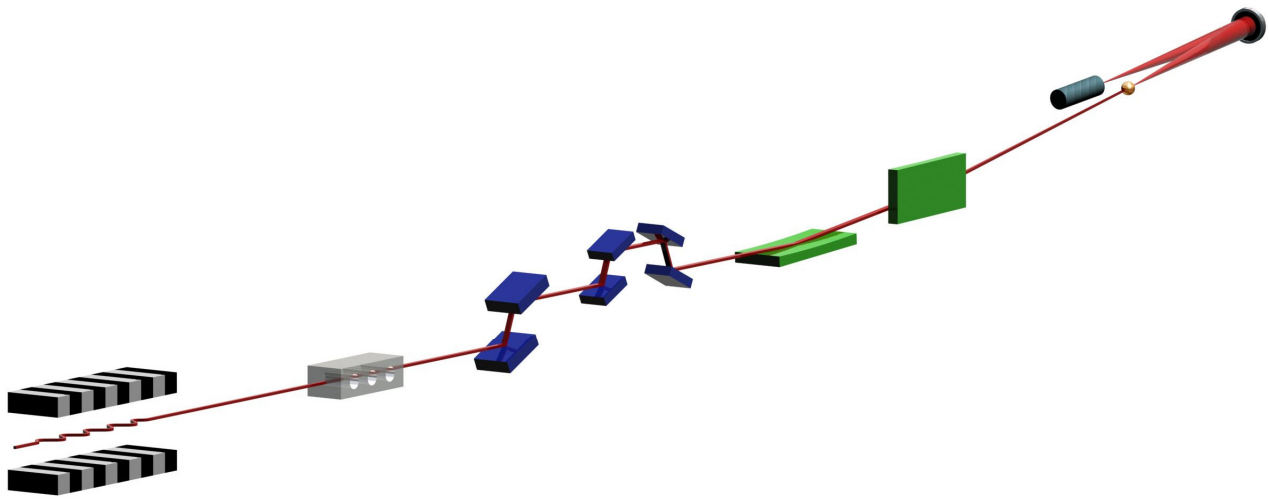

Figure 11.5.11 Conceptual layout for an IXS beamline at NSLS-II. Downstream of the undulator source is a collimating optic (if required), a high heat load monochromator (with eV bandpass), followed by a high-resolution monochromator (meV bandpass), and focusing optics. Downstream of the sample is a large-area analyzer (perhaps multiple analyzers) and a position-sensitive detector (see text).

11.5.3 Strip Detector

To allow for focusing and energy analysis, IXS spectrometers use a so-called Rowland circle geometry. This geometry requires a bent crystal analyzer with a bending radius that is the same as the diameter of the Rowland circle. Bending a perfect crystal causes strain and deformations of the crystal that make-high energy resolution impossible. To circumvent this difficulty, current analyzers use a diced crystal that results in thousands of small, flat, unstrained cubes.

The finite cube size contributes to the energy resolution. To minimize this contribution, one works very close to backscattering. This geometry can cause problems by constraining the sample environment; for example, it makes the use of large magnet cryostats difficult because of the requirement that the detector be near the sample. For Resonant Inelastic X-ray Scattering experiments, the need to be near backscattering is particularly problematic, since the incident energy is also constrained to be near the energy of an x-ray edge. In general, it is not possible to match a backscattering energy with a resonant energy, using the crystals that are currently available. This limitation has meant that high-resolution RIXS studies have been limited to one element (Cu) out of dozens of elements with K and L edges that would otherwise be suitable. Further improvements to this technique are limited by the loss of analyzer area and the inability to create cubes that are sufficiently small.

However, it is possible to circumvent the limit imposed by cube size, using a strip detector. Such a detector consists of pixels approximately 50 microns wide with a length on the order of several mm. Work by Huotari et al. [11.5.21], shown in Figure 11.5.12, has proven the feasibility of this method. As illustrated in Figure 11.5.12, the use of a position-sensitive detector allows one to resolve, spatially, the contributions from the different parts of the diced cube (rather then integrating them all, as is done traditionally with a point detector). Since there is a perfect angle–energy correlation (via Bragg's law), this corresponds to energy resolving the diffracted beam, with the energy resolution now being determined by the intrinsic Darwin width of that reflection (assuming the blocks are, in fact, unstrained). Thus, this approach both improves the energy resolution and relaxes the constraint on being near backscattering. Use of a strip detector would thus enable

high-resolution studies (tens of meV) at all the available edges—in most cases, a 10-fold improvement in resolution. Note that this increase in resolution comes at no loss in signal; in fact, because a position-sensitive detector can collect a range of energy transfers simultaneously, the net data collection rate can be significantly increased relative to point-detector schemes. Thus, the seemingly impossible dual feat of improved resolution and improved data rates is achieved. It will also allow the placement of analyzers closer to the sample, thereby improving the solid angle collected and further increasing the count rates. We anticipate that such schemes will be utilized in the medium-energy resolution instrument at NSLS-II.

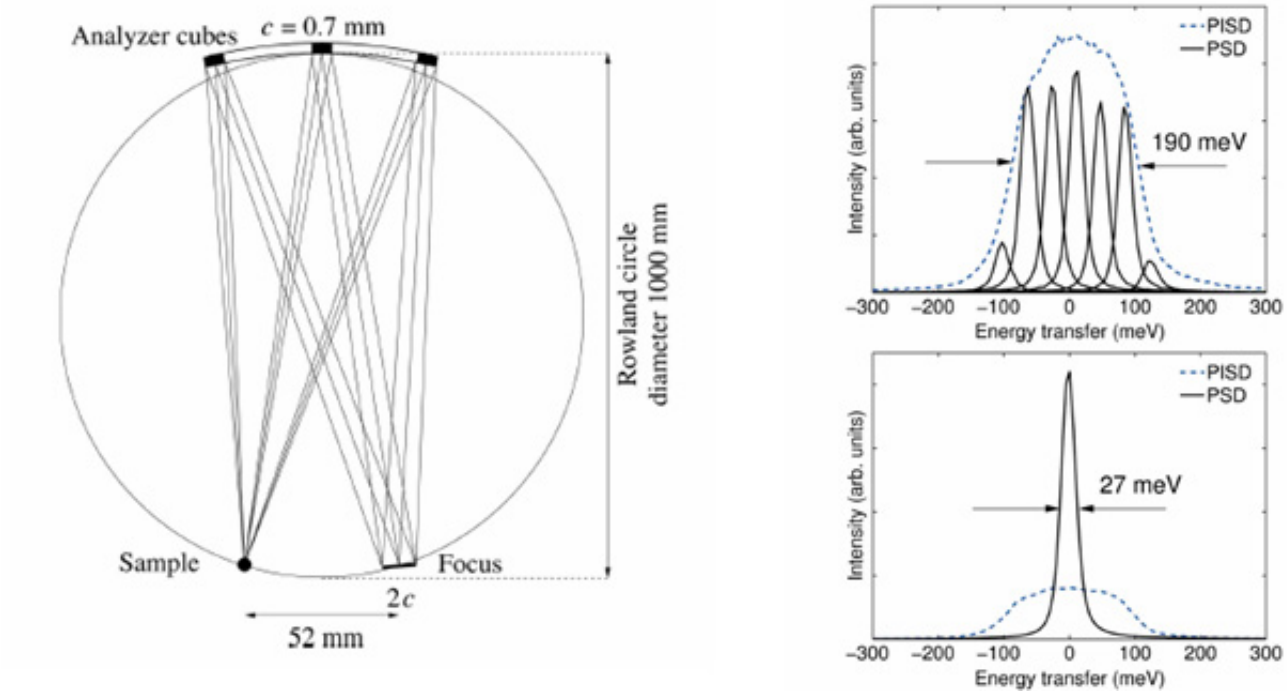

Figure 11.5.12 Rowland Circle geometry and improved resolution due to a strip detector [11.5.21].

11.5.4 Laboratory and Office Space

Several ancillary pieces of equipment would significantly improve the productivity of an IXS beamline and should be available to the users of such a beamline. These include optical conductivity/ellipsometry setups to measure $\sigma(\omega)$ in single crystals in the energy range up to ~6 eV. These measurements provide $\sigma(\omega)$ data that naturally complement the IXS measurement of $S(q,\omega)$ and related quantities that would be performed on the medium-energy resolution instrument and would thus provide a useful, quick cross-check of the data coming off the beamline. Similarly, SQUID magnetronometry and devices such as a Quantum Design PPMS, which provide growth characterization of bulk properties, would be extremely useful. Finally, single-crystal orienting (and possibly) facilities that would allow a sample to be oriented on a goniometer and transferred to the IXS spectrometer would be extremely useful, particularly for the very-high-resolution IXS instruments, which will not have full 6-circle capability and will require pre-orienting of the sample before taking data.

11.5.5 Outstanding Issues

IXS experiments will be among the most photon-hungry experiments performed at NSLS-II. As such, there is a strong case to be made to dedicate a straight section to each end station to optimize the amount of time available for data taking. In particular, the medium-resolution instrument is likely to be well served by a

dedicated set of upstream optics and would comfortably sustain a sufficiently large user community with great enough scientific impact to justify such a development. Finally, these experiments are mostly flux limited, not brightness limited; if, in the context of Title I design, it becomes apparent that longer straight sections are possible and that one could still close the gap in a U19-type device, then the IXS beamline(s) would greatly benefit from such developments. Optics that will be considered include multiple devices in a single straight section with focusing between them; three 2 m SCU devices would be the preferred alternative. Again, in an 8 m straight, accelerator studies need to be performed to determine the impact of such an approach.

References

[11.5.1] A.Q.R. Baron, Y. Tanaka, D. Miwa, D. Ishikawa, T. Mochizuki, K. Takeshita, S. Goto, T. Matsushita, H. Kimura, F. Yamamoto, and T. Ishikawa. Early commissioning of the SPring-8 beamline for high resolution inelastic x-ray scattering. *Nucl. Instrum. Meth. A* **467** 627 (2001).

[11.5.2] A. Bergamin, G. Cavagnero, G. Mana, and G. Zosi. Scanning x-ray interferometry and the silicon lattice parameter: Towards 10^{-9} relative uncertainty? *Euro. Phys. J. B* **9** 225 (1999).

[11.5.3] D.H. Bilderback, S.A. Hoffman, and D.J. Thiel. Nanometer spatial resolution achieved in hard x-ray imaging and Laue diffraction experiments. *Science* **263**(5144):201 (1994).

[11.5.4] E. Burkel. *Inelastic Scattering of X-ray s with Very High Energy Resolution*, Vol. 125 of *Springer Tracts in Modern Physics*. Springer, Berlin, 1991.

[11.5.5] E. Burkel. Phonon spectroscopy by inelastic x-ray scattering. *Rep. Prog. Phys.* **63** 171–232, 2000.

[11.5.6] M.R. Howells, D. Cambie, R.M. Duarte, S. Irick, A.A. MacDowell, H.A. Padmore, T.R. Renner, S. Rah, and R. Sandler. Theory and practice of elliptically bent x-ray mirrors. *Opt. Eng.* **39** 2748 (2000).

[11.5.7] C. Masciovecchio, U. Bergmann, M. Krisch, G. Ruocco, F. Sette, and R. Verbeni. A perfect crystal x-ray analyzer with meV energy resolution. *Nucl. Instrum. Meth. B* **111** 181 (1996).

[11.5.8] T. Matsushita and H. Hashizume. X-ray monochromators. In E. E. Koch, editor, *Handbook on synchrotron radiation*, Vol. 1, pp 261– 314. North-Holland, Amsterdam, 1983.

[11.5.9] Ch. Morawe, P. Pecci, J. Ch. Peffen, and E. Ziegler. Design and performance of graded multilayers as focusing elements for x-ray optics. *Rev. Sci. Instr.*, **70** 3227 (1999).

[11.5.10] V.V. Protopopov, V.A. Shishkov, and V.A. Kalnov. X-ray parabolic collimator with depth-graded multilayer mirror. *Rev. Sci. Instr.*, **71** 4380 (2000).

[11.5.11] M. Schuster and H. Göbel. Parallel-beam coupling into channel-cut monochromators using curved graded multilayers. *J. Phys. D: Appl. Phys.* **28** A270 (1995).

[11.5.12] Yu. Shvyd'ko. *X-Ray Optics – High-Energy-Resol. Appl.*, Vol. 98 of *Optical Sciences*. Springer, Berlin Heidelberg New York, 2004.

[11.5.13] Yu.V. Shvyd'ko. "Advanced designs of angular dispersive x-ray monochromators." *To be published*, 2006.

[11.5.14] Yu.V. Shvyd'ko, U. Kuetgens, H.D. Rüter, M. Lerche, A. Alatas, and J. Zhao. Progress in the development of new optics for very high resolution inelastic x-ray scattering spectroscopy. *Submitted for publication*, 2006.

[11.5.15] Yu.V. Shvyd'ko, M. Lerche, U. Kuetgens, H.D. Rüter, A. Alatas, and J. Zhao. Bragg diffraction of x-rays in asymmetric backscattering geometry. *Submitted for publication*, 2006.

[11.5.16] H. Sinn. Spectroscopy with meV energy resolution. *J. Phys.: Condens. Matter*, **13**(34) 7525 (2001).

[11.5.17] T.S. Toellner. Monochromatization of synchrotron radiation for nuclear resonant scattering experiments. *Hyp. Interact.*, 125:3, 2000.

[11.5.18] R. Verbeni, F. Sette, M.H. Krisch, U. Bergmann, B. Gorges, C. Halcoussis, K. Martel, C. Masciovecchio, J.F. Ribois, G. Ruocco, and H. Sinn. X-ray monochromator with 2×10^{-8} energy resolution. *J. Syn. Rad.*, **3**:62–64, 1996.

[11.5.19] J.P. Sutter, A.Q.R. Baron, D. Miwa, Y. Nishino, K. Tanasaku, and T. Ishikawa*, J. Syn. Rad*. **13** 278 (2006).
[11.5.20] C. Giles, C. Vettier, F. de Bergevin, C. Malgrange, G. Grubel, and F. Grossi, *Rev. Sci. Instr.* **66** 1518 (1995).
[11.5.21] Huotari et al., *J. Sync. Rad.* **12**, 467 (2005).

11.6 A Coherent X-Ray Scattering Beamline (CXS)

11.6.1 Introduction

In this section we discuss the conceptual design of an x-ray beamline that has been designed to take advantage of the extraordinarily high coherent flux that will be provided in the hard x-ray range by NSLS-II. We begin with a few notes on terminology used in this section:

- **Coherent X-Ray Scattering (CXS)** or **X-Ray Coherent Scattering** refers in general to scattering measurements exploiting the coherent nature of the hard x-ray beam.
- **X-Ray Photon Correlation Spectroscopy (XPCS)** or **X-Ray Intensity Fluctuation Spectroscopy (XIFS)** are two terms for the same technique, namely, measurements of the time evolution of fluctuating x-ray speckles, from which characteristic sample decay time(s) are obtained. Hereafter, for brevity, we will refer to this technique as XPCS.
- **Coherent X-Ray Diffraction (CXD)** or **Coherent Diffractive Imaging (CDI)** or **Coherent X-Ray Diffractive Imaging (CXDI)** or *lensless imaging* refer to problems of phase retrieval and object reconstruction based on over-sampled measurements of the scattered intensity

We describe here a beamline with two end stations operating in parallel. The first end station is optimized for coherent x-ray diffraction and large-angle x-ray photon correlation spectroscopy and the second is for small-angle x-ray photon correlation spectroscopy. Finally, we note that diffraction-enhanced imaging and full-field imaging are not part of the scientific mission of this beamline

11.6.2 Conceptual Design of the CXS

The basic concept of the proposed design of the coherent scattering beamline at NSLS-II is to substitute the intrinsic source with a secondary source that is controlled by the end user. This decouples uncertainties of position, stability, and emittance of the synchrotron source from those used for measurements. It also allows multiplexing of the source using horizontally deflecting mirrors so that two stations can be operated in parallel. A secondary source is employed only in the horizontal direction, which serves to enlarge the lateral coherence seen at the sample position and brings the horizontal and vertical coherence lengths closer to each other. For full exploitation of the coherent flux using the natural vertical source size, a moderate amount of vertical focusing can be added.

In its simplest configuration, the optical design can be reduced to a sequence of slits, as illustrated in Figure 11.6.1. Details of the design are presented in subsequent sections. For the time being, note that monochromator crystals and mirrors, the edges of which are used to separate the branches, are omitted from the figure as they do not affect the coherence properties, at least when they act as perfect reflectors. Some of the slits are made to operate in white beam at grazing angle, so these will be designed with a second anti-scatter edge. Some slit pairs have separated blades, comprising slit/mirror or slit/slit pairs, with an offset between the blades, but the effect of this is ignored, as this offset is small compared with the separation of the elements.

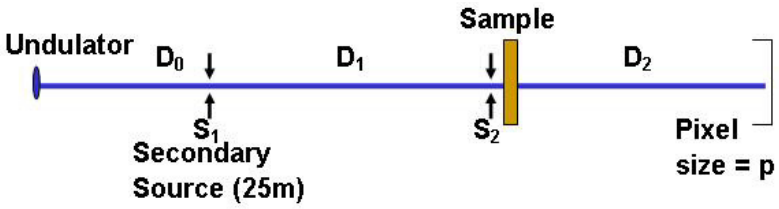

Figure 11.6.1 Schematic layout of a slit-based optical configuration of a CXS beamline.

Four equations relate the slit separations, S_1 S_2, and the distances D_0, D_1, and D_2 between the four optical planes: source (half-width σ_x), secondary slit (separation S_1), coherence-defining slit (S_2 with sample) and the detector (pixel size p).

The pixel size of the detector, p, must be less than half the fringe spacing arising from the sample slit: $\lambda D_2/ S_2 > 2p$. This ensures the speckles are sufficiently over sampled.

A similar equation defines the minimum detector distance needed to put the detector in the far field of diffraction from the sample: the fringe spacing must be wider than the geometric shadow of the sample: $\lambda D_2/ S_2 > S_2$ or $S_2 < \sqrt{(\lambda D_2)}$.

The coherence length at the sample is defined by diffraction from the secondary source. So for the sample to be illuminated coherently, $\lambda D_1/ S_1 > S_2$.

Finally, ray-tracing is used to trace back the minimum size of the synchrotron source itself needed to fill the secondary source with light: $2\sigma_x > S_1 + (S_1 + S_2)(D_0/D_1)$.

All four inequalities are nominal in the sense that the related quantities are distributions that do not cut off abruptly. For example, coherence degrades gradually with the slit separation, not abruptly. Also the throughput of the experiment (flux in the detector) diminishes when the inequalities are optimized, and is highest when they are just satisfied. An optimal design should therefore consider these to be defining equalities. For example, the coherent flux on the sample is best when the coherence length equals the sample size.

Based on these considerations, the following tables summarize the chosen and derived values of these parameters for both the small-angle XPCS branch line (Table 11.6.1) and the coherent diffraction and large-angle XPCS branch line (Table 11.6.2):

Table 11.6.1 Parameters for the Small-Angle XPCS Branch of the Coherent X-Ray-Scattering Beamline.

Item	Value	Comments
Maximum sample-to-detector distance	10 m	For desired maximum wave-vector transfer of 2 nm^{-1}, provides workable window size of ≈ 300 mm
S_2 horizontal slit size	≤ 30 μm	Otherwise in near field diffraction limit
Maximum S_1 secondary source size	80 μm	Using sample to secondary source size = D_1 = (52-27) m = 25 m and S_2 = 30 μm. (The corresponding mirror size is only ≈ 30 mm)
Desired pixel resolution	≤ 70 μm	Matching solid angle subtended by the source at the sample position to the solid angle of the pixels subtended at the sample position and moderately under-resolving speckles as described in the text.

Table 11.6.2 Parameters for the CXD Branch of the Coherent X-Ray-Scattering Beamline.

Item	Value	Comments
Maximum sample-to-detector distance	3 m	Larger separations are not practical because of the need to position area detectors over a range of large scattering angles
S_2 horizontal slit size	$\leq$ 100 μm	
Maximum S_1 secondary source size	70 μm	Using sample to secondary source size = D_1 = (97-29) m = 68 m and S_2 = 30 μm. (The corresponding mirror size is only $\approx$ 30 mm.)
Desired pixel resolution	$\leq$ 20 μm	Coherent fringe resolution on the detector

The division of the beam into two parallel operating stations will not compromise the performance of either one. The coherent part of the beam, even at NSLS-II, is still only a fraction (about 10%) of the total flux of the undulator at 12 keV. Two coherent beams can then be taken from the central cone of the undulator, side-by-side, without any loss of coherent flux. Because a hard edge is required to split the beam, a one-sided secondary source results anyway, so the method works best when a well-defined symmetric double-sided secondary source is utilized. One compromise of such a multiplexed beamline design is that the shared undulator source provides the same spectrum to both stations, and the freedom of either of these to tune the spectrum by varying the gap and/or taper has to be restricted. However, this is compatible with the scientific applications of both branches that are not often expected to require specific tuning of the energy or energy-width. Given that the choice of energy has historically been limited by detector efficiency, which is expected to improve considerably, a good "target" energy for both branches would be 12 keV; the lower energy limit is 7 keV.

The second innovation over previous designs is to extend the length of the beamline beyond the standard value of 60 m. This leads to a general improvement in performance for a number of experimental situations. With longer coherence lengths, radiation sensitive samples will receive less dose and will survive longer in XPCS measurements. This should allow the power of XPCS to be applied to biological samples that are more sensitive to radiation damage. Specifically, XPCS might now be used to study concentrated protein solutions such as the α and β crystallins of the eye. Furthermore, coherent diffraction (CXD) experiments using demagnification to concentrate a coherent beam on a nanoscale sample will attain either larger demagnification ratios (more flux) or create more space for the sample environment. The increased flux density at the sample position will facilitate atomic-resolution CXD. The atomic resolution will allow CXD to examine individual clusters in catalysts, in situ with reactions taking place. The proposed hutch layout for the sector is shown in Figure 11.6.2. Within this overall design concept, there are several additional design requirements:

- Mirrors and monochromators will be water cooled to avoid the vibration and maintenance issues associated with liquid nitrogen.
- Mirror and monochromator surfaces should all be polished to state-of-the-art finishes and figure errors to minimize degradation of the beam brilliance.
- Floor vibrations and ambient temperature fluctuations should be minimized.

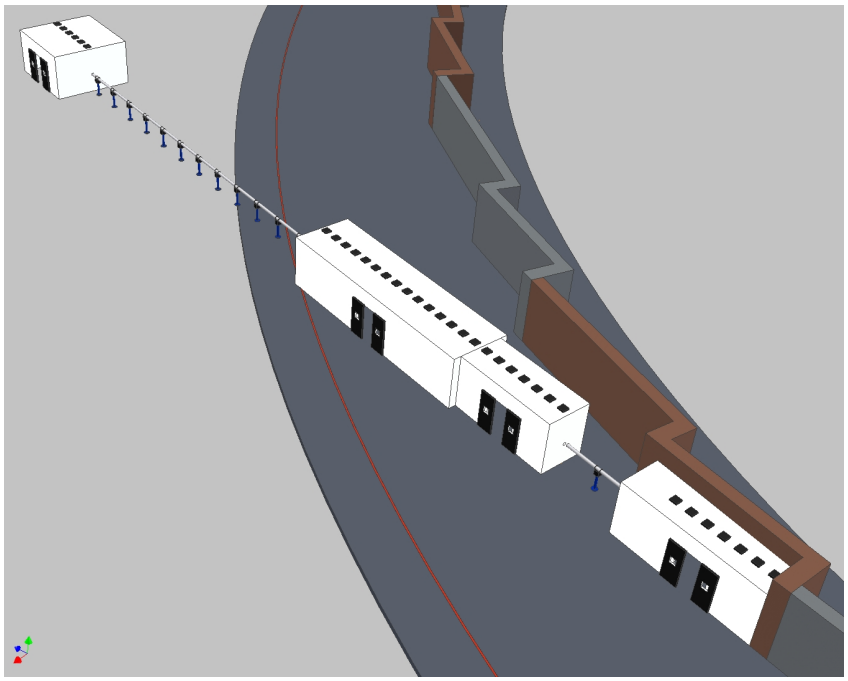

Figure 11.6.2 Proposed floor layout for the coherent scattering beamline at NSLS-II. Proceeding from the storage ring, the first hutches are optics hutches, the next hutch is the small-angle XPCS station, and the last hutch is the coherent x-ray diffraction and large wave-vector transfer XPCS station.

11.6.3 Source

A high-beta 8 m straight is requested with a standard U19 undulator placed at its center. A 3 m device is anticipated initially. We note that we do not require this device to operate at closed gap in the high-beta straight section; the minimum requested K value is K = 1.8 and corresponds to the cross-over from operation at lower x-ray energies on the third undulator harmonic to higher x-ray energies on the fifth harmonic. At the time of writing, the storage ring design parameters in the horizontal direction are: β_x=18.1 m, giving σ_x=100 μm and σ_x' = 5.5 μrad. This assumes the damping wigglers are operating to give the lowest overall emittance of ε_x = 0.55 nm. In the vertical direction, the source parameters are σ_y = 3 μm and σ_y' = 1 μrad.

The additional divergence of the radiation cone from this undulator is expected to be $1/\sqrt{N\gamma}$ = 13 μrad, which dominates the horizontal divergence. The expected typical operations would be at 12 keV, which falls on the fifth harmonic of the U19 tuning curve at K = 1.3. In the optical design presented here, higher harmonics would be cut off by the mirror and lower ones by use of a thin absorber. Such filtering reduces the incident power on the monochromator facilitating water cooling and enables wider bandpass pink beam operations for a small number of potential applications.

The diffraction-limited source sizes and divergences of the photon beam are $\sigma_r = \sqrt{2\lambda L}/4\pi$ = 2 μm and $\sigma_r' = \sqrt{\lambda/2L}$ = 4 μrad. We note, however, that in practice such values are not achieved in the vertical direction at higher harmonics because of the finite energy spread of the electron beam. We take, therefore, at 0.1 nm, the working values for the 1-sigma photon beam sizes ($\Sigma_{x,y}$) and divergences ($\Sigma_{x',y'}$) as Σ_x = 100 μm and Σ_y = 6 μm and $\Sigma_{x'}$ = 15 μrad and $\Sigma_{y'}$ = 12 μrad.

The U19 device is best-suited for these applications among the available devices proposed for NSLS-II. We note, however, that the superconducting mini-gap undulator (SCU) with 14 mm period (U14) is the preferred insertion device for the sector, should it become available as a result of ongoing research and development. The reason for this is quite simple: U14 has the highest proposed brightness in the specified energy range of the beamline (7–12 keV) of the insertion devices proposed. We note, however, that it might not be possible for such a device to reside in a high-beta straight section.

The shared undulator source provides the same spectrum to both branches of the beamline. To give greater flexibility, an upgrade path would be to add a second undulator in-line (tandem) with the first one. This is preferable to canting them, in that when all users agree on the same energy both undulators can be tuned to that energy, doubling the total flux. At other times, users can select their own energy by changing the gap of one of the undulators. This is the approach taken, for example, at the ESRF ID (Troika) beamline.

Finally, we discuss the reasons for choosing the operating x-ray energy of the beamline in slightly more detail. In addition to the explicit λ^2, several factors in the expression for the XPCS Signal to Noise Ratio, SNR, depend on the x-ray energy/wavelength. First, the brightness itself depends on the x-ray energy, as does the detector efficiency: For a 300-micron-thick Si sensor bump-bonded onto an XPCS detector chip, the efficiency would be near unity for x-ray energies up to about 12 keV (0.1 nm); for a similar GaAs or Ge sensor, the efficiency would be near unity beyond 20 keV. The effective sample thickness (W) also depends on energy, in that W should be picked to be more-or-less equal to the sample's x-ray absorption length, which, away from x-ray adsorption edges, varies as λ^{-3}. This factor is not relevant for surface XPCS measurements. Another important advantage of shorter wavelengths (i.e., higher energies), directly related to the energy-dependence of the sample adsorption length, is that sample damage is lower at higher energies. Since the optimum energy may be different for different samples and conditions, the optics of the XPCS beamline will allow for a tunable energy range from ~7 keV to ~20 keV for maximum flexibility.

11.6.4 Optics

Relatively few optics are employed in the design. The main reason for this is that imperfect optics can reduce the coherence in a way that is hard to control. A minimum number of windows are employed and the materials of these are chosen carefully, particularly for windows near the sample. Mirrors and monochromator crystals are made from dislocation-free silicon, germanium, or silicon carbide, polished to the best figure, to minimize the disturbance of the wavefronts passing their surfaces. The mirrors are operated at small angle (3 mrad) so that coatings, which are often not as flat as the substrate, will be unnecessary. Because of the overall length of the beamline, there is enough separation of the branches for sample environmental hardware.

The optical layout of mirrors and monochromators in the two branches is shown in Figure 11.6.3. The layout takes one of the experimental hutches outside the designated ring building walkway, but not outside the perimeter of the lab-office modules. Thus, the building construction associated with the project is kept to a minimum.

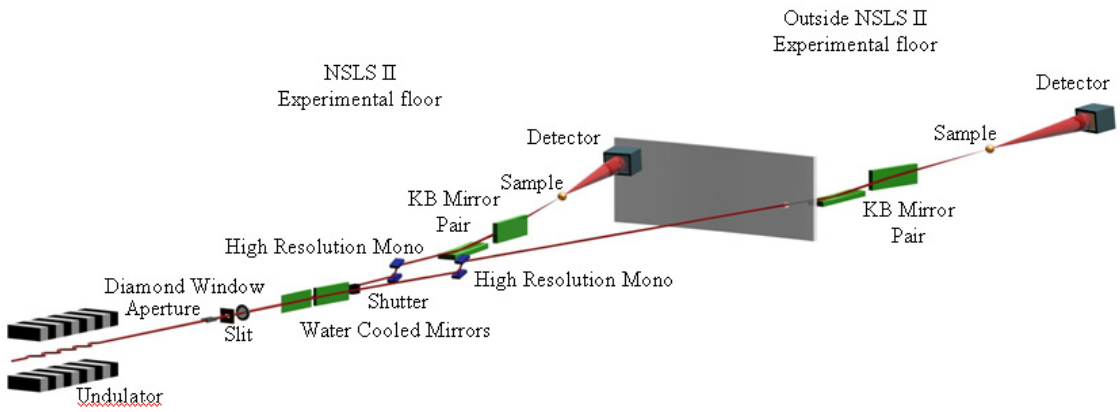

Figure 11.6.3 Conceptual layout of coherent scattering beamline. The two water-cooled upstream mirrors split the beam and feed two end stations simultaneously. The second end station, for XPCS, lies outside the experimental hall, the wall of which is denoted by the gray panel.

Table 11.6.3 lists, in upstream-to-downstream order, the major components comprising the CXS beamline at NSLS-II. Note that locations are approximate.

From the conceptual design outlined in Section 11.6.1.2 and the descriptions in Table 11.6.3, we can make more definitive statements about the required sizes and hence anticipated power loads for several key optical components. The secondary sources (mirrors) define the required horizontal aperture of the beamline. The mirrors for both branch lines each have a projected size of ≈100 μm. (At an incidence angle of 3 mrad, the corresponding mirror lengths are only 3.3 cm.). Summing these two projected sizes and allowing some horizontal offset between the 2 mirrors, we can limit the maximum horizontal aperture of the incoming x-ray beam to ≤500 μm. In the vertical, we must accept a larger portion of the beam because of the increased vertical coherence length. For the fixed vertical aperture, we accept several vertical coherence lengths by choosing a vertical aperture of ≈500 μm. To limit power on the downstream components and also mitigate concerns about placing U19 in a high-beta straight section, we anticipate running for 7 keV ≤E <9 keV on the third harmonic of U19 and for 9 keV ≤E <12 keV on the fifth harmonic. With this restriction and the restriction on the incident beam aperture (500 μm × 500 μm), we can estimate the worst-case power loading and typical power loading on the optical components.

With a minimum energy for the beamline of 7 keV, then the worst case condition is operation on the fifth harmonic at E_5 = 8.5 keV, corresponding to E_1 = 1.7 keV and a U19 K value of ≈ 1.8. The maximum incident angular power density is ≈70 kW/mrad^2. The 500×500 μm aperture at ≈25 m subtends a solid angle of ≈ 0.02 × 0.02 mrad^2, so the power transmitted through this aperture is ≈ 30 W, or 120 W/mm^2.

The next component in the beamline is a brilliance preserving high-pass filter. This might, for example, be composed of a small ≈100 μm-thick diamond crystal, discussed in Section 11.3.4. The power transmitted though such a filter and incident upon the horizontally deflecting mirrors is 20 W. Assuming an incidence angle of 3 mrad, then the incident power density on the mirrors is ≈ 20 W*0.003/(0.5×0.5 mm) = 0.24 W/mm^2, which is well within acceptable limits for mirror side cooling via water.

The final key optical component to consider in the worst case heat load scenario is the monochromator. Each mirror has a projected horizontal size in the beam of ≈100 μm, so the maximum power reflected by the mirror and incident upon the monochromator (ignoring the power at higher x-ray energies that is removed by mirror) is 4 W or, at normal incidence, 80 W/mm^2. The monochromators are at approximately a factor of 50% greater distance from the source than the mirrors are, so the normal power density is reduced to ≈ 40 W/mm^2. At 8.5 keV and for a Si(111) or Ge(111) monochromator, the incidence angle is ≈14º, so the power density is 10 W/mm^2. Further analysis and comparison with power loads on existing operational beamlines are needed to determine whether this power load can effectively be managed with only side cooling by water. The expectation is that it can, and that liquid nitrogen cooling and the maintenance and vibration considerations associated with such optics are not necessary.

For reference purposes, we repeat the above calculations but for the envisioned typical mode of operation, namely, λ = 0.1 nm, which corresponds to E_1 = 2.4 keV and K = 1.3. The power through the fixed aperture is 20 W, the power transmitted through the filter is 11 W, the power density on the mirrors is 0.13 W/mm^2, and the power incident upon the monochromator is 2 W or 3 W/mm^2. These very modest power levels will help ensure the stability of the coherent x-ray scattering beamlines, which is of critical importance.

Table 11.6.3 Principal Components of the Coherent X-Ray-Scattering Beamline at NSLS-II.

Item	Location	Description
U19 (or U14)	0 m	Radiation source
Front end		Beam and bremsstrahlung collimation
Shield wall	23.7 m	
First Optics Enclosure (FOE)	23.7 m (9 × 2.5 m^2)	White-beam radiation shielding enclosure
Differential pump	24 m	Windowless connection to the storage ring for brilliance preservation
Power limiting aperture	25 m	Aperture of (20 × 20) μrad^2
Filter	25.5 m	Brilliance-preserving high-pass filter. Filter material could be single-crystal diamond or a thin, highly polished silicon foil.
Variable aperture (white-beam slits)	26 m	Inboard side of this slit can be used to reduce the illuminated length of the outboard deflecting mirror
Outboard deflecting mirror	27 m	Acts as a low-pass filter and secondary source for the small angle XPCS end station. Deflection angle ≥ 6 mrad. For effective harmonic rejection at the nominal operating condition of λ = 0.1 nm, the mirror should be made of SiC provided it can be finished to a quality corresponding to the best Si mirrors.
Inboard beam-defining slit (white beam)	28 m	White-beam inboard ½ -slit that can be used to reduce the illuminated length of the inboard-deflecting mirror.
Inboard deflecting mirror	29 m	Acts as a low-pass filter and as a secondary source for the coherent diffraction and large angle XPCS end station. Deflection angle ≥ 6 mrad. Mirror materials and coatings will be identical to those for the outboard deflecting mirror.
White-beam and mis-steered pink beam stop	32 m	Critical components needed to prevent inadvertent personnel radiation exposure and equipment damage
PinKBeam shutter	33 m	Single shutter to stop the pink beam from exiting the first optics enclosure
Shielded transport	33–44 m	PinKBeam transport to the second optics enclosure
Second optics enclosure	44 m (4 × 3 m^2)	Contains 2× monochromators and 2× shutters for the end stations
Monochromators (×2)	45 m and 46 m	Small offset, vertical bounce Ge (small angle XPCS) and Si (coherent diffraction and large angle XPCS) monochromators
Shutters (×2)	46.5 m	Independent, pinKBeam capable shutters for the two end stations
Small angle XPCS end station	47 m (15 × 4 m^2)	See Section 11.6.6.1. Nominal sample position is 52 m from the source
Shielded transport	47–97 m	Shielded transport passing through the small-angle XPCS end station and the Laboratory Office Building
Coherent diffraction and small-angle XPCS end station	97 m (6 × 6 m^2)	Distance from the source will be maximized consistent with the hutch being entirely located in the adjoining lab and office complex.

11.6.5 End Stations

11.6.5.1 End Stations for XPCS

The small-angle XPCS station contains three main support platforms: 1) a motorized table (≈ 2 m wide × 4 m long) to support focusing optics and collimating slits, 2) a small motorized optic table (≈ 1 m wide × 4 m long) to support a variety of sample environments, and 3) a long table/double-rail-assembly (2 m wide × 10 m long) for supporting the exit flight path and detectors.

The first optical component in the end station, which is located 47 m from the source, will be a preliminary aperture that restricts the spatial extent of the beam entering the focusing optics. In spite of improving the horizontal coherence by use of the secondary source, there will still be a considerable asymmetry between the horizontal and vertical coherence lengths. In fact, the vertical coherence length at 50 m will be over 200 μm, while the horizontal coherence length will be ≈ 30 μm. For reasons of detector efficiency and to ensure that detection occurs in the far-field (Fraunhofer) diffraction regime, it is important that the effective vertical coherence length be reduced. This will be done with a 1D coherence-preserving vertical focusing optic (a promising option for this is the 1D kinoform lens), that creates a virtual source

upstream of the sample position. A second pair of slits will be located at the focal spot for aperturing of the focal plane. A third and fourth pair of slits will be located near the sample for selecting a coherent fraction of the x-ray beam and for eliminating parasitic scattering produced by the collimating slit. As well as the 1D focusing option described above, we will also require the option to introduce 2D focusing via such optics as Fresnel zone plates or KB mirrors.

A more detailed examination of focusing for XPCS is as follows. First, vertical focusing decreases the vertical dimensions of the illuminated region of the sample, so that the detector lies in the far field of the sample's speckle pattern. The XPCS SNR calculation given above is valid only in this limit. In the near field, the speckle contrast (A) is measured to be less than predicted by the far-field expression. Second, the SNR is maximized when the angular acceptance of the detector pixels equals the angular size of the source, so that with a detector composed of square pixels, the SNR is maximized with equal coherence lengths in the x and y directions.

Because of the very intense x-ray beams at the NSLS-II XPCS beamline, for many possible experiments, especially soft-matter experiments, it will be essential to implement strategies to avoid x-ray sample damage right from the start. We have already discussed that there may be some XPCS SNR advantage in using pink beam, rather than monochromatic beam. However, using pink beam increases the flux on the sample, and thus the sample damage, proportionally with the x-ray bandwidth. Therefore, pink beam should be used judiciously.

Therefore, with regard to the sample area of the small-angle XPCS end station, an important strategy to ameliorate the effects of sample damage follows from the observation that to carry out an XPCS measurement, in fact, it is necessary to illuminate a particular region of the sample for only a few times the sample's relaxation time. After that period the sample's configuration has become completely rearranged. This suggests a flow/translation scheme that moves a new portion of the sample into the x-ray beam on a time scale that is long compared to the sample's intrinsic relaxation time, but short compared to the time for sample damage to occur. For liquid samples, a micro-fluidics-based flow cell will transport fluid in and out of the beam. For solid samples, a rapid translation scheme will be implemented.

The final component in the end station is the detector support assembly, which must be capable of being positioned at any point along the long axis of the flight path support assembly, and it must have motorized stages that allow rapid positioning of the XPCS detector(s) in x and y. The latter translations are necessary because most XPCS-capable area detectors subtend only a relatively small solid angle. So, to perform measurements throughout the region of reciprocal space near it origin, detector translation in x and y is typically required.

11.6.5.2 End Station for CXD

The two coherence end stations will be differentiated by their complementary q-ranges. XPCS experiments can be carried out in both end stations, specifically in a small-angle geometry in the first hutch and at wider angles in the second hutch, using a diffractometer. The detector distance will be considerably longer for the small-angle setup, in which the detector is positioned on vertical and horizontal translation stages. In the CXD hutch, the detector will move on a compound diffractometer detector arm, which for reasons of mechanical strength and available space inside the hutch will be limited to 3 m.

The CXD experiment will consist of a focusing optics table, a diffractometer, and a long (3 m) detector arm. The hutch needs to be large enough for a detector arm of 3 m length to swing on two axes, reaching up to 120º in the vertical and 70º in the horizontal, with polarization losses limiting the horizontal range. (Horizontal detector motion is required for studying in-plane ordering of liquid-like samples and for possible very heavy detectors that can not be attached directly to the detector arm.) The optics table should be incorporated into the diffractometer design so that micron-level stability of the relative positions can be assured.

The first optical component in the end station, which will be located ~100 m (number to be finalized when more building details are known) from the source, is a coherence-defining aperture that restricts the spatial extent of the beam entering the focusing optics. In the vertical, this aperture is determined by the source parameters to be 1.7 mm, while in the horizontal, it is determined by the secondary source, which is adjustable. Typically, S_1~80 μm at D_0=25 m, giving an entrance aperture width of 100 μm. In spite of improving the horizontal coherence by use of the secondary source, there is still a considerable asymmetry between these numbers. It is possible that the full vertical coherence will not be achieved because of the effects of windows or imperfections in the upstream optics. As discussed above for the XPCS end station, it will be possible to introduce upstream collimating optics, for example, a 1D kinoform lens in the monochromator hutch, to increase the flux and reduce the vertical coherence to the range of a few hundred microns.

Immediately in front of the sample position, optics are used to demagnify the source, to concentrate it onto a nanometer-sized sample at the center of the diffractometer. Assuming a 100 m hutch center position, the focus will be located 75 m from the coherence-defining horizontal source and 100 m from the vertical source. The substantial divergence will introduce a degree of (coherent) spherical wave component, or wavefront curvature, in the beam illuminating the sample. The type of optics needed will be defined in the detailed design, but possible choices include KB mirrors, zone plates, or Compound Refractive Lenses, CRLs.

The diffractometer will be a five- or six-circle configuration with a compound detector arm to allow in-plane and out-of-plane scattering geometries. The sample goniometer might employ intersecting phi/chi arcs to give the most clearance around the sample position with limited scanning range. Alternatively, the open kappa geometry could be used. Much emphasis is placed on the amount of clearance in the immediate vicinity of the sample and the center of the goniometer axes,because many probes will be needed to operate in parallel at that point. Space for sample environments would also be shared with these intersecting probes: liquid, gas or vacuum, high pressure, and high or low temperature, for example. A good solution for the sample goniometer might be a “hexapod” that combines very high x-y-z positioning accuracy with phi/chi tilts and a high load-carrying capability (10 kg). Use of a long beamline is also part of the strategy for creating space around the sample, given a fixed choice of demagnification or focal spot size.

It is not expected that a nm-sized sample can be oriented at the center of this diffractometer within a sub-micron-sized beam by the sample rotation axes alone; these would be expected to have a sphere of confusion of at least 20 μm. To take data at multiple orientations of a sample, it will be necessary to guide its x-y-z position as the angles are turned. This will require high-resolution optical microscope objectives trained on the sample from at least two directions. Sample selection and registration by optical microscopy is an essential part of the experiment. Additional x-ray-based registration involving fluorescent markers placed on the sample will be employed as well; for this, a fluorescence detector will also be needed to look at the goniometer axis center.

The detector arm needs to be a flexible configuration that can be adjusted easily. The detector itself (see below), which might be 10 to 20 kg, needs to have a readily adjustable distance from the sample. A flight tube is needed to cut out parasitic scattering, and slits can be used to fine-tune the entrance and exit apertures. It is useful to have the additional ability to rotate the detector around the axis of the diffracted beam direction. This is used to align extended diffraction features with the pixel directions for ease of data analysis.

11.6.6 Detectors

Next to the brilliance of the source, the single most important enabling component of the XPCS branchline is the detector. The three essential features of an XPCS detector are 1) a large number of pixels, 2) high speed, and 3) high x-ray detector efficiency. In addition, it is important for 4) the pixel size to be small enough to partially resolve the speckle in the scattered scattering pattern. Each of these points is discussed in more detail below.

The above considerations reveal the importance of employing a detector with many pixels: The SNR with 10^6 pixels, corresponding to what might reasonably be available on a single detector chip, is 10^3 times improved compared to a single-channel detector. Using 25 or 100 separate chips yields a further SNR improvement by a factor of 5 or 10. It is these very large improvements in SNR from detection in multiple channels that will permit the characterization of short sample relaxation times, even when the number of scattered x-rays per pixel per accumulation time (relaxation time) is far less than 1. Under these circumstances, it will be especially important to discriminate against dark counts.

The detector speed determines the fastest processes that can be studied. Specifically, to be able to study processes occurring on 0.1 microsecond time scales, it is necessary to separately recognize x-rays that are incident in the same pixel separated by 0.1 microseconds. Here it is important to note that the essential output of an XPCS experiment is not the time-dependence of the scattered intensity itself, rather it is $g_2(Q,t)$. Therefore, we are lead to a novel XPCS detector that incorporates an in-pixel auto-correlator. This would allow massively parallel processing of the data and would enormously simplify XPCS data acquisition and data reduction; instead of the formidable task of having to transfer the intensity in each pixel versus time, with a time resolution of 0.1 microsecond, out of the detector to storage for subsequent reduction to $g_2(Q,t)$'s in software—a computational challenge itself, the XPCS detector will determine g_2 pixel-by-pixel in real-time in the detector hardware.

For the case of a coherence length at the sample (after vertical focusing) of 10 microns in both x and y, the maximum XPCS SNR can be achieved for slits set to illuminate about 20 microns. The corresponding speckle size for 12 keV x-ray at a distance $D_2 = 5$ m from the sample is 25 μm. As noted above, the best XPCS SNR is achieved when the speckles underfill the pixels, indicating that a pixel size of 50 microns or somewhat larger would be suitable in the case of a 5 m sample-to-detector distance. A similar value follows from maximizing the expression for the XPCS SNR with respect to the pixel dimension (s) for $D_2 = 5$ m. [Note that $\Delta\Omega = (p/D_2)^2$.] Pixels somewhat larger than 50 μm do not significantly degrade the XPCS SNR. Nevertheless, detectors with the electronics necessary for calculating a correlation function incorporated in each pixel are currently uncertain and may require larger pixels than 50 μm; therefore, hutch dimensions that permit a maximum 10 m sample-to-detector distance have been chosen.

11.6.7 Computing and Controls

Computing requirements for the coherent x-ray scattering beamline are somewhat contingent on developments with detectors. In general, however, we note that both branch lines intend to make extensive use of 2D detectors that produce large volumes of data.

For CXD, powerful computers are needed for efficiently performing phase inversions, but data volumes are not expected to be extraordinarily large. For XPCS, as mentioned in the section above, extensive effort needs to be devoted to performing raw data reduction as close to the sensor element as possible. In fact, significant advances in the experimental program will be achieved by performing all the raw data reduction in the detector itself. If such advances are made, then the computing and data storage requirements for the XPCS program are relatively modest. If such advances are not made, however, then the computing and data storage requirements for XPCS are enormous. In this latter scenario, it is easy to imagine sustained raw data acquisition rates for the XPCS experiments at NSLS-II exceeding gigabytes per second.

11.6.8 Laboratory and Office Space

Typical laboratory and office space is required for the coherent x-ray-scattering beamline. In particular, a simple chemical or wet lab will be required for final preparation of samples before and during beamtime.

11.6.9 Conventional Facilities Requirements

Typical laboratory conventional facilities are required. Specifically:

- Compressed air.
- Chilled air for proportional air conditioned temperature control of the shielded enclosures.
- Deionized water for direct and secondary cooling of beamline optics and heat exchangers. We anticipate cooling mirror and monochromators with low-vibration, gravity-fed water cooling systems that will exchange heat with the direct deionized water supply.
- "House" water for general multi-purpose use.

At this time, we do not anticipate needing liquid nitrogen for cooling optical components but an outstanding issue is whether the monochromators can be cooled efficiently enough with water so that thermal-induced slope errors are within an acceptable range.

11.6.10 Outstanding Issues

One outstanding issue for this beamline concerns the power loads. We estimate the worst case power load on the monochromator first crystals to be 4 W total power and 10 W/mm^2, and the typical power load to be 2 W total and 3 W/mm^2. Analysis and comparison to existing high-performance beamlines needs to be made to determine whether this heat load can effectively be managed with side-cooling via water.

11.7 A High-Resolution Soft X-Ray Beamline for Resonant Scattering and RIXS

The advantages of hard x-rays for scattering include the large penetration depth and high spatial resolution. In the soft x-ray range, resonant processes at relevant core levels can enhance the scattering amplitudes by orders of magnitude. Such resonant enhancements lie at the core of recent increased interest in the exploitation of soft x-rays for the investigation of wide classes of materials including technologically relevant compounds and alloys, and advanced nano-scale materials. Further, the wavelength of soft rays (~0.5 nm to a few nm) is well matched to many interesting and useful length scales, both those that occur intrinsically in many materials and those that have been engineered.

In particular, scattering studies in the soft x-ray range are uniquely suited to examining some of the most important issues surrounding correlated electron systems, spintronic materials, engineered ferromagnetic alloys, nano-patterned structures, advanced fuel cell electrodes, candidate hydrogen storage materials, and many other scientifically or technologically relevant materials. A large portion of the periodic table can be investigated via the use of soft x-rays, including the 3*d* transition metal *L* edges, rare-earth $M_{4,5}$ edges, and the *K* edges of C, N, and O. There are strong resonant enhancements in the vicinity of these dipole-allowed absorption edges. In addition, polarization-dependent studies, which are more practical with advanced undulators and novel end station designs, can reveal underlying order in the charge, spin, and orbital degrees of freedom in the system.

In this section we discuss the conceptual design of a soft x-ray beamline optimized for scattering studies and high resolution spectroscopy. The proposed design considers a single beamline serving two end stations; one is optimized for x-ray resonant magnetic scattering (XRMS) and the other is designed for resonant inelastic x-ray scattering (RIXS). A horizontal switching mirror will be used to divert the beam from one end station to the other. The source for the beamline will be two 2 m elliptically polarized undulators (EPU) in one of the NSLS-II 5 m straight sections. In addition to the standard set of experiments enabled by EPUs, the proposed design will call for independent control of the polarization in the EPUs to provide two separate soft x-ray photon beams. Separation of the two beams is accomplished via inclusion of a small canting angle in

the electron orbit between the EPUs and the novel design of the beamline optics permits separate collection and a coincident focus of the two beams. A mechanical optical chopper would then permit measurements of small, polarization-dependent signals via lock-in amplification.

X-ray Resonant Magnetic Scattering and Resonant Inelastic X-ray Scattering are two scattering techniques whose use in the soft x-ray range has increased considerably in recent years. XRMS exploits magnetic sensitivity in diffraction patterns to extract element-specific information on magnetic ordering processes on length scales from microns down to a few nm. RIXS, in contrast, examines inelastic processes. The energy lost in the process, which is measured in a RIXS experiment, can reflect important parameters such as the local partial density of states of an atomic species in a complex compound, low energy excitations (such as *d–d* interactions), and charge transfer from surrounding ligands. XRMS and RIXS are both photon-in, photon-out techniques, and have a number of advantages over electron-based spectroscopies and scattering processes. For example, photons are not affected by electric and magnetic fields, and multiple scattering events are negligible in the soft x-ray range.

The exceptional properties of NSLS-II will enable the implementation of soft x-ray beamlines with unsurpassed brightness, small photon spot size, energy resolution, and polarization control. These characteristics will be crucial in designing and ultimately using the next generation of XRMS and RIXS instrumentation. RIXS is inherently a very low-count-rate technique, and improvements in brightness and spot size translate directly to improved detection efficiency. In XRMS, the most valuable information is attained often only at high-momentum transfer or in off-specular scans. In both instances, the count rate at current instruments is often at the noise floor of the detectors.

Although XRMS and RIXS have some similarities, they are properly considered as separate and complementary probes of advanced materials. Therefore, the motivation for pursuing these techniques will be presented in separate sections.

11.7.1 Source

We propose that the beamline be equipped with two soft x-ray Elliptically Polarizing Undulators in a 5 m straight section, each approximately 2 m long, which could be operated either in phase as a single 4 m EPU for increased brightness or as two independent EPUs, where the polarization in each EPU would be set independently. The EPUs should be of an APPLE-II type device or an equivalent design that can provide linearly polarized photons, with the polarization axis oriented horizontally, vertically, or at an arbitrary angle in-between. The EPUs should also be able to provide right circular or left circular polarization across an energy range that is matched by the optics of the beamline. Note, the 5 m straight is desired because of the smaller source size.

Present plans for an EPU device for NSLS-II call for a period length of 45 mm and a magnetic gap of 10 mm (see Chapter 8). This would allow it to function as an out-of-vacuum device. However, an EPU42 device, with a period length of 42 mm and a magnetic gap of 8 mm would provide coverage over a slightly wider energy range than the EPU45 device. The EPU42 also has an advantage of a brightness about ~13% higher (averaged over the energy range of EPU45) than the EPU45. However, the 8 mm magnetic gap of the EPU42 may require that it be an in-vacuum undulator, which requires R+D. Absent such a device, the EPU45 would certainly be a good alternate.

As previously mentioned, the 2 m EPUs could be operated in-phase as a single 4 m insertion device. By canting the electron beam slightly through the EPUs (the canting angle is expected to be less than 0.25 mrad) the EPUs could be operated as independent devices and could be used to provide two beams to the end stations, each with a different polarization (e.g., linear and horizontal, or RCP and LCP). These two beams would be focused on the same spot on the sample. An in-vacuum chopper would be included in the beamline, allowing for rapid switching between the two polarizations, possibly at frequencies as high as a few kHz. This approach also eliminates the need to provide rapid polarization switching via movement of the magnetic

arrays in the EPUs, and hence minimizes any perturbations on the electron beam. For this approach to work, appropriate steering magnets and beam diagnostics must be included in the straight section.

The rapid polarization switching would enable the detection of extremely weak signals via use of phase-sensitive lock-in detection. Such approaches have already been exploited for the detection of very small induced ferromagnetic moments in nominally paramagnetic layers adjacent to strong ferromagnets [11.7.1]. Even lower absolute moments could be detected with the increased brightness and higher polarization switching frequencies of NSLS-II. This capability will be extremely useful in detecting small spin-currents in nonmagnetic layers [11.7.2, 11.7.3]. The rapid polarization switching could also be invaluable in detecting weak scattering peaks in orbital-ordered manganites, or in examining other correlated electron systems.

11.7.2 Beamline Design and Optics

11.7.2.1 Introduction and Proposed Design

State-of-the-art optical elements are required to match the very high resolving power achievable with the proposed beamlines at the NSLS-II ring. The XRMS/RIXS beamline will achieve a resolving power $>0.9\times10^5$ at 1 keV with a 5 μm exit slit width and with RMS slope errors of 0.1 μrad over ≈100 mm on the plane optical elements. A spot size with FWHM of less than 5×5 μm^2 requires RMS slope errors of approximately 0.5 μrad along the meridional direction on the sagittal cylinder and the elliptical cylinders used in the proposed design. In the beamline, almost 5×10^{10} ph/s will illuminate a spot with FWHM of less than 6×4 μm^2 (H × V) at 1 keV with a bandwidth of 11 meV. The flux at 1 keV would increase by two orders of magnitude with a different grating delivering a resolving power of 8500 to the same spot size. The requirements for the highest possible resolution and a fixed exit slit over a broad energy range can be fulfilled with the Collimated Plane Grating Monochromator proposed by Follath et al. [11.7.4]. The optical design of the CPGM includes a horizontally deflecting toroidal mirror that collimates along the vertical (dispersion direction) and focuses the beam horizontally at the exit slit. The vertically collimated beam is deflected (vertically) by a plane mirror illuminating the plane grating at an angle of incidence α. The beam dispersed by the grating, at an angle β, is focused onto the exit slit plane by a sagittally focusing cylindrical mirror. The collimation along the dispersion direction allows one to operate the monochromator at different values of c (=cosβ/cosα) by choosing the appropriate angle of incidence on the plane mirror. Large c values are used to improve resolution at the expense of flux. The CPGM design is almost free of aberrations, and the major contributions to its wavelength resolution are:

$$\Delta\lambda_{so} = \frac{2.7\,\Sigma_y \cos\alpha}{n\,k\,r_1}, \tag{11.7-1}$$

$$\Delta\lambda_{ex} = \frac{s\cos\beta}{n\,k\,r_2}, \tag{11.7-2}$$

$$\Delta\lambda_{Gr} = \frac{5.4\,\sigma_{Gr}}{n\,k}\cos\left(\frac{\alpha+\beta}{2}\right)\cos\left(\frac{\alpha-\beta}{2}\right), \tag{11.7-3}$$

and

$$\Delta\lambda_{PM} = \frac{5.4\,\sigma_{PM}\cos\alpha}{n\,k} \tag{11.7-4}$$

In the equation above, Σ_y is the RMS vertical source size, n is the diffraction order, k the grating line density, r_1 the distance from the source to the toroidal mirror, s the slit width, r_2 the distance from the refocusing mirror to the exit slit, and σ_{Gr} and σ_{PM} the RMS meridional slope errors on the grating and plane mirror, respectively. The slope errors on the collimating and refocusing mirrors also affect the resolution. However, their effect is very small due to the large "forgiveness factor," the cosine of the angle of normal incidence on the mirror.

The experimental stations to be installed at the end of the XRMS/RIXS beamline require a spot size in the micrometer range. Along the vertical direction this can be easily achieved with an elliptical cylinder demagnifying the exit slit width. Since the RMS horizontal size of the photon beam varies between 54 and 41 μm in the energy range 200 to 2500 eV, a demagnification of ≈2.35×50/5 =23.5 is required to obtain a spot with a horizontal FWHM of 5 μm. In the CPGM the horizontal demagnification of the source onto the slit is approximately 1. Therefore, the demagnification in this design needs to take place in between the slit and the sample. However, the requirement for a distance of ≈700 mm between the sample and the end of the refocusing mirror means that the entrance arm of the horizontally refocusing mirror needs to be larger than 10 m, which is impractical.

The very small horizontal divergence of the beam expected from a 4 m insertion device in the 5 m straight sections of NSLS-II, 32 μrad RMS at 200 eV, allows for a solution in which the beam diverges up to an elliptical cylindrical mirror located after the exit slit. This mirror then demagnifies the horizontal source down a few microns. One could implement this in the CPGM by replacing the toroidal mirror with a sagittal cylinder that provides the grating with a collimated beam along the dispersion direction. Unfortunately, the illumination of the refocusing cylinder after the grating by a divergent horizontal beam results in a large astigmatic coma aberration that significantly reduces the monochromator resolution.

The proposed monochromator [11.7.5] therefore uses a sagittal cylindrical mirror to collimate the beam along the vertical (dispersion) direction. The following optical element is a plane mirror that illuminates a variable line spacing plane grating. The line density of the grating is given by $k(w) = k_0 + 2b_2\,w + 3b_3\,w^2 \ldots$, where w=0 is at the grating center and is positive toward the exit slit. The linear coefficient term, b_2, can be chosen to zero the defocus term in the optical path function, i.e.,

$$f_{20} = \frac{\cos^2\beta}{dGrEx} + 2b_2\,n\,k\,\lambda, \tag{11.7-5}$$

at one wavelength, whereas b_3 can be chosen to zero the coma term in the optical path function, i.e.,

$$f_{30} = \sin\beta\frac{\cos^2\beta}{dGrEx^2} + 2b_3\,n\,k\,\lambda, \tag{11.7-6}$$

also at a single wavelength. In Eqs. 11.7-5 and 11.7-6, *dGrEx* is the distance between the grating and the exit slit. The important point in this design is the fact that the plane mirror can be used to zero f_{20} for all wavelengths by illuminating the grating at the required angle of incidence. Note that this design has one less mirror than the CPGM.

Eqs. 11.7-1–11.7-4 also give the contributions to the wavelength resolution in the proposed design, with r_1 being the distance from the source to the cylindrical mirror and by replacing r_2 with *dGrEx*.

11.7.2.2 Source Parameters

The machine parameters, the RMS electron beam sizes and divergences, and the insertion device parameters used in the calculations are listed in Tables 11.7.1 and 11.7.2. The flux emitted in the central cone by the two insertion devices with a 42 mm period when operated in phase to deliver linear polarized radiation is shown in Figure 11.7.1.

Table 11.7.1 Machine Parameters Used in the Calculations.

Energy (GeV)	3.0
Current [mA]	500
σ_x [μm]	40.2
σ_y [μm]	1.7
$\sigma_{x'}$ [μrad]	14.9
$\sigma_{y'}$ [μrad]	1.8

Table 11.7.2 ID Parameters Used in the Calculations.

	Beamline 1 and 2
ID type	2 x APPLE II
Length of each ID [mm]	2000
Period length [mm]	42

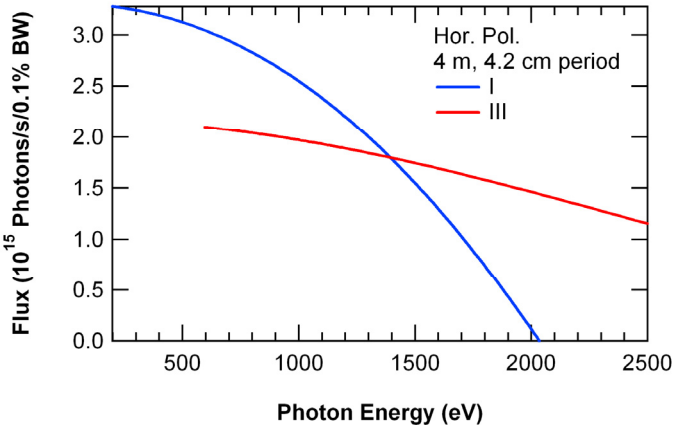

Figure 11.7.1 Flux emitted in the central cone by a 4 m undulator with a 4.2 cm period, operating in linear mode, as a function of the photon energy.

The total sizes and divergences used in the calculations were obtained as the vector sum of the electron beam parameters and the RMS values of the photon beam calculated using [11.7.6]:

$$\sigma_r = \sqrt{2\lambda L}/2\pi \text{ and } \sigma_\rho = \sqrt{\lambda/2L}\,, \tag{11.7-7}$$

where L is the undulator length and λ the radiation wavelength.

11.7.2.3 Monochromator Design

The discussion for the monochromator design will first consider the use of the two EPUs in-phase as a single insertion device. The modifications to the optical design required for canted operation will be presented at the end of the section.

A sketch of the proposed beamline is shown in Figure 11.7.2; the parameters of the optics are listed in Table 11.7.3. The first element (M1) is a sagittal cylindrical mirror located at 28 m from the source, outside the shield wall. The angle of normal incidence in this mirror (as well as that of M3 and M4) is determined as a compromise between the highest possible reflectivity in the energy range covered by the beamlines and a reasonable mirror length. Figure 11.7.3 shows a small set of the calculations performed [11.7.7] to determine the angle of incidence and the coating material on the mirrors. We selected an angle of incidence of 88.75° and a 30 nm coating of Au over the Si substrate. As shown in the figure, the selected parameters provide a good reflectivity up to 2.2 keV. We note that at this angle of incidence the *s* and *p* reflectivities are almost identical. Therefore, the beamline will not distort circular polarized radiation.

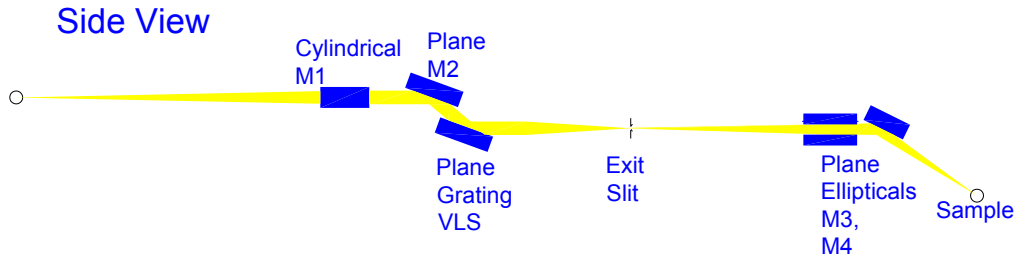

Figure 11.7.2 Sketch of the proposed soft x-ray resonant scattering and RIXS beamline.

Table 11.7.3 Attributes of the Optical Components for the XRMS / RIXS Beamline.

Element	Distance (mm)	Angle (deg)	Deflection
M1- Sagittal Cylinder	28000	88.75	Horizontal
M2- Plane	29611 to 29944	82.4-88.9	Vertical
Gr - Grating	≈30000	86.4- 89.6	Vertical
Slit	50000		
M3 - Plane Elliptical	51850	88.5	Horizontal
M4 – Plane Elliptical	52350	88.5	Vertical
Sample	53350		

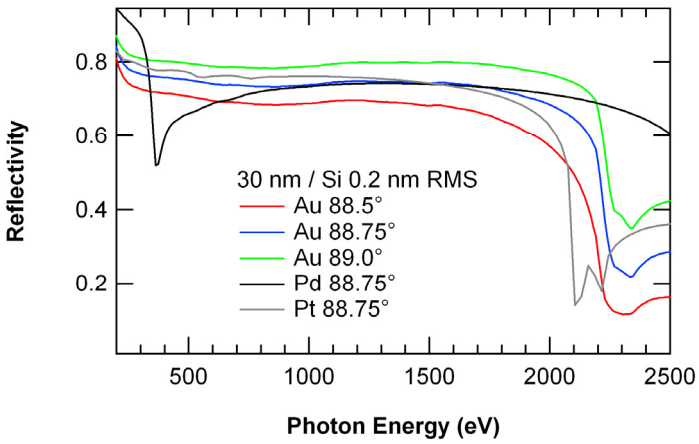

Figure 11.7.3 Reflectivities of possible coatings for s polarized light as a function of the photon energy. The substrate is Si and the coating is 30 nm thick. The RMS surface roughness is 0.2 nm.

The second optical element is the plane mirror (M2) that provides the required angle of incidence to the grating necessary to keep the selected energy in focus at the exit slit. The mechanical principle used in the PGM [11.7.8] can be used to achieve the required movements. The resolution in angle required in the current design (i.e., assuming five scanning steps at the highest resolution) is 0.03 μrad for the grating and 0.05 μrad for the plane mirror. These values are very close to the resolution of the angular encoder used in the CPGM (0.04 μrad).

Since the angle of incidence on the mirror for a given VLS grating is determined by the focusing condition and the grating equation at that energy, it is advantageous to have at least three gratings that allow exchanging resolution for flux keeping a fixed exit slit width.

11.7.2.3.1 Gratings for the XRMS/RIXS Beamline

We have specified a grating for ultra high resolution, one for high resolution and high flux, and one for moderate resolution and the highest flux). The parameters of the chosen gratings are listed in Table 11.7.4, assuming that the distance from the grating to the exit slit is 20 m. The gratings are operated in the +1 order.

Table 11.7.4 Parameters of the Gratings for Beamline 1.

	Ultra High Resolution (UHR)	High Resolution, High Flux (HR)	Medium Resolution, High Flux (HF)
k_0 [mm^{-1}]	3600	1200	300
b_2 [mm^{-2}]	5.1832×10^{-5}	6.288×10^{-5}	8.991×10^{-5}
b_3 [mm^{-3}]	2.57×10^{-9}	3.13×10^{-9}	4.49×10^{-9}
C	4.6-5.2	≈2.2	≈1.5

The UHR grating has 3600 lines per mm (l/mm) at its center and will operate with a c value increasing from 4.6 at 200 eV to 5.2 at 2.5 keV. The contributions to the resolving power for the UHR grating, calculated using Eqs. 11.7-1–11.7-4, and their vector sum are presented in Figure 11.7.4. The source size dominates the resolving power from 200 to 900 eV. At higher energies, the slope errors on the grating become the dominant term. A reduction of the grating RMS slope error to 0.05 μrad would improve the resolving power at 1 keV from 9.1×10^4 to over 11×10^4.

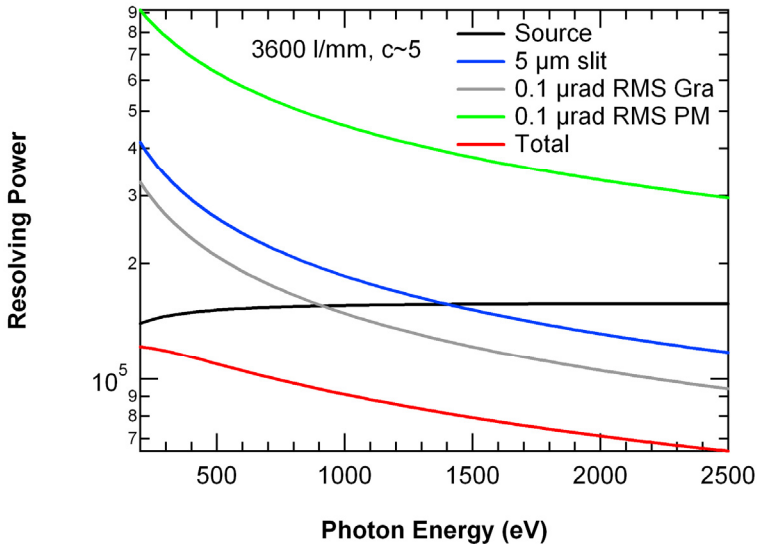

Figure 11.7.4 Contributions to the resolving power due to the source, 5 µm exit slit, 0.1 µrad RMS slope errors on the grating and M2, and their vector sum for the ultra high resolution (UHR) grating of the soft x-ray resonant scattering and RIXS beamline.

Figure 11.7.5 shows the contributions to the resolving power of the 1200 l/mm grating designed for high resolution. In this case the *c* value is approximately 2.2 and, as evident in the figure, the resolving power is dominated by the source size. A smaller slope error in this grating will not improve significantly the resolving power.

Figure 11.7.5 Contributions to the resolving power due to the source, 5 µm exit slit, 0.1 µrad RMS slope errors on the grating and M2, and their vector sum for the HR(high resolution, 1200 l/m) grating of the soft x-ray resonant scattering and RIXS beamline.

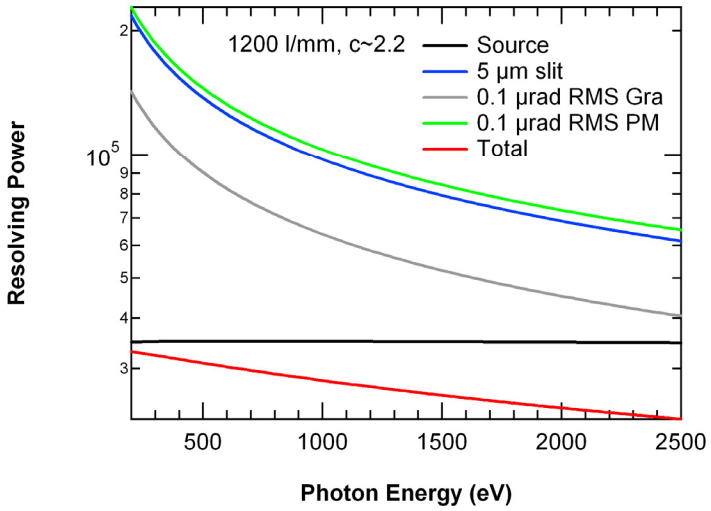

As for the HR grating, the total resolving power of the HF grating is also dominated by the source size (Figure 11.7.6). With a 5 µm exit slit width, even this grating provides a resolving power higher than 7000 between 200 and 2.5 keV.

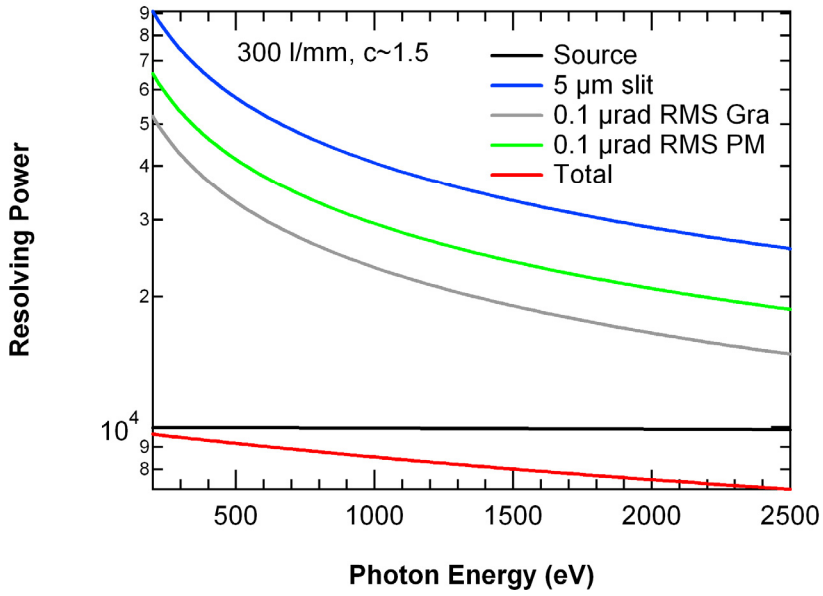

Figure 11.7.6 Contributions to the resolving power due to the source, 5 µm exit slit, 0.1 µrad RMS slope errors on the grating and M2, and their vector sum for the HF(high flux, 300 l/m) grating of the soft x-ray resonant scattering and RIXS beamline.

11.7.2.3.2 Refocusing

The refocusing onto the sample is performed with two elliptical cylinder mirrors. The first one (M3) is the horizontally refocusing mirror located at a distance of 51.850 m from the source with a nominal demagnification of 36. The vertically refocusing mirror (M4) is 0.5 m downstream of M3 and demagnifies the slit width by 2.3. The angle of incidence on both mirrors is 88.75°.

11.7.2.3.3 Flux

The absolute grating efficiencies were calculated using the differential formalism of the exact electromagnetic theory [11.7.9], assuming the central line density in each grating and blazed groove profiles. The results for the three gratings assuming Au coating and blazed angles of 1.8° for the UHR, 1.0° for the HR, and 0.4° for the HF grating are displayed in Figure 11.7.7. The high line density and high *c* value used in the UHR grating lead to an efficiency that varies only between 1.2 and 3.2%. The efficiency of the HR grating is higher than 10% between 300 eV and 2150 eV, whereas the efficiency of the HF grating is higher than 20% in the same energy range.

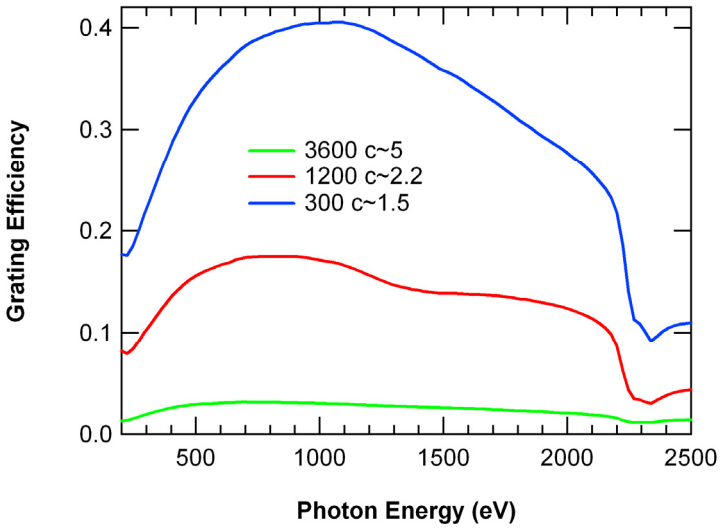

Figure 11.7.7 Absolute efficiencies of the three Au-coated, blazed, VLS gratings in the soft x-ray resonant scattering ant RIXS beamline, labeled by their central line density: UHR 3600 lines/mm, HR 1200 lines/mm, and HF 300 lines/mm.

The reflectivities of the Au coated plane mirror as a function of the photon energy when operated with each one of the gratings are shown in Figure 11.7.8. The penalty in reflectivity when very high resolution is required is evident in this figure. The total flux expected at the sample position with an exit slit width of 5 μm was calculated taking into account the undulator flux appearing in Figure 11.7.1 after correcting for the bandpass of the 5 μm exit slit width, the reflectivities of the Au coated M1, M2, M3, and M4, as well as the grating efficiencies. The results appear in Figure 11.7.9. For completeness, the resolving power expected with each grating is shown in the upper part of the figure. Switching from the UHR to the HR grating at 1 keV increases the flux 16 times while losing only a factor of 3 in resolving power. By switching from the HR to the HF grating, one gains an additional factor of 8 in flux with the same resolution loss.

Figure 11.7.8 Reflectivities of the (Au coated) plane mirror in the soft x-ray resonant scattering and RIXS beamline at the angle of incidence required for operation with each of the three gratings: UHR 3600 lines/mm, HR 1200 lines/mm, and HF 300 lines/mm.

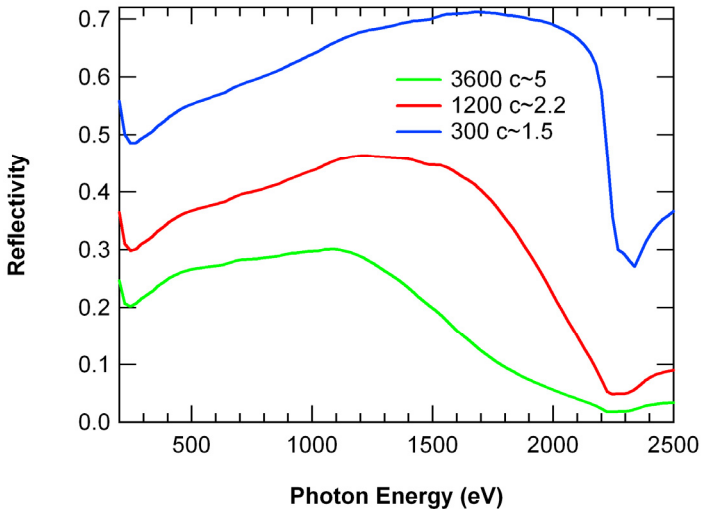

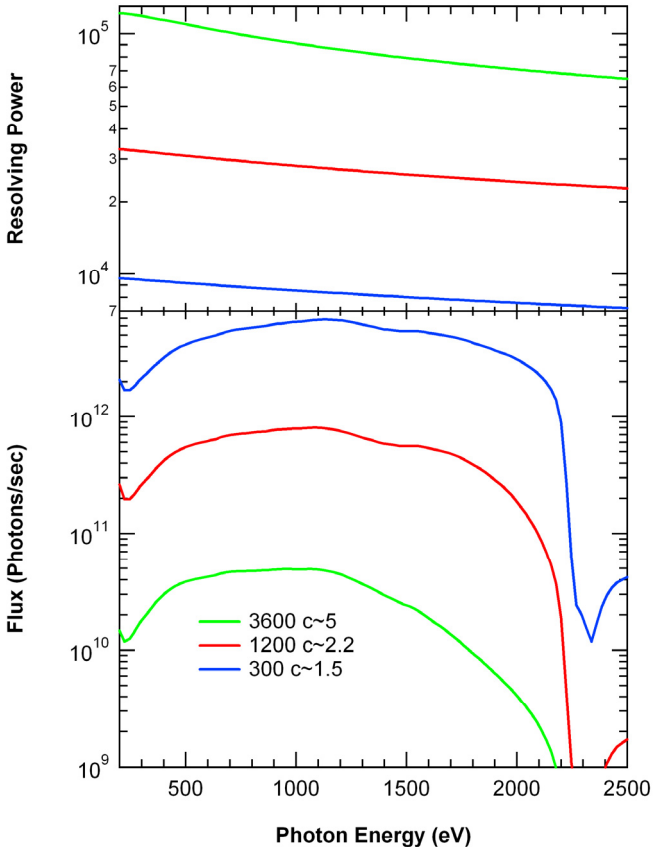

Figure 11.7.9 Flux (lower panel) and corresponding resolving power (upper panel) expected at the sample position for the three gratings of the soft x-ray resonant scattering and RIXS beamline, for a 5 μm exit slit width. The gratings are: UHR 3600 lines/mm, HR 1200 lines/mm, and HF 300 lines/mm.

The proposed design will result in a soft x-ray beamline with unparalleled performance. When operated in high flux mode, the beamline will provide close to 10^{13} ph/s, equal to any existing soft x-ray beamline, and still have a resolving power higher than the most recent soft x-ray beamlines at other DOE synchrotron facilities (i.e., beamline 11.0.02, the Molecular Environmental Sciences Facility, at ALS). When operating in high resolution mode, the beamline will have a resolving power close to 100,000 (an order of magnitude improvement over the capability of, for example, beamline 4-ID-C at APS), with a calculated flux of ~5 × 10^{10} ph/s, which is comparable to the flux at 4-ID-C.

11.7.2.4 Ray Tracing

The ray tracings for the XRMS/RIXS beamline were performed using the Shadow code [11.7.10]. The caption above the spot patterns gives the RMS values of the beam, either size or divergence, along the horizontal and vertical directions. The y-coordinate is along the dispersion direction at the exit slit and sample position and along the length of the optical elements. Slope errors (0.1 μrad RMS along the meridional direction of the plane elements and 0.5 μrad RMS along the meridional direction of the other optical elements) were included in the ray tracings by assuming a sinusoidal variation on the optical elements' surface. All the ray tracings were performed with sizes and divergences calculated as described in the description of the source.

Figure 11.7.10 shows the spot pattern at the cylindrical mirror (M1) when illuminated with 200 eV photons. As seen in the figure, a 300 mm-long mirror accepts most of the central cone radiation emitted by the undulator at this energy. The illumination of the plane pre mirror (M2) and the HR grating when they are tuned to 200 eV (Figure 11.7.11 and Figure 11.7.12) show that despite the divergence of the horizontal beam, the optical surfaces of these elements need to be approximately 7 mm wide. The total length of the plane

mirror, using the SX700 principle [11.7.8], needs to be approximately 400 mm. The gratings need to be less than 100 mm long. Figures 11.7.13 and 11.7.14 show the illumination of the refocusing elliptical cylinder mirrors (M3 and M4). The horizontally focusing mirror needs to be at least 400 mm long and the vertically focusing mirror needs to be less than 80 mm long.

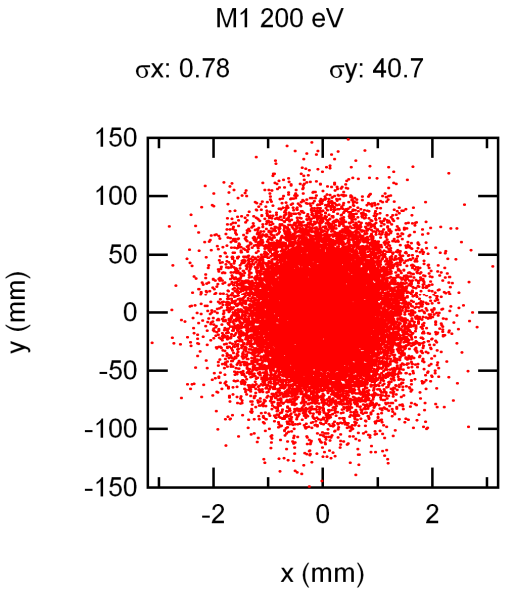

Figure 11.7.10 Spot pattern at M1 for 200 eV photon energy in the soft x-ray resonant scattering and RIXS beamline.

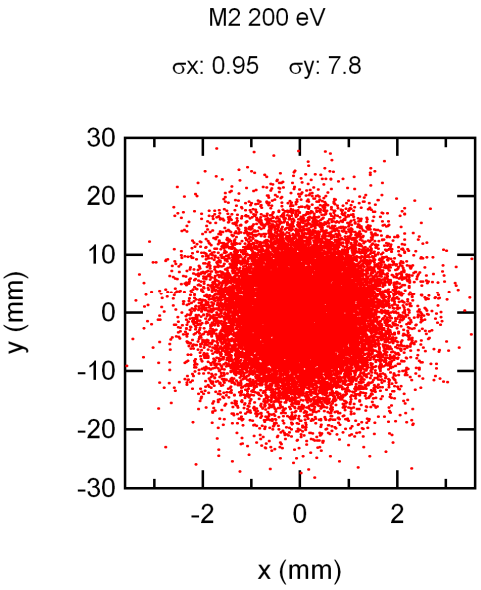

Figure 11.7.11 Spot pattern at M2 when tuned to 200 eV with the HR grating in the soft x-ray resonant scattering and RIXS beamline.

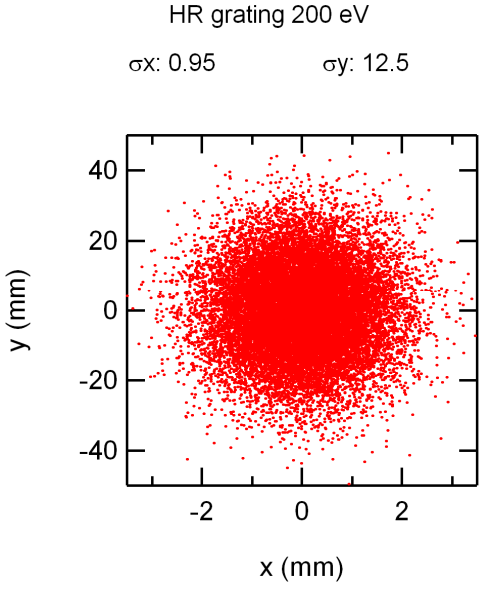

Figure 11.7.12 Spot pattern at the HR grating for 200 eV photon energy in the soft x-ray resonant scattering and RIXS beamline.

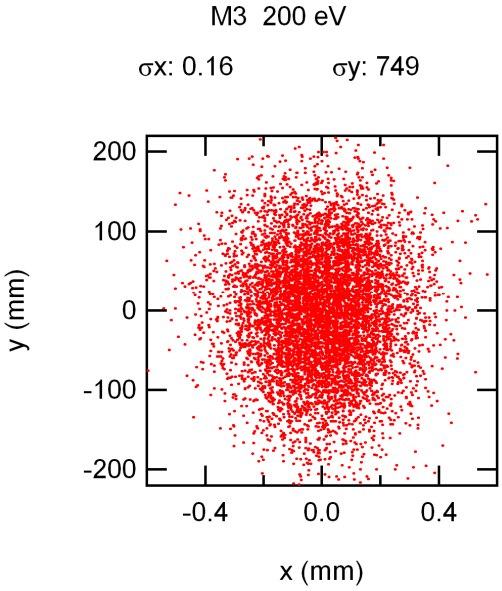

Figure 11.7.13 Spot pattern at M3 for 200 eV photon energy in the soft x-ray resonant scattering and RIXS beamline.

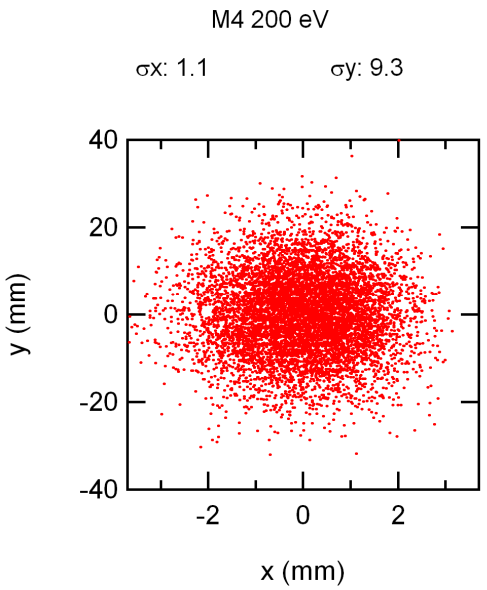

Figure 11.7.14 Spot pattern at M4 for 200 eV photon energy in the soft x-ray resonant scattering and RIXS beamline.

The resolution of the monochromator at 200 eV with the HR grating is demonstrated by the spot patterns shown in Figure 11.7.15. Clearly, the monochromator has a resolution better than 6 meV, in agreement with the analytical calculations (Figure 11.7.5) without including the contribution of the exit slit. The figure also shows that an exit slit length of 10 mm is required to let through the horizontally diverging beam. Another example showing the agreement between the analytical calculations and ray tracings results in the case of the UHR grating (Figure 11.7.4) is shown in Figure 11.7.16. This figure indicates that the resolution at 1 keV with these grating is better than 10 meV.

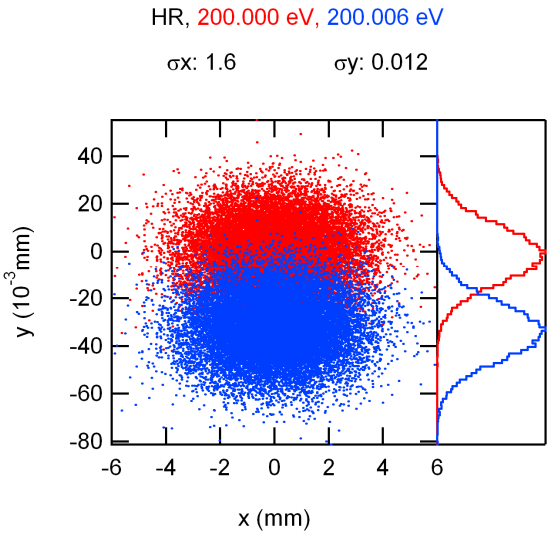

Figure 11.7.15 Spot pattern at the exit slit plane for 200 and 200.006 eV photon energies using the HR grating in the soft x-ray resonant scattering and RIXS beamline. The sigma values are for 200 eV.

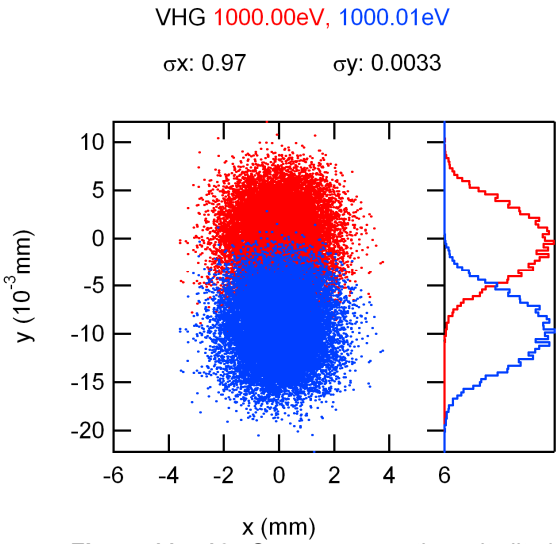

Figure 11.7.16 Spot pattern at the exit slit plane for 1000 and 1000.01 eV photon energies using the UHR grating in the soft x-ray resonant scattering and RIXS beamline. The sigma values are for 1000 eV.

The ray tracings illustrating the spot size and the divergence at the sample plane for 200 eV photons are shown in Figures 11.7.17 and 11.7.18, respectively. The RMS horizontal and vertical sizes and divergences shown in the figures are consistent with the values obtained from the vector sum of the source parameters (slit

for the vertical size) modified by the corresponding magnification and the contributions due to the assumed slope errors. Obviously, the RMS vertical size will not change with energy, while the RMS horizontal size will decrease from 2.3 μm at 200 eV to 2.0 μm at 2.5 keV. The largest vertical RMS divergence, less than 0.5 mrad, will occur when the UHR grating is used at 200 eV.

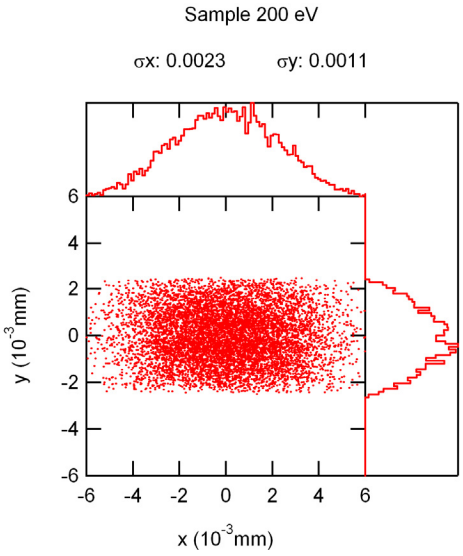

Figure 11.7.17 Spot pattern at the sample position at 200 eV photon energy for the soft x-ray resonant scattering and RIXS beamline.

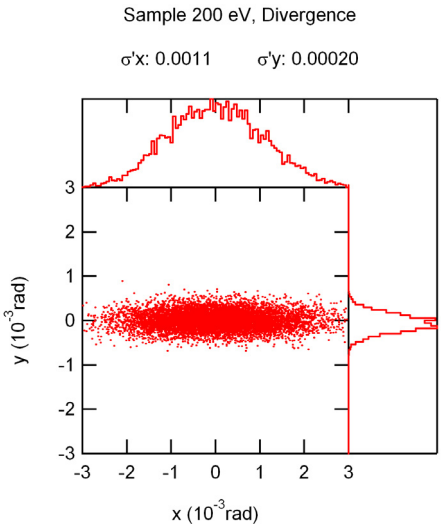

Figure 11.7.18 Spot divergence at the sample position at 200 eV photon energy for the soft x-ray resonant scattering and RIXS beamline.

11.7.2.5 Design for Use of Two Canted EPUs

In this mode of operation, the horizontal angle between the electron beam and the axes of the EPUs should be as small as possible to keep a reasonable exit slit length. On the other hand, the angle should be large enough that there is a minimal overlap between the two beams. We chose 0.17 mrad for the separation between the two beams, which corresponds to 4σ of the RMS divergence at 200 eV. Two sagittal cylindrical mirrors, designed to collimate along the vertical direction its respective source, replace M1. This ensures the two beams will be focused at the exit slit; but implies that the resolution of the far beam (upstream undulator) is a few percent better than that of the closer beam. The elliptical cylinder horizontally refocusing mirror (M3) also needs to be replaced with two elliptical cylinder mirrors when operating in the canted mode. The mirror refocusing the beam from the upstream undulator is designed to be slightly out of focus to obtain approximately the same horizontal beam sizes at the sample position.

Ray tracings were also performed for use of the canted EPUs, and Figures 11.7.19 through 11.7.26 summarize the results for 200 eV photons using the HR grating. The captions in the figures show the RMS beam sizes and their average positions. At 200 eV the "contamination" of the radiation from the upstream undulator on the downstream beam is less than 2.5%. This number decreases to practically zero at 1 keV. The contamination can be practically eliminated at the expense of some flux at lowest photon energies. This can be achieved by having a gap of 80 mm between the two M1 mirrors. This will reduce the flux at 200 eV by approximately 10% but will reduce the contamination to less than 0.3%. Practically no flux is lost for energies higher than 1 keV. With the above mentioned separation between the M1 mirrors, their length should be 240 mm, the plane mirror and the grating wider than 16 mm, each M3 at least 320 mm, and the exit slit length 20 mm. The latter means that some mechanism will need to be develop to control the slit to have the same opening at both extremes and be parallel to the floor to better than a few tens of a microradian. Comparing the spot size at the sample in the two cases (Figures 11.7.25 and 11.7.26) reveals that the horizontal sizes differ

by approximately 4% at 200 eV. From ray tracings performed at 1 keV, one obtains a 15% difference in the horizontal beam size.

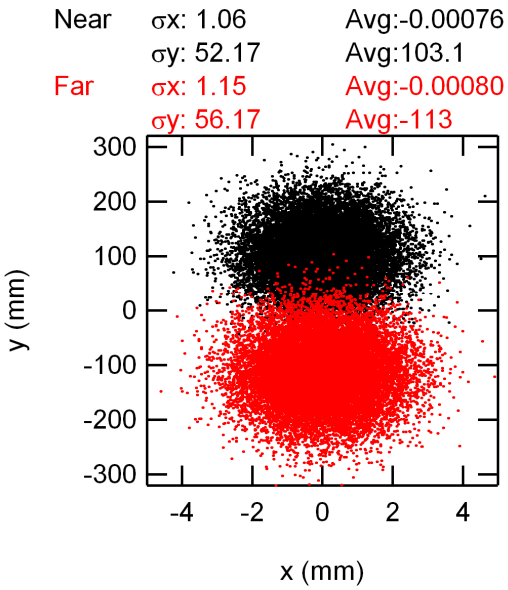

Figure 11.7.19 Illumination of the near and far M1 mirrors at 200 eV photon energy in the soft x-ray resonant scattering and RIXS beamline.

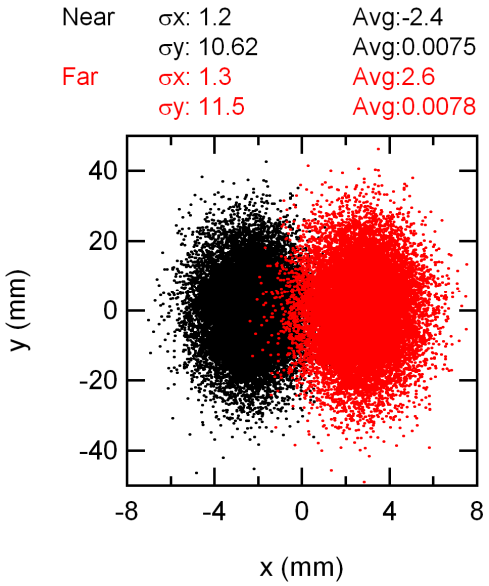

Figure 11.7.20 Illumination of the plane mirror (M2) with the two beams at 200 eV photon energy for the HR grating in the soft x-ray resonant scattering and RIXS beamline.

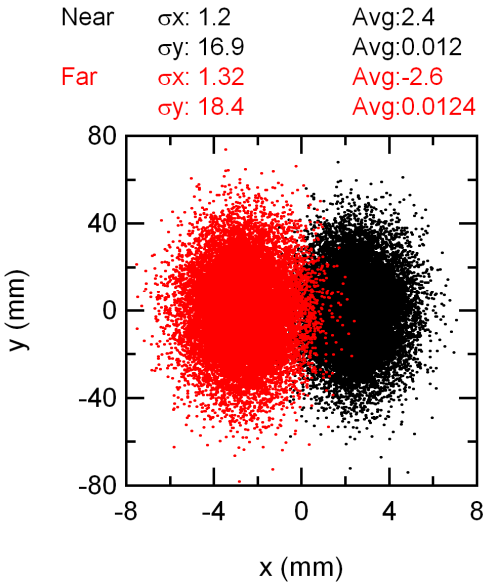

Figure 11.7.21 Illumination of the HR grating by the two beams at 200 eV photon energy in the soft x-ray resonant scattering and RIXS beamline.

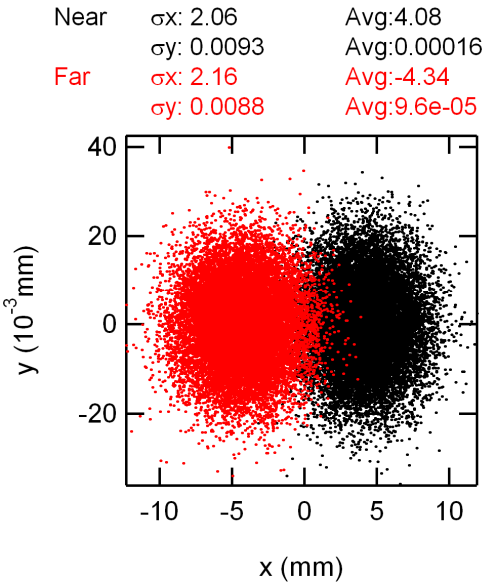

Figure 11.7.22 Illumination of the slit by the two beams at 200 eV photon energy for the HR grating in the soft x-ray resonant scattering and RIXS beamline.

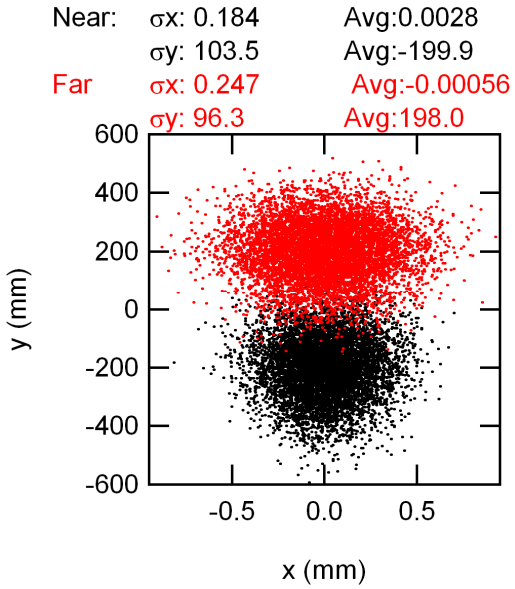

Figure 11.7.23 Illumination of the M3 mirrors by the two beams at 200 eV photon energy for the HR grating in the soft x-ray resonant scattering and RIXS beamline.

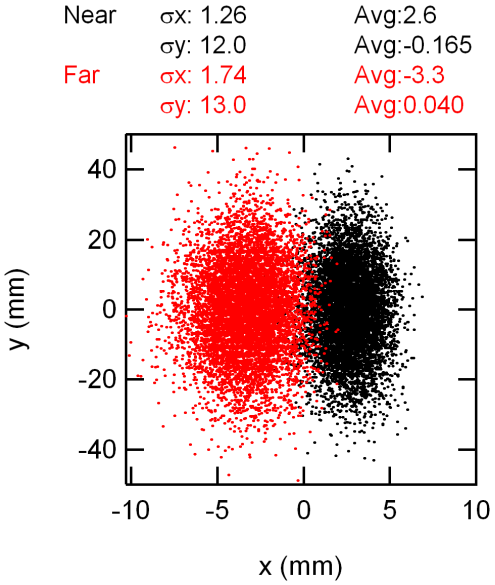

Figure 11.7.24 Illumination of M4 by the two beams at 200 eV photon energy for the HR grating in the soft x-ray resonant scattering and RIXS beamline.

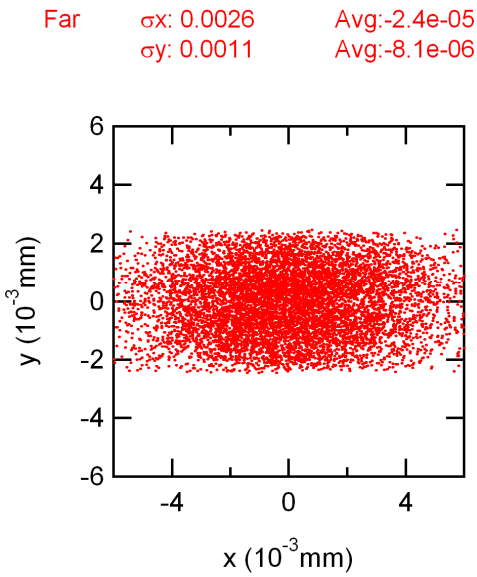

Figure 11.7.25 Sample illumination with the far beam at 200 eV photon energy for the HR grating in the soft x-ray resonant scattering and RIXS beamline.

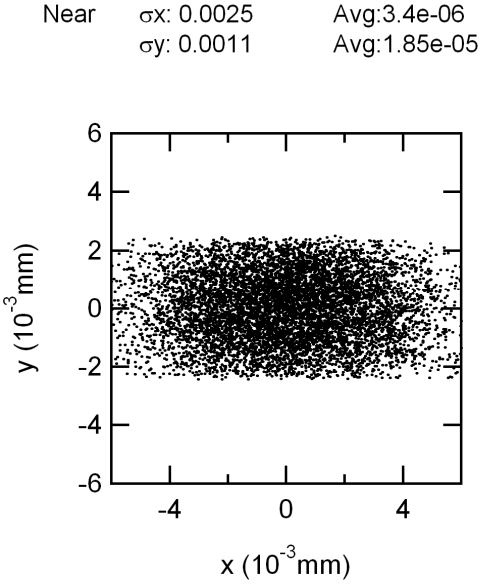

Figure 11.7.26 Sample illumination with the near beam at 200 eV photon energy for the HR grating in the soft x-ray resonant scattering and RIXS beamline.

11.7.2.6 Power Absorbed by Pre-Monochromator Mirrors

The calculated [7.19] power absorbed by the first optical element, i.e., the M1 mirror, when the two EPUs are phased to emit linear horizontally polarized radiation at 200 eV is shown in Figure 11.7.27. At 200 eV photon energy, for the UHR grating, the angle of incidence on the plane mirror is 82.4°, which is the smallest angle (largest grazing angle) required in the operation of the monochromator.

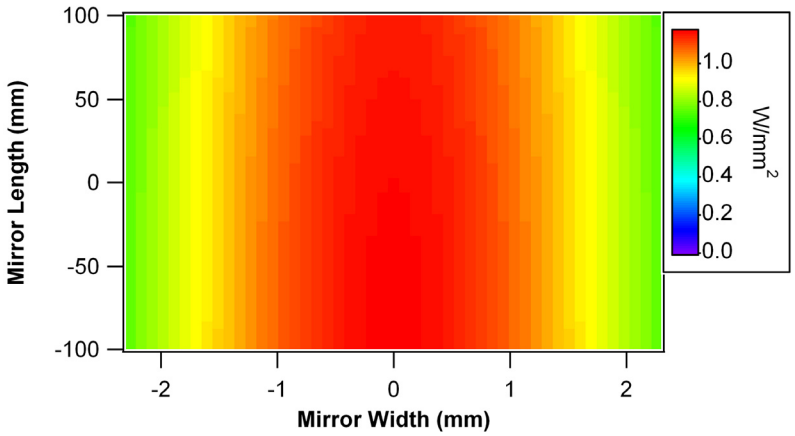

Figure 11.7.27 Power density absorbed by the M1 mirror of the soft x-ray XRMS/RIXS beamline when the EPU is tuned to 200 eV in linear polarization mode.

The maximum power density absorbed by M1 is 1.2 W/mm^2 (Figure 11.7.27) and the total power is almost 1 kW. The corresponding values for the plane mirror (M2) are 0.56 W/mm^2 and less than 100 W. The power, and power density, absorbed by the grating in this case is very small. Considerable cooling must be provided to both mirrors (M1 and M2) to avoid deformations of the ideal mirror shape. The cooling scheme for M1 needs to ensure that the heat-induced meridional RMS slope errors in M1 are below 0.5 μrad. In the case of the plane mirror (M2), a novel cooling design should be developed to preserve the ultra high resolving power. The development of such a cooling scheme will require iterations of finite element analyses and ray tracings performed with the calculated surface deformation.

11.7.3 Beamline Layout

Figure 11.7.28 depicts the proposed layout for the beamline. The M1 mirror tank and the M2 mirror + grating tank are contained in the front optics enclosure. After that, a horizontal diverting mirror separates the line into two branches. At an angle of incidence of 88.5º, a single mirror deflection would reduce the flux by only ~30% across the relevant energy range (see Figure 11.7.3). The RIXS branch takes the straight through beam to maximize the flux and the RIXS spectrometer points away from the shield wall. The XRMS station sits on the inboard branch. The large vacuum chambers just before the experimental chambers house the re-focusing mirrors.

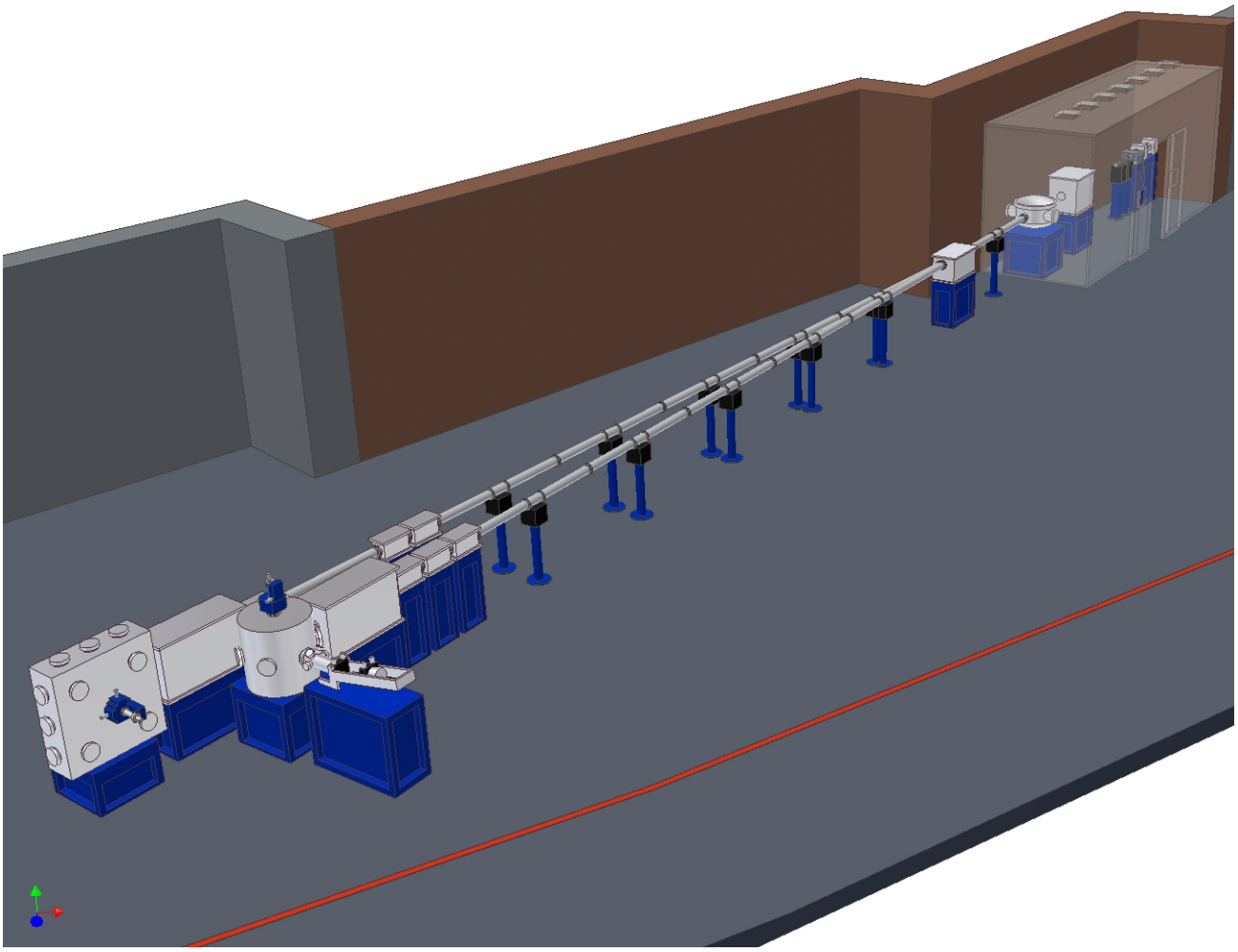

Figure 11.7.28 Proposed layout for a Soft X-Ray Resonant Scattering and RIXS Beamline.

11.7.3.1 XRMS End Station

To conduct measurements in the soft x-ray range, vacuum pressures of order 10^{-8} Torr or lower are necessary to eliminate scattering and absorption from residual gases, maintain the cleanliness of the sample and upstream optics, and prevent condensation onto sample surfaces during low-temperature operation. In essence, the XRMS end station is a good diffractometer contained in a vacuum vessel, which complicates the design of the instrument. The diffractometer must permit independent motions of sample θ to near 90°, detector 2θ to near 180° (back scattering), and as many other motions as is practical. The design goals for the XRMS end station will be to allow near 360° rotation of the sample azimuthal angle (ψ), and about ±10° on the sample flip axis (χ). Those motions would allow for specular scans along the Q_z direction (normal to the sample) and diffuse scans along Q_x (with the scattering plane parallel to the x-z plane). Of course, it would also be desirable to rotate the detector arm out of the scattering plane to conduct diffuse scans along the Q_y direction. In the past such motions have been difficult to attain as in-vacuum stepper motors generally were not available. However, in recent years, several suppliers have started offering such items. This development should simplify a design featuring detector motion out of the scattering plane. A conceptual sketch of the proposed diffractometer is presented in Figure 11.7.29.

On the detector side, it is envisaged that the detector arm will house a group of point detectors that are optimized for different dynamic ranges. In addition, a two-dimensional detector would be of great benefit for examining diffuse diffraction patterns as well as soft x-ray Small Angle X-ray Scattering, SAXS. The size and characteristics of the detector suite will be discussed in more detail in Section 11.7.4. However, all the detectors will require beam-defining slits between the sample and the detector to reduce the background counts. The slits also define the angular acceptance of the point detectors and being able to vary their acceptance angle would be beneficial. The most direct way of accomplishing this would be to have the detector and slit translate along the 2θ arm; the angular acceptance would increase as the detector approached the sample. For this implementation the detector stage or individual detectors should be mounted on a motorized linear translation stage.

As stated above, there are at least three related but separate user communities that would use the XRMS end station, and the sample environment required to support the science program in each group will be quite different. The correlated electron materials community would prefer, generally speaking, the ability to cool the sample as low as possible and also to be able to apply high magnetic fields on the order of 5 Tesla or larger. The large fields would be useful for driving complex materials across phase boundaries and then searching for ordering phenomena such as orbital ordering via the appearance of additional peaks in the scattering pattern. While such large fields and low temperatures would be useful for the magnetic multilayer and spintronics materials group, particularly in the case of magnetic semiconductors, a more useful ability for them would be to have more modest fields, on the order of 1 Tesla or lower, but have the ability to vary the field quickly by, for example, rotating the direction of the magnetic field both in-plane and out of plane. Also, since many of the properties of interest for these researchers involve interfacial chemical and magnetic ordering, the evolution of interface roughness could be studied via in-situ sample heating to at least several hundred degrees Celsius.

It is unlikely that a single experimental configuration would satisfy the needs of all the potential user communities. Therefore, having different inserts available for the XRMS chamber would provide the required sample environment. In the first configuration, the XRMS chamber would be equipped with a large field superconducting magnet with a maximum sustained field of 5 Tesla or greater. In all likelihood, this magnet would be of a split coil design and would be fixed (non-rotating), which would limit the angular range of the scattering. In the second configuration, the large magnet would be replaced by one with a smaller maximum field, on the order of ~1 T or so, but where the direction of the magnetic field could be varied. Also, the magnet should be designed to leave the scattering plane unobscured, perhaps by having the magnet poles rotate along with the sample θ angle. An in-vacuum octupole design might provide the solution that satisfies these requirements. In addition, the low-temperature cryostat could be replaced with a modest sample heating stage to permit in-situ annealing and subsequent measurement.

The sample environment should also provide for numerous electrical connections. These would be used to monitor sample temperature, conduct four-point conductivity and magneto-resistance measurements, and other probes. There should also be shielded cables capable of providing high voltage, which could be used to pole and de-pole ferroelectric and multiferroic materials. Similar shielded cables could be used for measuring sample current to conduct XAS measurements to complement the XRMS experiments. Finally, the sample manipulator and experimental chamber should be equipped with a load-lock device for rapid sample transfer.

11.7.3.2 RIXS End Station

The greatest design challenge for a RIXS spectrometer is to develop an instrument with the highest resolving power at soft x-ray energies while still maintaining a reasonable count rate. A RIXS instrument is a very good, compact soft x-ray spectrometer that is affixed to an experimental vacuum chamber (see Figure 11.7.30). The general characteristics and design tradeoffs of a RIXS instrument are:

- Plane Grating Monochromator or Rowland circle configuration
- several gratings to cover wide energy range and offer a choice of resolution

- blazed gratings to increase efficiency
- large area, 2D CCD detector that translates along the grating dispersion direction to increase accessible energy range
- entrance slit (higher resolution) vs. slitless entrance (requires small beam spot; provides more flux)

With regard to the last point, the exceptionally small emittance of NSLS-II results in a extremely small spot size on the sample (approx. 4 μm, vertical × 8 μm, horizontal) while still maintaining a high flux on the order of 10^{10} to 10^{12} ph/s. Thus it should be feasible to design a custom RIXS spectrometer with no entrance slit and achieve performance, in resolution and throughput, comparable to or better than the best instruments currently available. Alternatively, an entrance slit could be incorporated into the design to increase resolution further, but at the cost of decreased throughput. Of course, the entire instrument, as well as the sample environment, must be in continuous ultrahigh vacuum to maintain clean surfaces of cryo-cooled samples..

As mentioned above, one potential benefit of RIXS is dipole-allowed section rules that are present both in the photo-excitation process and in the radiative decay of the core hole. In principle, therefore, it should be possible to investigate, in an element-specific fashion, the valence-electron wave functions along different crystal symmetry directions. To accomplish this, it would be advantageous to have the RIXS spectrometer move with respect to the sample, thus accessing different momenta relative to the crystal while keeping fixed the polarization of the incident light. This will prove to be an engineering challenge as the RIXS spectrometer is likely to be at least 1 m to 2 m in length or longer. Moving such an instrument while maintaining vacuum in the 10^{-8} Torr range or better will be difficult. One candidate solution would have the RIXS chamber and spectrometer located on a rotary platform and connected to the beamline via a large diameter bellows. The sample would be mounted on a separate rotary seal. The whole chamber could thus rotate about the beam position while the sample counter-rotates to maintain its orientation relative to the photon beam.

The ability to vary the incident light polarization via use of the EPU insertion devices is of great utility. This will permit collection of RIXS spectra with the electric field vector of the incident radiation oriented horizontally and vertically without having to rotate the sample. Also, with the proposed rapid switching scheme, lock-in detection techniques become feasible, which would be of great utility in examining small spectral signals that might arise in linear dichroism effects. Finally, heretofore, RIXS measurements with circularly polarized soft x-rays have not been common. Such measurements could be quite useful, as they impose an additional selection rule on dipole-allowed processes, namely, the magnetic quantum number m_j should vary according to $\Delta m_j = \pm 1$ or 0. Such capabilities would be extremely useful in examining high-temperature superconductor and other correlated electron systems where ferromagnetic order either coexists or is nearly degenerate with other phases. Similar arguments would apply to novel materials such as multi-ferroic compounds

The sample environment should allow for as many perturbations on the sample as is practical. Certainly, the sample should be connected to a cryostat that can lower the temperature as low as possible. Closed-cycle, commercial cryostats that provide a temperature on the sample of 4.2K and are UHV compatible are currently available. Closed-cycle cryostats with a base sample temperature as low as 1.2K are also available, but they are not currently compatible with a good vacuum environment. However, commercial suppliers are currently investigating whether good vacuum performance and improved cooling is feasible.

In addition to the sample temperature, for many experiments it is critical to apply a large magnetic and /or electric field on the sample to drive a material across a phase boundary and examine the resulting changes on the RIXS spectra. Split core magnets with maximum sustained fields near 11 Tesla are commercially available. More complicated designs where the direction of the magnetic field can be varied are less common, but possible, at the cost of added expense and more limited field strengths. As with the XRMS chamber, the RIXS chamber should include numerous electrical connectors and suitable in-vacuum cabling for monitoring sample temperatures, applying fields, and recording sample currents. The chamber should also be equipped with a load lock and sample transfer mechanism.

11.7.4 Detectors

Three different classes of detectors will be required for the XRMS beamline: "point" detectors operating in current mode, "point" detectors operating in pulse counting mode, and 2D detectors. For the current-mode point detectors, we will use photodiodes whose response is optimized for the soft x-ray energies. These optimized silicon photodiodes, such as the AXUV series from International Radiation Detectors, Inc. have very high quantum efficiency (~50 – 200) in the soft x-ray range and a thinned silicon oxide junction that greatly reduces absorption in the nonresponsive oxide layer. Also, these photodiodes are inexpensive. They can be equipped with in-vacuum pre-amplifiers that reduce pick-up noise over the cabling to the data acquisition computer, which is indispensable for accurately recording low signal level. Alternatively, low-current GaAsP photodiodes are also available, but at increased expense. However, both types will be evaluated for use in the XRMS end station.

In addition to the current-mode photodiodes, we plan on installing pulse counting detectors suitable for extremely low-photon-flux detectors. These detectors are capable of single photon detection and they are extremely useful in examining weak, off-specular diffraction features; standard photodiodes are of limited use in those situations, as the count rate often approaches the noise floor. Two types of pulse counting detectors will be evaluated. The first is avalanche photodiodes, which are robust detectors operated at modest bias (~150 V), which provide internal gain. APDs are insensitive to repeated exposure to atmosphere, which makes them useful in situations such as the planned multiple configurations of the XRMS chamber, where the vacuum chamber is vented repeatedly. Also, they extend the accessible dynamic range down by one to two orders of magnitude over standard soft x-ray photodiodes. Modest cooling, to 0° to -20°C, improves the internal gain of the APDs by about an order of magnitude. Such temperatures are easily achieved using small Peltier cooling stages. A disadvantage of APDs is that strong absorption of incident x-rays occurs near the oxygen K edge; this limits their operating energies to above ~600 eV.

Another possible pulse counting detector is a channel electron multiplier (CEM) with a CsI photoelectric converter screen. These detectors are extremely sensitive, even more so than APDs, and they are sensitive over the entire spectral range covered by the beamline. However, the sensitivity of CEMs decreases with repeated exposure to atmosphere.

In addition to the point detectors, we will require high-efficiency 2D area detectors. Indeed, for the RIXS spectrometer, such detectors are crucial, as they permit designs of instruments that capture a much larger solid angle than would be possible with point detectors. Two types of detectors will be evaluated for use the two end stations. The first type is soft x-ray CCD cameras. These detectors have a reasonably high quantum efficiency of ~30% to 70% in the soft x-ray range. The current state-of-the-art CCD cameras have an active area of 25 mm × 25 mm with 2048 × 2048 pixels and a pixel size of 13.5 μm. In the near future, suppliers expect to produce CCD chips with 4096 × 4096 pixels with an active area of 50 mm × 50 mm. At the moment, the major soft x-ray CCD suppliers do not plan to reduce the pixel size below 13.5 μm, which would improve the resolving power of the RIXS spectrometer. Therefore, detector development should be monitored closely to ascertain whether improved detectors can be incorporated into the experimental design of the XRMS and RIXS apparatus.

For 2D detection of soft x-rays, CCDs offer the best dynamic range with the smallest pixel size. One disadvantage to CCD cameras is that they are rather bulky for in-vacuum use. A more serious limitation is that the cameras often require active water cooling. This is a bit inconvenient for the XRMS spectrometer, as it implies that the coolant supply pipes have to be inserted into the vacuum chamber and directed along the detector arm to the camera. Also, care must be taken so that the coolant lines do not limit the motion of the detector arm. An alternative 2D detector is a MultiChannel Plate detector with a delay line read-out. MCP detectors do not require cooling and typically have a lower dark count than the CCD cameras. The disadvantages are that the minimum spatial resolution of the MCPs is about 50 μm, they require high voltage, and the data rates are typically lower than CCDs. The lower spatial resolution would make the MCP detectors

more suitable for the XRMS diffractometer than the RIXS spectrometer, and developments in these detectors should be followed closely.

11.7.5 Laboratory and Conventional Facilities

Two laboratory spaces would be desired for such a high-resolution soft x-ray beamline. Some of these facilities, however, should be shared resources that will be used by other soft x-ray beamlines. The first laboratory space would be a clean lab where testing and assembly of the in-vacuum instrumentation and beamline components would occur. This should contain one or two laminar flow hoods, storage facilities (cabinets and drawer space) for various end station components and test equipment, ultrasonic agitators for component cleaning, and a generous number of lab benches. There should be specialized utilities such as deionized water and dry nitrogen gas available, and sufficient electrical capacity to run several rough pumps, ion pumps, turbo pumps, and other required instrumentation. The clean lab should also dedicate one laminar flow hood, lab benches, and storage for sample preparation and mounting. Clean tools should be supplied for this purpose. There should also be one or two vacuum desiccators for sample storage. Also, the clean lab will probably need a satellite storage area for temporary storage of waste solvents. Because of the necessity to guarantee cleanliness and availability of tools and instrumentation for UHV application, the clean lab should be accessible only via keyed access, with either electronic or mechanical keys.

The second laboratory would house sample characterization tools that complement the data collected on the XRMS and RIXS end stations. Many of the experiments on these end stations will be on samples where magnetism competes with or greatly influences other physics properties. Thus the support laboratory should include a suite of instruments to characterize the advanced samples measured on the beamlines. Candidate instrumentation should include MOKE (magneto-optic Kerr effect) in longititudinal, polar, and transverse modes, SQUID magnetometry, perhaps combined with AC susceptibility and PPMS (physical properties measurement system), which includes magneto-transport measurements, Hall effect, and critical current probes), high-frequency magnetic characterization (e.g., electron spin resonance or ferromagnetic resonance) and some form of magnetic microscopy (MFM or MOKE microscopy). The laboratory should also include a high-temperature vacuum furnace that can be used to anneal samples in a magnetic field to vary effects such as magnetic ordering and exchange bias, and also to produce magnetically soft pole pieces for specialized electromagnets used on the beamline.

11.7.6 Outstanding Issues

We propose the acquisition of a portable soft x-ray polarization analysis chamber, which could be mounted on any beamline. It is anticipated that the polarization analysis chamber could be shared between the two soft x-ray beamlines in the initial tranche of beamlines, and would support other soft x-ray beamlines at NSLS-II as they come on line.

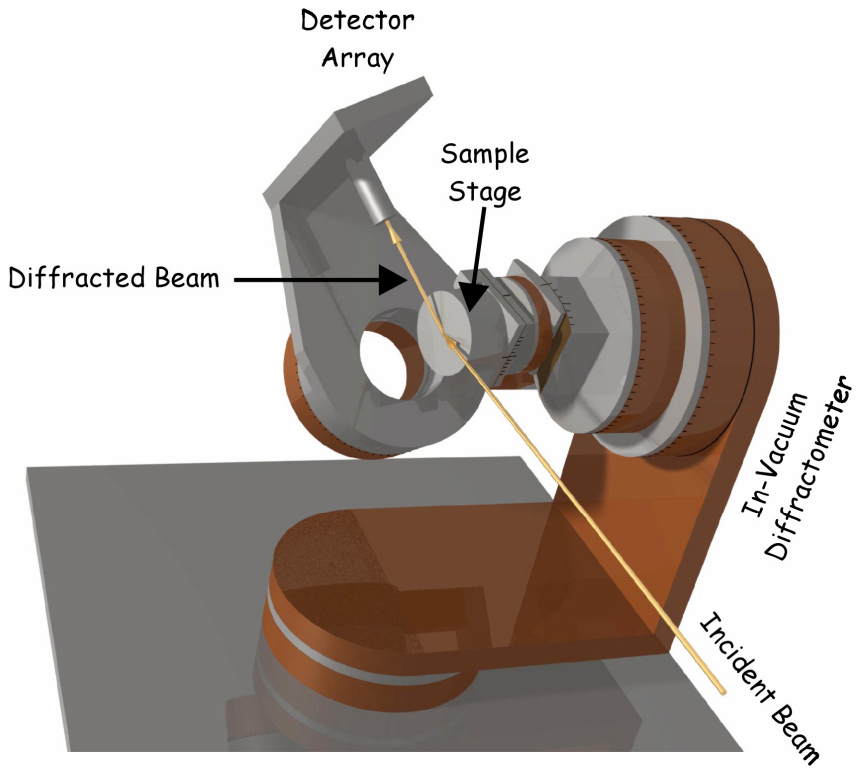

Figure 11.7.29 Schematic representation of a proposed XRMS in-vacuum diffractometer. The final design will incorporate multiple rotational degrees of freedom for sample and detector stages, sample cooling to LHe temperatures, and an electromagnet for applying an external magnetic field.

References

[11.7.1] C. Sanchez-Hanke, R. Gonzalez-Arrabal, J. Prieto, E. Andrzejewska, N. Gordillo, D. Boerma, R. Loloee, J. Skuza, R. Lukaszew, Observation of nitrogen polarization in Fe-N using soft x-ray magnetic circular dichorism, *J. Appl. Phys.* **99**, 08B709 (2006).

[11.7.2] B. Heinrich, et al., Dynamic exchange coupling in magnetic bilayers. *Phys. Rev. Lett.* **90**(18) (2003).

[11.7.3] M.G. Samant, et al., Induced spin polarization in Cu spacer layers in Co/Cu multilayers. *Phys. Rev. Lett.* **72** 1112 (1994).

[11.7.4] R. Follath, The versatility of collimated plane grating monochromators. *Nucl. Instr. & Meth. A* **467** 418 (2001).

[11.7.5] R. Reininger, and A.R.B. de Castro, "High resolution, large spectral range, in variable-included-angle soft X-ray monochromators using a plane VLS grating." *Nucl. Instr. & Meth. A* 538(1–3): pp. 760 (2005).

[11.7.6] P. Elleaume, Undulator Radiation, in *Undulators, Wigglers and their Applications*, H. Onuki and P. Elleaume, Eds. 2003, Taylor & Francis: London.

[11.7.7] R. Reininger, SRCalc, 2001–2006.

[11.7.8] F. Riemer, and R. Torge, Bessy Sx-700 Uhv Monochromator – Design-Features and Kinematic Concept. *Nucl. Instr. & Meth* **208**(1-3) 311(1983).

[11.7.9] M. Neviere, P. Vincent, and R. Petit, Theory of Conducting Gratings and Their Applications to Optics. *Nouvelle Revue D Optique* **5**(2) 65 (1974).

[11.7.10] C. Welnak, G.J. Chen, and F. Cerrina, "Shadow – A Synchrotron-Radiation and X-Ray Optics Simulation Tool." *Nucl. Instr. & Meth. A* **347**(1-3) 344 (1994).

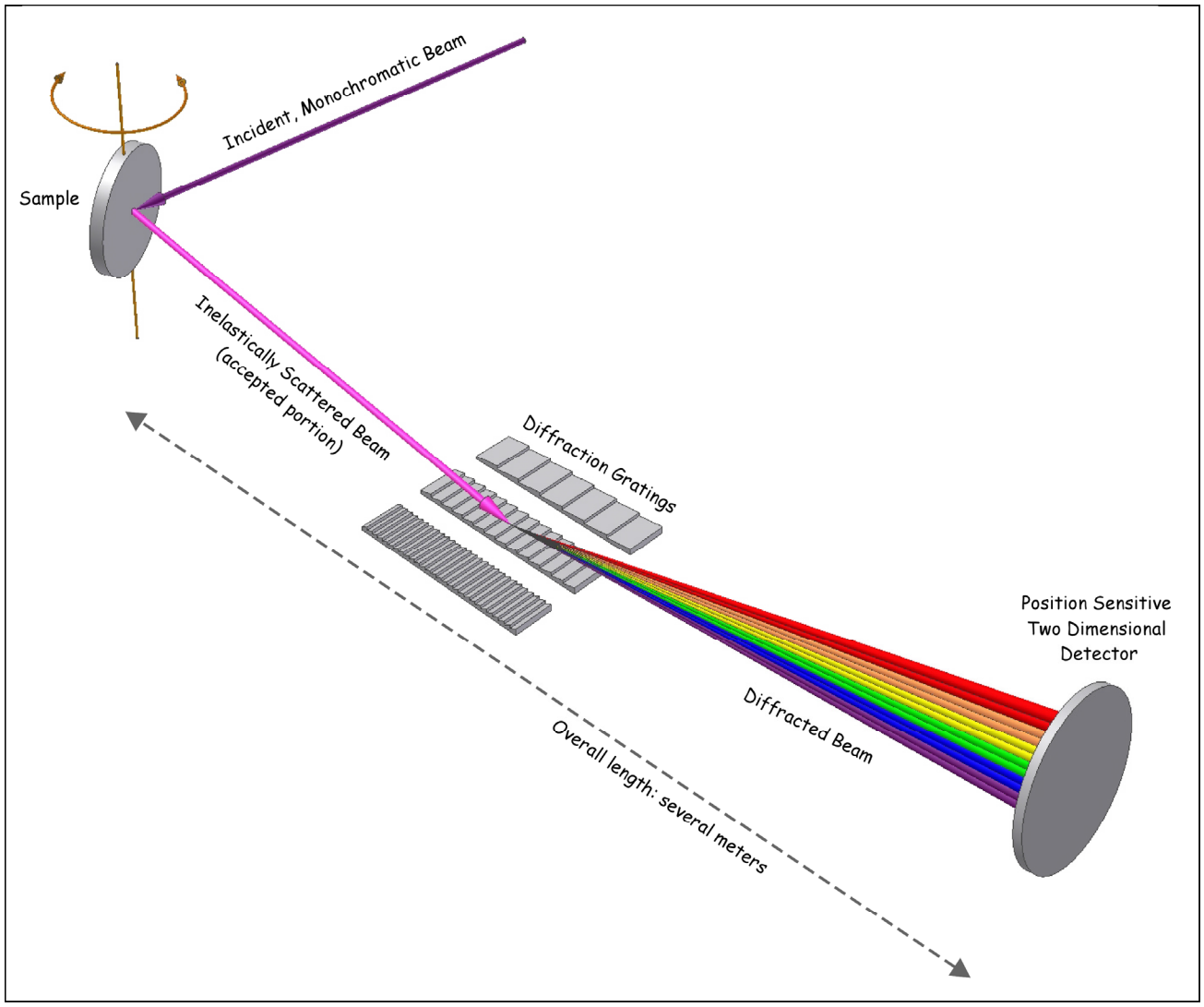

Figure 11.7.30 Schematic representation of RIXS spectrometer. The incident monochromatic beam undergoes inelastic scattering processes in the sample. A small portion of the emitted radiation (which is distributed over 2π steradians) is accepted by the RIXS spectrometer. User-selectable diffraction gratings cover different energy ranges and offer a choice of resolving power. The length of the overall instrument will be several m. In addition to sample rotation (shown in the figure), the entire RIXS spectrometer will rotate about the vertical sample axis to permit selection of different final states.

References (cont.)

[11.7.11] A. Remhof, et al., Shining light on magnetic microstructures. *Superlattices and Microstructures* 37(5) 353 (2005).

[11.7.12] V. Cvetkovic, et al., Observing the fluctuating stripes in high Tc superconductors. cond-mat/0607402 v1, 2006.

11.8 A High Flux Beamline for Soft X-Ray Coherent Scattering, Imaging, and Spectroscopy

The NSLS-II storage ring accelerator, fitted with appropriately matched undulators, will be an excellent source for soft x-ray beamlines that require either high brightness or high flux, or both. The high degree of transverse spatial coherence produced by these sources in the soft x-ray range will especially favor soft x-ray imaging and coherent scattering experiments. The additional concurrent capability to select the polarization of the soft x-ray beam, or to be able to switch the polarization rapidly between two polarization states, will greatly expand the scientific scope of this beamline.

The Soft X-Ray Coherent Scattering and Imaging Beamline is proposed to cover an energy range between 200 and 2000 eV with high flux at selectable resolving power from 4,000 to over 20,000. This beamline will provide x-rays of variable polarization with the important capability of fast switching between two polarization states. The combined properties of strong transverse spatial coherence and rapid polarization switching will be ideally suited to experiments that require either of these two properties, or both. Two experiments that require transverse spatial coherence are coherent imaging/scattering and scanning transmission x-ray microscopy. A class of experiments that benefit greatly from the magnetic sensitivity gained by rapid switching of the incident photon beam polarization is soft x-ray magnetic spectroscopy. This class of experiments includes soft x-ray magnetic circular dichroism (SXMCD), soft x-ray magnetic linear dichroism (SXMLD), and all of the variants of photoelectron emission microscopy (PEEM).

The beamline described in this section, based on optimally matched soft x-ray undulator sources described in Chapter 8, can serve all of the classes of experiments described above. Clearly, the number of end stations required to serve all of these experiments is too great to be housed at a single beamline. The actual buildout of soft x-ray undulator beamlines will be determined in a process that will involve input from all NSLS-II stakeholders. In addition to undulator beamlines, the NSLS-II bending magnets will be ideal sources for soft x-ray experiments, especially flux-driven soft x-ray experiments that require a larger étendue or illumination phase space than a coherent beam provides. One class of flux-driven experiments is full-field transmission x-ray microscopy (TXM), e.g., for tomography of biological specimens.

Coherent imaging and scattering involve the coherent illumination of a small specimen region (typically 5 to 10 μm, mapping pixel sizes of 2.5 to 10 nm into 1024^2 or 2048^2 detector pixels) with a spatially and spectrally coherent beam so that one records the Fourier transform of the exit wave on an area detector such as a CCD. In coherent scattering, the dynamics of this far-field intensity pattern can be used to monitor the dynamics of phase and absorption changes in the specimen, including over correlation distances as large as the illumination width. This is exploited in the Hard X-ray Coherent Scattering beamline described in Sec. 11.6, but the addition of coherent scattering capabilities in the soft x-ray region allows for coupling to the strong L-edge magnetic circular dichroism signal available for materials such as iron, nickel, and cobalt in the soft x-ray range, as well as to lower-Z elements in a coherent version of resonant scattering. In diffraction microscopy or coherent x-ray diffraction imaging (CXDI), partial information on the sample (such as knowledge or imposition of a "finite support," which is a region from which there is known to be, or is constrained to be, no scattering) is exploited to allow one to phase the far-field diffraction pattern and obtain a real-space image of the specimen without any resolution or efficiency limits imposed by lenses.

Scanning transmission x-ray microscopy (STXM) involves the use of a focusing optic to produce a microprobe beam through which the specimen is scanned. Whereas the hard x-ray nanoprobe described in Sec. 11.4 relies primarily on fluorescence detection due to low absorption, in the soft x-ray range, absorption dominates and the fluorescence yield for materials is low, so that transmission is the main signal used. As the resolution of soft x-ray focusing optics continues to improve, their diameter will increase dramatically, so in a STXM beamline it is generally preferred to have coherent illumination rather than a large beam diameter,

such as 100 to 500 μm. What has proven to be especially powerful is the coupling of spatial resolution with soft x-ray near-edge absorption spectroscopy in an approach termed *spectromicroscopy* [11.8.1] so that one can make nanoscale maps of chemical speciation for a number of low-Z elements for studies in biology, environmental science, polymer science, and a number of other fields. This requirement for high-quality spectroscopy drives the need for a high-energy resolution monochromator.

The classes of experiments which require rapidly switching source polarization but not a high degree of transverse spatial coherence, e.g., SXMCD, SXMLD, and PEEM, are generally based on flux-hungry techniques. Owing to the quest to measure ever smaller and ever more dilute samples, these techniques require ever smaller illuminated area. For example, modern PEEM end stations desire an illuminated spot size down to as small as 1 μm, thereby requiring the full brightness of an NSLS-II undulator source. At the same time, these classes of experiments require high, ~10^4, resolving power in order to provide selectivity among closely spaced (in photon energy) absorption features. The combined requirements of very high flux, high resolving power, small focused spot size, and rapid polarization switching make these experiments ideally suited to the undulator sources described in Chapter 8 and the beamline described here.

11.8.1 Soft X-Ray Spectromicroscopy

Scanning transmission x-ray microscopy with zone plate lenses was pioneered at NSLS by a group from Stony Brook led by Kirz [11.8.2]. The first instrument had a spatial resolution of about 300 nm, an energy resolution of about 1 eV, and a per-pixel dwell time of around 100 msec with a focused flux of 10^4 ph/s. Over twenty years, the Stony Brook group of Jacobsen, Kirz et al. have improved every figure of merit by one or more orders of magnitude simultaneously, while pioneering the development of various techniques of spectromicroscopy analysis. While the STXMs at NSLS beamline X1A continue to serve a vibrant community, STXMs at higher brightness soft x-ray sources such as the ALS have further improved the flux and energy tuning range.

The resolution that can be achieved in STXM is determined by three factors: the resolution of the optic, the resolution of the scanning system, and the radiation tolerance of the specimen. While the NSLS-II project proposes to push the development of multilayer Laue lenses (MLLs) and kinoform refractive lenses for the ultimate in image resolution with hard x-rays, these optics are not usable for soft x-rays due to absorption effects. Instead, all high-resolution STXMs employ Fresnel zone plate optics with finest outermost zone widths (and thus approximate spatial resolution) of 25 to 30 nm. As discussed in Chapter 12, there have been impressive recent demonstrations of 15 nm resolution soft x-ray zone plates; however, these zone plates had too small an efficiency and working distance to be usable in STXM. Instead, zone plate diameters of 100 to 500 μm are required to deliver a usable working distance for STXM experiments, and this requires the use of large-field-area electron beam lithography for optic fabrication. There is widespread consensus in the field that 10 nm resolution might be achievable in the coming years, though at that point sidescattering of even high-voltage electron beams in photoresists becomes the factor that limits the push to even finer zone widths. The extremely high brightness of an NSLS-II soft x-ray undulator should allow one to explore an alternative path toward achieving higher microscope resolution: the use of higher diffractive orders. For example, as one goes from first-order to third-order diffractive focusing in a zone plate, the resolution can, in principle, improve by a factor of three at a cost of a factor of 10 in focused flux. This loss of flux has been too severe, and the tradeoffs between optic diameter and focal length have been too daunting, for this to be exploited in present-day research, but with NSLS-II such a resolution/flux tradeoff might be more palatable.

A very attractive feature of the coherent scattering and imaging beamline is that the exit slit remains at a fixed position as the energy is tuned, yet its design is nearly aberration-free, so that high energy resolution is maintained. This is advantageous for STXM, because the beam must diverge from the exit slit to fill the aperture of the zone plate some distance away, where it is demagnified to a geometrical image that must be no larger than the diffraction-limited focus of the optic. By maintaining a constant exit slit position, this slit-to-zone plate distance can remain fixed as a function of photon energy.

The other two factors affecting ultimate resolution are the characteristics of the scanning system, and radiation tolerance of the specimen. While a STXM can benefit from the engineering of the hard x-ray nanoprobe end station described in Section 11.4, it will likely need to operate at considerably faster scanning speeds. The present-day NSLS STXM operates with pixel dwell times of about 1 msec, while the STXMs at ALS operate with 0.1 to 1 msec dwell times; in contrast, zone plate microprobes at APS typically operate with pixel dwell times of 0.1 to 1 seconds. (There are two reasons for the relative speed of soft x-ray STXMs over hard x-ray microprobes: the fact that spatially coherent flux scales as λ^2, and the fact that only a small fraction of incident photons get converted into fluorescent photons in hard x-ray microprobes). For NSLS-II, new scanning systems will need to be developed which can work with pixel dwell times as short as a microsecond. Indeed, the notion of "dwell time" is already inaccurate with present-day soft x-ray STXMs: they work not by stop-and-start motion of the specimen but by continuous scanning, with only the readout clocked at a specified pixel time. Even with this continuous scanning approach, the acceleration which the specimen undergoes in the "fast" scan direction will become more and more extreme at the turnaround point from each scanline. Possible solutions, such as double-mirror beam scanning systems similar to those used in confocal microscopy, bear consideration. We consider the scanning system speed and acceleration issues to be outstanding problems requiring further development.

Finally, radiation damage sets the ultimate limit on spatial resolution. The radiation exposure and thus dose needed to detect an object tends to increase as the fourth power of improvements in spatial resolution, so that it will become essential for a soft x-ray STXM to have cryo specimen capabilities for radiation sensitive specimens. Only one cryo STXM has been demonstrated, by the Stony Brook group; an improved version of this system will be key for exploiting the higher flux and tighter focus of a STXM at NSLS-II.

Ultimately, the growth of the x-ray microscopy user community is related to the straightforward understanding of the information delivered by the microscopes: "what you see is what you get." Such visualization depends on the spatial resolution of each microscope, allowing one to see in more or less detail the characteristics of the samples. The proof that this is a healthy, growing community is the fact that in the ALS five-year strategic plan presented in May 2006, two of the five beamlines that will be built or renovated in the next five years will feature microscopy-based instruments [11.8.3].

The NSLS-II soft x-ray beamline proposed here should provide higher brightness soft x-ray beams than are presently available, beams that are well-matched to the soft x-ray microscopes they will serve. The microscopy branch of the beamline proposed here will provide BNL with a 2013 state-of-the-art soft x-ray microscope. It will feature high spatial resolution with high photon flux at high resolving power and rapid-switching polarization, to serve the evolving needs of the NSLS-II scientific user community.

11.8.2 Coherent Scattering and Imaging

Coherence provides a known phase relationship between portions of a wavefield at different places across a specimen. This can be exploited to reveal patterns of long-range order in specimens, and to understand the dynamics of this ordering by correlation of the far-field diffraction intensity patterns acquired at various times. Fast point detectors can be used to explore short timescales, while area detectors can operate at much greater efficiency by collecting information from many "speckles" simultaneously. In addition, through the use of certain types of a priori knowledge of the specimen, the far-field intensity pattern can be inverted to yield a real-space image of the object.

Coherent scattering and imaging provides a simple benefit relative to the observation of real-space images using a lens: it dispenses with any of the limitations on resolution and transfer efficiency associated with lenses (which at present have a resolution limit of about 25 nm and an efficiency of about 10%). However, because coherent scattering and imaging provides a less direct measurement of real-space interactions in the specimen, its advantages are strongest when it is used to probe length scales finer than a lens can "see." As a result, coherent scattering and imaging experiments are generally performed with a requirement for purely coherent illumination over a field of view of only about 5 to 10 μm. In order to record the far-field diffraction

pattern at small scattering angles (as required for finite support image reconstruction, and measurements of long correlation distances), it is important to have the beam converge toward the detector so that the unscattered beam fills as few detector pixels as possible. As a result, while a STXM is best located several meters from an exit slit, a coherent scattering or imaging experiment is best done with the sample located essentially at the position of the exit slit or, even better, in an intermediate position between a coherence-preserving optic and a detector onto which an image of the exit slit is projected.

Because coherent scattering is well suited for studying micrometer-range correlations of nanostructure, it is of particular use for observing the dynamics of systems in response to a change in external condition. As an example, in the soft x-ray range one can study changes in thin-film magnetic media as a function of applied field, especially by working with circularly polarized radiation so as to exploit magnetic circular dichroism. The capability to control the magnetic field, temperature, stress/strain, and so on in the sample environment therefore becomes a key consideration in the design of the specimen chamber.

In diffraction microscopy or coherent x-ray diffraction imaging (CXDI), one seeks to obtain a real-space image of the object from its far-field diffraction intensity. This is fundamentally impossible due to the well-known phase problem unless one is able to compensate for the lack of experimental far-field phases in some way. The most common approach (used in remote sensing for nearly three decades) is to incorporate a priori knowledge of the specimen. The easiest is what is called a "finite support" constraint, which says that the specimen is known to fill only a small fraction of the illuminated region that contributes to the far-field diffraction pattern. This was first demonstrated for x-ray image reconstruction by Miao et al. [11.8.4] and there have been a number of important subsequent demonstrations by his group and others. At present the best 3D image resolution is 10×10×50 nm in soft x-ray experiments done by Chapman et al. [11.8.5] at ALS, and the first non-stained cell image has also been obtained there by the Stony Brook group [11.8.6]. Diffraction microscopy with hard x-rays allows one to image specific microcrystalline domains by recording diffraction not about the forward-scattered beam but diffraction about Bragg spots, and Pfeiffer et al. [11.8.7] have used this to map out strain in nanocrystals. Why then use soft x-rays with a longer wavelength and thus lower ultimate resolution? Because one needs a signal to be scattered at large angles, i.e., large momentum transfer, and soft x-rays undergo larger scattering from a given specimen size than hard x-rays do. As a result, it can be expected that one will use either the X-Ray Coherent Scattering Beamline described in Section 11.6, or this current beamline, depending on the total thickness and scattering strength of the specimen. By having both beamlines at hand, researchers at NSLS-II will be able to maximize the information they can obtain from any specimen through the use of diffraction microscopy.

11.8.3 Beamline Design

The scope of this beamline is to meet the need for soft x-ray spectromicroscopy, coherent imaging/scattering, and magnetic spectroscopy experiments to have the highest possible spatial resolution, high coherent flux (>10^{13} ph/s), high-energy resolving power, and rapid-switching polarization (linear, circular, or elliptical). These goals require the design of a coherence-preserving soft x-ray beamline that also provides the capability to switch rapidly between two polarization states. This beamline should also be able to provide the specific coherence, flux, and resolving power requirements of the potential target end stations: 1) transversely coherent illumination of large-diameter (100–500 μm) zone plates in a STXM end station, in order to reach optic-limited spatial resolution, 2) high coherent flux density delivered in a low-divergence beam with small (few μm) diameter for an imaging/scattering end station, and 3) very high flux in a ~1 μm spot for a polarization-sensitive soft x-ray spectroscopy end station. For all of these end stations/programs, it is our intent to reach photon energy resolving power of ~10.000 over the entire energy range.

11.8.3.1 Scope

This beamline will be designed to meet the needs of soft x-ray microscopy, coherent imaging/scattering, and magnetic spectroscopy experiments. To meet the goals anticipated for these experiments in 2013, the

beamline will need to provide very high coherent flux, $>10^{13}$ ph/s with spatial requirements described above, at a resolving power of 10^4 over the 200–2000 eV photon energy range, with rapid-switching polarization capability. The beamline we propose to meet these challenging goals is described in some detail below. It is served by a 4 m long elliptically polarized soft x-ray undulator that produces a brightness $>10^{20}$ ph/s/0.1%BW/mm^2/mrad^2 (see Chapter 8) over the 200–2000 eV photon energy range.

In addition to high flux and high resolving power, the beamline is designed to deliver beams of two distinct polarization states to a common focal spot, as provided by two canted (by ~0.25 mrad) 2 m long elliptically polarized undulators (EPUs) (see Chapter 8). These polarizations can be any that can be produced by the EPUs, which include circular, elliptical, and linear (along any in-plane axis). The beamline will provide the capability to rapidly switch the polarization between the polarizations states of the two EPUs, e.g., between σ and π linear polarization or between left and right circular polarization. The beamline design includes the capability to switch between the two selected polarization states, thereby enabling dichroism experiments to be performed under fixed sample conditions. Since the polarization switching is performed mechanically (chopper), the rate of switching can be high (up to kHz range), thereby significantly increasing the sensitivity of dichrosim measurements via phase-sensitive detection schemes. Rapid-switching polarization and phase-sensitive detection are crucial for detection of small dichroic signals, e.g., from low-cross-section processes or from small elemental concentrations in materials. The addition of rapid-switching polarization modulation capability to the flux, resolving power, and spot size properties of the proposed soft x-ray beamline will make it unique among existing DOE facilities.

In this beamline design, we pursue the goal of designing a beamline with the capabilities and the flexibility to perform state-of-the-art, highly demanding microscopy, coherent scattering/imaging, and magnetic spectroscopy experiments in the year 2013. These experiments require simultaneously high brightness, high photon flux, high energy resolution, and polarization modulation.

11.8.3.2 Choice of Fast-Switching EPW vs. Canted EPUs

We propose that this beamline be able to deliver two fast-switching polarization-modulated (e.g., left and right circularly polarized, or horizontal and vertical linearly polarized) beams of soft x-rays to a common focal spot. The soft x-ray polarization modulation can be produced by two main schemes. The first is the use of an electromagnetic insertion device that switches the polarization of the x-rays by changing the polarity of the current passing through the appropriate sets of magnets. The second scheme is the use of two identical insertion devices canted at an angle that allows the modulation of the soft x-rays to take place in space. This is the option taken by BESSY-II and SLS and recently also at SPring-8. Each of the two canted devices delivers one type of polarization, and the selection of the polarization takes place downstream of the beamline with a chopper. The chopper drives the switching frequency of the measurements.

Both polarization modulation schemes require a chopper to “clean” unwanted radiation from the signal. NSLS has a long experience in fast switching polarization experiments using an Elliptically Polarizing Wiggler. At present, the fast switching frequency of the NSLS EPW is 22 Hz, and an effort is ongoing to increase it up to 100 Hz [11.8.8]. We propose selecting the option with two canted insertion devices at NSLS-II. Electron beam stability is a critical goal of the NSLS-II storage ring and an electromagnet-based device could introduce beam instabilities via the constantly changing current in the electromagnets. The scheme based on two canted insertion devices involves canting the electron orbit but this orbit, when implemented, is time independent. Furthermore, the canted undulator scheme is capable of supporting much higher polarization switching rate than is the EPW scheme, owing to inductance-related limits on the ability to drive an electromagnet with a square-wave programming input.

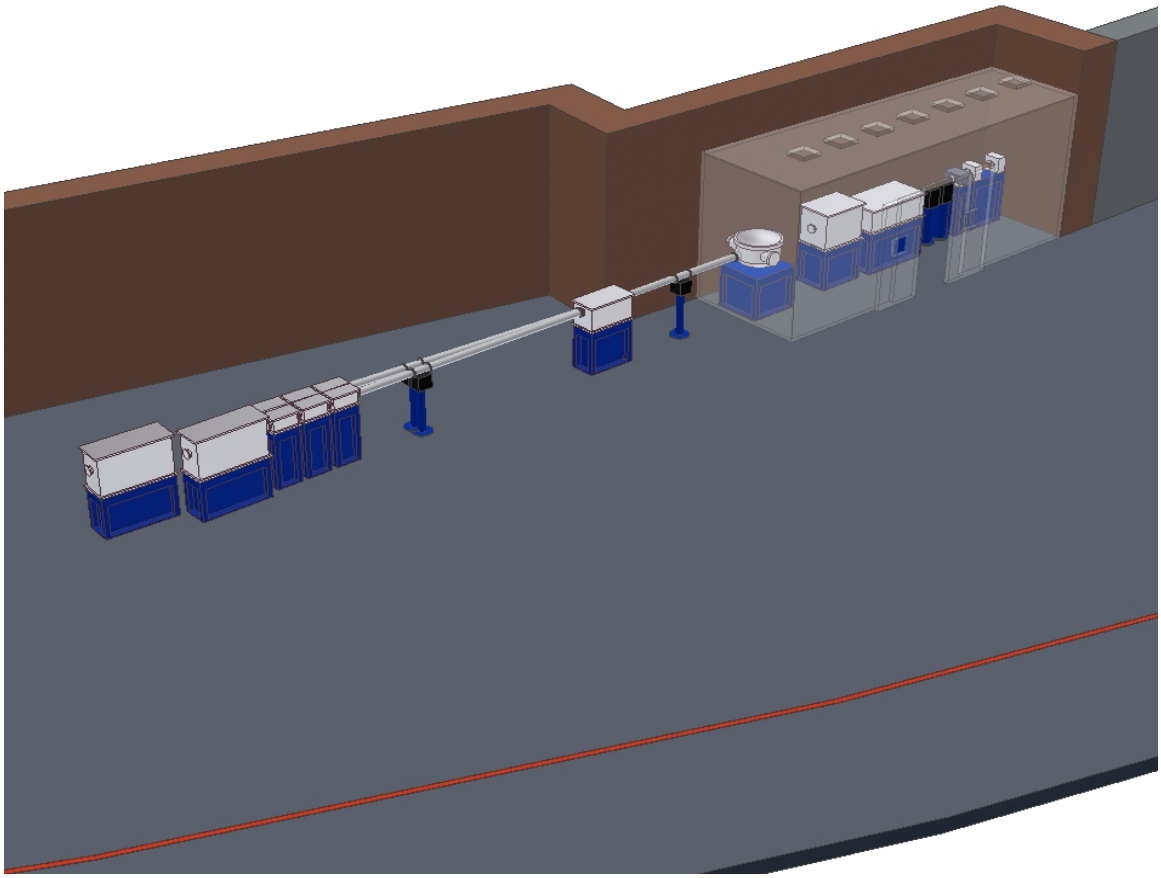

Figure11.8.1 Preliminary layout of soft x-ray beamline for soft x-ray coherent scattering, imaging, and spectroscopy.

11.8.3.3 Beamline Design

This section describes the optical design and the expected performance of a soft x-ray beamline optimized for coherent scattering, imaging, and spectroscopy. The source for this beamline would be the EPU45 elliptically polarized undulator described in Chapter 8. Two 2 m EPU45 undulators would be installed in a 5 m long ID straight section with provision for horizontal canting of the beams passing through the two EPU45s by an angle of 0.25 mrad or less. The two undulators could be operated, with proper phasing, as a single unit, providing horizontal, vertical, or circular polarized light, or independently, to provide two different polarizations for fast-switching dichroism experiments.

An alternative choice of ID straight section is an 8 m long ID. This choice would allow the undulator length to grow, but at the expense of larger source size owing to the larger beta function values in the 8 m ID straight compared to the 5 m IDs. Since the opening angles, both horizontal and vertical, of the electron beam in either the 5 m or 8 m ID straights is less than the diffraction-limited photon divergence angle, there is no angular divergence benefit to larger beta function for soft x-ray beamlines at NSLS-II. Therefore, we have chosen the 5 m ID straight sections for the soft x-ray beamlines, in order to provide the smallest possible focal spots on sample (or on other end station pinholes or focusing optics). One could envision providing the same spot size and flux using undulators in an 8 m ID straight, but only by fabricating longer undulators than proposed here and then throwing away photons spatially (via baffles or apertures), which is wasteful and not necessary.

The major components of this Soft X-ray Beamline monochromator design would be a cooled cylindrical first mirror, variable line spacing plane gratings (VLSPG), *no* entrance slit, and plane elliptical KB-type post-focusing mirrors. The beamline would be optimized for the energy range between 200 eV and 2.3 keV.

State-of-the-art optical elements would be required in order to simultaneously produce the very high flux, high photon energy resolution, and small focused spot size. A soft x-ray beamline would achieve a resolving power ~1.8×10^4 at 1 keV with a 10 μm exit slit width, if RMS slope errors of 0.1 μrad can be achieved over ≈100 mm usable meridional dimension on the plane optical elements. A spot size with FWHM of less than 5×5 μm^2 requires RMS slope errors of approximately 0.5 μrad along the meridional direction on the sagittal cylinder and the elliptical cylinders used in the proposed design. These mirror figure requirements are beyond the current state of the art and will therefore require research and development.

In the proposed soft x-ray beamline, ~4×10^{12} ph/s will illuminate a spot with FWHM of less than 6×4 μm^2 (hor×ver.) at 1 keV within a bandwidth of 56 meV (~18,000 resolving power). The calculated flux at 1 keV increases by an order of magnitude with a different grating delivering a resolving power of 4500 to the same spot size.

11.8.3.4 Beamline Optics

The requirements for the highest possible resolution and a fixed exit slit over a broad energy range can be fulfilled with the collimated plane grating monochromator proposed by Follath et al. [11.8.9]. Its optical design includes a horizontally deflecting toroidal mirror that collimates along the vertical (dispersion direction) and focuses the beam horizontally at the exit slit. The vertically collimated beam is deflected (vertically) by a plane mirror illuminating the plane grating at an angle of incidence α. The beam dispersed by the grating, at an angle β, is focused onto the exit slit plane by a sagittally focusing cylindrical mirror. The collimation along the dispersion direction allows operation of the monochromator at different values of c (=cosβ/cosα) by means of choosing the appropriate angle of incidence on the plane mirror. Large c values are used to improve resolution at the expense of flux. The CPGM design is almost aberration-free. The major contributions to its wavelength resolution are:

$$\Delta\lambda_{so} = \frac{2.7\,\Sigma_y \cos\alpha}{n\,k\,r_1}, \tag{11.8-1}$$

$$\Delta\lambda_{ex} = \frac{s\cos\beta}{n\,k\,r_2}, \tag{11.8-2}$$

$$\Delta\lambda_{Gr} = \frac{5.4\,\sigma_{Gr}}{n\,k}\cos\left(\frac{\alpha+\beta}{2}\right)\cos\left(\frac{\alpha-\beta}{2}\right), \tag{11.8-3}$$

and

$$\Delta\lambda_{PM} = \frac{5.4\,\sigma_{PM}\cos\alpha}{n\,k}, \tag{11.8-4}$$

where the suffixes on Δλ refer to the source (*so*), the exit slit (*ex*), the grating (*Gr*), and the plane mirror (*PM*). In these equations, Σ_y is the RMS vertical source size, n is the diffraction order, k the grating line density, r_1 the distance from the source to the toroidal mirror, s the slit width, r_2 the distance from the refocusing mirror to the exit slit, and σ_{Gr} and σ_{PM} the RMS meridional slope errors on the grating and plane mirror, respectively.

The slope errors on the collimating and refocusing mirrors also affect the resolution. However, their effect is very small due to the large "forgiveness factor," the cosine of the angle of normal incidence on the mirror.

Some of the experimental stations to be installed at the end of the soft x-ray beamlines at NSLS-II require a spot size in the micrometer range. Along the vertical direction this can be easily achieved with an elliptical cylinder that demagnifies the exit slit width. Since the RMS horizontal size of the photon beam varies between 54 and 41 μm in the energy range 200-2500 eV, a demagnification of ≈2.35×50/5 =23.5 is required to obtain a horizontal spot size of 5 μm FWHM. In the CPGM, the horizontal demagnification of the source onto the slit is approximately one. Therefore, the demagnification in this design needs to take place in between the slit and the sample. However, the requirement for a distance of ≈700 mm between the sample and the end of the refocusing mirror means that the entrance arm of the horizontally refocusing mirror needs to be larger than 10 m, which is impractical.

The very small horizontal divergence of the beam expected from a 4 m long insertion device in a 5 m straight section of NSLS-II, 32 μrad RMS at 200 eV, allows for a solution in which the beam diverges up to an elliptical cylinder located after the exit slit. This mirror then demagnifies the horizontal source down a few microns. One could implement this in the CPGM by replacing the toroidal mirror with a sagittal cylinder that provides the grating with a collimated beam along the dispersion direction. Unfortunately, the illumination of the refocusing cylinder after the grating by a divergent horizontal beam results in a large astigmatic coma aberration that reduces significantly the monochromator resolution.

The proposed monochromator [11.8.10] uses a sagittal cylindrical mirror to collimate the beam along the vertical (dispersion) direction. The following optical element is a plane mirror that illuminates a variable line spacing (VLS) plane grating. The line density of the grating is given by $k(w) = k_0 + 2b_2 w + 3b_3 w^2 \ldots$, where w=0 is at the grating center and positive towards the exit slit. The linear coefficient term, b_2, can be chosen to zero the defocus term in the optical path function at a single wavelength,

$$f_{20} = \frac{\cos^2 \beta}{dGrEx} + 2 b_2 n k \lambda, \tag{11.8-5}$$

whereas b_3 can be chosen to zero the coma term in the optical path function, i.e.,

$$f_{30} = \sin\beta \frac{\cos^2 \beta}{dGrEx^2} + 2 b_3 n k \lambda, \tag{11.8-6}$$

also at a single wavelength. In Eqs. 11.8-5 and 11.8-6, *dGrEx* is the distance between the grating and the exit slit. The important point in this design is the fact that the plane mirror can be used to zero f_{20} for all wavelengths by illuminating the grating at the required angle of incidence. Note that this design has one less mirror than the CPGM, owing to the meridional focusing provided by the VLS plane grating.

Eqs. 11.8-1–11.8-4 also give the contributions to the wavelength resolution in the proposed design with r_1 being the distance from the source to the cylindrical mirror and by replacing r_2 with *dGrEx*.

11.8.3.5 Source

The undulator source for this beamline will be two canted soft x-ray EPUs, as described in Chapter 8. Either the EPU42 or the EPU45 will be chosen, depending on allowed magnetic gap considerations not finalized at the time of the writing of this document. Here we will assume an EPU42 source, but the baseline EPU45 device will provide similar performance. The EPU42 soft x-ray undulators cover the energy range between 200 and 2000 eV with pure circular polarization, and a larger energy range with linear polarization. In canted mode, the two undulators will generally be set to different polarizations, and a fast-switching chopper will be used to alternate the polarization delivered to the sample. In un-canted mode, the two

undulators are set to the same polarization and, if properly phased (e.g., by use of a "modulator" between the two devices), will act as a single long undulator.

The machine parameters, the RMS electron beam sizes and divergences, and the insertion device parameters used in the calculations are listed in Tables 11.8.1 and 11.8.2.

Table 11.8.1 Machine Parameters Used in the Calculations.

Energy (GeV)	3.0
Current (mA)	500
σ_x (μm)	40.2
σ_y (μm)	1.7
$\sigma_{x'}$ (μrad)	14.9
$\sigma_{y'}$ (μrad)	1.8

Table 11.8.2 ID Parameters Used in the Calculations.

	Soft X-ray Beamline II
ID type	2 x APPLE-II EPU
Length of each ID (mm)	2000
Period length (mm)	42

Figure 11.8.2 shows the flux emitted in the central cone by the two insertion devices with a 4 mm period when operated in phase to deliver linear polarized radiation.

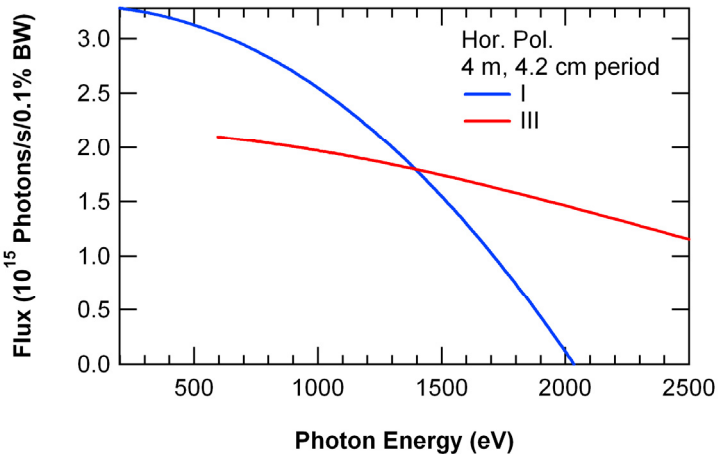

Figure 11.8.2 Flux emitted in the central cone by a 4 m ID linear device with a 4.2 cm period, as a function of photon energy.

The total sizes and divergences used in the calculations were obtained as the vector sum of the electron beam parameters and the RMS values of the photon beam were calculated using $\sigma_r = \sqrt{2\lambda L}/2\pi$ and $\sigma_\rho = \sqrt{\lambda/2L}$, where L is the undulator length and λ the radiation wavelength [11.8.11].

11.8.3.6 Beamline Layout

A soft x-ray beamline for imaging and coherent scattering requires very high flux, and spot sizes at the experimental stations in the micron range. The proposed monochromator can fulfill these requirements. To achieve high flux at good, but not the highest possible, energy resolution, the distance between the gratings and the exit slit is relatively short (~10 m) and low-line-density gratings are chosen. A cartoon of the proposed beamline is shown in Figure 11.8.3, with parameters listed in Table 11.8.3.

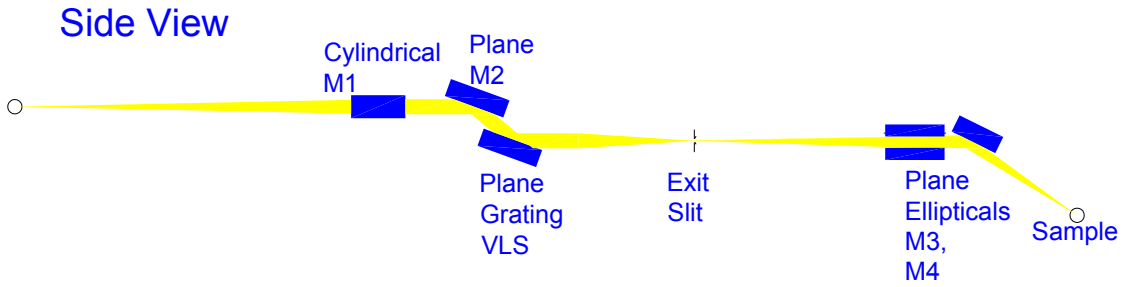

Figure 11.8.3 Sketch of a possible soft x-ray microscopy, coherent imaging/scattering, and magnetic spectroscopy beamline.

Table 11.8.3 Distance from the Source, Angle of Incidence, and Deflection of the Optical Components for a Soft X-Ray Beamline for Imaging and Coherent Scattering.

Element	Distance (mm)	Angle (deg)	Deflection
M1- Sagittal Cylinder	28000	88.75	horizontal
M2- Plane	29611-29944	82.4-88.9	vertical
Gr – Grating	≈30000.	86.4- 89.6	vertical
Slit	40000		
M3 - Plane Elliptical	41200	88.5	horizontal
M4 – Plane Elliptical	41700	88.5	vertical
Sample	42500		

There is space between the shield wall (25 m from the undulator source) and M1 to insert an experimental station to host coherent experiments that are illuminated directly by the undulator source, with no optics in between to degrade the coherence of the beam.

11.8.3.6.1 First Mirror

The first element in the beamline is a sagittal cylindrical mirror located at 28 m from the source, outside the shield wall. The angle of normal incidence in this mirror (as well as that of M3 and M4) is determined as a compromise between the highest possible reflectivity in the energy range covered by this beamline and a reasonable mirror length. Figure 11.8.4 shows a small set of the calculations performed [11.8.12] to determine the angle of incidence and the coating material on the mirrors. An angle of incidence of 88.75° and a 30 nm coating of Au over the Si substrate were chosen. As Figure 11.8.4 shows, the selected parameters provide good reflectivity up to 2.2 keV. Note that at this angle of incidence, the s- and p-reflectivities are almost identical. Therefore, the beamline will not distort circular polarized radiation.

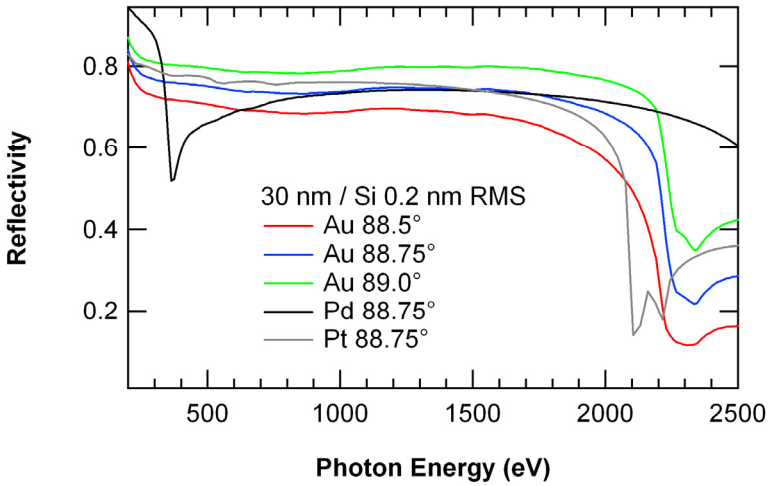

Figure 11.8.4 Reflectivities of possible coatings for s polarized light as a function of the photon energy. The substrate is Si and the coating is 30 nm thick. The RMS surface roughness is 0.2 nm.

11.8.3.6.2 Monochromator

The second optical element is the plane mirror that provides the required angle of incidence to the grating necessary to keep the selected energy in focus at the exit slit. The mechanical principle used in the PGM [11.8.13] can be used to achieve the required movements. The resolution in angle required in the current design[1] is 0.03 μrad for the grating and 0.05 μrad for the plane mirror. These values are very close to the resolution of the angular encoder used in the CPGM (0.04 μrad).

Since the angle of incidence on the mirror for a given VLS grating is determined by the focusing condition and the grating equation at that energy, it is advantageous to have at least three gratings that allow trading off resolution for flux while keeping a fixed exit slit width.

For this beamline we have chosen three gratings: One for ultra high flux (UHF), one for high flux and good resolution (HF), and one for high resolution (HR). The parameters of the chosen gratings are listed in Table 11.8.4 assuming that the distance from the grating to the exit slit is 10 m. The gratings are operated in the +1 diffraction order.

Table 11.8.4 Parameters of the Gratings for a Soft X-Ray Beamline for Imaging and Coherent Imaging/Scattering.

	UHF	HF	HR
k_0 [mm^{-1}]	150	400	1200
b_2 [mm^{-2}]	1.7991×10^{-4}	1.7977×10^{-4}	1.2576×10^{-4}
b_3 [mm^{-3}]	1.80×10^{-8}	1.80×10^{-8}	1.25×10^{-8}
C	≈1.5	≈1.5	≈2.2

The resolving power expected with these gratings when using a 10 μm exit slit width is shown in the upper panel of Figure 11.8.5. The HR grating will provide a resolving power higher than 10^4 in the full energy range, whereas the UHF grating resolving power is better than 4000 up to 1.7 keV.

[1] Obtained by requiring five scanning steps at the highest resolution.

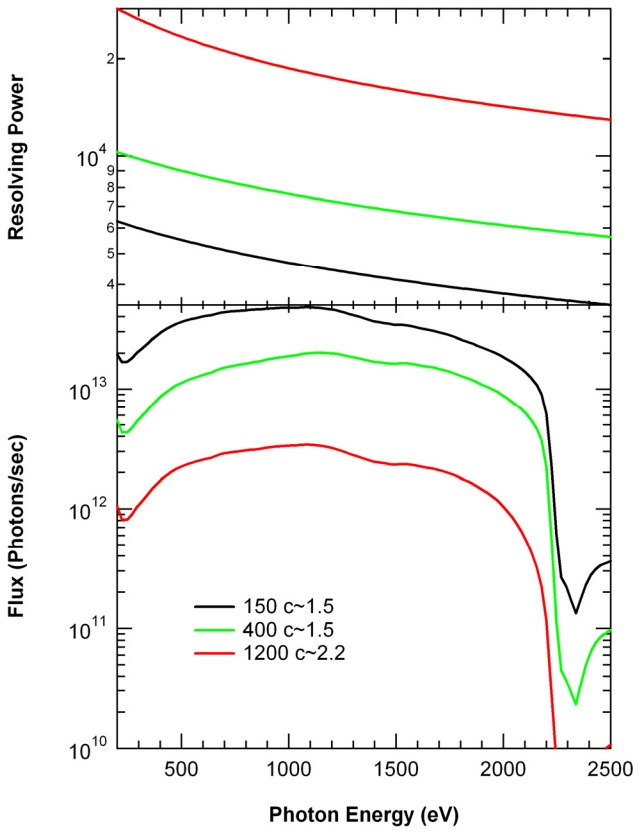

Figure 11.8.5 (upper panel) Flux expected at the sample position of a soft x-ray imaging, coherent scattering, and spectroscopy beamline with a 10 μm exit slit width and three gratings.

(lower panel) Flux and corresponding resolving power of a soft x-ray imaging, coherent scattering, and spectroscopy beamline with a 10 μm exit slit width and three gratings.

The ability to tune this monochromator to zero order is important for certain experiments envisioned for this beamline, as well as for setup and alignment. Since the VLS gratings provide vertical focusing only at soft x-ray wavelengths, the zero-order counterpart would be a vertically focusing mirror. Such a mirror could be provided as an additional in-vacuum-selectable choice in a multiple-grating instrument. Heat loading issues should be considered for components downstream of the monochromator, e.g., the exit slit, which could be illuminated by the intense focused zero-order light.

11.8.3.6.3 Refocusing Mirrors

The refocusing onto the sample is performed with two elliptical cylindrical mirrors. The first one (M3) is the horizontally refocusing mirror located at a distance of 41,200 mm from the source and has a nominal demagnification of 32. The vertically refocusing mirror M4 is 0.5 m downstream of M3 and demagnifies the slit width by a factor of 2.1. The angle of incidence on both mirrors is 88.75°.

11.8.3.6.4 Flux

The efficiencies of the gratings for this beamline were optimized for blazed groove profiles. The resulting blaze angle for the 150 l/mm grating is 0.3°, that of the 400 l/mm grating is 0.45°, and that for the 1200 l/mm grating is 1.0°.

The total flux expected at the sample position with a 10 μm exit slit width is presented in the lower panel of Figure 11.8.5. For the high-flux (HF) grating, more than 1.5×10^{13} ph/s are expected at the sample at a resolving power higher than 4000 for energies between 200 eV and 1.7 keV.

11.8.3.6.5 Ray Tracings

The ray tracings were performed using the Shadow code [11.8.14]. The caption above each spot pattern gives the RMS beam sizes and divergences along the horizontal and vertical directions. The y coordinate is along the dispersion direction at the exit slit and sample position and along the length of the optical elements. Slope errors (0.1 μrad RMS along the meridional direction of the plane elements and 0.5 μrad RMS along the meridional direction of the other optical elements) were included in the ray tracings by assuming a sinusoidal variation on the optical elements surface. All the ray tracings were performed with the source sizes and divergences shown in Table 11.8.1.

Figure 11.8.6 shows the spot pattern at the cylindrical mirror when illuminated with 200 eV photons. As seen in this figure, a 300 mm long mirror accepts most of the central cone radiation emitted by the undulator at this energy.

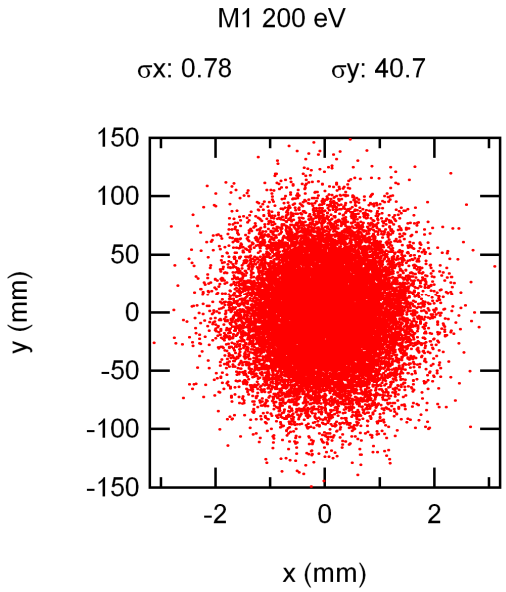

Figure 11.8.6 Spot pattern at M1 for 200 eV, for the soft x-ray coherent scattering, imaging, and spectroscopy beamline.

The illumination of the plane pre-mirror determines that its minimum dimensions are approximately 7 mm wide by 400 mm long. In contrast, the gratings need to be less than 100 mm long. An exit slit length of ~8 mm is required to let through the horizontally diverging beam. The illumination of the refocusing elliptical cylinders determines that the horizontally focusing mirror needs to be at least 300 mm long and the vertically focusing mirror needs to be less than 80 mm long.

As was demonstrated with ray traces for the soft x-ray monochromator in Section 11.7, the resolution of the monochromator for this soft x-ray beamline can be shown to match the analytically determined values shown in Figure 11.8.5.

The RMS horizontal and vertical sizes and divergences values obtained by ray tracing are consistent with the values obtained from the vector sum of tthehe source parameters (slit for the vertical size) modified by the corresponding magnification and the contributions due to the assumed slope errors. The expected RMS sizes at the sample are 2.3 μm horizontal and 1.6 μm vertical. The largest vertical RMS divergence at the sample, less than 0.5 mrad, will occur when the HR grating is used at 200 eV.

11.8.3.6.6 Canted IDs

In this mode of operation, the horizontal angle between the electron beam and the undulators' axes should be as small as possible to keep a reasonable exit slit length. On the other hand, the angle should be large enough that there is a minimal overlap between the two beams. We chose 0.17 mrad for the separation between the two beams, which corresponds to four times the 1-σ RMS divergence at 200 eV. Two sagittal

cylindrical mirrors, designed to collimate along the vertical direction its respective source, replace M1. This ensures that the two beams will be focused vertically at the exit slit, i.e., the photon energy of the two beams will be the same; but implies that the resolution of the far beam (upstream undulator) is a few percent better than that of the closer beam. The horizontally focusing M3 elliptical cylinder mirror focusing also needs to be replaced with two elliptical cylinder mirrorrs when operating in the canted mode. The mirror refocusing the beam from the upstream undulator is designed to be slightly out of focus to obtain approximately the same horizontal beam sizes, one from each of the two M3 mirrors, at the sample position.

Section 11.7.2.4 details the ray tracing results for 200 eV photon energy with the high resolution grating. The corresponding ray traces for the Soft X-Ray Coherent Scattering, Imaging, and Spectroscopy Beamline will be similar, and will be carried out as part of the NSLS-II Title I effort. At 200 eV photon energy, the "contamination" of the radiation from the upstream undulator on the downstream beam is less than 2.5%. See Figure 11.8.7, which presents the illumination spot diagrams for the near and far EPU beams on the M1 cylindrical mirrors.

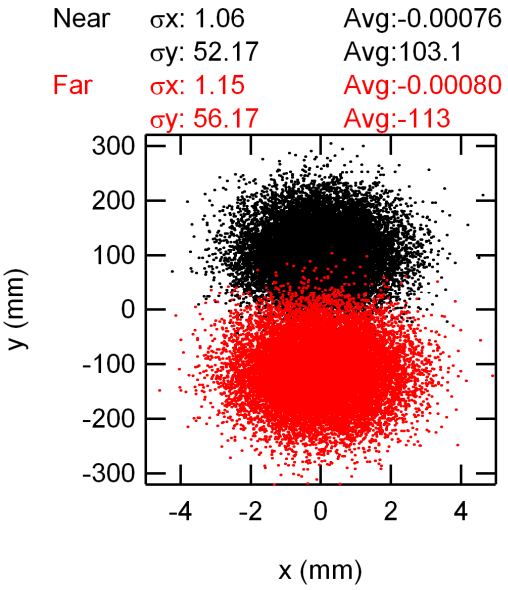

Figure 11.8.7 Illumination of the near and far M1 mirrors at 200 eV for the coherent imaging, scattering, and spectroscopy beamline.

This "contamination" value decreases to nearly zero at 1 keV, and can be practically eliminated at the expense of some flux at lowest photon energies by having a gap of 80 mm between the two M1 mirrors. This will reduce the flux at 200 eV by approximately 10% but will reduce the contamination to less than 0.3%. Practically no flux is lost for energies higher than 1 keV. With the above mentioned separation between the M1 mirrors, their length should be 240 mm, the plane mirror and the grating wider than 16 mm, each M3 at least 240 mm long, and the exit slit length 15 mm. The exit slit length is rather large, given the requirement of identical opening (to better than ~0.5 μm) across the entire 15mm length; the slit blades also must be aligned parallel to the floor to better than a ~20 microradians. Sample illumination spot diagrams for the far and near beams at 200eV photon energy are shown in Figure 11.8.8. The horizontal and vertical dimensions of both beams are identical to two significant figures and overlap to better than 0.02 μm.

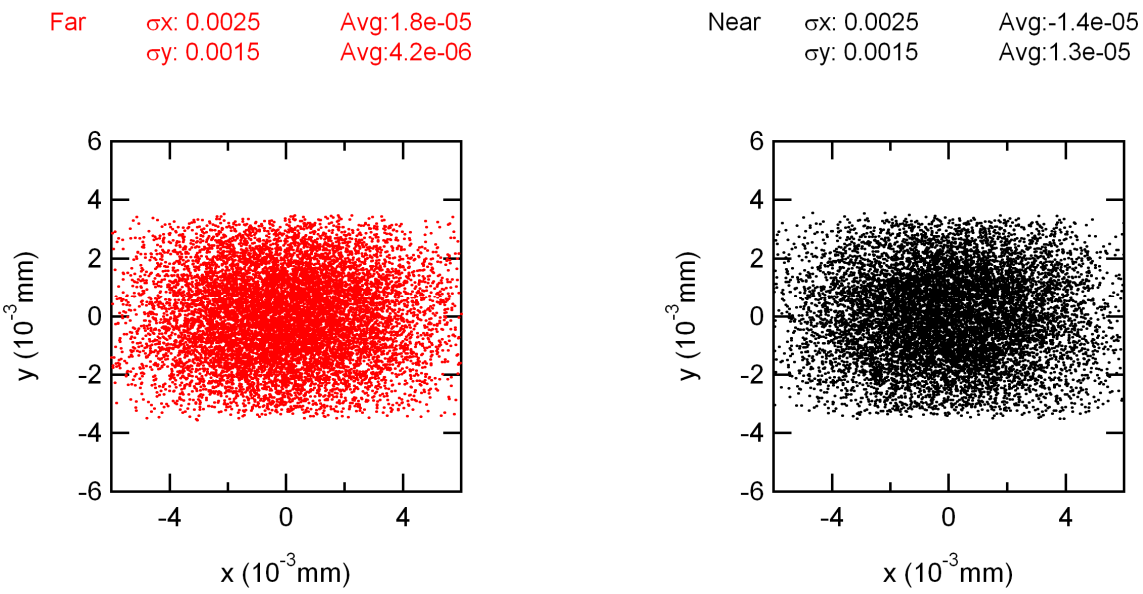

Figure 11.8.8 Sample illumination with the far beam (left) and near beam (right) at 200 eV for the coherent imaging, scattering, and spectroscopy beamline.

11.8.3.6.7 Polarization Selection: Variable Apertures and Chopper

The beamline would have variable-opening white beam apertures to define the sizes, and therefore intensities, of the polarized beams from the two canted undulators. A fast-switching, up to a few kHz, mechanical chopper would be installed downstream of these apertures, to alternately select one of the two polarized beams. The apertures and chopper could be located anywhere along the beamline, but would likely be located after the monochromator to minimize power loading issues. The horizontal location of the apertures and chopper would need to be precisely controlled to eliminate any overlapping polarized beams.

11.8.3.6.8 Calculated Power

The calculated power absorbed by the first three optical elements when the two IDs are phased tuned to emit linear horizontally polarized radiation at 200 eV is similar to the power distributions shown for the other proposed soft x-ray beamline (Section 11.7.2.4). The maximum power density absorbed by M1 is 1.2 W/mm^2 and the total power is almost 1 kW. The corresponding values for the plane mirror will also be close to those calculated for the soft x-ray XRMS/RIXS beamline: 0.56 W/mm^2 and less than 100 W. The power and power density absorbed by the grating in this case are very small.

The cooling scheme for M1 needs to ensure that the heat-induced meridional RMS slope errors in M1 are below 0.5μrad. In the case of the plane mirror, a novel cooling design should be developed to preserve the high resolving power. The development of such a cooling scheme will require iterations of FEA and ray tracings performed with the calculated surface deformation.

11.8.3.6.9 Vacuum Issues

A soft x-ray beamline for resonant scattering and imaging would be windowless (i.e., would share ultra high vacuum with the NSLS-II storage ring). All of its components would be UHV-compatible, including all of the end station components. As is the case for all UHV beamlines, this beamline would be divided into sections separated from each other by metal-sealed UHV gate valves. These valves would be part of the equipment protection system, acting to isolate beamline components from each other or the storage ring if the

constantly monitored vacuum readings rise above a maximum permitted level. The beamline would have approximately 15 sections, some of which require extra pumping speed owing to high undulator head loads and large total surface area of components.

Beam position (BPM) and intensity (I_0) monitors, as well as polarization ratio monitors, would be required upstream of each end station. The small lateral spatial dimensions of the beams would be a challenge for positioning all of these monitoring devices.

11.8.3.6.10 End Stations

As described in the introduction to this section, we anticipate this beamline will have two end stations, to be determined based on user input and demand, among three or more possible choices: 1) an end station optimized for scanning transmission x-ray microscopy, 2) an end station optimized for coherent scattering and imaging, and 3) an end station optimized for rapid-switching polarization-sensitive spectroscopies, including SXMCD, SXMLD, and PEEM. It is likely that the two chosen branch lines will experience heavy demand; why then put two end stations on one beamline when beam-sharing is precluded by the small phase space of the NSLS-II beam at soft x-ray wavelengths? The best experiments involve a combination of sample preparation, data collection, and on-line analysis; consequently, user productivity with 24 hour access to an experiment is not twice what it is with 12 hour access. If both end stations can be left with the specimen in place during the off-hours, and if experiment changeover can be made rapid, reliable, and reproducible such as by using a well-engineered switching mirror, then two different end stations can be accommodated with high productivity from each.

Based on user demand at the STXMs at the present-day NSLS, at the ALS, and elsewhere, it is reasonable to expect that NSLS-II will have several STXMs around the facility, since even the NSLS-II bending magnets are very bright sources and can be used for coherent soft x-ray experiments with appropriate spatial filtering. As a result, it is conceivable that NSLS-II will host one STXM optimized for handling room temperature specimens at atmospheric pressure for convenience and for the ability to work with specimens in wet chambers, another optimized for studies of frozen hydrated specimens in vacuum and at liquid nitrogen temperature, and another that is configured with various switchable fields for studies of magnetism. The current choice for the soft x-ray undulator beamline proposed here is a room temperature STXM with specimen at atmospheric pressure. Much of the engineering of this end station can be done in common with the Hard X-ray Nanoprobe described in Section 11.4. However, as noted above, a STXM is likely to require significantly faster scanning speeds than the hard x-ray nanoprobe will, and these engineering challenges must be addressed in the end station design. Fortunately an excellent base of experience exists based on the STXMs now operating at NSLS and ALS.

The same might be said of end stations for coherent scattering and imaging: there may ultimately be more than one beamline able to do these experiments at NSLS-II. One or more of there may be optimized for magnetic specimens while others are optimized for frozen hydrated biological specimens at liquid nitrogen temperature. The current choice for the soft x-ray undulator beamline proposed here is a chamber optimized for studies of magnetism, with a load lock for sample insertion and removal in a high vacuum environment, provision for ~1T magnetization of the sample along any axis (esp. in-plane and out-of-plane), and rapid energy tunability.

Since the STXM and coherent scattering experiments will work with a nearly fully coherent beam, there is no built-in tolerance to beam motion that would otherwise be provided by “overfilling” limiting apertures or focusing optics. For this reason, it is essential that the beamline have full diagnostics on the beam position and flux at multiple locations. For polarization-sensitive measurements, e.g., of magnetic samples, it is also crucial to monitor the beam polarization accurately. It is only with proper diagnostics that one can troubleshoot problems in flux variation or resolution loss in coherence experiments, variations that can otherwise render the data from an experiment worthless for quantitative analysis.

The key parameters for rapid-switching polarization-sensitive spectroscopy are well-defined, stable polarization of the beams from the two canted undulators and as close as possible to 100% overlap of the two polarized beams at the sample position. The development and characterization of diagnostics for these purposes, both in the ID straight section where the canting takes place, and in the beamline where the chopper provides the time-dependent polarization modulation, is crucial to the success of all of the spectroscopy end station experiments.

11.8.3.6.11 Alternatives to the Design

To maximize utilization of this flagship beamline, we propose to leave two well-engineered end stations more or less permanently in place, so that scientists can rely on a constant, always-aligned apparatus for carrying out their experiments. At the same time, one can expect that some dedicated users will bring their own end station equipment for specialized experiments. Experiments of this type surely need to be accommodated at NSLS-II. One alternative to the above design is to add a third, mirror-switchable end station to the beamline. Given the space constraints of fitting two permanent end stations around a small separation angle at the end of the beamline, this may be of questionable utility but this may change based on proposals received.

11.8.4 Detectors

Detectors for scanning transmission x-ray microscopy (STXM) must be able to handle high transmitted flux signal levels with fast readout time, since per-pixel dwell times might be as fast as a microsecond. Segmentation is also important to provide the ability to record dark field images from strongly scattering objects (such as immunogold labels in biological specimens), and to sense phase contrast, which provides a way to detect molecular resonances with less radiation damage than absorption contrast involves. Fortunately, a collaborative effort between Brookhaven, Stony Brook, and the Max Planck Institute silicon lab has already produced detectors that are able to perform these roles at sub-millisecond dwell times. With further development, it should be possible to have new versions of these detectors that are able to work at the microsecond dwell times anticipated for STXM research at NSLS-II. Additional detector capabilities that should be developed include total electron yield detectors when working with a sample at high vacuum, and visible light detectors for luminescence studies.

Coherent scattering and imaging place a different set of demands on detector performance. The preferred situation is to collect a large 2D measurement of scattered intensity, such as in a large-pixel-count area detector with at least 1024^2 but ultimately 2048^2 or even 4096^2 pixels. Because the scattered signal can be strongly concentrated near the forward direction for most specimens, a detector with very high dynamic range (or, alternatively, fast, low-noise readout to gain dynamic range through multiple signal measurements) is required. Backside-thinned, direct detection CCD cameras presently serve as the main detector for soft x-ray coherent scattering and imaging experiments, but they leave much to be desired both in terms of dynamic range (typically only around 10^3:1) and readout time (typically many seconds for low-noise operation). A much more promising approach is to use pixel array detectors with on-detector processing of the signal to provide high dynamic range and rapid readout time. Again, such detectors are already being developed at Brookhaven, so there is considerable in-house expertise to draw upon. For experiments exploring the fastest possible correlation times, one may instead turn to a speckle-sized aperture in front of a small area detector to record intensity fluctuations at a single location in the scattering plane. Several such detectors can be used to gain additional signal, but never to the same value as provided by a fast-readout area detector such as a pixel array detector.

11.8.5 Laboratory Space

The laboratory requirements for applications of soft x-ray microscopy and coherent dynamics are determined largely by those of the different application areas. For biology and environmental science, access to a nearby wet lab is essential, with fume hoods and wet chemical mixing areas, oxygen-free glove boxes for the study of anaerobic bacteria, sterile laminar flow hoods for handling cell and bacteria cultures, and high resolution light microscopes with transmission, phase contrast, and fluorescence capabilities plus a stage that can be indexed to allow for rapid location of pre-screened sample locations. Equipment for plastic and sulphur embedding of specimens, and an ultramicrotome for thin sectioning, should also be included. An additional area is needed in the wet lab room for the preparation of frozen hydrated specimens for cryo microscopy; this area should include a high-pressure freezer, cryo plunger, and cryo ultramicrotome.

Studies in magnetism require the preparation of thin films on transparent substrates such as silicon nitride, in some cases with nanopatterned structures. Fortunately the Center for Functional Nanomaterials at Brookhaven plans to have the necessary processing equipment, as well as complementary, non-synchrotron-based analytical tools such as scanning probe microscopes. However, proper studies of magnetic samples require access to additional complementary instrumentation such as P-MOKE, SQUID, Kerr microscope, and electron spin resonance spectrometer.

These soft x-ray beamlines will be especially demanding of ultra-high vacuum conditions, requiring continuous access to the NSLS-II vacuum group facilities. The beamline would require a clean environment (laboratory space) for the cleaning and assembly of ultra-high vacuum parts.

Shared access to sample preparation and mounting facilities is required. For handling cryo specimens, steady use of liquid nitrogen is required both at the end stations and in the sample preparation laboratory, including equipment for inspection and crystal orientation.

References

[11.8.1] H. Ade, X. Zhang, S.Cameron, C. Costello, J. Kirz, and S. Williams, *Science* **258**, 972 (1992).
[11.8.2] J. Kirz, *J. Opt. Soc. Am*. **64**, 301 (1974).
[11.8.3] http://www-als.lbl.gov/als/ourorg/strategicplan.html
[11.8.4] J. Miao, *Nature* **400**, 342 (1999).
[11.8.5] H.N. Chapman et al., *J. Opt. Soc. Am*., **A23**, 1179 (May 2006).
[11.8.6] D. Shapiro et al., Proc. Nat. Acad. Sci. **102**, 15343 (2005).
[11.8.7] S. Marchesiniet al.., *Phys. Rev. B* **68**, 140101-1 (2003).
[11.8.8] A. Friedmanet al., Proceedings of the Particle Accelerator Conference (1993) pp. 1599.
[11.8.9] R. Follath, *Nucl. Instr.& Meth. A* 467-468, 418 (2001).
[11.8.10] R. Reininger and A. de Castro, *Nucl. Instr. & Meth. A* **538**, 760 (2005).
[11.8.11] P. Elleaume, "Undulator Radiation," in *Undulators, wigglers and their applications*, H. Onuki and P. Elleaume, Editors. 2003, Taylor & Francis: London.
[11.8.12] R. Reininger, *SrCalc*, 2001-2006.
[11.8.13] F. Riemer and R. Torge, *Nucl. Instr. & Meth A.*, **208**, 313, (1983).
[11.8.14] C. Welank, G.J. Chen, and F. Cerrina, *Nucl. Instr. & Meth. A*, **347**, 344, (1994).

11.9 A Macromolecular Crystallography Beamline

11.9.1 Scientific Case for Macromolecular Crystallography

Understanding the living cell is the utmost challenge of modern biology. The expectation that a deeper understanding of the biological process can be achieved, once the three-dimensional structure of countless molecules and their functional roles have been conquered, is the driving force behind the revolution structural biology is undergoing today. Numerous cellular mechanisms are now being described at a molecular level. Examples of these are protein synthesis, RNA transcription, DNA replication, immune response, enzymatic metabolism, signal transduction, cellular division, and the production of energy, to name just a few. In addition we should emphasize the dramatic impact that structural biology has on the development of new drugs, wherein drug designers count upon being able to look in three dimensions at the molecular fit of their proposed drug into the active site of its target enzyme.

We're truly in a golden age for macromolecular x-ray crystallography (PX for short). The growing use of synchrotron sources for PX is in part due to the continuing hypothesis-driven investigations launched by structural biologists and drug-target studies performed by pharmaceutical scientists, and also to the recent organized efforts in structural genomics. More than three structures out of four deposited in the Protein Data Bank were solved using synchrotron data and this fraction keeps increasing [11.9.1.1]. The availability of brighter x-ray sources and the improved quality of instrumentation and methods that we see today has driven researchers to attempt increasingly difficult scientific problems. Indeed, the size and complexity of macromolecules that can be studied has increased by an order of magnitude in the last roughly 15 years.

The most difficult problems, which quite often are the most interesting ones, represent the pinnacle of the structural biologist's craft. Structure of large macromolecular assembly, such as the three-dimensional structure of the 150,000 atoms of the bacterial ribosome [11.9.1.2], gives detailed information about the machinery of the cell, e.g., protein synthesis. Also found in this category are the structures of viral particles which have possible application in treatment of diseases and nanotechnology. Major challenges also need to be overcome in working with membrane proteins which perform many cellular functions and responses, representing about 30% of all proteins produced in a cell (making them quite interesting to the pharmaceutical industry). To address this issue structural genomics effort specifically targeting membrane proteins have recently been launched. The work on the voltage-dependent K^+ channel, these "life's transistors" which control electrical activity in nerve and muscle, and for which Roderick MacKinnon, Rockefeller University, was co-awarded the 2003 Nobel Prize in Chemistry, is a perfect illustration of the exciting science obtained from structural studies on membrane proteins (Figure 11.9.1). More recently even structure determinations of macromolecular assemblies of membrane proteins are being conquered, e.g., a transient intermediate in the mechanism of nutrient uptake across Gram-negative bacteria [11.9.1.3].

NSLS-II will have a dramatic impact in structural biology. The two highest priorities are to handle very small weakly diffracting crystals, and to treat very large molecular assemblies; this is where dramatic progress in structural biology will lie. Investigators in the Northeastern United States are at a serious disadvantage: neither the current NSLS, nor CHESS at Cornell University, can provide the small beam size with high intensity and excellent collimation that is required for this sort of progress. The ultrahigh source brightness of NSLS-II, in combination with anticipated developments in optics, detectors, and computing power, will allow structural biologists to tackle macromolecular assemblies of exceptional complexity, bringing our understanding of the macromolecular machinery of the cell to an unprecedented level. Also, in selected cases, time-resolved studies of macromolecular dynamics and interactions down to microsecond time scales or beyond will be possible, adding an additional dimension to the value of the results.

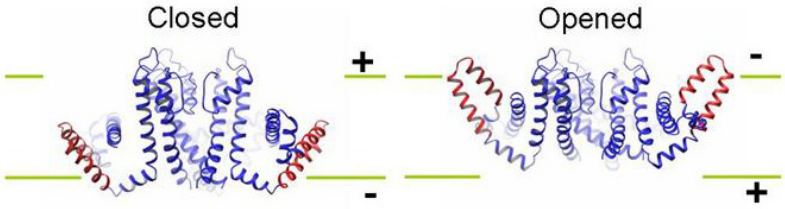

Figure 11.9.1 A model for control of passage of potassium ions through a channel in the cell membrane, in response to changes in the cell membrane voltage. From the work of Prof. Roderick MacKinnon, Rockefeller University.

References

[11.9.1.1] BioSync http://biosync.rcsb.org/BiosyncStat.html.
[11.9.1.2] Ban et al., (2000) *Science* **289**, 905; Harms et al., (2001) Cell **107**, 679; Wimberly et al., (2000) Nature **407**, 327; Pioletti et al., (2001) EMBO **20**, 1829; Yusupov et al., (2000) *Science* **292**, 883; B.S. Schuwirth et al., (2005) Science **310**, 827.
[11.9.1.3] Shultis et al., (2006) *Science* **312**, 1396; Pawelek et al., (2006) Science **312**, 1399.

11.9.2 X-Ray Damage to Biological Samples

One of the major problems facing the characterization of biological materials at NSLS-II will be damage to experimental samples. The damage to biomaterials from strong x-ray beams can be attributed to thermal effects, radiation effects, or a combination of both.

11.9.2.1 Thermal Damage

Thermal damage is the result of the local heating of the sample. Increased thermal vibrations cause atomic bonds to break and the subsequent destruction of the molecules [11.9.2.1]. Heating effects can be minimized by increasing the irradiated sample volume and by keeping the dose distribution within the sample as uniform as possible, or by proper cooling. Assuming a time-averaged power of the x-ray beam, i.e., a time-independent thermal input source, Kuzay et al. estimated that for an 8 keV x-ray beam and 10^{13} ph/mm^2/s^{-1}, a cryo-cooled protein crystal that is 100 μm thick will suffer a temperature increase of 6 K and stabilize in 4.5 s, while a 300 μm crystal will suffer a temperature increase on the order of 20 K and take more than 52 s to stabilize. Moreover, their results showed that gradient effects became negligible for thinner crystals. On the other hand, in each case, the sample temperature rise was estimated to be roughly linear in incident flux. Keeping the number of photons incident on the sample constant (at 10^{12} photons), this dose over 10 s led to a 6 K temperature increase, whereas exposures over 0.1 s led to a 40 K temperature increase. Conversely, if duration of the x-ray exposure is much shorter than the time the system takes to reach thermal equilibrium, then the maximum temperature is not reached and the system temperature will be smaller than the equilibrium temperature—as long as enough cooling time is provided through the entire data collection cycle.

Using finite element analysis, Nicholson et al. [11.9.2.2] modeled the heating of a 100-μm-cube protein crystal suspended in vitrified ellipsoidal cryosolution film, 300 μm long by 100 μm at its widest point, in a nitrogen and helium gas stream kept at 100K. Considering a 50 μm incident beam perpendicular to a plane where the thickness of the cryoprotectant was almost zero, these authors determined that a temperature difference of 4.1^{o}C in ~400 ms and 1.6^{o}C in ~100 ms, for nitrogen and helium respectively, can be expected between the “no beam” state and the “beam on” state. They further concluded that the most noticeable

changes would occur if beam and crystal sizes were comparable. This is borne out by experience at the ESRF multipole wiggler (10^{15} ph/s/mm^2), where up to 11 beam positions have been used on long, needle-shaped crystals.

11.9.2.2 Radiation Damage

Radiation damage results from the interaction of the ionizing photon beam and the electrons in the biological material, and is commonly classified into primary and secondary damage [11.9.2.3]. Primary damage is caused by the direct interaction of the x-ray beam and the electrons (photoelectric, Auger, and Compton effects), leading to a breaking of chemical bonds and the destruction of molecules. In contrast, secondary damage results from reactions caused by radiolytic products (e.g., free radicals generated by solvent atoms absorbing the ionizing radiation). Primary damage depends only on the photon energy, x-ray dose, and number of photons absorbed, but is independent of temperature [11.9.2.4]. Secondary damage varies with the nature of the radiolytic products and with other factors, such as temperature, reactivity, and mobility of the free radicals. To maximize the signal-to-noise ratio of the data collected and minimize local heating effects, the rate at which the dose is given and the lifetime of the free radicals in the biological sample need to be considered. It should be possible, at very high photon fluxes (10^{16} ph/s/mm^2), to capture all images before significant damage by the migrating radiolysis products [11.9.2.5, 11.9.2.6] can be observed. At these photon fluxes, the inverse dose effect (the probability of free radical recombination) should limit dose effects as the number of incident photons per unit time per unit area (dose rate) rises.

Ravelli's group at ESRF [11.9.2.7] have recently addressed the cause of radiation damage. Addressing the question of whether radiation damage in biological macromolecules is caused by dose accumulation or by dose rate, they concluded that the dose-rate effect observed is a secondary problem when compared with the compounding absorbed-dose radiation damage. This is consistent with results previously obtained by Sliz et al. (2003). However, at the atomic level these authors found that structural changes increase in magnitude as dose rates become higher. Why does a dose rate effect exist at all? The answer to this apparently trivial question is not easy. One possible explanation might be related to a free-radical steady-state. The formation, recombination, and diffusion of free radicals would all contribute to the total free-radical population, including electrons generated by x-ray exposure. As Leiros et al. speculate, at high dose rates the free radical recombination rate may not be fast enough and may lead ultimately to free radical diffusion and the creation of damage. As beams become more and more focused (micro and sub-micro focusing) and smaller sample volumes are probed, sample heating would foster radical diffusion and a free-radical steady-state may not be attained. It is not yet clear what implications there would be of such a non-equilibrium state for the radiation damage issues discussed here.

Radiation damage is a particularly severe problem for experiments that involve kinetics, as cryogenic mitigation techniques are usually not viable. As for semiconductors and demonstrated on a number of occasions for biomaterials [11.9.2.8], the chief source of radiation damage is mobile electrons and electron-holes, both of which pose considerable mobility at room temperatures as well as at cryogenic temperatures. The amount of damage suffered by a given material is commonly measured in terms of the amount of energy deposited, or *dose* (1 Gray [Gy] = 1 Joule/kg). Several authors agree that for biological samples, the upper limit is of the order of 10^7 Gy. Recently, Howells et al. [11.9.2.9] made an assessment of the maximum tolerable dose. They found that biological materials seem to be tolerant to a dose 10 to 1,000 times higher than that initially predicted by Henderson [11.9.2.10].

Table 11.9.1 is a summary of different approaches at third-generation sources. Under these conditions, O'Neill and others found that the total dose delivered by 12 keV photons in 10 s to an average protein crystal containing 50% solvent, $\mu/\rho = 2.6$ cm^2/g, through a sample area of 80 μm^2, will be 2×10^5 Gy. Using these values, the dose per second delivered to a similar sample was estimated for the flux observed by Henderson, Teng, Kuzav, O'Neil, and Sliz; the current flux at NSLS beamline X25; and the flux proposed for NSLS-II.

Table 11.9.1 Dose, Biomolecular Crystal Size, and Useful Lifetime for Different Photon Fluxes.

	Henderson [11.9.2.10]	Teng [11.9.2.3]	Kuzay [11.9.2.1]	O'Neil [11.9.2.5]	Sliz [11.9.2.11]	X25 (wiggler)	NSLS-II
Photon Energy [keV]	8	12	8	12	12	12	12
Flux [ph/s/mm^2]	2×10^{11}	3×10^{12}	$10^{13} - 10^{15}$	4×10^{13}	4×10^{15}	2×10^{13}	5×10^{18}
Dose [Gy]	2×10^{7}	1×10^{7}	10^{5}- 10^{3}	2×10^{15}	1×10^{6}(a)	1×10^{4} (a)	2.5×10^{9}(a)
Time to (1/e) death [s]	–	11×10^{3}	–	–	25	2.5×10^{3}	0.01
Dose to (1/e) death [ph/mm^2]	–	2×10^{16}	–	–	5×10^{16}	5×10^{16} (b)	5×10^{18} (b)
Minimal crystal size[μm]	–	35	–	–	20	–	–

(a) Estimated after O'Neil et al. [11.9.2.5] (b) Estimated after Sliz et al. [11.9.2.11].

Assume a cubic sample of size a and n_o incident photons on a cross-section of area A. The total dose (energy per mass) will be given by:

$$D = \frac{\Delta E}{m} = \frac{\Delta E}{\rho \times A \times a} \tag{11.9.2-1}$$

where $m = \rho$ x V . If it is assumed that all absorbed photons deposit energy in this volume and that the sample is thin:

$$n = n_o e^{-\mu d}; \quad n = n_o [1 - \mu d]. \tag{11.9.2-2}$$

The number of absorbed photons will be:

$$n = n_o \mu d \tag{11.9.2-3}$$

and the deposited energy for d=a and photon energy E in (keV):

$$\Delta E = n_o \mu a E \tag{11.9.2-4}$$

or

$$\Delta E(J) = n_o \mu a e E(eV), \tag{11.9.2-5}$$

where e is a conversion factor, 1.6×10^{-19} J eV^{-1}. Therefore, the dose per unit time is given by:

$$\frac{D}{t} = \frac{n_o \mu a e E}{\rho A a} \tag{11.9.2-6}$$

and the total dose is :

$$D = \frac{n_o t(\mu/\rho) eE}{A}. \qquad (11.9.2\text{-}7)$$

Assuming that the limit for data collection for a given protein crystal is reached when the contribution of the unit cells in the crystal to a Bragg reflection falls to *1/e* of its initial value at the 3.5 Å resolution, Sliz et al. estimated that the accumulated dose would be 5×10^{16} ph/mm^2. With the incident photon flux given in Table 11.9.3, these authors estimated that the crystal would survive for a total of 25 s in the beam. Using these approximations, we can estimate the dose that will be deposited in a crystal for the total intensity of Bragg reflections to decrease by 1/e. The values obtained are of the order of 10^{16} ph/mm^2 (Table 11.9.1). This allows us to estimate the useful life time of a crystal in a flux, such as observed currently at X25 and being proposed for NSLS-II. The values found are in good agreement with experimental observations at X25 and with the values found by Teng and Mofat [11.9.2.4].

Further, following the assumption that for each elastically scattered photon about 10 photons are absorbed by the sample (i.e*.,* each unit cell will contribute one photon to the Bragg reflection before the crystal is declared dead [11.9.2.11]), it is possible to determine the minimum crystal size needed to obtain a complete data set. The value determined by these authors is in good agreement with the values obtained by Teng and Mofat [11.9.2.4] and other authors [11.9.2.12, 11.9.2.13].

Therefore, it should be possible to combine short exposures (in the μs range), proper crystal cooling, and improved detector technologies to study biological crystals at NSLS-II. An alternate strategy could be the exploitation of the improved resolution, via use of monochromator optics, that allow higher-energy resolution, such as, for example, Si (511) or (331), which incur lower dose rates.

References

[11.9.2.1] T.M. Kuzay, M. Kazmierczak, and B.J. Hsieh; *Acta Cryst.* **D57** 69 (2001).

[11.9.2.2] J.M. Nicholson, C. Nave, F. Khalid, B. Fell, and E. Garman; *Nucl. Inst. & Meth. A* **467** 1380 (2001).

[11.9.2.3] T.-Y. Teng and K. Moffat; *J. Sync. Rad.*. **7**, 313-317 (2000.)

[11.9.2.4] (T.-Y. Teng and K. Moffat; *J. Sync. Rad.* **9**, 198-201 (2002).

[11.9.2.5] P. O'Neill, D.L. Stevens, and E.F. Garman; *J. Sync. Rad.*. **9,** 329-332 (2002).

[11.9.2.6] V. Cherezov, K.M. Riedl, and M. Caffrey; *J. Sync. Rad.***9,** 333-341 (2002).

[11.9.2.7] K.S. Leiros, J. Timmins, R.B.G. Ravelli, and S.M. McSweeney; *Acta Cryst*. *D* **62** 125 (2006).

[11.9.2.8] Cherezov, K.M. Riedl, and M. Caffrey; *J. Sync. Rad.* **9** 333 (2002).

[11.9.2.9] R. Howells, T. Beetz, H.N. Chapman, C. Cui, J.M. Holton, C.J. Jacobsen, J. Kirz, E. Lima, S. Marschesini, H. Miao, D. Sayre, D.A. Shapiro, and J.C. Spence; arXiv:physics/0502059 v1 11Feb2005.

[11.9.2.10] Henderson; Proc. R. Soc. Lond. **B241** 6 (1990).

[11.9.2.11] Sliz, S.C. Harrison, and G. Rosenbaum, *Structure* **11** 13 (2003).

[11.9.2.12] Glaeser, M. Fracciotti,, P. Walian, S. Rouhani, J. Holton, A. MacDowell, R. Celestre, D. Cambie, and P. Padmore; *Biophys*. J. **78** 3178 (2002).

[11.9.2.13] P. Burmeister; *Acta Cryst.* **D56** 328 (2000).

11.9.3 Source and Optics

An intense and well-collimated source of x-rays, ideal for x-ray crystallography applications, will come from either the 2 m long, 14 mm period superconducting undulators, or the 3 m long, 19 mm period cold permanent magnet undulators,. The small angular divergence of the x-ray beam emitted by these undulators allows the collection of the entire photon beam with a relatively compact KB mirror assembly. For example, at ~35 m from the undulator source, the width of the horizontal fan of x-rays is ~2.2 mm (4σ) at a photon

energy of 12 keV (employing the fifth harmonic of a SCU), and a 74 cm horizontally focusing mirror would intercept the full beam at a grazing incidence angle of 3 mrad. These optics will allow the x-rays to be focused onto small crystals that are a few tens of microns in diameter with relatively small convergence angles—as low as 147 μrad (H) × 81 μrad (V). With typical mirror coatings, one can cover x-ray energies up to ~30 keV at this grazing angle. For comparison, this mirror acceptance is simply not possible on an undulator or wiggler beamline on the existing NSLS x-ray ring; at best, such a mirror could intercept only ~15% of the much wider horizontal beam fan.

The NSLS-II shield wall lies 25 m from the source point, and we would prefer to position the monochromator assembly (double-crystal monochromator based either on cryogenically cooled silicon crystals or water-cooled diamond crystals) immediately after the shield wall, followed by a KB focusing mirror assembly (shown conceptually in Figure 11.9.2; parameters are listed in Table 11.9.2). Placing the KB assembly here rather than further downstream allows these mirrors to be relatively short, thereby reducing their residual figure error. The KB mirrors would be outfitted with dynamical curvature adjustments, employing either conventional construction with purely mechanical bending, or segmented bimorph construction with electromechanical bending. This would allow them to produce a focused x-ray beam over a range of demagnifications from ~2:1 to ~10:1, depending on the preferred experimental configuration. One could either choose one focusing mode for each experimental station, or employ a long experimental hutch, within which the diffractometer could be moved to provide either mode or could be placed at an intermediate position with the optics demagnification adjusted to suit.

Table 11.9.2 KB System Parameters for an NSLS-II X-Ray Crystallography Beamline.

Mirror Coating	Rhodium and/or platinum			
Grazing Incidence angle	3 mrad			
Operating energy range	~5-30 keV			
Efficiency of KB system at 12 keV	90% (Rh), 75% (Pt)			
VFM Length (optical surface only)	37 cm			
HFM Length (optical surface only)	74 cm			
	High Demagnification Mode		Low Demagnification Mode	
VFM (undulator to mirror distance, 36 m)	Focal length	5 m	Focal Length	12 m
	Demagnification	7.2:1	Demagnification	3:1
HFM (undulator to mirror distance, 35 m)	Focal Length	6 m	Focal Length	13 m
	Demagnification	5.8:1	Demagnification	2.7:1

VFM = vertical focusing mirror; HFM = horizontal focusing mirror

11.9.3.1 Performance of the Optical System

A critical physical parameter determining the image quality of the focused beam, because of the ultra low emittance of NSLS-II, will be the residual figure errors of the KB mirror surfaces. Indeed, one reason to keep the distance from these KB mirrors to the focus relatively short is because their surface figure errors contribute to the focused spot size roughly proportional to this distance. On the other hand, the state of the art in x-ray mirror optics will continue to improve, with the ultimate goal being <0.1 μrad figure error. Table 11.9.3 shows the expected improvement in x-ray beam focus in relation to the surface figure error of the KB mirrors in these beamlines. The perfect mirror case is included as a point of reference. Typical figure errors that are routinely achieved in 2006 in long mirrors of this kind are about 2 μrad, although reports about much

lower figure error have appeared recently; for example, a mirror 78 cm long with a figure error of 0.8 μrad has just been installed on beamline ID23-1 at ESRF [11.9.1].

Table 11.9.3 NSLS-II Undulator-Based X-Ray Beamline Performance vs. Mirror Figure Error. The red (upper text line in each pair) signifies the "high" demagnification mode, and the blue (lower text line) signifies the "low" demagnification mode (see Table 11.9.2). The FWHM beam convergences for the low demagnification mode are 0.147 mrad (H) and 0.081 mrad (V), and for the high demagnification mode are 0.317 mrad (H) and 0.195 mrad (V).

RMS figure error [μrad]	0	0.1	0.5	1.0	2.0
Vertical focus size FWHM μm]	1.0	2.6	11.8	23.5	47.0
	2.4	6.1	28.3	56.5	112.8
Horizontal focus size FWHM [μm]	15.5	15.8	21.0	32.2	58.5
	33.6	34.2	45.4	69.7	126.7
Monochromatic intensity at 12 keV [ph/s/μm^2]	1.0×10^{13}	4.5×10^{12}	7.9×10^{11}	2.7×10^{11}	7.7×10^{10}
	2.0×10^{12}	8.6×10^{11}	1.5×10^{11}	5.2×10^{10}	1.5×10^{10}

Note: FWHM = Full Width at Half Maximum

Fairly frequently, experimenters have great difficulty growing crystals larger than a few microns in size. These situations would benefit from focused beam sizes (particularly in the horizontal direction) smaller than those quoted in Table 11.9.3. For these applications, a secondary optical element, placed in the experimental hutch just before the sample, could be used to focus the beam further, to a dimension as small as 1 μm. This could be another focusing mirror (or KB mirror pair, shorter than the KB mirror pair that would be used upstream in the beamline), a refractive lens system, a Fresnel zone plate, a tapered capillary, or simply an aperture (followed by a suitable guard). Setups of this kind are presently in operation at ESRF and SLS, and are being installed at a few beamlines at APS. This need not be a permanently installed feature; it can be inserted on demand.

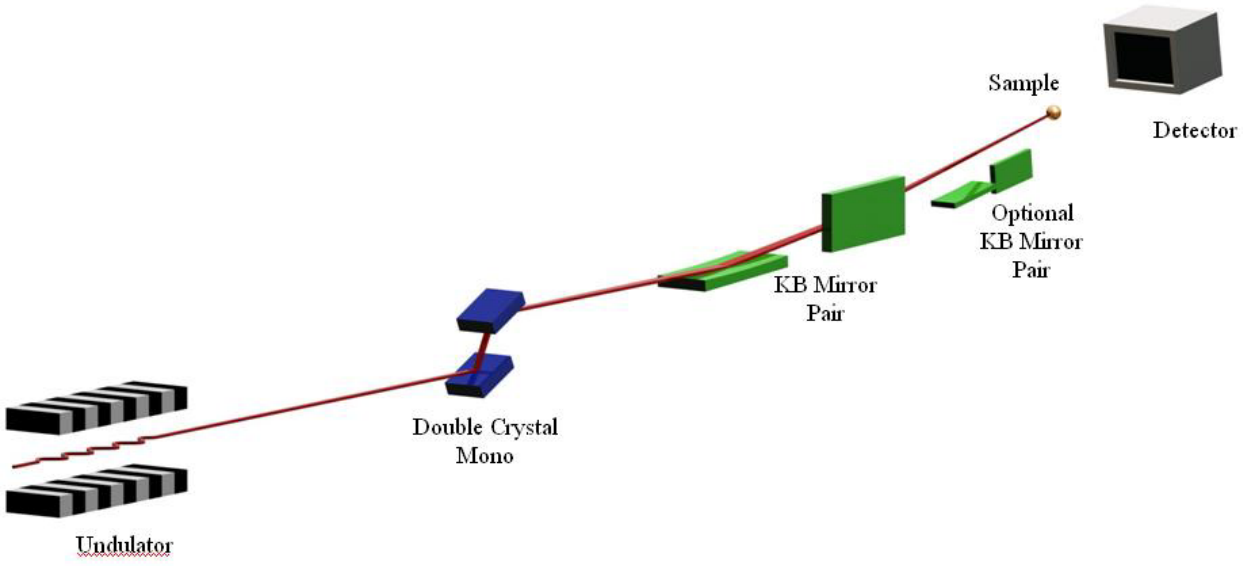

Figure 11.9.2 Conceptual layout of undulator-based crystallography beamline. The optional KB mirror pair may be inserted into the beam path before the sample to deliver a microbeam.

11.9.3.2 The Usefulness of Dual Undulators

Finally, we mention that crystallography beamlines, which have a fairly compact footprint in the direction perpendicular to the beam, are prime candidates for being placed to view multiple "canted" undulator sources installed in a single straight section of the storage ring. The concept of two canted undulators in one straight section has become the standard for new PX beamlines at APS, as demonstrated by GM/CA-CAT [11.9.2] and NE-CAT; the concept was also adopted at the ESRF [11.9.1].

The key accelerator parameter that influences the design of the beamline is the canting angle between the two undulator sources, because this defines the separation between the undulator beams along the sector length. We are envisioning a canting angle, between two successive undulator sources in a straight section, of between 0.25 and 2 mrad (this is discussed briefly elsewhere in the current CDR, and will be addressed in more detail in the Title I and Title II designs); at a later stage it will be determined what canting angle could be achieved. Canting angles used at APS and ESRF are 1.0 and 1.5 mrad respectively. A canting angle of 0.25 mrad would provide a horizontal beam separation between the two undulator beams of 7.5 mm at a distance of 30 m from the nominal source position, where the first optical element would be located. In this circumstance, a horizontally deflecting mirror or monochromator would probably need to act on one of the undulator beams to separate it far enough from the other beam to permit the construction of two independent beamlines farther downstream. A canting angle of 2 mrad, on the other hand, would provide a horizontal beam separation between the two undulator beams of 6 cm at a distance of 30 m from the nominal source position. This should be sufficient to allow the placement of a standard first optical element for one of the beams without disturbing the other beam. In this circumstance, the first optical element would be the double-crystal monochromator that would serve one of the two beamlines; the first crystal of this monochromator, probably to be cryogenically cooled silicon, will be somewhat substantive, underscoring the importance of providing adequate separation between the two undulator beams at the monochromator location. The other undulator beam would pass through this monochromator chamber undisturbed, and continue farther downstream before encountering the monochromator that would serve the other beamline. To give an acceptable horizontal separation of the two monochromatic beams at the location of the first experimental station (at least 0.5 m to accommodate an appropriate experimental apparatus), multiple horizontally deflecting mirrors could be used, as pursued by GM/CA-CAT. Alternatively, a rather large horizontal separation could be afforded by employing a horizontally deflecting monochromator, as pursued by NE-CAT at APS. Beamline designs that are compatible with canted undulator sources will be examined carefully.

11.9.3.3 End Stations

Below we describe the apparatus and software that would be developed or acquired to equip experimental stations where the principal scientific discipline is single-crystal x-ray diffraction studies on biological macromolecules, known as (not quite accurately) *PX,* for *protein crystallography*. We presume that there may be several NSLS-II straight sections available for PX, each of which might support more than one undulator. We also acknowledge that although PX is the principal target, the capabilities of the instruments, and likely the interests of the local scientists, could embrace broader disciplines, say powders of macromolecular crystals or highly ordered "crystalline" fibers of specimens such as filamentous viruses. To provide focus for this section, we will describe the sorts of experiments to be accommodated, and will show how NSLS-II can have a dramatic impact.

11.9.4 Experiments Driving This Development

No end is in sight for the paradigm of modern PX: single crystals grown from cloned components will be subjected to monochromatic x-ray diffraction measurements, and distinctive scattering from a few heavy atoms will provide information to allow calculation of the three-dimensional electron density. The possibilities provided by NSLS-II, especially its brightness, guide the variations one might play on this theme,

and suggest the importance each might have in the early years of its operation. Here is a list of experimental demands on the PX stations for NSLS-II, in approximately decreasing order of importance.

1. A critical and enduring need will be to wring the best from increasingly smaller crystals. Every experimental station will employ the brightness of NSLS-II to exploit crystals in the range down to 10 μm, and one station will be equipped to study crystals at the ultimate focusing limit of NSLS-II.
2. The trend in biological sciences is the study of increasingly large molecular assemblies. This is where the future lies. The current state of the art is on the order of 150,000 individual atoms in an asymmetric object, and atomic resolution requires the high-brightness synchrotrons. The brightness of NSLS-II will provide extraordinary collimation to provide excellent diffraction from these very large-unit-cell crystals
3. A significant value of NSLS, and potential value of NSLS-II, is simply being able to handle quite good crystals expeditiously, both for investigators who want to visit to take their own data, and for mail-in service. Rapid diffractometers with excellent shutter/axis synchronization and high-quality detectors should be able to provide automated crystal screening followed by full data collection and processing.
4. To provide phasing power from inherently weak signals from low-abundance heavy atoms, the brightness of NSLS-II can be focused on narrowing the bandwidth of radiation, and thereby enhancing the signal, of sharp K-shell transitions by use of high diffraction-order monochromators [11.9.3].
5. The exploitation of the sulfur and phosphorus edges to study DNA complexes is gaining increased interest as new generation synchrotrons are capable of delivering bright beams at longer wavelength. Longer and shorter wavelengths will be explored at NSLS-II to provide a larger range of possibilities to the user.
6. Something over 10% of proteins contain a transition metal that contributes to the molecule's biological function. Provision of a relatively simple energy-dispersive x-ray detector at each experimental station would provide a quick way to survey for these metals in any specimen.
7. A straightforward and inexpensive facility to provide at several stations would be a single-crystal UV/Visible spectrophotometer. This would find service for the monitoring of x-ray damage in crystals, examining redox states of chromophoric functional groups, and other similar tasks.
8. The crystal-growth "industry" has a continual need to assess the diffraction quality of newly grown crystals. We would provide a station with flexible means to couple crystal-growth automation with diffraction specimen automation to provide the rapid screening that is required.
9. Following on the aim to study the smallest possible crystals, we would provide a versatile environment to explore various avenues, such as performing short measurement sweeps on individual micro-crystals swept up and cryocooled together on a tiny mesh, or performing one-shot exposures on micro-crystals passing the beam in a flow cell.
10. In the context of study of micro-crystals, each of which might be capable of providing only a small fraction of a complete data set, one station would be capable of exploring innovative methods for their use. Examples might be use of increased angular divergence, or broader energy bandwidth, to integrate the diffraction rocking curve for stationary crystals.
11. A small fraction of investigators at NSLS-II will want to follow the time course of some reaction in their crystalline molecule. Use of the white-beam Laue method would not be particularly effective with the undulators we propose. However, to exploit freeze-trapping of intermediates and other methods we have not envisioned, there would be space to install flash lamps or lasers to trigger reactions. These will complement the sharp time structure of the ring and the UV/Vis spectrophotometer we propose above.

11.9.5 Experimental Apparatus

We propose equipment that might serve a suite of experimental stations that could be served by two canted NSLS-II undulators, each producing a hard x-ray spectrum in the range 5 – 30 keV. Components of this sector can be replicated in other sectors to serve expected demand. Since progress in automation is exploding right now, we plan that several of the beamlines will be fully automated, capable of following a sample-in/structure-out model.

The downstream undulator beam would be designed to deal with the most challenging problems, with a range of optical characteristics available, including the smallest possible microfocus that is accompanied by a convergence less than 1 mrad. It would be set up to attack any crystallographic problem, with multiple options for micro-focusing (KB mirrors, graded multilayers, refractive lenses, elliptical capillaries), a monochromator that can produce higher harmonics to narrow the bandwidth, full automation for high-throughput data collection, microspectrophotometer, energy-dispersive x-ray detector, and so forth.

The upstream undulator could provide a beam for two to three stations with fixed energy, say at 13.6 keV (just above the bromine K edge), one being an end station (similar to the station described above that uses the beam from the downstream undulator) and the others being side stations. Here are potential roles for the stations that use the beam from the upstream undulator:

- Station 1: Set up to serve as a crystal-screening station. There would be robotics for conventional specimens and for various crystal-growth apparatuses. Any economies in detectors and other components. can be taken here.
- Station 2: Setup to provide rapid throughput for fixed-wavelength operations: drug-binding studies, SAD structure solving, molecular replacement, and so on.
- Others: Likely there would be substantial demand for both of these, and they could be replicated.

We expect large demand for the sort of station defined for the downstream undulator. Most of the PX sectors should have two of these high performance stations. We explore each component of the experimental stations further, below.

11.9.5.1.1 Crystal Orienters

Every station would be equipped with quick orienters capable of holding a crystal on an axis within 2 μm, fully automated x-y-z alignment mechanism, and excellent crystal visualization. The current state of the art in crystal drives is represented by direct-drive servo-motor ω axes employing an air bearing that provides positional reliability on the few-micrometer scale. These rotate at about 30 rpm (180 deg/sec). Mechanized crystal-alignment mechanisms give accuracy on the same few-micron scale.

Several sources of software are available today that can automatically center crystals in the x-ray beam. These will be better by 2013. All stations would be equipped with a full ω-κ-φ orienter or equivalent. Already in 2006 there is software in use at ESRF that allows flexible use of a demountable κ-φ orienter. This code allows one to orient a crystal to a particular orientation, for example to rotate about the longest unit-cell edge, and to keep the crystal stationary in the x-ray beam while κ and φ are rotated to position the crystal. There are available computer-controllable front- and back-lighting systems, and automated microscope zoom mechanisms, to provide the best possible specimen visualization.

11.9.5.1.2 Detectors

By 2013, position-sensitive detectors will be available that will provide roughly $4k^2$-pixel images in a ~400 mm format with essentially continuous readout (no need to close the shutter nor to stop the rotation axis) on the 100–500 ms time scale. We would install the very best systems that we can afford. By that time, to store data that are produced at this pace should be straightforward.

11.9.5.1.3 Automation

Writing in 2006, the standard of mechanical specimen changing is to have individual crystals mounted, each on its own cartridge or pin, carried in a magazine or cassette, for automated cryogenic mounting and dismounting. The 2013 equivalent of this will be available at every station.

11.9.5.1.4 Ancillary Features

Modern PX would be impossible without cryogenic cooling of specimens, which are otherwise exquisitely sensitive to x-ray damage. Therefore, every station would have a cryogenic system appropriate for keeping specimens at ~100 K; there will be at least one system capable of ~20 K.

A particular problem with small specimens, especially when photon energies less than about 12 keV are used, is high x-ray background that results from scattering from air in the space between the exit aperture and the beam stop. Therefore, stations would be provided with helium chambers to surround the collimator / specimen / beam-stop volume, which would be used to minimize background from air scatter when it's appropriate.

Amplifying experiments 8–10 above, one can imagine inventive ways to employ multiple microcrystals to measure complete data sets. These might include ones picking up a few tens of microcrystals on a network or sieve, or flowing microcrystals through a flow cell, exposing each for one shot as it passes by. Each of these might require special optics, say a focusing capillary that would provide a wide convergence to sample a wide rocking curve, or white or pink radiation to perform Laue crystallography. One of the end stations could be made versatile enough to accommodate this work.

11.9.6 Experiment Control

All stations would have hardware for control of beamline components that is as similar as possible to minimize trouble shooting and maintenance of spare parts. Also the user software at every station would be recognizably similar to the others. There would be the transparent possibility for secure remote observation and operation. There would be easy-to-use software to allow automated assessment of crystal quality, data-collection strategy, and full processing of raw data. Examples of this exist now; the "dna" software package of the European consortium (http://www.dna.ac.uk) is one of the most complete. It incorporates the program BEST [11.9.4], which provides excellent analysis of quality and recommends data-collection parameters. There are other sources of this sort of evaluation. There will be invisible database software to provide complete tracking of every specimen, and collection of meta data for future publication and deposition of results into the Protein Data Bank.

11.9.7 Computing Environment

For the purchase of computing hardware, two principles would rule: 1) all of the stations at each sector employed for PX would have, inasmuch as possible, interchangeable computing and storage hardware; 2) computing hardware would be purchased to be replaced at the end of its practical lifetime (the three-year Moore's Law rule). Therefore, with a replacement plan on a three-year time scale, a similar style of computing engines would be selected for instrument control at all of the stations, and similarly for data reduction and processing. We have shown at the PXRR that this is an excellent use of a capital computing budget. A redundant supply of disk farms on the scale of several tens of TB would be available for interchangeable use by the individual stations. Depending on the climate of activity in the field, the possibility exists to archive raw data at NSLS-II.

11.9.8 User-Assistance Environment

Given the pace of modern PX, investigators must have access to synchrotron-based data collection when they need it. A model that assures users rapid access to beam time, already in place at NSLS, would be followed at NSLS-II. As technical developments allow, we envision that future users will take advantage of robotic and automation developments. The proposed facility would address the needs of the emergent user community, allowing for remote or virtual access with limited staff assistance and the use of modern teleconferencing technologies. In parallel, at least one station would provide full assistance to the user who chooses to address his or her studies locally at the facility.

Two other aspects of the user-assistance environment now in place at NSLS would also be in the makeup of the environment at NSLS-II. Night-time and weekend support would be provided by PX operators, assuring overall quality control of the experimental stations, facilitating communications among them, and giving investigators the ability to collect data at several different stations, when warranted. Also, modeled on the popular PXRR Mail-In program, there would be a program at NSLS-II whereby specimens can be sent by rapid courier to the facility and measured at the beamline either through collaborative assistance using local scientific staff, or through assistance by local technical staff to enable investigators to manage their experiments remotely.

11.9.9 Crystallography Conventional Facility Requirements

Here we describe the supporting biological laboratory and the equipment for sample preparation and characterization that would be required to support the proposed NSLS-II x-ray macromolecule crystallography beamlines. We also propose to establish a crystal-growth facility to serve a broader audience. We embrace the "Biology Village" concept proposed for the Diamond facility, in which beamlines for biology research are clustered at one section of the ring. This model would be cost effective, with users sharing centralized support. Not only would it avoid duplication in laboratory space and equipment, but also it would strengthen interactions among users and staff.

11.9.9.1 Protein Sample and Crystal Handling

11.9.9.1.1 Characterization

A laboratory with a cold room attached would provide basic biochemistry equipment to all users. The supporting laboratory for the proposed NSLS-II PX beamlines would include at least these instruments:

- balances, centrifuges, and pH meters
- gel electrophoresis apparatus
- UV/visible spectrometer
- dynamic light scattering system
- mass spectrometer
- chromatography equipment (FPLC)
- refrigerators and –20^{o}C and –80^{o}C freezers

11.9.98.1.2 Crystal Manipulation and Freezing

While most users will bring or send frozen samples for x-ray data acquisition, others will bring crystals still in crystallization chambers. They will need equipment and supplies to manipulate and cryopreserve the crystals for their studies. The best possible facilities will be provided to allow visitors to cryopreserve their own specimens. In addition to basic resources such as microscope, dewars, mounting pins, and cryobuffers, we would provide a resource to allow use of the high-pressure (~2 kBar) cryocooling technique developed by Cornell scientists [11.9.5].

11.9.9.2 Crystallization Facility

Standing on the shoulders of the NIH Protein Structure Initiative, we propose to serve the structural biological community more broadly by creating a high-throughput pipeline that will carry purified proteins to high resolution 3D protein structures in a high-throughput way. This would assist scientists in fields other than structural biology to obtain structure information for proteins of their interest. It would be established in the supporting biological laboratory adjacent to the NSLS-II PX beamlines. This pipeline would employ approaches and technologies that exist now to streamline and automate the steps of protein structure determination. Acting on protein samples that would have been prepared and characterized in advance, crystallization and optimization steps would be carried out through use of crystallization robotics. Technology exists for crystallization-plate bar coding, movement of crystallization plates into and out of a storage vault, and crystallization-plate imaging and image processing.

Technology that is missing, to which we would contribute, includes automated methods to screen for diffraction crystals still in their crystallization cells, and robotics to mount single crystals from these cells. The ultimate goal is to establish a system that allows the beamline scientific staff to determine molecular structures in a high-throughput manner with minimum of time and cost.

References

[11.9.1] D. Nurizzo et al., *J. Sync. Rad*. **13** 227 (2006).
[11.9.2] R. Fischetti et al., in Proceedings of 9th International Conference on Synchrotron Radiation, to be published as an AIP Conference Proceedings.
[11.9.3] J.L Smith, and A. Thompson, *Structure*, **6**, 815 (1998).
[11.9.4] A.N Popov, and G.P. Bourenkov, "Choice of data-collection parameters based on statistic modeling," *Acta Cryst.*, **D59** (Pt 7):1145-53, (2003).
[11.9.5] C.U. Kim, R. Kapfer, and S.M. Gruner, "High-pressure cooling of protein crystals without cryoprotectants," *Acta Cryst*., **D61** 881 (2005).

11.10 An Optics R&D Diagnostic Beamline

In addition to facility beamlines, which will focus on scientific innovation and productivity, we propose to establish a beamline dedicated to optics and instrumentation R&D. It is important to do so, since such developments can not be carried out at the facility beamlines due to the scheduling pressure from the user community. Experience shows that the conflict between carrying out user science and making beamline upgrades tends to minimize innovation in favor of productivity.

11.10.1 Conceptual Overview

An Optics R&D beamline should be kept simple. Its purpose is to develop new optical systems, so it should not, by definition, contain any permanent optics. It should have provision for inserting optics into the line at any point without major reconfiguration of safety systems. This implies a series of optics enclosures into which it should be possible to insert monochromators, mirrors, and other equipment relatively easily.

11.10.2 Source

The primary need is to have a source of radiation that matches closely the properties of a typical facility beamline, which is available for significant blocks of time to allow optics development to be pursued independently of a user program. Such beamlines have been available at all synchrotrons since one was established at NSLS in the mid 1980s.

Because the properties of most beamlines at NSLS-II will be determined by the type of insertion device used, it is not straightforward to decide on the appropriate source for the optics R&D beamline. The situation is made much more difficult by the fact that the bending-magnet radiation spectrum will be significantly different from that produced by undulators and wigglers. Most of the optics R&D beamlines installed at current machines are based on a bending magnet source. For most existing machines, the spectrum available at such a port is not much different in energy from the spectrum produced by insertion devices, so this is acceptable—although the spectra differ dramatically in brightness and intensity. For optics development, intensity is generally not as important as the ability to schedule large blocks of time.

It could be that the proper functioning of an optic depends on the angular and spatial properties of undulator light. In this case, it is essential that an undulator beamline be available. Since it is not anticipated that all of the beamlines will be populated immediately, then it may be reasonable to allocate one of them to optics R&D, locating a user program on the beamline when the need arises. If this option is chosen, it is important to plan for an alternative location for new developments to be able to continue to be made.

In summary, preference would be for an undulator source since that will be the most common Facility Beamline source. A bending magnet beamline would not have adequate spectral coverage in the hard x-ray range, and the few available wiggler beamlines will be in high demand for user science.

11.10.3 Beamline Optics

In order to keep the required flexibility in such a beamline, the beamline design would be exceptionally simple. Specifically, it would consist of series of well-shielded, white beam–compatible optics enclosures, threaded with a number of vacuum pipe sections. These would be easily removable, allowing optics test beds to be placed at any desired distance from the source point. The final enclosure should be larger than the others to accommodate extended optics setups. It is expected that computing and controls and conventional facility requirements would all be relatively standard for such a beamline.

11.10.4 Optics Test Beamline – Experiment Plan

The beamline outlined above would provide the facility for at-wavelength testing and R&D of synchrotron optics that is essential in the development of components that will utilize the full brightness and coherence of the NSLS-II source. There are four basic optical testing techniques that would be implemented at this beamline as soon as photons are available. These are described below.

An easily implemented at-wavelength test setup can be modeled after the work done at SPring-8 by Souvorov et al. [11.10.1] This group developed a measurement technique and an image inversion algorithm for reconstructing the surface profile of a reflector from a series of through-focus images recorded with a high resolution CCD camera. This technique works for flat as well as figured surfaces, and can be extended to look at wavefronts from focusing optics, such as Bragg-Fresnel optics and refractive lenses. The diagnostic capability of this technique will enable one to determine the source and location of phase errors in these optics, providing much more information to the fabricator than available from a simple image size measurement. Implementation of this technique requires a high resolution camera to extract intensity information as a function of position from the small image space area. Initial testing on this beamline can be done with prototype Bragg-Fresnel optics and kinoform optics, and with polished flats and spheres available from other optics suppliers.

Another test set-up that can be implemented rather easily is the wire or knife-edge scanning system, as reported by Yamauchi et al. [11.10.2]. This system was used to measure the focal quality of KB elliptical cylinder mirrors on the 1 km beamline at SPring8. By measuring the intensity profiles in various transverse planes around the point of focus, one can reconstruct the aberrated wavefront of the incident beam and learn something about the optical component that produced it. This measurement technique requires only a single element detector and a precision translation stage with nanometer positioning accuracy.

The third measurement technique that can be considered for implementation is an at-wavelength interferometry technique pioneered by Weitkamp et al. [11.10.3]. This technique involves development of a shearing-type interferometer based on Moiré patterns produced from the Talbot effect with two fine-pitched gratings. The instrument requires a high resolution camera to view the Moiré pattern produced by the Talbot effect system. The complete instrument is a small, robust unit that is insensitive to the usual vibrational instabilities of other interferometer techniques. It is ideally suited for direct measurement of wavefronts transmitted by refractive optics.

The fourth test method that can be implemented on this beamline is in-situ profilometry of optical surfaces under normal and accelerated heat load conditions. This entails using a portable Long Trace Profiler setup to view surfaces through a window as they are irradiated with the direct white beam or monochromatic beam. The LTP technique has been used to measure nanometer distortions in water-cooled mirrors on an APS beamline. It is an invaluable tool for validating thermal and mechanical designs of mirror substrates, coating materials, mounting mechanisms, and bending mechanisms. The portable LTPs are currently under development in the BNL Optical Metrology Lab. Implementation at NSLS-II would require the placement of viewports and mirror test chambers at the appropriate locations along the beamline.

References

[11.10.1] Souvorov et al., *J. Sync.Rad.* **9** 223 (2002).
[11.10.2] Yamauchi et al., *J. Sync. Rad.* **9** 313 (2002).
[11.10.3] Weitkamp et al., *Opt. Express* **13** 6296 (2005); SRI 2006 Workshop on Metrology for X-ray Optics, abstract No. 34050005, "X-ray Interferometric In-situ Characterization of Reflective and Refractive Optics."

11.11 A High-Magnetic Field Beamline

In addition to temperature and pressure, magnetic field is an important thermodynamic variable for studies of a variety of condensed matter systems ranging from molecular conductors to superconductors to heavy fermion systems. Ongoing improvements in magnet technology enable studies of such systems at ever increasing fields, and new phases with exotic and intriguing behaviors continue to be revealed. The coupling of high-field magnets and synchrotron radiation is an obvious avenue for high-resolution structural and spectroscopic studies of these new phases. Yet presently, there are few high-field magnets at synchrotron radiation facilities, and the highest DC field worldwide is 15 T. Given the size and complexity of high-field magnets, such a facility will require a dedicated beamline. In this section we consider a high-field magnet beamline for hard x-ray scattering and spectroscopy.

Figure 11.11.1 shows the schematic layout of a high-field magnet beamline.

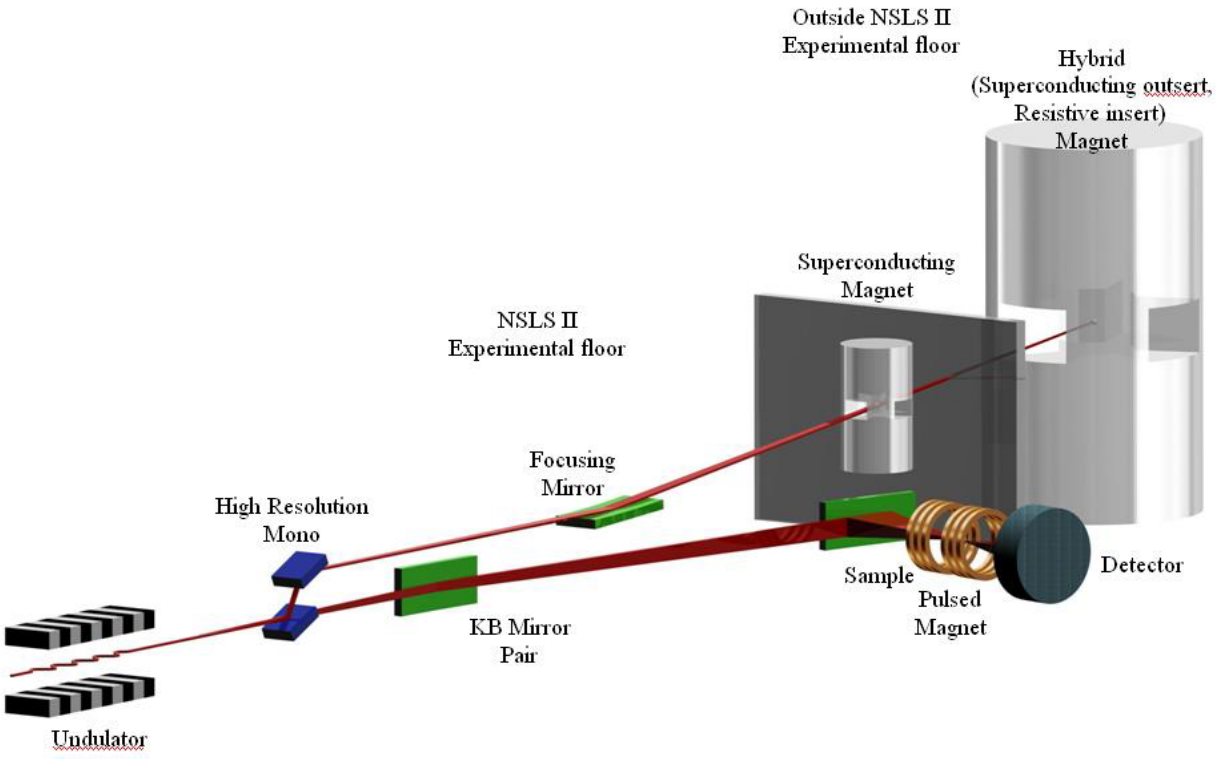

Figure 11.11.1 Conceptual layout of high magnetic field beamline. The large hybrid magnet would be located outside the experimental hall, the wall of which is denoted by the gray panel in the figure.

11.11.1 Source

The high-field magnet beamline would require an undulator source due to the need to have the DC hybrid magnet located outside of the main building (for size, safety, and stray field issues). A standard high-brightness undulator would meet the anticipated experimental needs, and no special requirements for the machine parameters are expected.

11.11.2 Optics

The optics for this beamline are expected to be relatively standard, with a double-crystal monochromator to allow an energy range of ~5–30 keV, with a spot size of ~1×1 mm^2 for either of the fixed field magnets. In addition, in-line phase retarders (for producing circularly polarized beam at rare earth L and transition metal K edges: ~5 – 10 keV) will be utilized. The monochromator would require a wide beam. A mirror that accomplishes this by defocusing the beam is shown in the beamline layout, Figure 11.11.1.

11.11.3 Beam Transport and Enclosures

There would be a single first-optics enclosure of size ~10(W)×20(L)×12 ft (H) for the aforementioned optics (except the dispersive mono, which would be in the first hutch for use with the pulsed magnet).

11.11.4 End Stations

A high-field magnet beamline would ideally consist of two hutches. The first, which would be located inside the main building, would accommodate “medium-field” magnets such as a 4 T cryogen-free magnet

that can be operated with vertical or horizontal field and a ≥13 T superconducting magnet as well as a ≥50 T pulsed magnet. Such magnets would make possible a variety of scattering experiments (PD, single-crystal XRD, SAXS, and GISAXS) and spectroscopy (XAS and XMCD). This would provide a versatile and relatively low-cost high-field magnet facility.

The second hutch, which would be housed in a separate building, would accommodate a 30 T, DC, split-coil, series-connected hybrid magnet. The utilities (e.g., power supply, water cooling components, and closed-cycle helium refrigerator/liquefier) for the hybrid magnet would be contained in a second building.

The specifications for the split-coil, series-connected, hybrid magnet (National High Magnetic Field Laboratory conceptual design) are: 30 T DC magnet with four 45-degree (11-degree vertical) ports, with vertical field. The magnet can be rotated ~15 degrees about a vertical axis. The magnet can also be rotated 90 degrees to provide a horizontal field, with four ~1-degree (32 mm diameter) windows appropriate for XAS and SAXS experiments.

11.11.5 Conventional Facility Requirements

The nonstandard requirements for the first hutch are its size and structural floor load limit. An in-line arrangement of magnets, which would simplify experimental changeovers, and sample insertion and liquid helium refills of the superconducting magnet, necessitate a longer and taller hutch: 16 ft (W)×30 ft (L)×16 ft (H). In addition, due to the weight of the capacitor bank for the pulsed magnet, a structural floor load limit of 200 psf is required.

The nonstandard facility requirements for the second hutch are 1) its size: 30(W)×30(L)×26 ft (H)— with a hutch 6 ft below ground and a 600 ft^2 structural floor load limit at the site of the magnet, 2) an auxiliary building to house a utility plant for the hybrid magnet, which would supply 10 MW of power and 120 l/s of cooling water for the resistive part of the magnet, and 3) a commercially available, closed-cycle helium refrigerator/liquefier, which requires an input of ~2 l/min of liquid nitrogen for the superconducting part of the magnet and the cryostat; this would also be housed in the utility plant.

11.12 A High-Energy Beamline

There are a number of advantages to using high-energy x-rays, including a larger q range and reduced absorption, allowing large samples to be studied and extreme conditions to be accessed. Focused high-energy x-rays are essential for high-resolution x-ray scattering of samples in multi-anvil and diamond anvil cells. Newly developed x-ray focusing optics and detectors can take advantage of the enhanced flux and brightness of the NSLS-II superconducting wiggler source to enable a myriad of crystallographic and spectroscopic measurements.

A **s**uper**c**onducting **w**iggler beamline would provide x-rays in the energy range 20 keV to 150 keV. While the damping wiggler sources will provide a harder source of x-rays than the undulators, the flux from a SCW is an order of magnitude higher than that provided by a damping wiggler, at typical high-energy x-ray scattering energy of 80 keV. SCWs are therefore the desired source for high-energy x-rays.

For the SCW wiggler proposed here, the radiation fan is about 10 mrad wide. Focusing of the x-rays is thus crucial to collect the large fan in order to increase the available flux at the sample. Recent developments in sagittal focusing Laue optics make it possible to focus a large divergence of high-energy x-rays.

The use of white radiation and energy-sensitive detectors for energy dispersive diffraction is an established technique for kinetic experiments in high-pressure (either in a diamond anvil cell or large-volume press) and high-temperature experiments. With the optical elements withdrawn from the center beam, the end station will accept white radiation, thus allowing for energy dispersive experiments.

11.12.1 Conceptual Overview

Figure 11.12.1 shows a sketch of a possible arrangement for beamlines utilizing one such wiggler source. The experimental stations would likely include two side stations utilizing fixed wavelength and two center stations that can utilize both the white beam and focused monochromatic beam.

Considerations have been given in the conceptual design to facilitate changing of configurations in the future in anticipation of unforeseen future needs. Beam can be passed through the hutches in a manner that allows experiments to run simultaneously.

11.12.2 Source

The highest energy photons are produced by very-high-field wigglers. The radiation is broadband with high power at high x-ray energies. The wiggler for the beamline would need to cover the 20 to 150 keV energy range, which requires a critical energy E_C of more than 20 keV, corresponding to a wiggler field of over 3.5 T at the NSLS-II energy of 3 GeV. The brightness should be as high as possible, which means the wiggler period length should be as small as possible. The combination of high field and small period requires a superconducting wiggler design. SCWs are available commercially with a peak field of up to 7 Tesla [11.12.1].

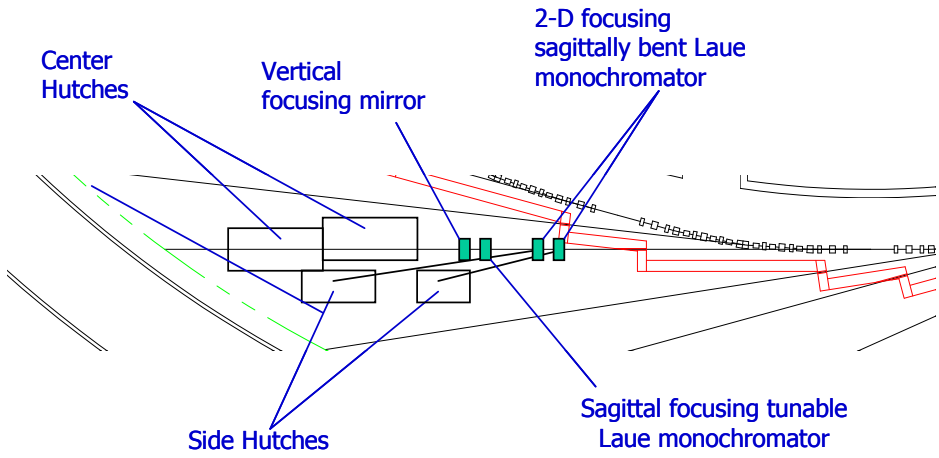

Figure 11.12.1. Layout of the superconducting wiggler beamlines. The length from the ID to the aisle is 60 m.

The wiggler for the beamline covers the 5 to 150 keV energy range, which requires a critical energy E_C of more than 30 keV and a wide beam fan with K of approximately 30. The specifications of the wiggler are listed in Table 11.12.1. Specifications of similar SCWs that are currently in service at medium-energy synchrotrons are listed in Table 11.12.2. A 1 m SCW with 60 mm period and 6.0 T peak field is proposed, as discussed in Chapter 8. We note that a radiation horizontal fan of 10 mrad is difficult to accommodate within the current design of the ring vacuum chamber. Thus accommodating multiple beamlines in this way may require a specialized design of that chamber. Such issues will be looked into in the title I design phase of NSLS-II.

The performance of the proposed wiggler for a 3.0 GeV ring energy was shown in Chapter 8. The wiggler outperforms other options at energies above 30 keV. The critical energy is almost twice that of the NSLS X17 superconducting wiggler (21.6 keV). Having substantial flux at energies above 100 keV is essential for strain mapping and MRT. The deflection parameter is chosen to be wide enough to generate a large horizontal beam profile of a more than 0.5 m at 50 m from the source point. This allows splitting of the fan into multiple

experimental hutches. In addition to the 29 full-size poles, a number of poles in the entrance and exit may be used for better electron beam orbit maintenance.

11.12.3 Optics

Sagittal focusing using Laue crystals was pioneered at NSLS [11.12.2, 11.12.3]. The concept is shown in Figure 11.12.2a. This new x-ray optics concept makes it possible to focus the large divergence of high-energy x-rays produced by the NSLS-II SCW. The extent of such focusing is similar to that of sagittal focusing by a Bragg crystal, except for a factor related to the asymmetry angle. The anticlastic bending facilitates the use of inverse-Cauchois geometry in the meridional plane to provide better energy resolution and to increase the photon flux by an order-of-magnitude compared to traditional sagittal focusing with Bragg crystals. Furthermore, sagittal focusing by a Laue crystal is preferred over a Bragg crystal at x-ray energies above 30 keV because, unlike Bragg crystals, the length of the beam's footprint on a Laue crystal is small and insensitive to energy. For many experiments, beam divergences on the order of 1 mrad at the sample will be tolerable. In diffraction experiments with a vertical scattering plane, a larger divergence in the horizontal plane can also be tolerated.

A double-crystal sagittally focusing monochromator based on this concept has been constructed and tested and has been in use at the X17B1 beamline for two years, providing 67 keV x-rays (Figure 11.12.6). It focuses a horizontal divergence of 3 mrad to a brightness-limited horizontal dimension of 0.2 mm. The x-ray flux density at the focus was a few hundred times larger than that of unfocused x-rays. Currently, using this device, flux on a small sample in a diamond-anvil cell is limited by the brightness of the NSLS storage ring. Combined with a vertically focusing mirror, the same monochromator can be implemented at the upgraded NSLS wiggler beamlines to provide 50 to 100 keV photons of about 10^{12} ph/s, with an energy resolution of 10^{-4} $\delta E/E$, in a spot of less than 50 microns in diameter. This intensity is two orders of magnitude larger than the current state of the art at NSLS X17B1 and will enable studies of smaller samples at higher pressures and higher temperatures.

The conditions imposed on the asymmetry angle of a sagittally bent Laue crystal to achieve 2D focusing have been determined. This simple design diffracts beam into side stations, providing a high-flux beam of 67 keV with moderate energy resolution of 10^{-3} $\delta E/E$ with a flux of about 10^{13} ph/s/mm^2, in a spot of less than 50 microns (V)×100 microns (H). This, when coupled with a matching bent-Laue crystal analyzer, allows high-resolution experiments at high energies. This arrangement is suitable for pair distribution function measurements and powder diffraction measurements in difficult environments, e.g., stainless steel reaction tubes and high temperature capillaries. It will also be valuable for certain single-crystal experiments, such as charge density studies, where data must be collected to very high q values.

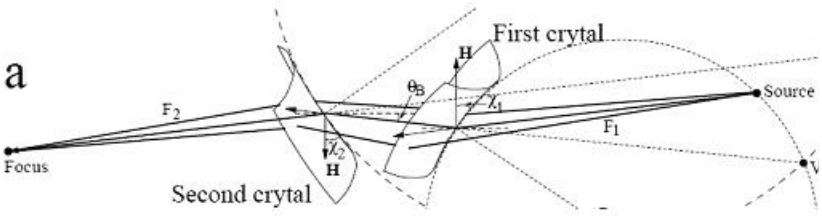

Figure 11.12.2

a) The mechanism of the sagittal focusing with asymmetric Laue crystals. Bending of the crystals causes precession of the diffraction vector (H) around the axis of sagittal bending, and the resulting focusing of the diffracted beams.

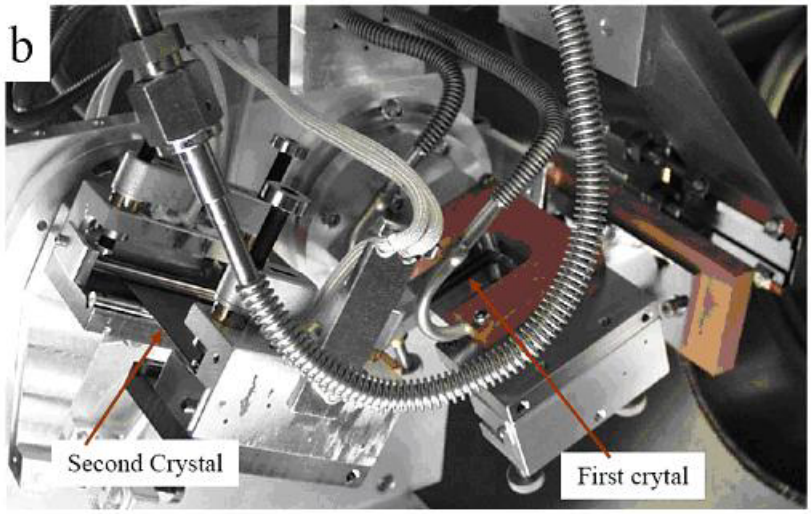

b) Photograph of a monochromator installed at the NSLS X17B1 beamline.

11.12.4 Beam Transport and Enclosures

The demand for the wiggler beamline for different experimental configurations is expected to be high, as has been the case with the X17 beamline at NSLS. The design of the beam transport and enclosures will therefore use the same principle as adopted at X17, to allow maximum flexibility both in terms of the science and in experimental configuration.

Due to the high energy of x-rays generated by the SCW, the entire beamline will be fully enclosed in radiation shielding, as is done at the NSLS X17 beamline. A single enclosure will house the beam-splitter, white beam filters, shutters, and monochromators for the four experimental hutches downstream. The effect of the high power of the wiggler on the optical components will be minimized by aggressive filtering of the white beam radiation with a few millimeters of aluminum or silicon material.

The monochromators for the sidescattering branches would be of the single-crystal, sagittal focusing Laue type described above. The monochromators for the inline hutches would be of the double-bounce Laue type, which can be withdrawn, thus allowing white beam to enter the inline experimental hutches. The same design has been in use at the X17 beamlines at NSLS.

11.12.5 End Stations

Four hutches, two inline with white beam capabilities and two sidescattering monochromatic-beam branches, are considered for the wiggler beamline. Each hutch will be served by a part of the wiggler fan of a few mrad wide. Each hutch will have its own shutter and can operate independently from other hutches. Note, only the first in-line hutch has a beampipe passing through it.

The first hutch will host a Diamond Anvil Cell instrument (first inline hutch in Figure 11.12.4) with both EDXD and low-resolution powder diffraction setup. The second hutch (first side branch in Figure 11.12.4) will host a high-resolution, high-energy x-ray diffraction instrument for pair distribution function and diffuse scattering measurement, and a separate liquid spectrometer for buried interface study. These two hutches will be 12-ft W × 16-ft L × 10-ft H on the floor level.

Two 16 -ft (W) × 24 -ft (L) x16 -ft (H) hutches, one inline for EDXD white beam experiments and one as a side branch for ADXD experiments, are 3 feet *below* floor level. The height of these hutches above the floor is 13 feet. Each will host a large-volume press of approximately 20 tons weight, on a pedestal of 10×10 ft, resulting in an average floor loading of approximately 500 psf. In addition to the large-volume press, the long inline hutch, which is the most downstream hutch at the beamline, will host a strain mapping instrument with in-situ deformation capability, a MRT and DEI setup. The three experimental arrangements will be a permanent setup but will operate on a time-share basis. This arrangement allows longer term experiments, such as creep and stress corrosion fatigue, or thermal crack growth studies that require intermittent monitoring on a time scale of days.

In addition to experiments currently ongoing at the NSLS SCW beamlines, the higher critical energy, higher brightness, and optimized experimental infrastructure at the NSLS-II wiggler beamline will allow a new range of exciting experiments currently not possible anywhere else in the world. These will include experiments to simulate service conditions experienced by real engineering components while their internal stress state and structures are continually monitored by diffraction.

References

[11.12.1] E. Weihreter, et al., Proc. EPAC 2004, Lucerne, Switzerland (2004) 324-326. http://accelconf.web.cern.ch/AccelConf/e04/PAPERS/MOPKF012.pdf

[11.12.2] Z. Zhong, C. Kao, D.P. Siddons, H. Zhong, and J.B. Hastings, "X-ray reflectivity of sagittally bent Laue crystals," *Acta. Cryst. A* **59** 1-6 (2003).

[11.12.3] Z. Zhong, C. Kao, D.P. Siddons and J.B. Hastings, "Rocking-curve width of sagittally bent Laue crystals," *Acta Cryst, A* **58** 487 (2002).

11.13 A Hard X-Ray Imaging Beamline

11.13.1 Introduction

In a variety of synchrotron applications in materials science and engineering as well as in biological and medical sciences, X-ray imaging is the key to the investigation of structures from nanometer to millimeter scales. The subject areas of x-ray imaging studies vary widely and include materials microstructure/properties research, bone and cartilage growth and formation, small animal and soft tissue research, biomedical research such as tumor detections, structure and development of foams, and dynamics of complex fluid flow and nanofluidics. Additional areas where x-ray imaging is expected to have a significant impact in the future include time-resolved imaging of materials processing such as electrodeposition, imaging of subcellular organelle structures in frozen-hydrated biological cells, and 3D nanocrystallites, nanoclusters, and other nanostructures.

To satisfy the growing needs in the scientific community for x-ray imaging and to perform state-of-the-art research to advance x-ray imaging techniques, we proposes to build a 300 m long beamline dedicated for full-field imaging research and applications (see below). The beamline will be furnished with three core capabilities:

- static and time-resolved Phase-Contrast Imaging
- Diffraction-Enhanced Imaging with density reconstruction
- Fresnel Diffraction Imaging with high-resolution image retrieval

All three core techniques will include 3D tomographic capability. With the synchrotron x-ray beam brightness and coherence proposed at NSLS-II, this long beamline with the above core capabilities will be a unique, premier x-ray imaging facility in the United States, and thus will offer the scientific community a powerful tool for advanced structural and dynamic imaging applications in materials and biological sciences that is not currently available at existing DOE synchrotron facilities.

This section summarizes the preliminary plans of the scientific scope and the preconceptual design of the x-ray imaging facility at NSLS-II.

11.13.2 Scope of Scientific Program

X-Ray Imaging covers a wide range of techniques and applications. The NSLS-II XRI facility will focus on the following core experimental techniques: 1) Phase-Contrast Imaging, in both static and time-resolved modes, 2) Diffraction-Enhanced Imaging capability, 3) coherent Fresnel Diffraction Imaging, and 4) image retrieval and tomographic 3D reconstruction as an integral part of the facility.

A good portion of the scientific program requires a highly coherent x-ray beam in an energy range of 7–50 keV, and a large field of view with minimal source-size smearing. In addition, time-resolved imaging experiments will make use of the pulsed nature of the NSLS-II synchrotron x-rays with an aim to achieve a single-pulse temporal resolution of ~50 ps and a simultaneous high spatial resolution of ~1 μm.

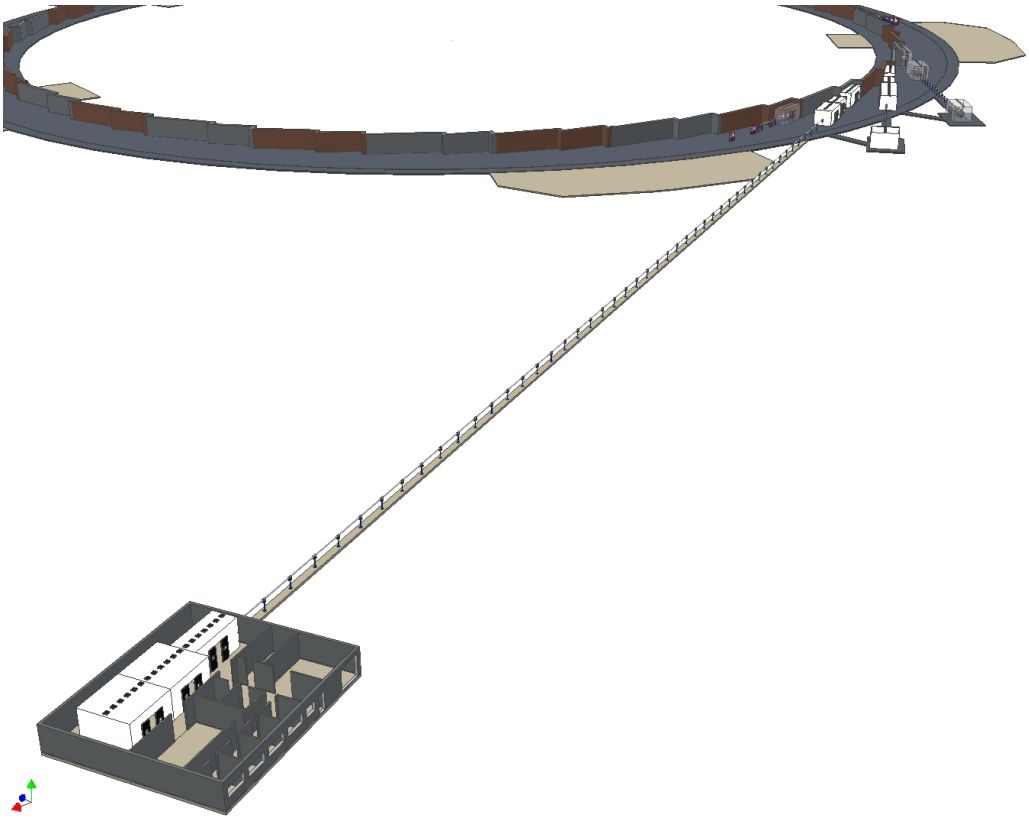

Figure 11.13.1 Conceptual layout of x-ray imaging facility showing a remote end station with three optical enclosures, the first of which is 300 m from the source.

11.13.2.1 Phase-Contrast Imaging

PCI is a coherence-based technique that makes use of the edge enhanced effects in near-field Fresnel diffraction and allows detections of weakly absorbing features in a specimen that are otherwise not observable in conventional absorption-based x-ray radiography. The spatial resolution with PCI is generally limited by the detector spatial resolution of 1–10 μm, which is well suited for many biological, medical, and materials science applications. A KB mirror system is planned, to provide a projection-imaging capability to allow increased spatial resolution down to 0.1–1 microns, if necessary.

Phase sensitivity directly depends on the source-to-specimen distance and the specimen-to-detector distance thus leading to the requirement of a long beamline for PCI applications, as illustrated in Figure 11.13.1. In addition, a long beamline provides an unobstructed larger field of view, which will be needed for imaging larger specimens in materials and medical sciences. Based on the designs and experiences of the existing synchrotron beamlines in the world, we propose to build a 300 m long beamline, which (assuming σ_x = 84.6 μm) will provide a phase sensitivity of 2 mrad within the typical spatial resolution of 1 μm, and will be able to detect minute refractive angular deviations of <1 μrad. These specifications will represent the state of the art in worldwide x-ray PCI capabilities.

PCI will be the work-horse facility of the XRI beamline, perhaps comprising 60 to 70% of the scientific work. Examples of anticipated research topics include:

- fracture mechanics of composites and biological materials
- materials microstructure/properties such as deformation and sintering
- bone and cartilage growth and formation
- small animal and soft tissue research on vascular and pulmonary functions
- porosity distribution in foods
- structure and development of plant seeds
- characterization of geological structures and microfossils
- cement mortar research
- structure and development of foams
- granular packing of non-equilibrium systems
- time-resolved studies of internal complex fluid flow and fluid sprays
- multi-phase fluid flow using particle image velocimetry

11.13.2.2 Diffraction-Enhanced Imaging

DEI, developed at NSLS by Dean Chapman et al. in the 1980s, makes use of a high-quality crystal analyzer to detect refracted or small-angle-scattered x-rays from the specimen. Because of high angular selectivity of the crystal analyzer, DEI can image very minute phase shifts due to density inhomogeneity in the specimen. In addition, in Ultra Small Angle X-ray Scattering (USAXS) mode, it can be used to image density inhomogeneities and fluctuations at a given spatial frequency of interest. Technically, DEI can be set up in one or all of three regimes: a) top of analyzer rocking curve for scattering background rejection, b) side of analyzer rocking curve to convert refraction-angle into intensity contrast, and c) far from analyzer rocking curve on direct beam to pick up USAXS signals at a given scattering angle. Examples of DEI applications include:

- microstructures and defects in materials
- deformation, sintering, and cracks formations
- porosity in bones and calcification effects
- soft tissue and vascular network detections in x-ray radiographs
- diagnosis of cancerous tumors in soft tissues

11.13.2.3 Coherent Fresnel Diffraction Imaging

Coherent FDI involves the collection of Fresnel or in-line holograms in near-field regimes and the reconstruction of original nonperiodic objects by image retrieval techniques. Compared to PCI, FDI seeks to record a complete set of Fresnel diffraction fringes at a greater detector-to-specimen distance, which allows quantitative determination of an object density function and permits spatial resolution reaching well beyond the detector pixel resolution. When working in the intermediate regime of a few Fresnel zones, FDI essentially becomes the far-field coherent diffraction imaging technique. Examples of potential applications include:

- structures of large biological functioning units (e.g., tissues, myocytes, muscles, bones, cartilage, etc.)
- identification of organelles and critical protein assemblies in biological cells
- self-assembly of macromolecule arrays with nano-templates and nano-grids
- structural imaging of multi-unit inorganic/small-molecule/biomolecule composites
- noncrystalline nanoparticles such as nanoclusters and nano-wire assemblies
- structural imaging of precipitates and defects in engineering materials
- topographic imaging of domain growths in ferroelectrics

11.13.2.4 Image Reconstruction

Image reconstruction software packages and associated user support will be an important and integral part of the XRI facility at NSLS-II. The software package will be developed either in-house or collaboratively with other research groups, and will include such programs as image analysis and pattern recognition in PCI, density reconstruction in DEI, phase-retrieval and reconstruction in FDI, and 3D tomographic capabilities in all three core research areas. Due to an extremely diverse scientific user community in this field, considerable user support and additional personnel are envisioned and will play a crucial role in enhancing the scientific productivity of the XRI facility.

11.13.3 Preliminary Conceptual Design

The proposed long x-ray imaging beamline (Figure 11.3.1) will consist of an undulator located on one of the low horizontal beta 5 m straight sections, a standard beamline front-end, a first optics enclosure, an experimental hutch at ~50 m from the source, a long beam transport, and a satellite XRI facility building that houses two experiment hutches at 300 m from the source. An optional second optic enclosure is included in the conceptual design to accommodate additional imaging optics in the future.

11.13.3.1 Undulator Source and Front End

The x-ray source for the XRI beamline will be an undulator 3 m long with a 1.9 cm period, producing a highly brilliant x-ray beam from 7–50 keV using third and higher harmonics in order to satisfy the partial coherence requirement for x-ray imaging applications. The undulator will be situated at a low-horizontal-beta straight section, producing a source size that is smaller than usual, with a correspondingly larger beam divergence. Based on experience at APS, this arrangement can improve phase contrasts considerably for low-density objects. Furthermore, it will increase the field of view to allow phase-contrast imaging of larger objects, such as an entire mouse.

The front-end will consist of standard beamline components, with special emphasis on beam position monitors and feedback to ensure a stable x-ray beam with <1 μrad angular variations.

11.13.3.2 X-Ray Optics and Window

The FOE will accommodate an x-ray beam aperture to filter unwanted radiation outside the undulator central cone, an adjustable white-beam slit, a liquid nitrogen–cooled, Kohzu-style Si (111) double-crystal

monochromator, and a harmonic-rejection double mirror with a low offset. Both the silicon crystals and the mirror will be highly polished with ultra-low slope errors (<1 μrad). The monochromator will cover a tunable energy range of 7–50 keV, while the mirror will consist of multiple coating stripes to provide fixed cut-off energies at 9 keV, 15 keV, 18 keV, and 24 keV. For higher energy applications (>24 keV), the mirrors will be moved out of the beam.

Both the monochromator and the double mirror optics, as well as other beamline components, will be designed to allow white beam to pass through. It is envisioned that all x-ray optics and beamline components will be in ultra-high vacuum, with an x-ray window at the upstream end of the hutches as the only vacuum barrier. The window will be made of highly polished beryllium or diamond or some other materials such as SiN_3 to minimize any phase contrast effects from inhomogeneities and/or imperfections.

11.13.3.3 Experiment Hutches

There will be three experiment hutches at the XRI beamline. Hutch B will be the first experimental enclosure downstream of the FOE and will be located at around 50 m from the source within the NSLS-II building. This hutch will be about 5×10 m in footprint and will be white-beam compatible. It will be used mostly for coherent FDI development and for time-resolved imaging using both monochromatic and pink beams.

Experiment hutches C and D will be located in the XRI satellite building at around 300 m and 315 m from the undulator source, respectively, both 5×15 m in footprint. Hutch C will focus on materials applications using direct PCI, while Hutch D will be dedicated to biological and biomedical imaging applications. The separation of the two experiment enclosures is necessary due to environmental safety concerns for certain biomedical and small animal specimens. It is also envisioned that Hutch D may be an integral part of a future expansion to form a clinical laboratory at the XRI facility, much like the existing enterprise at Elettra Light Source in Trieste, Italy.

The current plan is build the C and the D hutches as monochromatic enclosures so that the beam transport connecting the remote building and the main building will not require white-beam capability.

11.13.3.4 Second Optic Enclosure and Beam Transport

A Second Optic Enclosure just upstream of Hutch C will be designed and constructed inside the XRI facility building. This SOE will serve two purposes. First, it will offer the possibility of housing a second double-crystal monochromator in case the first monochromator in the FOE, more than 250 m upstream, introduces significant stability issues magnified by the long lever arm. Second, the SOE may house secondary focusing optics, such as a compound refractive lens or a pair of KB mirrors to allow projection imaging using a focused monochromatic x-ray beam.

11.13.3.5 Experimental Instrumentation

The proposed XRI facility will provide state-of-the-art instrumentation for coherent FDI, PCI, and DEI applications, with 3D tomographic and time-resolved capabilities. Essential instrumentation components include long (>3 m) optical tables, precision translation and rotation stages, precision polished adjustable slits and apertures, motion controls and signal detection electronics, and a variety of area detectors, including lens-coupled and direct-detection Charge-Coupled Device cameras with small pixel sizes (0.5–10 μm), low noise, and large dynamic range (>50,000). In addition to CCDs, fast area detectors such as pixel-array detectors with MHz frame rates will be essential for time-resolved imaging experiments. Other important instrumentation includes x-ray beam shutters and timing choppers, highly polished silicon single-crystals for DEI, and a computer cluster for image analysis and tomographic reconstruction and visualization.

11.13.3.6 Conventional Laboratories and Offices

The XRI facility in the satellite building will house one dry laboratory and one wet laboratory space, plus an enclosure or laboratory space that is suitable to accommodate live small animals. At least 10 standard office spaces and a small conference room will be included in the satellite building, along with a common area for users.

11.14 A Small-Angle X-Ray Scattering Beamline

The high-brightness x-ray beam of NSLS-II will greatly improve the capabilities of Small Angle S-ray Scattering. The lowest accessible scattering vector (q), a benchmark specification for SAXS instruments, will be significantly extended. This is true even with small beam sizes (on the order of microns) and at relatively high x-ray energies (>20 keV). A successful SAXS beamline will directly translate into an array of new scientific opportunities, such as the possibilities to follow dynamical events in biological systems with time resolution as fast as microseconds and to use SAXS as a scanning probe microscope to examine the local structures that underlay micro-textures.

11.14.1 Conceptual Overview

This beamline will be based on a 3 m long undulator source located in a high-β 8 m straight section. The beamline is expected to be ~90 m or longer and include two end stations. The main end station will have two hutches, with the extra downstream hutch housing the USAXS detector. The side station will only utilize part of the x-ray beam produced by the undulator. It will therefore have reduced performances compared the main station and will operate in a quick-access mode to accommodate preliminary study type of measurements.

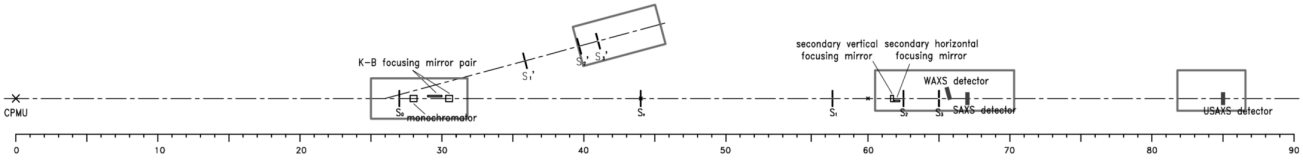

Figure 11.14.1 Conceptual layout of the SAXS beamline. See text for details.

The optical elements for the main SAXS station include a cryogenically cooled monochromator, two KB focusing mirror pairs and a series of collimating slits. This branch of the beamline will operate windowless to provide the best support for experiments at low x-ray energies (phosphorus and sulfur K-edges at ~2 keV) or those where beam coherence is a concern.

The side station is intended for simple exploratory measurements. Its monochromatic x-ray beam will be provided by a graded multilayer upstream of the main monochromator. Three sets of slits along the beam path provide beam collimation. No other optical component is necessary. Since the monochromator does not capture synchrotron radiation in the central cone and the x-ray beam continues to diverge after the monochromator, the flux at the sample will be much lower compared to that in the main station (a factor of ~100, depending on the position of the monochromator transverse to the beam direction). Nonetheless, this end station is still expected to provide performance similar to that of the current undulator-based SAXS beamline at NSLS—or better.

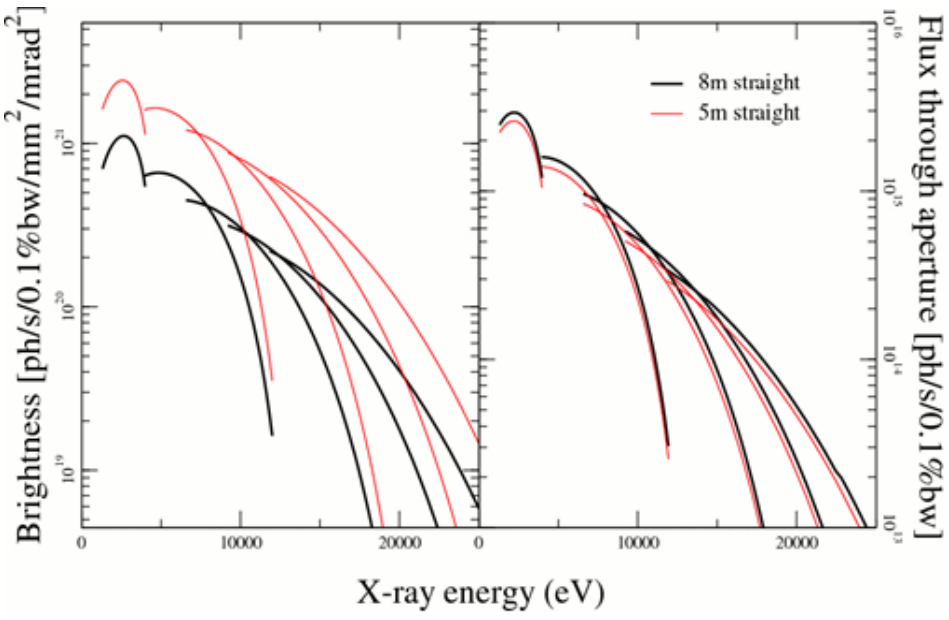

Figure 11.14.2 The characteristic of the 3 m CPMU. The aperture used in the calculation is 1.2 mm (H) by 0.6 mm (V) at 30 m from the source, corresponding to the beam size intercepted by the primary KB mirrors.

11.14.1.1 Radiation Source

The source will be a 3 m long CPMU, with 158 1.9 cm periods located in a high-β 8 mstraight section. Its brightness and flux through an aperture as calculated by SPECTRA are shown in Figure 11.14.2 (see also Section 11.2.). Note that due to the lower beam divergence, this device produces higher flux through the aperture in a high-β 8 m straight section than in a 5 m straight.

11.14.1.2 Focusing Optics

Tentatively, the focusing optics at this beamline will be a pair of KB mirrors. At 30 m from the source, the FWHM beam spot is ~0.53 mm (H) × 0.34 mm (V) (calculation by XOP/XUS, 12 keV, fifth harmonic). Assuming that the x-ray incident angle onto the primary KB mirror pair is 3 mrad, mirror lengths of 0.4 m (H) and 0.2 m (V) result in an effective aperture of 1.2×0.6 mm^2 and will capture most of the x-ray beam. With these short lengths, it is relatively easy to achieve low figure error.

Note that the field of x-ray focusing optics is quickly developing. By the time this beamline is built, alternative focusing optics such as compound refractive lenses may offer better performance then mirrors, especially for experiments that require relatively high x-ray energies (>20 keV).

11.14.2 Performance Estimate for the Main SAXS Station

The performance estimate below assumes 12 keV x-rays (K=1.322). At this energy, the flux captured by the primary focusing mirror, or an equivalent aperture of 1.2 mm × 0.6 mm at 30 m from the source is 3.7×10^{14} ph/0.1%BW. As this is only a preconceptual design, the figure error of the mirrors will be ignored in the simulations.

11.14.2.1 USAXS/SAXS/WAXS

For the majority of the SAXS/WAXS/GISAXS measurements, the primary KB pair will 1:1 focus the beam midway between S_1 and S_2. The sample will be located immediately after the guard slits, S_3. The SAXS detector will be located 2 m downstream of the sample. This detector will be specially designed so that the

scattering at very low angles will pass through the detector and reach the USAXS detector located at the end of the second hutch, 20 m from the sample. The following table shows two typical beamline configurations.

Table 11.14.1 Two Typical SAXS Configurations.

	SAXS/WAXS	USAXS/SAXS/WAXS
S_1 and S_2	0.4 mm (H) x 0.2 mm (V)	0.1 mm x 0.1 mm
S_3	0.8 mm (H) x 0.4 mm (V)	0.2 mm x 0.2 mm
Beamstop	2 mm (H) x 1 mm (V) at 2 m	3 mm at 20 m
q_{min}	$3x10^{-3}$ Å^{-1}	$5x10^{-4}$ Å^{-1}
Beam utilization*	91%	28%

* Percentage of the photons reflected by the KB focusing mirrors that reach the sample.

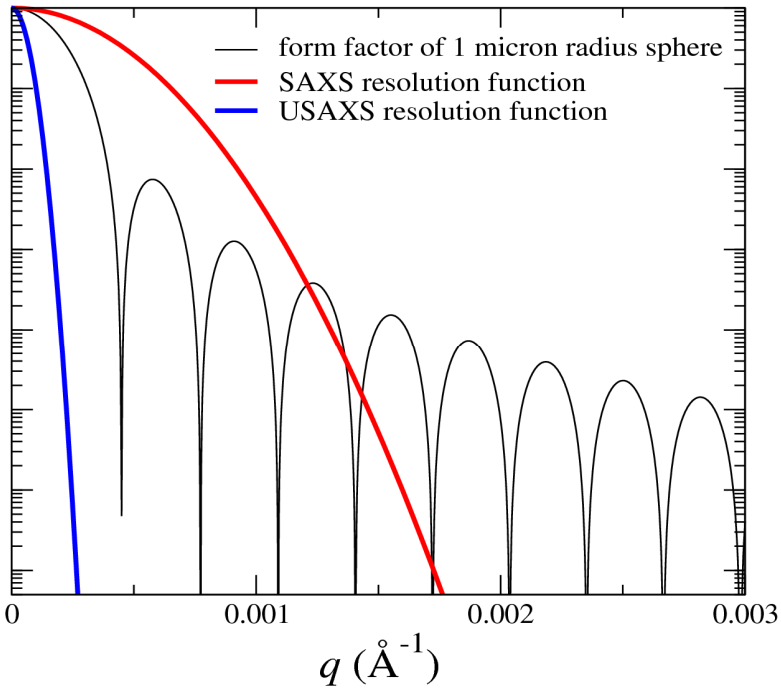

Figure 11.14.3 Width of the resolution for the SAXS and USAXS configurations. Clearly, at very small q, a sharp resolution function is necessary for measurements that involve near-micron length scale.

In the USAXS configuration, the lowest q of 5×10^{-4}Å^{-1} corresponds to more than 1 μm in real space and should be satisfactory for the vast majority of measurements. In fact, this is also roughly the lowest q achievable with Bonse-Hart cameras. For instance the UNICAT at APS advertises a q_{min} of 0.0001Å^{-1} , and corrected example data only go as low as 5×10^{-4}Å^{-1}. For samples with even larger characteristic lengths, topography, or scanning probe microscopy might work better than SAXS.

Note that the USAXS station is an inseparable part of this instrument. The angular resolution in SAXS measurements using slit collimators is determined by three factors. Both the detector point spread function and the beam spot size on the sample in effect smear out the scattering pattern and result in degraded angular resolution. So does the beam divergence seen by the sample. Increasing the sample-to-detector distance reduces the first two contributions; reducing the slits size improves the last two; increasing the distance between S_1 and S_2 improves the last. Although in principle the SAXS detector covers qs that are nearly as low as the USAXS detector, the long distance between the sample and the USAXS detector is necessary. This is because of the q-resolution due to the pixel size of the detector; the beam size on the sample improves with longer sample-to-detector distance. One way to visualize this q resolution improvement is the following. The

beam size and pixel size both smear out the scattering pattern on the detector. The degradation of the image is reduced if the pattern itself is magnified before smearing.

11.14.2.2 Microbeam SAXS

The second pair of KB mirrors provides beam sizes down to a few microns. This is done in combination with the primary KB pair, which first focuses the beam at S_B with ~2:1 demagnification. The second KB pair then images the virtual source defined by S_B to the sample position. The combined effective demagnification is ~10:1.

Since the FWHM source size is ~300 μm (H) and ~10 μm (V), a 10:1 demagnification is not sufficient to reduce the focused beam size to ~1 μm in both directions. Instead, the actual beam size at the sample will be tailored by adjusting the aperture size of S_B. On the other hand, the beam divergence, limited by the accepting angles of the first KB pair, is 0.04 (H) × 0.02 mrad (V) (1.2×0.6 mm at 30 m). The divergence of the beam focused at the sample will be therefore 0.4×0.2 mrad, translating into minimum qs of 0.005 $Å^{-1}$ (H) and 0.003 $Å^{-1}$ (V). The aperture size of S_0 provides control on the beam divergence. Again, the micro-focusing optics is not required to be a KB mirror pair, but it should have long working distance to allow space for auxiliary instruments such as an optical microscope to perform simultaneous multi-probe measurements.

11.14.2.3 USAXS with a Linear Detector

For measurements that request very low q, it is possible to use the beamline in a configuration similar to a Kratky camera. In this configuration, the beam is focused the vertical micro-focusing mirror to a linear detector at the end of the beamline. The FWHM beam size will be ~60 μm at the detector, mainly due to figure error of the focusing mirror (assumed to be 0.1 μrad, which will be the target of R&D). A beam stop size of 0.3 mm is feasible. The lowest q can therefore be reduced by a factor of 10 compared to the USAXS configuration described in Section 11.14.2.1, not considering the background scattering from the slits. Again, the discussion above on angular resolution still applies. A tight slit collimation or data de-smearing will be necessary.

11.14.2.4 USAXD with Long Working-Distance Focusing Optics

Compound refractive lenses can focus the x-ray beam into a sub-micron spot. As in visible optics, when the sample is positioned before the lens, the pattern at the back focal plane of the lens is the Fourier transform of the sample transparency. The resolution of the scattering pattern is limited by the size of the focused beam (in fact, this is always the case when focusing the beam at the detector in a diffraction experiment). It has been demonstrated [11.14.1] that, with long lens working-distance (3 m) and sufficient resolution of the detector, this method can record diffraction patterns from crystals of micron-sized and larger particles.

11.14.3 Supporting Facilities

Ideally there should be two labs associated with this beamline. One will be used for preparing biological samples that require wet chemistry. Beside a water purifier and several sinks, this lab should also be equipped with standard biochemistry instruments such as balances, pH m, refrigerators and incubators, etc. The second lab will be used for polymer type of work using organic solvents (e.g., chloroform) and must have one or two fume hoods that can handle these solvents. A shared clean room is also desirable.

Reference

[11.14.1] A.V. Petukhov, J.H.J. Thijssen, D.C. 't Hart, A. Imhof, A. van Blaaderen, I.P. Dolbnya, A. Snigirev, A. Moussaïd, and I. Snigireva, "Microradian X-ray diffraction in colloidal photonic crystals," *J. Appl. Cryst.* **39**:137 (2006).

11.15 A Photoemission Beamline, ARPES, at 0.1 meV and 10 meV

11.15.1 Conceptual Overview

Strongly correlated electron systems present some of the biggest challenges in condensed matter physics today. The unscreened interactions between the electrons result in a range of exotic and poorly understood phenomena including high T_c superconductivity in the cuprates, colossal magneto-resistance in the manganites and giant thermoelectric effects in the cobaltates. Several factors can influence the properties of strongly correlated materials including dimensionality, competing orders, disorder and inhomogeneities. By way of example, the nature of the low-energy excitations in any system depends on the *dimensionality* of the system; in 3D systems, the excitations are typically well-defined quasiparticles, whereas in 1D systems, the elementary excitations are collective excitations that represent spin-charge separated entities. In 2D systems the situation is much less clear. Indeed, the nature of the low-energy excitations in the 2D cuprates remains a topic of considerable debate.

Driven by the quest to understand high T_c superconductivity, Angle-Resolved PhotoEmission Studies has again emerged as one of the key probes of the electronic structure and associated dynamics of condensed matter systems. Among the many spectacular successes using ARPES in the study of the cuprates, are the measurement of the doping dependent electronic structures and Fermi surfaces and their dramatic deviation from the conventional rigid band picture, the detection of the d-wave superconducting gap, the observation of an anisotropic pseudo-gap, and the discovery of a mass-renormalization associated with possible strong electron boson coupling. Indeed the latter observation has raised the hope that the mechanism of high temperature superconductivity may finally be resolved.

Outside of studies of the cuprates, the ARPES technique has had significant impact on a range of other problems in condensed matter including electron-phonon coupling, charge density wave transitions, and the formation of quantum well states in thin films and multilayers. In the latter area, the extension of the technique to include the capability of measuring spin polarization of the photoemitted electrons as well as energy and momentum has enabled the identification of spin-polarized quantum well states in the technologically important magnetic multilayers. Indeed, it was the Spin Polarized PhotoEmission Studies of these systems that first pointed to the importance of understanding the spin-dependent scattering at the interfaces in the multilayers. SPPES has also proven important in the study of a range of other low-dimensional magnetic systems, including surface and thin films.

The classical Fermi surface probes—such as de-Haas, van-Alphen, positron annihilation, and Compton scattering—apply only to the analysis of bulk materials but do not easily allow the mapping of the Fermi surfaces of 2D structures such as ultrathin films. Photoemission, on the other hand, can provide k-resolved maps of the Fermi surfaces of these interesting systems. This information is an important component in obtaining a full understanding of the physical behavior of such nanostructures. This is particularly true in the field of magnetic nanostructures, where the possibility of useful technological application has stimulated a considerable effort in generating remarkable spintronic devices.

Here we outline the preconceptual design for a beamline that will combine the unique capabilities of NSLS-II with further developments in these spectroscopies and with the use of Molecular Beam Epitaxy for the growth of thin oxide films. This latter capability will dramatically enhance the range of materials available for study as it will remove the current restrictions associated with the “cleavability” of samples and will also allow the detailed study of atomically engineered nanoscale systems with both magnetic and nonmagnetic ground states.

11.15.1.1 Source

Undulators to cover the range 8–1500 V must be slightly aperiodic to suppress higher orders and must be capable of circular polarized light over the range 400 to 2000 V, to cover the TM L edge and the RE N edge.

11.15.1.2 Optics

This beamline optics is essentially similar to the one for high-resolution soft X-rays, but extending its range down into the UV, from 8 – 1500 V. The design is with plane gratings of variable spacings. Energy resolution will be ~0.2 meV at 10 eV and ~15 meV at 1000 eV. The spot size for the first end station is 10 μm and for the second end station is 1 μm.

11.15.1.2.1 Motivations/Justifications for Source and Optics

The **very low energy range** (down to 8 eV) is required for bulk-sensitive measurements, because at the lower energies the escape depth of the photoemitted electrons is considerably longer. Furthermore, the very highest energy resolution will be achievable at the lowest energies.

The **high-energy r**ange (up to 1500 eV) allows the excitation of many core-levels and therefore permits XPS for sample characterization. However, the high energies can also be used as a means of achieving more bulk sensitivity, both in direct photoemission and in resonant photoemission. The latter technique will allow studies of the site-specific electronic structure. The limit of 1500 eV has been chosen as a compromise to cover the L edges of the TM and some of the N edges of the RE, but at the same time allow the dimensions of the (entrance) mirrors to be reasonable.

11.15.1.2.2 Circular Polarization

In the study of magnetic multilayers, is it very useful to have an element-sensitive probe of the magnetic properties of a multilayer; this also provides a bulk sensitivity that will complement the surface sensitivity of SPPES.

Well-focused photon beams on the samples will enable studies of nanoscale systems, with an emphasis on studies of the inherent inhomogeneities. This also recognizes that in the field of strongly correlated systems, many newly discovered materials are initially very small in size, on the order of tens of microns.

11.15.1.3 End Stations

The proposed beamline would have two photoemission end stations. The first would be optimized for ultrahigh-resolution photoemission for Fermi surface mappings and studies of low-energy excitations, and would have as its main components a 2D electron spectrometer coupled to a low-temperature cryostat for sample cooling down to 1K. It is also possible that the 2D electron spectrometer in this end station will be replaced by a new time-of-flight detector currently being investigated at BNL. The second end station will also be equipped with an electron spectrometer, but this will be coupled to a vectorial spin-detector for studies of magnetic systems. In this second end station the sample cryostat will cool down to approximately 10K. These two end stations will be in-line, separated by refocusing optics to further reduce the spot size in the second end station. A state-of-the-art MBE system for in-situ preparation and characterization of films and multilayers with atomic level control will be shared and accessible by the two end stations.

A schematic of the envisioned system is shown in Figure 11.15.1.

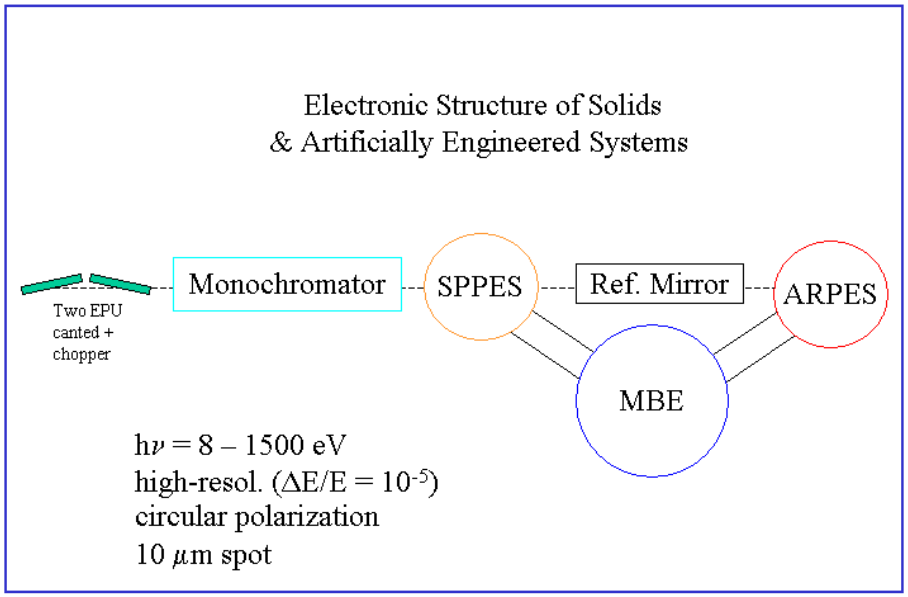

Figure 11.15.1 Schematic of the proposed photoemission beamline at NSLS-II.

11.16 X-Ray Bending Magnet and Damping Wiggler Beamlines

Three different general kinds of beamlines that view bending magnet or damping wiggler sources are envisioned.

One type of beamline would deliver white beam to the experimental station. X-ray topography and x-ray footprinting alike would benefit from access to such a beamline. A focusing mirror could be installed to increase the intensity of the white beam delivered to the sample and also tailor the spectrum (i.e., eliminate high photon energies).

A second type of beamline would be a tunable, monochromatic beamline using a double-crystal monochromator with no focusing elements. Various kinds of EXAFS, powder diffraction, x-ray standing wave, and x-ray topography experiments would benefit from access to such a beamline. Also, for experiments that require high photon energies (above ~20–25 keV), this sort of beamline might be useful, because focusing mirrors are unlikely to work well at such high energies, and sagittal focusing using the second monochromator crystal becomes more challenging using the Bragg geometry.

A third type of beamline would be a tunable, monochromatic beamline using a double-crystal monochromator with focusing elements, either focusing mirrors or sagittal focusing crystals, or both. EXAFS, photoemission, some x-ray standing wave, and some powder diffraction experiments would benefit from access to this beamline. X-ray crystallography and scattering experiments in general would also benefit, but those beamlines are addressed by other aspects of the proposed design. A tunable monochromatic beamline might also incorporate a collimating mirror upstream of the monochromator, to reduce the vertical beam divergence as much as possible, improving the energy resolution of the monochromator.

All three types of beamlines could be arranged to view bending magnet and damping wiggler sources alike. They would, however, possess distinguishing characteristics, depending on which kind of source is viewed. The beamlines that view the damping wiggler sources would require crystal monochromators and white beam mirrors (if desired) that must cope with the high heat load produced by such sources. The

beamlines that view the bending magnet sources, on the other hand, would not be faced with such a challenge, and crystal monochromators that are used on x-ray bending magnet beamlines might need only relatively minimal cooling. (NSLS-II bending magnet beamlines would have to deal with half the power of current NSLS x-ray bending magnet beamlines, and a beryllium window, if used, would absorb most of that power.)

Owing to the higher energy spectra produced by damping wiggler sources, the damping wiggler beamlines and hutches would need significantly more radiation shielding than the bending magnet beamlines would. In fact, for the bending magnet beamlines, the stainless steel vacuum beam tubes and chambers that will be used in these beamlines would probably provide sufficient shielding.

Finally, given the foreseen high demand for access to beamlines that will view damping wiggler sources, we are investigating the possibility of using canted damping wigglers installed in single straight sections, with each canted wiggler serving an independent beamline. We envision a canting angle, between successive damping wigglers, of between 3 and 5 mrad (this is discussed briefly elsewhere in the CDR, and will be addressed in more detail in the Title I and Title II designs); at a later stage it will be determined what canting angle could be achieved. Designing a sector of such beamlines could pose a significant challenge due to space restrictions, but could be simplified if one beamline in such a sector is designated to provide strictly white beam to the experimental station, without optical components (or perhaps just a single mirror). The white beam experimental station that terminates such a beamline could be positioned somewhat upstream in the sector, and beam tube(s) through which the adjacent canted wiggler beam(s) would transit could span through such a station, with the relevant optics positioned downstream. Also, horizontally deflecting optics such as mirrors or monochromator crystals could be installed to further separate the beams that are produced by the canted damping wigglers.

Because of the range of experimental techniques that would be addressed by these beamlines, in this section we address the implications of selected techniques for the beamline and end-station designs, beginning with EXAFS, which is likely to be the application most in demand on these beamlines. Thus, most of this section addresses EXAFS considerations for these beamlines. Many of these considerations apply also to the other techniques that would be addressed by these beamlines. X-ray photoemission would benefit from access to these beamlines as well, but would have end-station needs similar to those of photoemission setups on VUV and soft x-ray beamlines; therefore, the relevant considerations are not described here. In fact, photoemission setups would benefit from simultaneous access to the VUV, soft x-ray, and hard x-ray ranges, and therefore a photoemission beamline might incorporate optics that address each of these energy ranges.

11.16.1 EXAFS Considerations

The two paramount requirements for EXAFS are energy range and stability. EXAFS scans typically extend 1 keV above the absorption edge, and edges for elements of interest range from 1 to 35 keV. The available broad-spectrum ranges for damping wiggler and bending magnet sources (7–35 and 1–7 keV, respectively) combine to fit this requirement, with 80 to 90% of expected analyses needing a damping wiggler source.

Stability requirements include both energy and positional stability. Energy stability, the repeatability or energy drift over time, is vital to near-edge spectroscopy for speciation and oxidation-state identification. The required energy stability is <0.1 eV. Positional stability, critical for heterogeneous samples and for Grazing Incidence XAS applications, refers to the location of beam relative to the sample over time and over a 1000 eV energy scan. For bulk XAS, beam position should not vary by more than 50 μm, or 10% of the microbeam spot size. Both the required energy and positional stability can be achieved with a combination of engineered design and dynamic feedback within beamline optics. For example, NSLS beamline X15B achieves <10 μm positional and <0.1eV energy stability over 72 hours, 140–280 mA ring current, and 800 eV scans, with a 0.75 mm spot size at 2.15 keV [11.16.1]. It is anticipated that *ring* stability issues will be significantly improved at NSLS-II as a result of top-off mode and the increased attention placed on electron beam stability and noise mitigation (mechanical, thermal, and acoustic) throughout the facility. It is imperative, then, to

ensure that *beamline* design maintains that degree of stability, and does not introduce noise or variations with energy.

11.16.2 Configuration for Canted Damping Wiggler Sources

Here we describe an example beamline layout and optics configuration for two beamlines that view canted damping wiggler sources, as shown in Figure 11.16.1. The associated hutches are shown in Figure 11.16.2 These examples are optimized for 7–25 keV, the energy range applicable to most bulk XAS and microbeam applications, and illustrate some application-specific requirements (e.g., environmental science and geoscience). Beamline and end-station components in these examples are as follows:

1. A beryllium window isolates the beamline vacuum system from the ring vacuum, and absorbs much of the lowest-energy power/heat load. For a high-power damping wiggler source, it will also be necessary to provide carbon filters (described elsewhere in this document) before the beryllium window to absorb the lowest-energy portion of the wiggler spectrum, or to furnish a diamond window (instead of a beryllium window) that would also serve a filtering purpose (this is described elsewhere in the CDR).
2. There will be beam-defining apertures and beam diagnostic instrumentation.
3. A harmonic-rejection/collimating mirror conditions the beam prior to the monochromator to eliminate higher harmonics and to enable maximum energy resolution from the monochromator. This may not be needed for the higher energy ranges of the damping wiggler beamlines (where harmonics are not an issue and the source is already well collimated), but would be important for most XAS applications in the 7–25 keV range. For microbeam applications, the focusing optics can assume the harmonic-rejection role.
4. A double-crystal monochromator, water- or cryogenically cooled, will have the required energy and positional beam stability (a fuller description appears in Section 11.3). Current monochromators for conventional hard x-ray beamlines employ two nondispersive (parallel) Bragg reflections from an appropriate crystalline material, the most common being Si(111), suitable for 2–24 keV. Other materials include Si(311) for higher energies, and Ge, InSb, YB_{66}, quartz, and beryl for lower energies. For silicon monochromators it is possible to fabricate such double-crystal monochromators as a monolith (i.e., a channel-cut monochromator), although consideration must then be given to the change in exit-beam height with energy. New natural and synthetic crystalline and assembled multilayer or grating materials are being developed that will have improved resolution and stability, compared with materials currently in use. Because higher resolution naturally results in narrower bandpass (and lower flux), the brighter sources at NSLS-II will enable the use of these new materials.
5. Macro-focusing optics will be used to collect a substantial fan of radiation (up to ~1 to 2 mrad) and focus it to ~1 mm at the sample. This allows for smaller samples, lower concentration, and also provides a longer beamline length for the geometric considerations of having two canted damping wiggler beamlines separated by only a few mrad. Focusing can be achieved using either a mirror or sagittal focusing of the second crystal of the monochromator.
6. There will be a final beryllium window vacuum barrier.
7. Micro-focusing optics will consist of advanced KB mirror optics or hard x-ray zone plates. Variable focus (~10 to ~1 μm) will tailor resolution to specific experiments. Focal length needs to be long enough to accommodate a variety of sample types as well as fluorescence detection and optical imaging apparatus.
8. The sample stage will have important features including high translation and rotation resolution, cooling capability, high-quality optical imaging, and adaptability for various sample types, in-situ cells, solid or liquid samples, and different mounting materials. Motion should include rotation and should enable both horizontal and vertical sample orientations for Grazing-Incidence XAS. Detectors will include I_0, transmission and reference channels, advanced solid state detector arrays for high-throughput/low target

signal fluorescence detection, simultaneous powder/micro-diffraction, and available electron-yield detection.

9. The end-station enclosure (within the experimental hutch) will be suitable for experiments requiring a controlled atmosphere (e.g., environmental science and catalysis). This enclosure will be capable of operation open to air, as a vented fume hood, or as a "glove box" for sample manipulation and analysis under controlled atmospheres (especially for oxygen-sensitive samples). Both the stage and enclosure should be designed to accommodate radioactive samples, with respect to containment, survey, and decontamination.

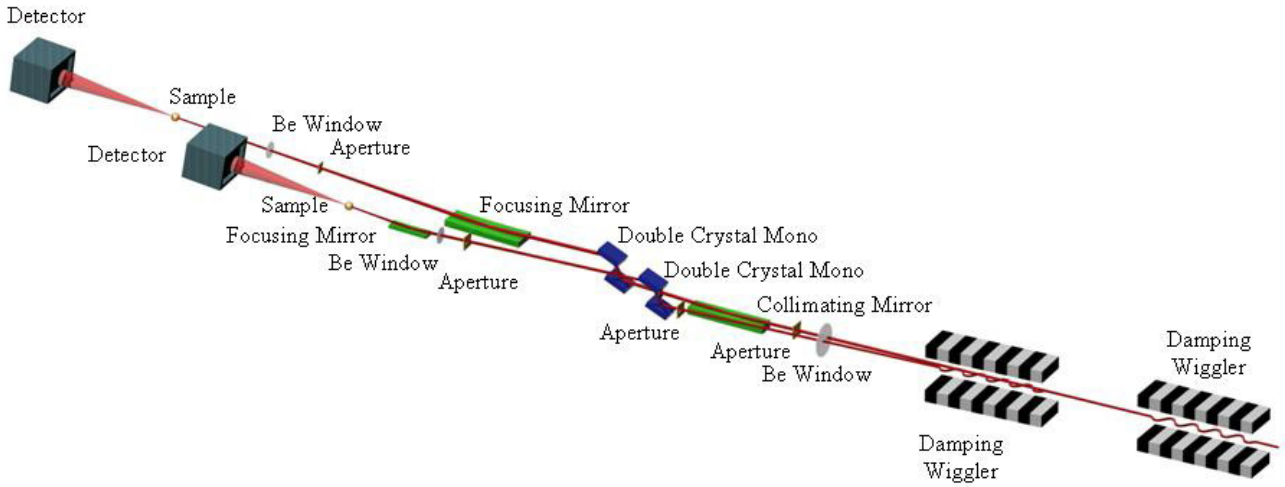

Figure 11.16.1 Conceptual view of canted damping wiggler beamlines.

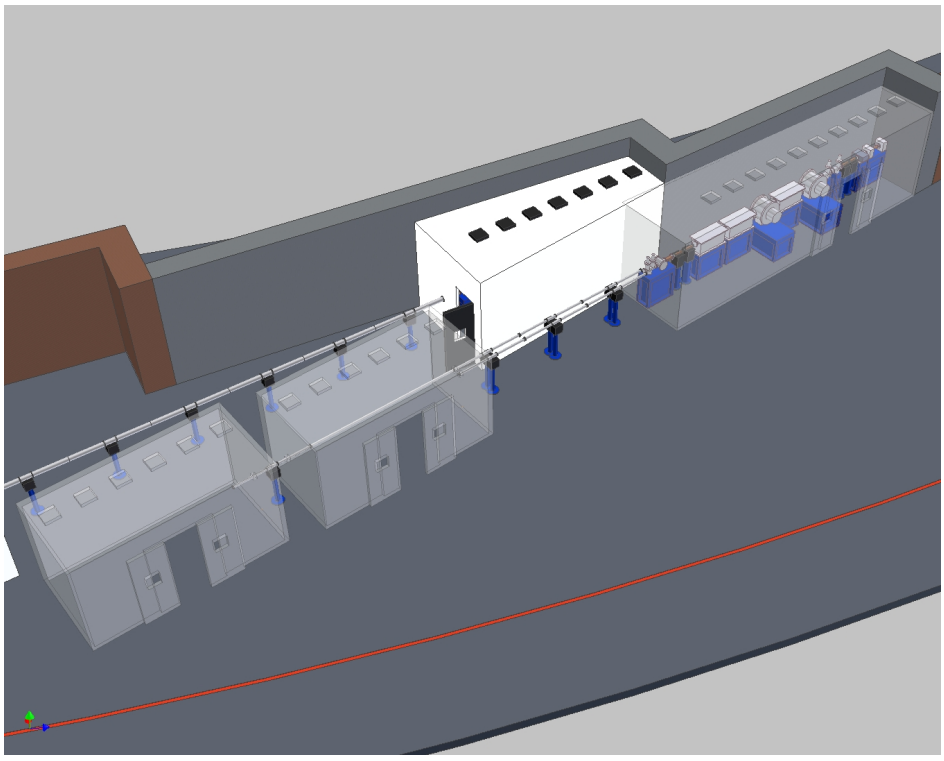

Figure 11.16.2 Conceptual layout of hutches associated with canted damping wiggler beamlines shown above. The white hutch illustrates a potential adjacent bending magnet first optics enclosure.

11.16.3 Configuration for Bending Magnet Sources

Here we describe an example beamline layout and optics configuration for beamlines that view bending magnet sources, as shown in Figure 11.16.2. Note that these examples are optimized for 1–7 keV, the energy range applicable to light element and specialized bulk XAS and microbeam applications (e.g., applications described in [11.16.2]). Here we call attention only to differences in the components compared with their counterparts in damping wiggler beamlines:

1. Bending magnet beamlines used below 4 keV cannot have a primary beryllium window. Instead, for these beamlines a thin (~2 μm) carbon foil would serve as a differential-pumping vacuum barrier and an absorber of very-low-energy power.

3. Harmonic rejection is especially important for lower energy ranges, where the harmonics are likely to reach absorption edges of transition metals or other common matrix elements. This mirror also protects monochromator crystals that are sensitive to radiation damage. For example, beryl crystals, used in the 800–1500 eV range, are destroyed by radiation of energy greater than 5 keV.

5. Macro-focusing optics on bending magnet beamlines would collect a wider (~3 mrad) fan than counterpart optics on damping wiggler beamlines. Essentially, this is made possible by the steeper incidence angles at lower photon energies used with focusing optics such as toroidal mirrors.

6. The final beryllium window vacuum barrier must be ultrathin and suitable for x-rays of energy >1 keV. A polymer-supported beryllium window 12 μm thick has been tested and is currently in use at NSLS beamlines X15B and X19A. This is essentially transparent above 1.8 keV and has acceptable transmission down to ~1 keV, while isolating high vacuum from He atmosphere (Moxtek Corporation).

7. There would be secondary focusing optics for microbeam.

8. This end-station enclosure would typically operate with a helium atmosphere for the transmission of low-energy beam.

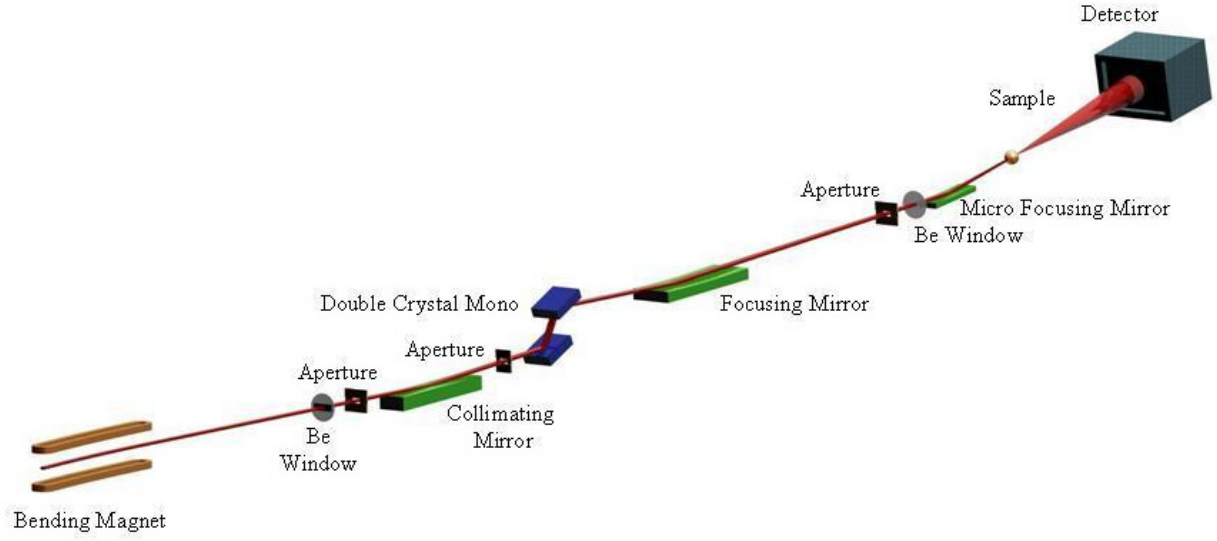

Figure 11.16.3 Conceptual view of a generalized bending magnet beamline. The second focusing mirror (“micro focusing”) is optional.

11.16.4 Computing and Controls

All NSLS-II beamlines will have a uniform control system interface, as described in Section 11.6. Specific operations for XAS and microbeamlines include control of monochromator energy, spot size and focus, sample position, optical image capture, and detector control. It will be useful to have capabilities for automation of a series of scans or sequence of samples, as well as for on-the-fly data evaluation. Quick-EXAFS data collection (i.e., very rapid scanning of the monochromator through the entire EXAFS scan range) will be important, as will 2D and 3D spectroscopic image analysis.

11.16.5 Conventional Facilities

Conventional laboratory facilities are needed for sample preparation, mounting, and characterization; microscopy with image capture; powder and solution mixing; anaerobic handling in a glove box (with anaerobic transport of samples to interface with the beamline end station enclosure); and handling of the BNL "benchtop dispersibles" classification of radioactive materials. These needs are expected to be met with the Laboratory Office Buildings of NSLS-II.

11.16.6 Special Considerations for Biological X-Ray Absorption Spectroscopy

X-ray Absorption Spectroscopy can be used to measure the transition of a metal atom from core electronic states to excited electronic states [11.16.3]. Spectral analysis near this transition, "X-ray Absorption Near-Edge Structure," provides information on the metal's charge state and geometry. Spectral analysis above the absorption edge (up to 10–15% above the edge in energy), "Extended X-ray Absorption Fine Structure," provides complementary structural information, such as numbers, types, and distances of ligands or neighboring atoms. Both techniques are valuable for studying a variety of metal sites in biological systems. Recently, these techniques have been extended to metallo-proteomics methods, where hundreds of proteins are assayed for their metal content [11.16.4]. The user group for biological XAS at the existing NSLS has been substantial and is expected to be productive for the foreseeable future.

Traditionally, XAS, like most other spectroscopies, has been used as a static probe of structure. NSLS-II, with the 100-fold higher flux densities available from damping wigglers compared to NSLS x-ray bending magnet sources, provides the opportunity to extend x-ray absorption measurements into the time-resolved realm, potentially revolutionizing the study of biochemical and bioinorganic systems. For example, proteins containing metal (hemoglobin is an example) react over extremely quick time scales, sometimes as fast as a picosecond. NSLS-II will allow much faster time scales to be probed than can be done currently with XAS; this capability will be provided by a combination of timing studies (pump-probe), fast mixers (on the microsecond timescale), and freeze–quench devices [11.16.5].

11.16.7 Anticipated Beamtime Demand vs. Capacity

Most EXAFS applications and demand will be for damping wiggler sources. Efforts to increase this capacity include using canted shorter damping wigglers to supply radiation to multiple beamlines, and using more creative beamline designs, such as beam-splitting optics. Although this is still under evaluation, as described elsewhere in the CDR, for canted damping wiggler sources the photon beams radiated by each may only be separated by up to a few mrad. This geometrical challenge can be addressed by sharing enclosures and shielding, staggering the position of optical elements and of end stations, and incorporating opposite vertical offsets for monochromators and mirrors to afford the greatest possible separation between beamlines.

While the NSLS-II damping wiggler beamlines will far outperform the current NSLS EXAFS and microprobe beamlines (as well as all second- and third-generation synchrotron bending magnet lines worldwide), that does not necessarily translate into faster throughput of experiments. The historic trend in

worldwide synchrotron development is that brighter beam enables more difficult experiments, which use as much, or more, beamtime.

11.16.8 Powder Diffraction Considerations

Powder diffraction is one of the most widely used techniques in modern materials science, and the advent of synchrotron radiation sources has enormously broadened the power of the technique. It is now nearly routine to solve complicated crystal structures from powder data alone, and time-resolved in-situ powder diffraction measurements of materials such as catalysts being formed are of great interest. These measurements are generally possible only with intense synchrotron sources. Every major synchrotron x-ray source in operation has a beamline dedicated to powder diffraction, and NSLS-II will be no exception.

We propose a station very similar to the successful (former) BM16 at ESRF or 11BM at APS. In general, bending magnet sources are suitable for general-purpose powder diffraction, because the experiments make use of rather large beams (on the order of millimeters in each dimension), and good angular resolution is required in only one (vertical) direction. The comparative flux characteristics of the NSLS-II damping wiggler and bending magnet sources, however, make it clear that the needs of powder diffraction at NSLS-II will mainly have to be addressed by damping wiggler sources. Requirements for a general-purpose powder diffraction beamline are as follows:

Tuning range of 5 to 50 keV to allow resonant diffraction experiments across a wide range of the periodic table and to be able to measure samples of high Z in capillaries.

Sufficient access to the sample to allow environmental chambers (e.g., cryostats, furnaces, reaction cells) to be used. With careful design, this can probably be realized from only one side, so that components of another beamline can be, say, 30 cm on one side of the sample position. This would permit the powder beamline to share floor space with another beamline using canted damping wigglers to provide radiation to both beamlines.

Two detector sets should be provided to permit high resolution ($\delta d/d \sim 10^{-4}$) and moderate resolution (5×10^{-3}), with the latter capable of providing continuous readout. We propose to equip the beamline with a tunable multi-analyzer stage, so that on the order of 10 diffraction angles, separated by approximately 2°, are read out simultaneously with an angular resolution on the order of 0.005°. The beamline would also have a position-sensitive detector such as a multichannel Si strip detector. Both detector sets would be permanently mounted on a single two-theta axis, so they could be used with negligible setup time. Siddons has demonstrated a technique to obtain high-resolution data sets in real time based on a bright converging beam, such as from a multilayer, with a detector in Rowland circle geometry; the proposed beamline could also be used in that mode, and it would be again developed to minimize setup time.

The source flux available from a damping wiggler, ranging from 4×10^{15} to 1×10^{14} ph/s/10^{-3}BW/mrad over the range of 5 to 50 keV, compares extremely favorably to that from bending magnets at ESRF (1×10^{13} to 5×10^{12}), APS, and current NSLS (1.5×10^{13} at 5 keV, 1×10^{12} at 30 keV). Proposed beamline optics would consist of an initial collimating/focusing mirror and a double-crystal monochromator containing a sagittally bent second crystal, providing a focal spot size on the order of 0.5 mm square (and unfocused beam could be provided by flattening the second crystal). The beam would be sufficiently intense that it could be easily masked down to ~100 $(\mu m)^2$ for diamond anvil cell experiments. Focusing could be relaxed for samples that are available in larger quantities, to reduce radiation damage, if needed.

11.16.9 X-Ray Topography Considerations

X-ray topography techniques benefit greatly from access to extended beam fan, continuous spectrum sources, such as bending magnet sources [11.16.6]. Most useful topography experiments are carried out using

photons in the energy range from 6 to 120 keV. To address the need for continuous spectrum, extended beam fan for this photon energy range, we envision that access to damping wiggler beamlines will be necessary.

Two types of beamlines would be useful for x-ray topography experiments. The first would be, simply, a beamline that delivers white beam to a five-circle goniometer at the experimental station. Small source size and long beamline length would be essential for such a beamline, to maximize both the spatial resolution capability and the area of the beam delivered to the experimental station. For example, beamline X19C at NSLS has a length of 25 m, which results in a very respectable spatial resolution capability of 0.1 μm per cm of specimen-film distance and a beam size of 5(H)×0.6(V) cm at the crystal. Beamline ID19 at ESRF (which has two undulators and one wiggler) has a length of 145 m, resulting again in submicron spatial resolution per cm of specimen-film distance and a beam size of 4.5×1.5 cm. The small source size and long beamline length also provide a high degree of coherence, which opens up the possibility of phase-contrast imaging supplemental to x-ray topography imaging.

The second type of x-ray topography beamline would be a tunable, monochromatic beamline using a double-crystal monochromator with no focusing elements. This would be suitable for monochromatic x-ray topography experiments and especially suitable for studies of relaxation in heteroepitaxial layers (particularly dynamic studies). This facility would be equipped with accurate slits (down to a few μm in width) to allow section topography imaging. On this beamline, a high-precision vertical diffractometer to allow high-resolution diffractometry in combination with diffraction imaging would also be very desirable, with the built-in possibility for small beam size spatial mapping of rocking curves.

Since high-resolution x-ray film is still the best large-area, high-resolution, continuous-contrast detector available, both types of beamline would require access to darkroom facilities located near the beamline. (X-ray topography is a very labor-intensive technique that requires constant online decision making based on the results of iterative changes in diffraction geometry.) Currently, high-resolution film is capable of 1 to 2 microns spatial resolution over a field of view as large as a sheet of 8×10 inch film (large fields of view become increasingly important as the size range of semiconductor wafers continues to expand). This, coupled with the dynamic range necessary to provide good defect contrast offered by these x-ray films, means that this type of detector will remain the one of choice for the foreseeable future.

11.16.10 X-Ray Footprinting Considerations

For several years, Synchrotron Footprinting technology has been used to map the solvent accessibility of reactive probe residues in proteins and nucleic acids as a function of binding interactions, conformational changes, and folding processes [11.16.7]. SF combines a number of state-of-the-art techniques. These include 1) the use of synchrotron radiation light sources, 2) the chemistry of radiolysis and interactions of hydroxyl radical with nucleic acids and proteins in aqueous solution, 3) mixing technologies to initiate rapid reactions, and 4) analytical tools for the detection of radiolysis products of nucleic acids and proteins. These technologies have been implemented at NSLS with great success. Footprinting studies of nucleic acids are routinely conducted with x-ray exposures of tens of milliseconds, which include studies of nucleic acid folding and their interactions with proteins. This technology can also be used to study protein structure and dynamics in solution as well as protein–protein interactions in large macromolecular complexes. Their success has stimulated adoption of these approaches at ESRF and the Brazilian synchrotron source, LNLS.

At NSLS-II, the higher white beam flux densities available at damping wiggler beamlines will allow highly enhanced footprinting studies to be carried out. These beamline improvements will overcome the effects of intrinsic and extrinsic scavengers and allow faster time-resolved experiments. Time-resolved measurements using SF, both in vitro and in vivo, would provide a unique approach to better understand fundamental processes relating to macromolecular folding and the assembly of nucleic acids and proteins and their complexes essential to cell biology. The timescales of these processes are seconds to milliseconds to microseconds, depending on the system under study. For in vitro studies, current technology can access the millisecond timescale, but many processes on the microsecond timescale are not amenable to study, due to

insufficient flux density. For in vivo studies, even structural examination on the seconds timescale is not achievable, in many cases. The new NSLS-II facility could allow structural probes on biologically relevant timescales (milliseconds or faster) in real time, in vivo. The SF technique continues to have unique capabilities, one of which is the prospect for examining macromolecular structure in vivo. Proof that such approaches are feasible was recently demonstrated by an NSLS user at X28C; this provides an exciting new avenue for technology development for the resource. However, the limitations of existing beamlines make it unlikely that these advances can be fully exploited without NSLS-II.

References

[11.16.1] See, for example, Brandes and Northrup (2006), "High-resolution phosphorus K-edge XANES of phosphate minerals," in prep for *American Mineralogist.*

[11.16.2] Akabayov et al., 2005 "Using softer X-ray absorption spectroscopy to probe biological systems" *J. Synchrotron Radiation* 12, 392).

[11.16.3] Ascone, I., et al., Metallogenomics and biological X-ray absorption spectroscopy. *J Sync. Rad*, 2005. **12**(Pt 1): p. 1–3; Ascone, I., R. Fourme, and S.S. Hasnain, Introductory overview: X-ray absorption spectroscopy and structural genomics. *J Sync. Rad*., 2003. **10**(Pt 1): p. 1–3; Lippold, B., et al., Towards an automated quality control of XAS data. *J Sync. Rad*, **12**(Pt 1) p. 45 (2005); Scott, R.A., et al., Bottlenecks and roadblocks in high-throughput XAS for structural genomics. *J Sync. Rad*. **12**(Pt 1) p. 19 (2005).

[11.16.4] Shi, W., et al., Metalloproteomics: High-throughput structural and functional annotation of proteins in structural genomics. *Structure* **13**(10) p. 1473 A9 (2005); Chance, M.R., et al., High-throughput computational and experimental techniques in structural genomics. *Genome Res*. **14**(10B) p. 2145 (2004).

[11.16.5] Kleifeld, O., A. Frenkel, and I. Sagi, Time-dependent XAS studies of trapped enzyme-substrate complexes of alcohol dehydrogenase from Thermoanaerobacter brockii. *J Sync. Rad*. **8**(Pt 2) p. 978 (2001).

[11.16.6] White beam synchrotron radiation topography. Miltat, J. NATO Advanced Study Institutes Series, Series B: Physics (1980), B63 (Charact. Cryst. Growth Defects X-Ray Methods), 401-20; Monochromatic synchrotron radiation topography. Sauvage, Michele. NATO Advanced Study Institutes Series, Series B: Physics (1980), B63 (Charact. Cryst. Growth Defects X-Ray Methods), 433-55.

[11.16.7] Maleknia, S.D., et al., Determination of macromolecular folding and structure by synchrotron x-ray radiolysis techniques. *Anal Biochem*. **289**(2) p. 103 (2001); Brenowitz, M., et al., Probing the structural dynamics of nucleic acids by quantitative time-resolved and equilibrium hydroxyl radical "footprinting". *Curr Opin Struct Biol*. **12**(5): p. 648 (2002); Guan, J.Q., et al., Structural reorganization of proteins revealed by radiolysis and mass spectrometry: G-actin solution structure is divalent cation dependent. *Biochemistry*. **42**(41) p. 11992 (2003); Guan, J.Q. and M.R. Chance, "Footprinting Methods to Examine the Structure and Dynamics of Proteins." *Encyclopedia of Molecular Cell Biology and Molecular Medicine*, 2nd ed., R. Meyers, Ed., Wiley Inc. (2004); Guan, J.Q., S.C. Almo, and M.R. Chance, Synchrotron radiolysis and mass spectrometry: A new approach to research on the actin cytoskeleton. *Acc Chem Res*. **37**(4): p. 221 (2004); Takamoto, K. and M. Chance, Footprinting Methods to Examine the Structure and Dynamics of Nucleic Acids. *Encyclopedia of Molecular Cell Biology and Molecular Medicine*, 2nd ed., R. Meyers, Ed., Wiley Inc., 521 (2004); Guan, J.Q. and M.R. Chance, Structural proteomics of macromolecular assemblies using oxidative footprinting and mass spectrometry. *Trends Biochem Sci*. **30**(10): p. 583 (2005).

11.17 VUV and Soft X-ray Bend Magnet Beamlines at NSLS-II

The NSLS-II bending magnets will be excellent sources for certain classes of experiments, particularly in the vacuum ultraviolet and soft x-ray range. The VUV/soft x-ray range provides unique capabilities which coincide with the interests of numerous, diverse research fields. These include investigations into complex materials / correlated electron systems, magnetic materials and spintronics, semiconductor materials and devices, nanomaterials, catalysis and surface science, geology and environmental sciences, polymers and soft matter, structural and cellular biology and other biosciences, planetary science, atomic and molecular electronic structure, and others. VUV and soft x-rays can probe the electronic structure of these materials (spectroscopy) and the physical distribution of spectroscopic features, either by collecting scattering data to arrive at a statistical representation of the sample or by performing real-space imaging using advanced microscopy techniques.

An example from cellular biology will serve to illustrate some of the unique aspects of this spectral range and the benefits of bending magnet sources. With appropriate instrumentation, such as a full-field transmission microscope, soft x-ray imaging can be used to acquire 3D tomograms, with unprecedented resolution, of complete cellular structures in a hydrated environment [11.17.1]. Three characteristics contribute to this capability: illumination by photons with much shorter wavelengths than visible light microscopes; incoherent illumination of the focusing optics, which avoids image speckle; and exploitation of the "water window," that is, the spectral range between the C K-edge (~285 eV) and the O K-edge (~540 eV). In this region, the penetration depth through water is several mm, while absorption of the cellular proteins can be an order of magnitude higher than the surrounding water. Improvements in soft x-ray optics and strategies of "tagging" proteins of interest with various elements, particularly transition metals, should lead to even better cellular imaging capabilities. Also, much of the instrumentation and technique development that is pursued for cellular imaging can be adapted for resonant imaging of other non-crystalline materials.

Of course, the damping wigglers anticipated for NSLS-II will provide very broad spectral coverage (see Chapter 8). In fact, they will be far more powerful sources, in terms of both flux and brightness, than the bending magnets, even in the soft x-ray range. However, the relatively low critical energy of the NSLS-II bending magnets (2.4 keV) severely limits their performance at high photon energies. Therefore, it is anticipated that the damping wigglers primarily will serve the needs of communities that require access to higher energy photons. Some hard x-ray beamlines may be developed on the NSLS-II bending magnets which will provide higher flux and brightness than the current NSLS bending magnets—up to ~4 keV and significantly higher brightness, up to ~12 keV. Nonetheless, it is expected that the available bending magnet ports will be allocated primarily to infrared (see Section 11.18) and VUV / soft x-ray uses.

11.17.1 Monchromator Options

Because of the large variation in wavelengths in the VUV / soft x-ray spectrum, different monochromator designs are required to cover the entire spectral range. Some options are reviewed below.

11.17.1.1 VUV Range: <10 eV–~50 eV

At the low-energy range, a standard monochromator is the Normal Incidence Monochromator design. The typical NIM implementation utilizes a fixed included angle between entrance and exit slits and pre-grating mirrors to focus the beam onto the entrance slit. Post-monochromator mirrors are used to provide a good beam focus at the sample. A major advantage of the design is compactness. For example, at beamline U13UB on the NSLS VUV/IR ring, the total length of the NIM is about 6.5 m and the instrument still provides an impressive resolving power of ~20,000 across its entire operating range (5 – 30 eV).

A major limitation of the NIM is the narrow energy range that it supports. Recently, an extension of the Variable Line Spacing – Plane Grating Monochromator has been proposed. This design, discussed more fully

in Section 11.7.2, has been developed to cover the soft x-ray range (around 100 eV and upwards). The monochromator can cover a lower energy range, down to ~8 eV, with the inclusion of suitable gratings and modifications to the motion of the mirror and grating. In future design stages, the VLS-PGM approach will be evaluated in greater detail to determine its suitability to a versatile bending magnet beamline that can span both the VUV and soft x-ray ranges.

11.17.1.2 Soft X-Ray Range: ~50 eV–2000 eV

In this energy range, compact designs are not feasible; the reflectivity of optical components becomes small at grazing angles larger than a few degrees and optical components are longer. The most common selections are either the fixed-included angle Spherical Grating Monochromator and its derivatives and the variable angle plane grating monochromator and its variants, particularly the VLS-PGM [11.17.2].

Most soft x-ray lines at NSLS use an SGM or variant (e.g., the double-headed dragon design used at beamline U4B). At the time these beamlines were designed, the SGM offered the best solution of design tradeoffs with the available optics; in particular, the figure errors of optics were ~1 arcsec or larger. The SGM approach usually requires the use of gratings at angles away from their most efficient point. Also, a characteristic of SGM designs is a wavelength-dependent focus of the monochromator, which produces a moving source point for downstream optics and end stations. A benefit of the SGM design is simplicity, which is particularly important in alignment of the optics and in operations.

The VLS-PGM approach offers a number of advantages over the earlier SGM designs. The variable incident angle on the gratings improves the efficiency of the monochromator and the gratings are used over a wider energy range. Also, the fixed exit slit provides a fixed source point for downstream components. However, the design requires higher quality optics, and the motions of the monochromator are more complex. Despite these obstacles, the VLS-PGM design and its variants has gained favor at third-generation synchrotron sources.

11.17.1.3 Medium X-Ray Energy Range: ~1000 eV–~5000 eV

This energy range is underutilized in many synchrotron sources. The efficiency of grating monochromators begins to drop off considerably above ~2.5 keV, but the x-ray wavelength at those energies is still not well matched with the lattice spacing of common monochromator crystals. Double-crystal monochromator designs at these energies typically use less common crystals with larger lattice spacings; a list of commonly used crystals is shown in Table 11.17.1. Often, several crystal sets are required to provide coverage across the desired energy range.

Table 11.17.1 Common Crystals in Medium Energy Monochromators [11.17.3].

Crystal type	2D spacing(Å)	Energy Range(eV)	Typical Absorption Edges
Beryl	15.954	800 - 1560	Cu *L*, Na *K*, Mg *K*
YB_{66}	11.76	1070 - 2000	Mg *K*, Al *K*
Quartz	8.512	1500 - 1830	Al *K*
InSb(111)	7.481	1680 - 4000	Si *K*, P *K*, S *K*
Ge(111)	6.532	1930 - 4000	P *K*, S *K*, Cl *K*
Si(111)	6.271	2010 - 4000	P *K*, S *K*, Cl *K*

11.17.1.4 Zone Plate Optics as Monochromators

Zone plates are diffractive lenses whose focal length is wavelength-dependent. In microscopy applications, zone plate lenses are often used as the monochromator as well as the magnification/demagnification optical elements. Zone plates provide modest energy resolution; $E/\Delta E$ is typically only around 500–700. Zone plate monochromators are therefore used primarily in situations where elemental contrast in the soft x-ray range is desired for imaging purposes, but detailed spectroscopy is not required.

11.17.2 BM Ports and Beam Extraction

The NSLS-II lattice will accommodate 30 DBA cells. In each DBA cell, however, only the downstream dipole chamber will contain a beam extraction port; an extraction port on the upstream dipole chamber would interfere with the front end of the preceding insertion device.

A choice that must be addressed early in the detailed design process is the location of the first mirror for the BM beamlines. The source divergence from the bending magnets in the vertical direction will be quite small (on the order of 1 μrad) and a mirror of reasonable size will capture all of the beam in the vertical direction. The situation is much different in the horizontal direction. Each dipole will have a horizontal source arc of approximately 105 mrad. At the current design stage, the beam extraction port in the dipole vacuum chamber will accept only 3 mrad of the horizontal fan, with the center of the accepted angle located approximately 10 mrad along the dipole bend. A mirror outside the shield wall will be ~20 m away from the dipole source.

At that distance, even a long (~1 m) mirror positioned at grazing angle of 2° to 3° will accept only ~1 to 2.5 mrad of the horizontal synchrotron radiation fan from the dipole. To decrease the distance to the source and hence increase the collection angle, the first mirror would need to be located inside the shield wall.

In the current design, the beam pipe from the dipole source will run adjacent to the shield wall. This precludes adding a second beam extraction port on a single dipole magnet, as the beam pipe would run inside the shield wall. If all the bending magnet dipoles at the NSLS-II are populated with beamlines, additional capacity may be developed by increasing the number of beam ports available from a single dipole, as is done, for example, at NSLS, SSRL, and ALS. Because of the constraints imposed by the shield wall, this would require the use of mirror optics inside the shield wall to increase the deflection angle and direct the beams through the shield wall.

Any beamline design that incorporates optical elements inside the shield wall may interfere with other components within the storage ring tunnel, and in particular the front end systems. Furthermore, such designs must have fully automated motion, adding cost and complexity. From an operational perspective, beamline modifications that are not automated and require access to the first optic must wait until scheduled maintenance periods. Finally, the higher radiation levels inside the shield wall may affect the optics over time. Should this option be considered in future design stages, a comprehensive assessment of potential radiation damage to the first mirror should be undertaken as soon as practical.

For the reasons outlined in the previous paragraph, it seems prudent to propose beamline designs for the soft x-ray bending magnet ports where the first optic is outside the shield wall. The topic of optics inside the shield wall, however, should be revisited in future design phases of the project.

11.17.3 UV Circular Dichroism

One class of experiments that deserves special consideration is structural biology measurements using UV **c**ircular **d**ichroism (UV-CD) spectroscopy. The wavelength range of interest here is around 150–400 nm (~3–8 eV). The UV-CD technique provides complementary information to protein crystallography and is used to determine, for example, the percentage of α-helix or β-sheet constituents in a protein sample, often in an aqueous environment. UV-CD is particularly useful in situations where protein crystals are not available.

However, signal levels are small and require sensitive polarization modulation and lock-in detection. The difficulty in migrating this program to NSLS-II is the large opening angle used in the collection optics for UV-CD experiments. For example, the two UV-CD beamlines operating on the VUV ring (U11 and U9) accept very large horizontal opening angles: 37 mrad for U9 and 55 mrad at U11. Even with the higher flux of NSLS-II dipoles, at least 20 mrad of horizontal fan will be required to provide a capability similar to current instrumentation. At the current design stage, plans for standard dipole chambers will only accept ~3 mrad of horizontal fan.

The approach envisaged for the NSLS-II infrared beam ports may provide a solution. A mirror that is integral to the dipole vacuum chamber can be inserted. The beam would be focused onto a smaller opening where a second mirror deflects the beam upwards; the beam can then be transported through the shield wall and on to the monochromator and experimental station. Because of the shorter wavelengths used in UV-CD, the number of mirror deflections should be minimized to maintain the flux. Also, the UV mirrors would require different coatings and a more stringent shaping and polishing requirements than IR mirrors.

References

[11.17.1] M.A. LeGros, G. McDermott, and C.A. Larabell, X-ray tomography of whole cells. *Current Opinion in Structural Biology* **15** p. 593 (2005).

[11.17.2] R. Follath, The versatility of collimated plane grating monochromators. *Nucl. Instr. & Meth. in Phys. Res. A*, **467** p. 418-425 (2001).

[11.17.3] From X-Ray Absorption Fine Structure Spectroscopy Group at Daresbury, http://srs.dl.ac.uk/XRS/index.html.

11.18 Infrared Beamlines

11.18.1 Introduction

Infrared synchrotron radiation is a high-brightness, continuum source that excels for microspectroscopy and other low-throughput infrared techniques (diamond anvil cell spectroscopy, very high spectral resolution, very far-infrared and THz spectroscopy) [11.18.1]. Dipole bending magnets serve as optimal long wavelength radiation sources (in contrast to insertion devices) [11.18.2]. Our plans for supporting infrared science are based on extracting long wavelength radiation from the NSLS-II ring. Our goal is to provide a level of performance comparable to, or exceeding, that of the existing facilities at the NSLS VUV/IR ring in terms of brightness and spectral range. Since the infrared performance of most synchrotron facilities is typically limited by beam motion and environmental noise, the NSLS-II facility offers the potential for outperforming the existing VUV/IR ring through significant reduction in these noise sources. With bunch lengths of a few tens of psec, the NSLS-II ring will also offer benefits for time-resolved spectroscopies.

Infrared spectroscopy senses both vibrational and electronic degrees of freedom in materials. The energy of mid-infrared photons matches the characteristic vibrations of molecules, making infrared spectroscopy an important tool for identifying chemical content and structure. Principle applications include investigating the chemical content of heterogeneous materials (e.g., diseases in biological tissues, soils in the environment, and interplanetary particles from comets) and in materials science. The far-infrared and THz spectral range is sensitive to phonons and other collective modes. This includes transport phenomena and the various interactions between electrons and other excitations in a solid, making infrared spectroscopy an important tool for studying complex electronic systems. Phenomena range from excitons in semiconductor nanoparticles to ferroelectricity, magnetoresistance, and superconductivity in complex metal oxides. In many cases, the information complements that obtained from higher energy photons (e.g., photoemission, x-ray spectroscopy, diffraction and scattering), yielding a more complete picture of a material's structure and behavior. The high-

brightness of infrared synchrotron radiation is crucial for a variety of low-throughput techniques. These include microprobes and imaging microspectroscopy, the study of materials at extreme pressures and temperatures in diamond anvil cells, millimeter wave spectroscopy and ellipsometry through high-field magnet cryostats, and ultra-high resolution spectroscopy (to ~100 nanovolt energy resolution). The science mission defines performance goals reaching from the mid-infrared (λ ~3 μm as needed for chemical imaging) to the very far-infrared (λ~5 mm) for magnetic resonance spectroscopies. Such an extremely broad spectral range (at times extending into the visible and beyond) is also crucial for analysis methods that employ Kramer Kronig and sum rule techniques. Dynamical processes can be investigated using any of these techniques by exploiting the pulsed nature of the synchrotron source. Though lasers can probe shorter time scales, no other source allows for such wide spectral coverage.

11.18.2 Conceptual Design

Our original plans called for re-building the existing VUV/IR ring and infrared beamlines into a dedicated source for low-energy radiation and short pulses. This plan was modified due to siting considerations within the NSLS-II facility and the recognition that NSLS-II bending magnets will provide a highly competitive source (and in some spectral ranges, world-leading) in terms of both flux and brightness. The infrared program can then benefit from the same ultra stable, high-brightness electron beam and environment available to x-ray users, including shorter pulses for time-resolved spectroscopies. The proposed front-end design will follow concepts similar to the existing IR extraction from the VUV/IR ring, including a first extraction mirror inserted into the dipole chamber and adjacent to the electron beam [11.18.3]. The balance of a given beamline will have a more robust design to exploit the lower noise environment of the NSLS-II facility. The number and types of infrared beamlines will be comparable to the existing program [11.18.1] on the NSLS VUV/IR ring, plus compatibility with future expansion of ~50%. Our source requirements dictate optimal performance to wavelengths approaching 5 mm, necessitating careful design of the infrared extraction and dipole chamber geometry. We also envision the synchrotron source serving two beamlines equipped with mid-IR microspectrometers having large area focal plane array detectors [11.18.4]. An extended source is suited better than a single point-like source for illuminating an array, so we anticipate using a large horizontal collection of bending magnet radiation for this application.

11.18.2.1 NSLS-II as an Infrared Source

NSLS-II will be a powerful source of IR radiation. See Section 8.4 for a full description of the IR radiation produced by NSLS-II bending magnets.

11.18.2.2 Infrared Beamlines

11.18.2.2.1 Capacity

We propose that the number and type of NSLS-II infrared beamlines roughly match the existing NSLS VUV/IR beamlines at the time of transition to NSLS-II, plus provide the capacity for at least 50% growth. We anticipate the following:

- three mid-IR microprobe beamlines for biological, chemical, materials science, and space sciences (These would share a single standard NSLS-II dipole extraction.)
- two mid-IR beamlines for biological and chemical imaging using FPA detectors, each with an entire horizontal extraction
- one far-IR beamline focusing mostly on magneto-spectroscopy
- one combined mid-IR and far-IR beamline for materials science, including time-resolved spectroscopy
- one combined mid-IR and far-IR beamline for studies of materials at extreme temperatures and pressures (diamond anvil cells with cryostats and laser heating)

As noted in Chapter 8, two or three mid-infrared microprobes can share a single dipole extraction. The mid-infrared imaging microscopes will need the entire 50 mrad of horizontal collection, so each imaging end station will require its own dipole extraction. The far-infrared beamlines will also each require a full dipole extraction, plus the modified, large-gap dipole and chamber to collect the ~32 mrad (or 48 mrad, if feasible) of vertical aperture. Thus, we envision three extraction ports on conventional-type dipoles (one for the three microprobes, two each for the FPA imaging beamlines) and three extraction ports on large-gap dipoles (one each for the three far IR and THz beamlines). A symmetric placement of the large-gap dipoles within the NSLS-II lattice offers potential benefits from an accelerator physics standpoint. Thus, we expect the large-gap dipoles to be arranged in pairs (both dipoles of a cell superperiod) and symmetrically around the ring itself. Installing three sets meets the DBA 30 overall symmetry, and by placing one of these sets immediately downstream of the injection or RF straight sections will allow both dipoles in that cell to be used for infrared extraction. Indeed, we may be able to use the upstream dipole in the other two large-gap cells by suitable construction of the first extraction optic to allow insertion device radiation to pass. Nonetheless, we foresee that a set of three dipole pairs will meet the expected need at the time of transition from NSLS-II plus provide a growth capacity of from one to three additional far-infrared beamlines. The situation for mid-infrared-only beamlines is less complicated, since they will employ conventional dipoles. Three extractions will meet the anticipated needs when NSLS-II begins operations, and the growth capacity for two or three additional extractions can be included to meet future needs.

11.18.2.2.2 Mid-IR Microprobe

The microprobe beamlines require only a small horizontal segment of source (~15 mrad), making these mid-infrared beamlines among the simplest to design and meet performance requirements. We expect to employ a design similar to our existing U2A/U2B ad U10A/U10B mid-IR beamlines on the NSLS VUV/IR ring, using off-the-shelf mirror optics for focusing and steering the beam from the extraction point to the microprobe end station. Small-aperture CVD diamond windows are sufficient for separating storage ring vacuum from the rough (or medium high) vacuum environment of the mid-IR transport optics leading to the end station. These transport optics will provide for horizontal separation of the beam into two or three segments for delivery to individual end stations. A KBr or CsI window at the end of these transport sections will provide added vacuum protection and still provide complete spectral coverage.

11.18.2.2.3 Mid-IR imaging

Here, we intend to use the full horizontal swath (50 mrad) of beam to produce an extended source having significant depth (due to the ~1 meter long source segment). Though segmented mirrors have been used to collect a large angular swath and match it the planar profile of a focal plane array detector, this approach may also introduce undesirable multiple-beam interference effects (between different beam segments). Therefore we will investigate contiguous optical designs (e.g., anamorphic) for reshaping the source and matching it to the square format of most FPAs, while simultaneously matching the large numerical aperture of the FPA objective across the entire field of view. Though the mirror surface may be complex, computer-assisted diamond-turned optics are expected to meet performance requirements. Similar to the microprobe end stations, we expect to use CVD diamond for the UHV window material, and KBr or BaF_2 for the last window before the end station. NSLS is currently attempting to procure a Bruker Hyperion 3000 imaging microspectrometer system with a 64×64 element FPA detector. When combined with a 74X objective, the total effective area sampled by the FPA is about 35 μm squared, and each FPA element corresponds to 0.51 μm, well beyond the diffraction limit. This provides spatial oversampling and enables point-spread-function deconvolution to enhance spatial resolution. Such a system was tested at NSLS beamline U10 in June of 2005 [11.18.4] in order to demonstrate the principles, including the ability to match an extended source to the 35 μm area being sampled. Based on developing interest at NSLS and other SR facilities, we expect the need for two such end stations at the time of NSLS-II operations startup.

11.18.2.2.4 Far-IR and THz

As with the mid-infrared, we will be extracting a large horizontal segment. Even though optical requirements are more relaxed for longer wavelengths, we anticipate using the same extraction system as designed for the mid-infrared imaging. The balance of the beamline can be assembled with conventional mirror optics (like the NSLS VUV/IR far-infrared beamlines). Diffraction loss from small apertures is of great concern, and we expect the beamline's optical transport system to consist of larger mirror optics and vacuum components than for mid-infrared beamlines. The window separating machine vacuum from beamline vacuum also requires special consideration. In situations where only the THz and near IR portions of the spectrum are needed, a crystalline quartz window performs well and allows for large apertures (50 cm or larger). A more likely approach will be to use thin (<1 mm) CVD diamond so as to include the mid-infrared. Though this limits the aperture to below 2 cm, fast optics can be used immediately before and after to achieve good performance into the millimeter wave region.

11.18.2.2.5 Extension to Visible and Near UV

We note that several UV beamlines currently exist on NSLS VUV/IR ring bending magnet ports, supporting experiments in biology, chemistry, materials science, and condensed matter physics. Techniques include absorption, spectral and diffuse scattering, natural and magnetic circular dichroism, linear dichroism, fluorescence excitation, and emission and polarization from solid, liquid, and gaseous samples. For these beamlines, high flux (rather than high brightness) is the important source characteristic. Though NSLS-II undulators can meet the flux requirements, they are better suited to experiments requiring their exceptionally high brightness. NSLS-II dipole bends provide a similarly large flux when 50 mrad of horizontal angle is collected. Fortunately, we expect the optical design for extracting 50 mrad horizontal of infrared radiation (described in Chapter 8) to perform well for photon energies approaching 20 eV, spanning both the visible and UV spectral ranges. We anticipate that the first mirror will require a more sophisticated optical figure and polishing to maintain optimal source brightness for these much shorter wavelengths, plus control of any surface oxidation. Thus, NSLS-II bends (standard gap) should be capable of meeting the needs of this particular research community.

11.18.2.3 Beam Transport and Distribution Optics

The optics for managing and delivering the infrared radiation will follow design principles developed for the existing NSLS VUV/IR ring beamlines. The typical optic set includes combinations of plane, toroidal, paraboloidal, and sometimes spherical or elliptical mirrors. These and other special optical surfaces can now be manufactured by diamond diamond-turning methods, yielding surface quality (smoothness and accuracy) that exceeds infrared requirements. The extraction optics (first few mirrors inside the storage ring UHV) will deliver the beam through a transparent UHV window such as diamond. The remaining optical components will transport the beam and match it to a particular end station. Infrared beam transport does not entail complex optical components, UHV conditions, or special considerations for radiation shielding. Achieving diffraction-limited performance at long wavelengths is reasonably straightforward, but attention must be paid to other issues, such as diffraction losses. A key concern is mechanical stability for all the optical components, and we plan to use robust mechanical systems for mounting optical components. These supports will provide for in-vacuum beam steering controls, plus dynamic feedback to further reduce any low-frequency beam motion. Thermal loading is an issue only for the very first extraction optic inside the ring dipole chamber (discussed in a previous section).

11.18.2.4 End Stations

We expect that, in most cases, the end stations for the NSLS-II infrared beamlines will be those already in existence on the NSLS VUV/IR beamlines. These are mostly commercial FTIR spectrometers, some with dry nitrogen purging, others operating in a rough vacuum environment. These spectrometer end stations are

normally paired with an optical system (instrument) used to bring light to the sample under study. Examples are scanning microprobes, imaging microscopes, optical cryostats, diamond anvil cells, and magnet cryostats. It is assumed that NSLS will be maintaining these instruments at the state-of-the-art level between now and the operational startup of NSLS-II. The current NSLS infrared beamlines and end stations are listed here for convenience.

U2A Bruker 66 mid and far IR spectrometer, plus diamond anvil cells and cryostats
U2B Nicolet 860 mid IR spectrometer and scanning microprobe end station
U4IR Bruker 66 mid and far IR spectrometer, plus optical cryostat with laser for time-resolved spectroscopy
U10A Spectra-Tech IR spectrometer with scanning microprobe and microstat cryo system for far IR
U10B Nicolet 860 mid IR spectrometer and scanning microprobe end station, with fluorescence
U12IR Bruker 125HR high-resolution far IR spectrometer, plus 16 T magnet cryostat

11.18.2.5 Hutch Enclosures

The last several years have brought the realization that climate control, especially humidity, is critical for most mid-infrared microprobe and imaging experiments. Following the example of other synchrotron facilities (ANKA, CLS, Soleil, etc.), we plan to implement complete hutch enclosures for beamline end stations and instruments. These hutch enclosures will provide not only a stable climate (temperature and humidity) but will also reduce the detrimental effects of acoustic noise from neighboring beamline systems and provide a dark environment for performing optical alignment. It should be noted that these hutches are designed to be occupied at all times, i.e., they play no role in radiation protection. However, they could also serve for access control to hazardous experimental conditions such as laser light, high magnetic fields, and biological toxins.

11.18.2.6 Computing and Controls

The infrared beamlines do not present any unusual requirements for beamline controls. A basic system will be necessary for monitoring vacuum integrity and controlling various valve protection systems. Few of the mirror systems require regular adjustment, and the beam's position on optical surfaces can be monitored using conventional CCD cameras to view the visible radiation that is collected with the infrared. Requirements for positioning accuracy can be managed with conventional optomechanics, including stepper and DC servo motors. To ensure optimal stability at the experiment end station, we plan to include a two-mirror stabilization control system in the design. Such a system has been in use at ALS for several years, and a similar system is under development for NSLS.

Most infrared beamlines utilize commercial Fourier-transform infrared spectrometer systems. FTIR systems and their commercial software will need to be interfaced with NSLS-II injection signals to avoid collecting data during a top-off cycle. Converting all the systems to an EPICS-type interface will be considered, to allow better control of the data collection. We can expect to benefit from the experience of other storage ring light sources planning top-off operation, e.g., SLS in Switzerland and Soleil in France. Other ring signal requirements (in addition to an injection signal) are 1) beam current, 2) bunch synchronization signal (RF, RF/N where N is the bucket population factor), and 3) ring orbit RF frequency (i.e., RF/1300). Beam current should be accurate to at least 1 part in 1000.

11.18.3 Conventional Facility Requirements

11.18.3.1 Support Labs

Each beamline will need conventional laboratory space for tasks such as cryogen handling (IR detector operations), cryostat modifications and preparations, sample mounting and handling with optical microscopes,

etc. We also anticipate that biological imaging beamlines will need access to refrigeration and other facilities associated with cell culturing and tissue preparation. Placing these beamlines in relative proximity to other biological beamlines will allow for commonality of equipment and optimization of laboratory space. In other cases, specialized space will be needed in association with a particular beamline or combination of beamlines. Examples include the preparation and setup of LHe-cooled detectors and cryostats, especially magnet cryostats, where the area must be controlled for both personnel and equipment safety. The operation of class IIIB and class IV lasers is also typical for materials science IR beamlines, whether for fluorescence in high-pressure cells, micro-Raman, or time-resolved spectroscopy. For these situations we expect the beamline hutches to be divided into two or more sections to provide independent control and personnel and equipment protection (interlocks).

11.18.3.2 User and Equipment Access

The infrared beamline end stations should be sited such that users can occupy them at all times (including during injection). Additionally, they must be 100% accessible to equipment such as electronic racks, large cryostats, and LHe storage dewars. This motivates placing the infrared beamlines on the experimental floor along with the other NSLS-II beamlines (and not on the storage ring tunnel shield wall or another elevated surface).

11.18.3.3 Services

The infrared beamlines will require local access to liquid nitrogen (LN_2) for detectors and cryostats, dry nitrogen gas (for continuous purging of mid-IR spectrometers and end stations), and He gas (for detectors and cryostats). Electrical power requirements are comparable to those of a small experimental physics laboratory. Chilled water is needed for the first mirror in the optical extraction. This water must be extremely "quiet" (no pressure fluctuations) to avoid introducing mechanical noise into any of the optic components.

11.18.4 Example Infrared Beamline Schematics

Though the purpose of a given infrared beamline varies, the overall extraction, beam transport, and spectrometer end station layout does not differ greatly. Figure 11.18.1 shows a generic beamline layout consisting of three sections: 1) extraction optics and vacuum protections systems that collect the light and bring it around the fixed radiation protective shielding and through a UHV window; 2) the optical system for matching the source to the particular spectrometer and end station requirements, compensate for any beam noise, and transport the beam (under vacuum); and 3) a hutch enclosure that contains the beamline's FTIR spectrometer and specialized end station (e.g., an imaging microscope with focal plane array detector, a diamond anvil cell system, an optical cryostat with laser excitation, or a high-field magnet cryostat). For these beamlines it is assumed that the full horizontal collection of the source is delivered to a single end station.

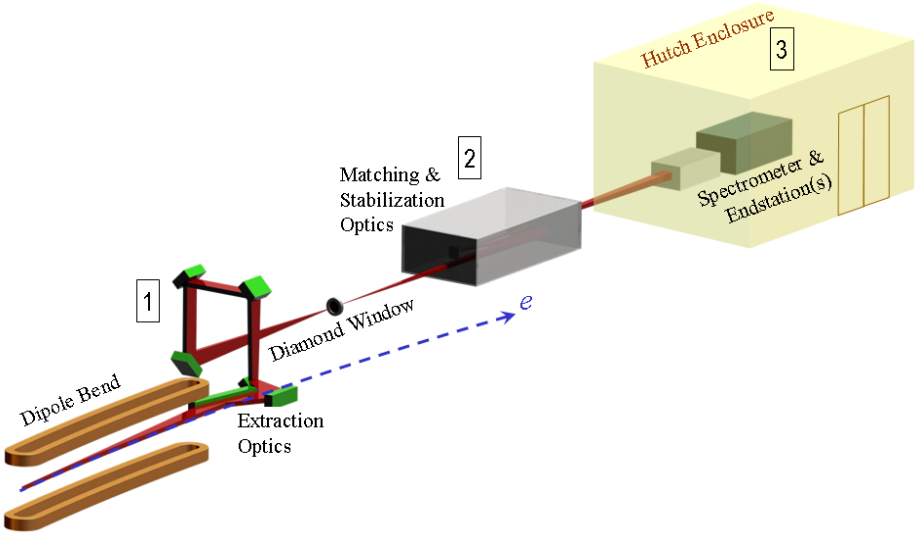

Figure 11.18.1 Schematic Infrared Beamline showing the three sections: 1) optics extract the infrared and bring it from the shielded storage ring enclosure and UHV environment out to the experimental hall and through a diamond window; 2) the optical system is designed to match the infrared beam to the experiment end station, plus provide for dynamic mirror alignment to eliminate mechanical beam movement, and 3) a hutch enclosure contains the FTIR spectrometer system and experiment end station.

The mid-infrared microprobe beamlines will require, typically, a horizontal collection that approximately matches the vertical collection (about 16 mrad for a standard dipole extraction). Thus, the 50 mrad of horizontal collection can be divided into two or three segments, delivered to independently operating microprobe end stations. Figure 11.18.2 illustrates a single extraction being split to serve three such end stations, where each receives about 15 mrad horizontal. This arrangement closely resembles the 40×40 mrad beamlines U2A/U2B and U10A/U10B on the VUV/IR ring where a ~90 mrad horizontal extraction is split to serve two beamlines.

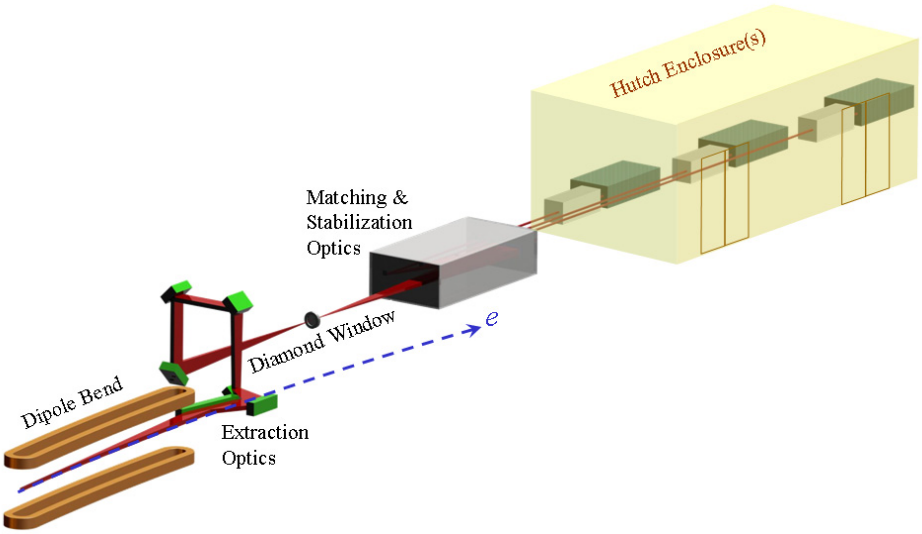

Figure 11.18.2 Multiple Microprobe End Stations. Same as the previous figure, but illustrating how the broad horizontal swath of infrared radiation can be split and fed to two or three simultaneously operating mid-infrared microprobe end stations. Each of the actual hutches would extend to the upper right a greater distance (deeper) than shown.

References

[11.18.1] See, for example, G.L. Carr, P. Dumas, C.J. Hirschmugl, and G.P. Williams, and other articles in *Infrared Synchrotron Radiation*, P. Roy and P. Calvani, eds. *Nuovo Cimento*, **20D** 375 (1998).

[11.18.2] W.D. Duncan and G.P. Williams, *Appl. Opt.* **22**, 2914 (1983).

[11.18.3] G. P. Williams et al., *Nucl. Instrum. & Meth. Methods Phys. Res.* A **246**, 165 (1986).

[11.18.4] G.L. Carr, O. Chubar, and P. Dumas, in *Spectrochemical Analysis Using Infrared Multichannel Detectors,* R. Bhargava & I. Levin, eds. (Blackwell Pub., 2005). Also R.L. Jackson, et al., WIRMS 2005, Rathen, Gy).

11.19 Time-Resolved Studies

11.19.1 Scientific Scope and Method

Synchrotron radiation, as a probe of physical (electronic, vibrational, structural) and chemical properties can serve to study the time-dependent properties of materials as well. The time scale of interest varies over many orders of magnitude, from femtoseconds to seconds and longer. In most cases, an event is triggered by some stimulus, and the properties are studied as a function of time following that stimulus. That time dependence can be followed using a sufficiently fast (gated) detector into the millisecond and shorter time range. However, fast detectors do not exist for all photon energy ranges of interest, and even when they do, there is always a tradeoff between speed and signal-to-noise. An alternative approach is to convert the temporal dimension into a spatial dimension that can be then sensed by a microprobe. The study of protein folding dynamics using flow/mixing cells and a synchrotron microprobe is an example of this approach, pushing into the microsecond time scale. In both of these cases, a higher brightness SR source provides increased performance, whether by simply increasing the signal-to-noise at the detector, allowing for smaller area (more sensitive, more rapid response) detectors to be used, or enabling a smaller area to be probed. These methods make use of specialized synchrotron beamline end station components, but do not require special or non-standard beamline designs.

A third approach exploits the time structure of the synchrotron storage ring source. Here, the individual pulses of synchrotron radiation (produced by the bunched electron beam) serve as a "strobe light" to capture an instant of time. This is the standard pump-probe technique commonly used to study fast and ultra fast processes and can completely relieve the detector of any requirement for time-resolution, thus providing the best combination of time resolution and signal-to-noise. There are, however, constraints to the technique. For example, the initiating stimulus must be synchronized to the SR pulses, and the specimen to be studied must allow for repetitive stimulus (within the limits of the pump and probe sources as well). Such issues are not unique to synchrotron radiation studies, and certainly not to NSLS-II. But the design of the NSLS-II accelerator system does present constraints on both the available bunch lengths and pulse patterns.

11.19.2 Review of Basic NSLS-II Properties

11.19.2.1 Bunch Length

The calculated bunch length (σ_z) for NSLS-II is 2.89 mm, which corresponds to σ_t=9.64 ps, or a FWHM of about 23 ps. These are zero current values. The bunch length for practical currents is more difficult to predict, but could be a factor of 2 larger (i.e., about 45 ps). This sets the limit for most time-resolved experiments without intentionally manipulating the electron bunches to produce shorter pulses. Those methods are discussed below.

11.19.2.2 Bunch Fill Patterns

The two factors that control the available pulse repetition frequency for a synchrotron radiation source are the RF frequency and harmonic number. The NSLS-II harmonic number of 1300 and RF frequency of 499.46 MHz allows for a variety of symmetric fill patterns to match the Pulse Repetition Frequency of common mode-locked lasers. The industry standard Ti:sapphire oscillator operates optimally around 80 MHz. Although NSLS-II does not have a symmetric fill for 83.2 MHz (499.46 MHz / 6), there are a number of fill patterns that yield PRFs matching Ti:sapphire oscillator subharmonics. Such subharmonics can be readily selected using Pockels-cell type electro-optic modulators. Except for its fundamental, a mode-locked laser at 76.84 MHz offers substantial flexibility for matching useful NSLS-II symmetric fill patterns.

Table 11.19.1 NSLS-II Fill Patterns Compatible with Mode-Locked Ti:Sapphire Laser Oscillators.

# of filled RF buckets	SR effective pulse repetition frequency (MHz)	Compatible laser oscillator frequency (MHz)	Laser divide by N (pulse selection)
1300	499.46		
650	249.73		
325	124.865		
260	99.892		
130	49.946		
100	38.42	76.84	2
65	24.973	74.919	3
52	19.9784	79.9136	4
50	19.21	76.84	4
26	9.9892	79.9136	8
25	9.605	76.84	8
20	7.684	76.84	10
13	4.9946	74.919	15
13	4.9946	79.9136	16
10	3.842	76.84	20
5	1.921	76.84	40
4	1.5368	76.84	50
2	0.7684	76.84	100
1	0.3842	76.84	200

Note that most storage rings operate with a gap in the fill pattern. This is not a problem when the SR serves as a probe, as long as the remainder of the fill pattern retains the overall symmetry. The only consequence is a loss of signal-to-noise, as some of the pump/excitation events are not probed.

Other mode-locked lasers (e.g., Er-doped fiber lasers, Nd:YAG, Nd:YLF, custom oscillators) will likely have other requirements or can be specially designed to work at these and other frequencies (e.g., 49.946, 99.892, 124.865 MHz). The optimal pulse rate for a given measurement depends on a variety of factors, but in very few cases are pulse rates much above 100 MHz useful, due mostly to limitations on extracting thermal energy from the sample. In situations where more laser power is required, an amplified system can be employed. Such systems usually operate at frequencies even lower than the orbital ring frequency (single bunch mode), in which case a gated detector is necessary to sample the appropriate synchrotron pulse.

Other “pump” stimuli can be employed, such as electrical. Since these are not constrained to an oscillator, the synchronization is usually much simpler than with a laser system. In any case, electrical synchronization signals, accurate to 5% of the electron bunch length, will be needed as a clock for the stimulus source.

11.19.2.3 Special Operating Modes for Timing

Timing experiments often have additional concerns beyond optimized flux and brightness. In timing measurements, the bunch length and PRF are critical. With regard to the PRF, for limited periods during the year, special operating modes are often employed at synchrotron facilities. Simplest among these modes is single-bunch or few-bunch operation, where a small fraction of the RF buckets are filled with more electrons than the standard bucket charge in normal operation. At NSLS-II, single-bunch operation would lead to a PRF of 384 kHz. This type of operating mode, or other few-bunch operations, might be useful for classes of experiments where the relaxation time of the samples is on the order of microseconds or where the detectors used have a long rise time or reset time. However, the cost in terms of overall flux for the general user community would be unacceptable. A common operating mode for timing operations that attempts to resolve this conflict is the so-called “camshaft” operation. In this mode, the majority of the RF buckets are filled as usual, but a large gap of unfilled buckets is placed in the distribution. In the middle of the gap, a single RF

bucket, the camshaft, is filled with several times the charge in the other buckets. Users can synchronize to the camshaft bucket and reject the contribution from the other filled buckets by using gated detection. The overall flux is not reduced much, as the proportion of the buckets in the gap to the number of filled buckets is relatively small. While potentially useful, this operating mode has not been studied in detail and should be evaluated more fully in future design phases.

11.19.2.4 Short Bunch Operations

The length of electron bunches in a storage ring can be reduced by adjusting several accelerator parameters. Examples include reducing the momentum compaction, reducing the ring energy, and increasing the RF slope (higher voltage, higher frequency). Unfortunately, most of these adjustments reduce the performance of the ring for other (non-time-resolved) users. Therefore, the availability of such modes will depend on the demand from the user community. Lowering the momentum compaction is usually accomplished at the expense of non-zero dispersion in the insertion device straight section. Should NSLS-II include a harmonic RF cavity to provide bunch stretching (to enhance the lifetime), such a cavity could be used, in reverse phase, to reduce the bunch length somewhat.

In addition, short photon bunches for a fraction of the NSLS-II beamlines may be generated by methods that preserve the beam properties for the majority of the (non-time-resolved) users. In general, these approaches provide short bunches to one or a few beamlines and do not provide reduced bunch length to the other beamlines. On the other hand, these approaches strive to provide short bunches while maintaining the desirable beam properties (low emittance and high flux and brightness) for most users. Two methods that have been implemented or proposed in recent years are laser time-slicing and implementation of additional accelerator RF systems (such as “crab” cavities).

Laser time-slicing, pioneered at Lawrence Berkeley National Laboratory, is the only accelerator-based method to date to demonstrate generation of femtosecond x-ray pulses. In this approach, high-power femtosecond laser pulses are synchronized with the electron bunches in the storage ring as they both propagate collinearly through an undulator. The interaction of the strong electric field from the femtosecond laser modulates the energy of a fraction of the electrons in the bunch, and the synchrotron radiation from these modulated electrons can be separated out in a subsequent dispersive section of the storage ring.

Crab cavities are RF cavities that impart a vertical deflection to the electron bunches. While the emitted radiation from the deflected bunch is larger in the vertical direction, the projection of the bunch along the time axis at given vertical position is considerably shorter than the undeflected pulse length. With suitable aperturing, a pulse on the order of one or a few ps can be generated at the cost of a reduction in flux by one to two orders of magnitude. Alternatively, asymmetrically cut crystals can be used without apertures to compress the entire bunch and preserve the flux. The attractive feature of crab cavities is that they can be operated in pairs where the second cavity applies a reverse deflection, which restores the electron bunches to their low emittance distribution. Thus crab cavities can produce short bunches with relatively high flux to several beamlines and straight sections while minimizing the impact on the general user community.

It must be stressed that the methods outlined above for producing short bunches have not been studied in detail. In future design stages, they must be evaluated more rigorously to determine the compatibility of the various options with the NSLS-II project goals.

11.19.2.5 Synchronization Signals

Generally, experiments on ultrafast timescales utilize a pump-probe architecture, where some excitation source, such as a high-power laser or an RF generator, perturbs the state of a sample and the subsequent response can be probed with the x-ray pulses from the storage ring. Accurate synchronization of the excitation is indispensable for these measurements, and the key to synchronization is the availability of accurate and fast bunch clock signals at the beamlines.

Signals from the storage RF system are an indirect measure of the photon bunch clock. While the frequency of the RF matches the frequency of the electron bunches in the storage ring, the phase between the RF and the electrons may shift for two reasons: 1) injection bumps during top-off may affect the relative phase of the RF and the electron bunches, and 2) for special operation modes that allow beam decay and re-injection (i.e., non- top off operations), the variable loading of the RF cavity as the beam decays will cause a shift in the phase of the cavity relative to the electron bunches. Thus RF signals are adequate for timing experiments involving gated detection and for samples with characteristic response times in the range of microseconds or longer. For ultrafast experiments where the systems responds in nanoseconds or less, a more direct measure of the electron bunches is required for synchronization.

The most precise manner of deriving a synchronization signal is to use the electron bunches as the source for the signal. This can be accomplished by either: 1) using an Avalanche PhotoDiode with a fast risetime to detect the visible light emitted as synchrotron radiation in the dipole magnets, or 2) inserting a floating stripline into the storage ring vacuum chamber and detecting the induced voltage on the stripline from the image charges that develop as the electron bunches pass in front of the stripline. The advantage to these methods over the RF signal is that the pulses derived from the electron bunches automatically correct for any phase drift between the electrons and RF.

Once generated, the signals from the APD or stripline must be discriminated and then distributed to the beamlines. We propose conversion of the signals to optical pulses and distribution over optical fiber rather than coaxial cable to minimize electromagnetic interference. Careful attention should also be given to minimizing any timing jitter that is introduced in converting timing signals and distributing the signals to the beamlines and end stations. In particular, it may be advantageous to have several sources of timing signals (APDs or striplines), with each source serving as a local timing signal for a cluster of beamlines.